AMERICAN UNIVERSITY OF BEIRUT

CONTROLLING THE THERMAL TRANSMITTANCE OF GLASS BY COATING WITH A BROAD-BAND HYPERBOLIC MATERIAL

by
SAHAG SETRAK BOZOIAN

A thesis
submitted in partial fulfillment of the requirements
for the degree of Master of Science
to the Department of Physics
of the Faculty of Arts and Sciences
at the American University of Beirut

Beirut, Lebanon
January 2022

AMERICAN UNIVERSITY OF BEIRUT

CONTROLLING THE THERMAL TRANSMITTANCE OF GLASS BY COATING WITH A BROAD - BAND HYPERBOLIC MATERIAL

by
SAHAG SETRAK BOZOIAN

Approved by:

Signature

Dr. Michel Kazan, Associate Professor
Department of Physics

Advisor

Signature

Dr. Malek Tabbal, Professor
Department of Physics

Member of Committee

Signature

Dr. Mohammad Haidar, Assistant Professor
Department of Physics

Member of Committee

Date of thesis defense: January 27, 2022

AMERICAN UNIVERSITY OF BEIRUT

THESIS RELEASE FORM

Student Name: Bozoian Sahag Setrak
Last First Middle

I authorize the American University of Beirut, to: (a) reproduce hard or electronic copies of my thesis; (b) include such copies in the archives and digital repositories of the University; and (c) make freely available such copies to third parties for research or educational purposes:

☐ As of the date of submission

☒ One year from the date of submission of my thesis.

☐ Two years from the date of submission of my thesis.

☐ Three years from the date of submission of my thesis.

Sahag R February/01/2022
Signature Date

ACKNOWLEDGEMENTS

“ […] For I know the plans I have for you”, declares the Lord, “ plans to prosper you and not to harm you, plans to give you hope and a future.[”] (Jeremiah 29: 11)

[“] Trust in the Lord with all your heart and lean not on your own understanding, and in all your ways acknowledge him, and he will make your paths straight. [“] (Proverbs 3: 5-6)

[“] I will give thanks to the Lord because of his righteousness

and will sing praise to the name of the Lord Most High. [“] (Psalm 7:17)

First and foremost, I would like to thank my God and Lord for all of the generous blessings that He bestows on us daily, praising and thanking Him for showing me His plan and purposes for my future, for granting me this path and opportunity, for guiding me, and for introducing me to warm and kind-hearted people... I would glorify Him with joyous prayers and songs, and I would honor Him for these accomplishments and degrees, which would not have been possible without His love and strength... praising the Lord for all eternity

I would like to express my gratitude to my adviser, Prof. Michel Kazan, for your assistance, kindness, friendship, and guidance. Thank you for giving me the chance to be a part of your research team and for believing in and encouraging me during difficult moments. I'd want to extend my appreciation and honor to life for having the opportunity to know, learn from, and work with such an amazing, intelligent, friendly, kindhearted adviser. I wish you all the best, especially prosperity and progress in your professional endeavors, objectives, and life.

In the same vein, I'd want to thank all of the committee members, Prof. Mohammad Haidar and Prof. Malek Tabbal, for their encouragement, support, and guidance in reaching the aims and outcomes of this research work and academic scripts. Similarly, I wish them the best of luck in their future endeavors and life.
I'd like to express my deepest gratitude to all of the professors in the physics department at AUB, especially Prof. Jihad Touma, Prof. Ali Chamseddine, Prof. Leonid Klushin, Prof. Sara Najim, and Prof. Waffic Sabra, for their incredible dedication in guiding me through these master's years and providing me with the tools, creativity, knowledge, and analytical thinking to overcome difficult problems not only in academic and research sectors but also in life.

This academic effort would not have been possible without the experimental tools and labs provided by the American University of Beirut and the Center for Research and Scientific Laboratories (CRSL). Furthermore, we are grateful to warmhearted, friendly persons, particularly Mrs. Rania Shatila, Mr. Joan Younes, Mr. Samer, and many others, for instructing, aiding, and manufacturing the essential experimental tools and instruments. I'd want to take this opportunity to extend my heartfelt gratitude and admiration to Dr. Joan

Younes, for his warm smile and kind heart, as well as his inspirational expertise in dealing with challenging difficulties and experimental instruments. I wish Dr. Joan the best of luck in your future work and life, as well as prosperity, good health, and happiness for your family.

Most importantly, my genuine and heartfelt gratitude goes to my parents and the Bozoian, Boghossian, and Yeterian families, for their prayers, encouragement, support. I would not have gotten this far without their unending love and wisdom, and I dedicate my academic script to them, especially my mother, wishing them all the best, good health, and happiness in life…

I am grateful to Lebanon for giving me shelter, culture, traditions, relatives, and a place to call home. Hoping and praying that present challenges will be overcome, expanding into the light of prosperity and brightness. I also hope that the world would use scientific knowledge and wisdom for greater goodness, peace, prosperity, and most importantly to preserve the life and beauty of our planet Earth for future generations. Finally, I would advise the future generation to believe in themselves and their faith, to dream big, and to never give up on trying and exploring life to the fullest.

ABSTRACT
OF THE THESIS OF

Sahag Setrak Bozoian for Master of Science
Major: Physics

Title: Controlling the Thermal Transmittance of Glass by Coating with a Broad-Band Hyperbolic Material

Hyperbolic metamaterials are nano-engineered materials with dielectric function components of opposite signs, allowing them to function as metals in some directions and as dielectrics or insulators in others. They are expected to play an important role in future optical, electrical, and thermal applications. Some natural anisotropic materials or combinations of natural materials, such as transparent conducting oxides or nitrides, function as potential hyperbolic metamaterials over a narrow infrared spectral range.

Due to the fact that the structure of ZnO thin films obtained by pulsed laser deposition is columnar and often contains a high density of free electrons, these films can exhibit strong anisotropy and hyperbolic behavior in a wide spectral range. This process can be of utmost importance to control solar infrared radiation and prevent heating of the vehicle interior. The main objective of this thesis is to study the planar and transverse dielectric constants of ZnO thin films grown on glass over a wide infrared spectral range and to investigate the potential application of coating glass with ZnO films to reduce the transfer of solar radiation to absorbing materials in the vehicle.

Using the pulsed laser deposition methods, thin ZnO thin films of different thicknesses were deposited on glass substrates of different thicknesses. The obtained samples were analyzed using XRD, UV-VIS spectroscopy, SEM, and FTIR spectroscopy. XRD and SEM measurements indicated that the produced films are granular, but well oriented along the c-axis. Spectroscopic measurements in the UV-VIS-NIR range showed that the samples ellaborated transparent in the visible spectrum, which is crucial to maintain the vehicle glasses transparent. The in-plane and cross-plane complex infrared dielectric functions of the samples ellaborated were investigated using accurate analysis of the infrared reflectivity spectrum. It was demonstrated that thin ZnO films deposited on glass exhibit hyperbolic behavior over a wide infrared spectral range and the ratio of the cross-plane to the in-plane dielectric constant can be tuned through the film thickness. The results of this thesis would allow controlling the direction of the solar radiation incident on the vehicle glass when it is coated by a ZnO film of a specific thickness

TABLE OF CONTENTS

ILLUSTRATIONS

Figure

TABLES

Table

CHAPTER I

INTRODUCTION

In recent years, technological advancement and development have resulted in a deeper understanding of the physical processes that occur in semiconductors. This progress has led to successful manufacturing and growth micro/nano-sized systems and devices [1]. Nanostructured semiconducting materials are now used in integrated circuit manufacturing, acoustic, optical, and optoelectronic applications, as well as numerous industrial developments.

The understanding of the laws governing the behavior of light in semiconductors has also opened the door to many applications in which energy is transported and guided very precisely using photons as heat carriers. The confinement and guidance of infrared light has been of particular interest since the discovery of hyperbolic materials. These materials exhibit sub-diffraction, highly irectional, volume-confined polariton modes. Subdiffracted wave propagation in hyperbolic media offers many unusual optical possibilities such as hyperlensing, negative refraction, quantum enhanced radiation, nanolithography and subdiffracted resonators. It has been shown that the highly directional propagation of hyperbolic polaritons (HP) confined in the volume is the key to these sub-diffracton phenomena. Their directionality derives from the sign and magnitude of the two principal components (in-plane and cross-plane) of the dielectric permittivity tensor, which have opposite signs in hyperbolic materials. The propagation angle θ (e.g., the angle between the Poynting vector and the z-axis) of HPs in hyperbolic media can be approximated by the following formula $\theta = \pi / 2 - arctan\left(\frac{\sqrt{\varepsilon_z}}{i\sqrt{\varepsilon_x}}\right)$, where $\varepsilon_z = \varepsilon_{zz}$ and $\varepsilon_t = \varepsilon_{xx} = \varepsilon_{yy}$ are the cross-plane and in-plane dielectric permittivity, respectively. Therefore, by controlling the ratio between the two main dielectric components, the direction of HP propagation can be changed.

In addition to their potential application in photonic technologies, hyperbolic materials can be used to guide heat, if they are functional in a wide infrared spectral range. They can also be used to deflect solar infrared radiation and reduce the heating of vehicle interiors when exposed to the sun for long periods on a hot summer day. This application of hyperbolic materials is of particular interest given the large number of annual deaths of children from heatstroke after being left unattended inside vehicles. Indeed, 42 such cases were recorded in 2019, compared to a national average of 29 in the previous five years. Previous research found that when ambient temperatures exceeded 86°F, internal vehicle temperatures rose rapidly to 134 to 154°F.

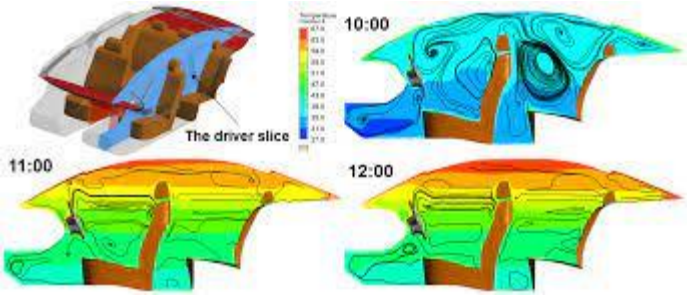

Figure 1: illustrates the heat distribution in the interior of a vehicle left under the sun through the day [2].

Indeed, the hyperbolic material used on vehicle glasses must be transparent. The best candidate for this application is zinc oxide (ZnO) semiconductor grown by pulsed laser deposition (PLD) technique for the following reason. In addition to its transparency in the visible spectral range, it is known that PLD-grown ZnO has a well-oriented columnar structure, which makes the free carriers more confined in the plane direction. This effect can increase the anisortopy of the ZnO Wurtzite lattice structure and lead to the desired hyperbolic material.

In this thesis, we study the application of thin ZnO films as a hyperbolic material on glasses.

An additional factor that contributed to the selection of ZnO as a coating material is that it is an oxide, and unlike nitrides or other materials, it does not oxidize when exposed to oxygenized or oxygen-containing environments, which reduces the generation of impurities or vacancies that alter its properties.

Thesis is divided into sections. The chapters in the theoretical section introduce the theories needed to fully comprehend and address the optical, and radiative properties. The second chapter concentrates on revising the Maxwell Equation, which serves as the foundation for the remaining optical and radiative theoretical derivations. The third chapter highlights the concept of the dielectric function, which is necessary to study the optical properties of thin films, by introducing free carriers and oscillation images, within the Drude and Lorenz models. It also presents the Cauchy integral, which is required for measuring and estimating the dielectric function's real and imaginary parts.

Chapter IV looks at some of the previous scholarly research and work on this topic. This literature review briefly covers the deposition methods and conditions, as well as recent findings related to some of the properties of ZnO.

The experimental section follows by an introduction to the pulsed laser deposition technique (Chapter V) used in growing ZnO films on glass substrates, covering its components and advantages over other deposition techniques. Chapters VI, VII and VIII are devoted introduce the characterization techniques used in the thesis. They provide the basic theories of X-ray SEM, and UV-VIS spectroscopy. Finally, Chapter IX discribes the infrared spectroscopy and the FTIR. It covers; including the theory and experimental apparatus that underpin these spectroscopic systems.

The results obtained in this thesis are presented in Chapter X, and the fundamental properties will be evaluated. Then a summary of the thesis, as well as concluding remarks and recommendations for future research in our field are provided.

SECTION I

THEORETICAL BACKGROUND

CHAPTER II

ELECTROMAGNETIC WAVE THEORY

Maxwell's equations govern the interaction of light or electromagnetic waves with semiconductors, they were developed by Scottish physicist James Clerk Maxwell in 1873 [1]. Semiconductors contain both free and bound charged particles; the former are electrons and holes in the conduction and valence bands, while the latter are electrons or holes or any other particles bound to core atoms within the lattice, forming ions. The theoretical foundation of optical phenomena will begin with Maxwell's equations, which are given below:

$$\nabla \times E = -\frac{\partial B}{\partial t} \qquad \text{Eq. (2.1)}$$

$$\nabla \times H = J + \frac{\partial D}{\partial t} \qquad \text{Eq. (2.2)}$$

$$\nabla . D = \rho \qquad \text{Eq. (2.3)}$$

$$\nabla . B = 0 \qquad \text{Eq. (2.4)}$$

Where E is the electric field, H is the magnetic field given by $H = \frac{B}{\mu}$, B being the magnetic flux density and μ is the magnetic permeability of the material. J is the electric charge density given by $J = \sigma E$ where σ is the electrical conductivity. D is the electric displacement given by $D = \varepsilon E$; where ε is the electric permittivity of the material. [1]

In describing the above Maxwell equations, Eq. (2.1) is known as Faraday's law, which simply states that time variation of the magnetic field creates an electric field lines, and Eq. (2.2) is known as Ampere-Faraday law, which states that time variation of the electric field or electric displacement creates a magnetic field within the material. Magnetic fields are created by the density and displacement of electric charges. In other words, these two laws can be summarized by the following absurd description: a variation in the magnetic field produces electric fields and vice versa. " Eq. (2.3) represents Gauss's law, which states that the sum of the electric fields within a closed surface is proportional to the total charge within this surface with the permittivity of the materials as the proportionality constant. Finally, Eq. (2.4) is analogous to the Gauss law but for magnetic fields, stating that no magnetic monopoles exist". [1]

The following second order differential equation expresses the propagation of the wave within the medium as depicted by the Maxwell equations:

$$\nabla^2 E = \mu\varepsilon \frac{\partial}{\partial t}\left(\frac{\partial E}{\partial t}\right) \qquad \text{Eq. (2.5)}$$

That has a solution of the form:

$$E = Eo\left(e^{-i(\omega t - K.r)}\right) \qquad \text{Eq. (2.6)}$$

"Where Eo is the amplitude of the wave, K is the wavenumber and ω is the angular frequency with the following relation $vp = \frac{\omega}{K} = \frac{1}{\sqrt{\mu\varepsilon}}$, where v_p is the phase velocity of the wave and in the vacuum, it is equal to the speed of light c ($c \approx 3*10^8$ m/sec)" [1]. The magnetic and electric fields within the material (i.e. the Maxwell equations) can be written in operator form using the above Eq. (2.6) as follows:

$$K \times E = \omega\mu H \qquad \text{Eq. (2.7)}$$

$$K \times H = -\omega\varepsilon E \qquad where\ J = 0 \qquad \text{Eq. (2.8)}$$

Finally, the ratio of the phase velocity of the wave within the medium to the speed of light yields the medium's index of refraction, which is expressed as:

$$n = n(\lambda) = \frac{c}{vp} = \sqrt{\frac{\mu\varepsilon}{\mu_o\varepsilon_o}} \qquad \text{Eq.(2.9)}$$

The electric and magnetic fields present on the medium polarize the material by creating dipole moments, with a net dipole moment per volume $Dm = \rho d$, where Dm is the net dipole moment per unit volume, ρ charge density per unit volume, and d is the distance between charges within the dipole, as shown in Fig (2). [1]

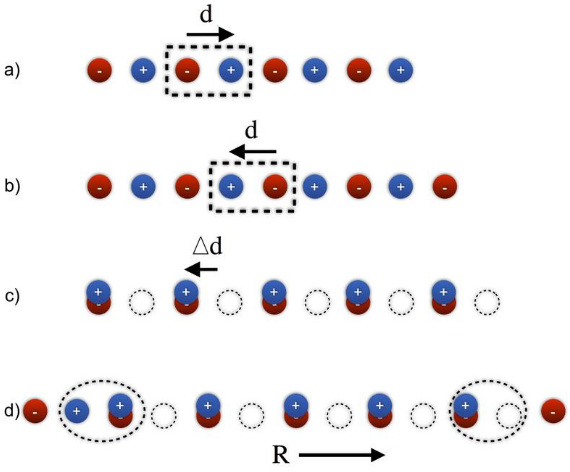

Figure 2 : schematic representation of the polarization of charged particles within a medium under external electromagnetic field [14,15]

The microscopic dipoles formed within the medium will be aligned in the direction of the applied external electromagnetic fields [14,15], as shown schematically in Fig (3) for a hexagonal lattice as an example, with polarization proportional to the electric field, as shown below for isotropic and homogeneous materials:

$$P = \varepsilon_O \chi E \qquad \text{Eq. (2.10)}$$

Where ε_o is the permittivity of the free space and χ is the susceptibility of the medium or the material. It should be noted that the directional optical properties of anisotropic or inhomogeneous materials are expressed using the above Eq. (2.10) but in tensor notations. [1]

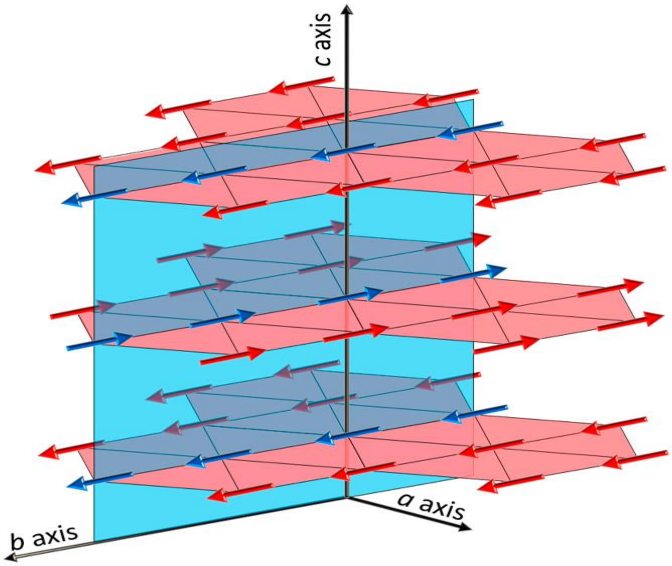

Figure 3: schematic representation of the alignment of microscopic dipoles with a hexagonal shaped and isotropic material following the direction of the externally applied field [194]

The electric displacement of the material changes when it is polarized, and it is expressed by the basic eqs. given below:

$$D = \varepsilon_O E + P = \varepsilon_o (1 + \chi) E = \varepsilon_o \varepsilon_r E \qquad \text{Eq. (2.11)}$$

With

$$\varepsilon_r = \varepsilon_{latt} = \frac{\varepsilon}{\varepsilon_o} = 1 + \chi \qquad \text{Eq. (2.12)}$$

Where E, D, and P are the electric fields, electric displacement, and polarization respectively, $\varepsilon_{o(r)}$ are a dielectric function of free space (dielectrics) and the relative or lattice dielectric function, respectively, and χ is the susceptibility of the material. It should be noted, that the relative dielectric functions vary with frequency. [1]

Using the definition of current charge density given above, the dielectric functions for non-magnetic materials can be extracted from the waveequation, Eqs. (2.5) to (2.8), as follows: [1,5-15]

$$\nabla^2 E = \mu_o \sigma \frac{\partial E}{\partial t} + \mu_o \varepsilon_r (\frac{\partial}{\partial t^2}^2 E) \qquad \text{Eq. (2.13)}$$

Using the notations given in Eq. 2.6, the above differential equation for waves is reduced to:

$$K^2 E - K.(K.E) = i\omega\mu_o \sigma E + \omega^2 \mu_0 \varepsilon_r \varepsilon_o E \qquad \text{Eq. (2.14)}$$

The above equation, namely Eq. (2.14), is further reduced by using Maxwell's equations:

$$K^2 = i\omega\mu_o \sigma + \omega^2 \mu_o \varepsilon_o \varepsilon_r \qquad \text{Eq. (2.15)}$$

Therefore the total dielectric response function of a nonmagnetic material under the influence of an external field is defined as [1, 5-15]

$$\varepsilon(\omega) = \frac{K^2}{\mu_O \varepsilon_O \omega^2} = \varepsilon_r(\omega) + i\left(\frac{\sigma}{\varepsilon_o \omega}\right) = \varepsilon 1 + i\,\varepsilon 2 \qquad \text{Eq. (2.16)}$$

where ε1(2) denotes the real and imaginary parts of the dielectric response function and ε is the material's total dielectric response function, which translates the interaction of semiconducting materials with linear electromagnetic waves. In the case of nonlinear electromagnetic fields, such as elliptical or circular polarized fields, a similar equation to that of Eq. (2.16) can be expressed for longitudinal or transverse directions, i.e., $E = E_T + E_l$, where $E_{T(l)}$ is the transverse and longitudinal components of the electric field, thus splitting the above Eqs. (2.16) into desired directional components, with Eq. (2.14) modified as follows:

$$[\left(\frac{\omega}{c}\right)^2 \varepsilon(\omega) - K^2\Big] E_t t + \left(\frac{\omega}{c}\right)^2 \varepsilon(\omega) E_k k = 0 \qquad \text{Eq. (2.17)}$$

The transverse and longitudinal components are reduced by the above equation:

$$K^2 = \left(\frac{\omega}{c}\right)^2 \varepsilon(\omega) \quad \text{and} \quad (K_l)^2 = \varepsilon_l(\omega) = 0 \qquad \text{Eq. (2.18)}$$

The medium's index of refraction is defined as:

$$n_r{}^2 == (n + ik)^2 = \frac{K\,c}{\omega} = \varepsilon(\omega) = \varepsilon 1 + i\varepsilon 2 \qquad \text{Eq. (2.19)}$$

With the dielectric response function's real and imaginary parts expressed as:

$$\varepsilon 1 = n^2 - k^2 \qquad and \qquad \varepsilon 2 = 2nk \qquad \text{Eq. (2.20)}$$

where n is the index of refraction and k is the decay coefficient, these are referred to as optical constants [1], and nr is the complex index of refraction of the nonmagnetic medium, which is related to the complex dielectric response function of the nonmagnetic material as expressed above. Similarly, the index of refraction n and decay coefficient k can be expressed in terms of dielectric respond function as shown below: [5-15]

$$n = \left(\frac{1}{\sqrt{2}}\right)\sqrt{\varepsilon 1 + |\varepsilon|} \quad \text{and} \quad k = \left(\frac{1}{\sqrt{2}}\right)\sqrt{-\varepsilon 1 + |\varepsilon|} \qquad \text{Eq. (2.21)}$$

Then the Eq. of the wave becomes:

$$E = Eo(e^{-k2.r})\left(e^{-i(\omega t - K1.r)}\right) \qquad \text{Eq. (2.22)}$$

It shows that the amplitude of the modified wave equation decays. This demonstrates that as the wave enters the medium, it begins to decay as a result of its interaction with the medium. The exponent of the exponential in the amplitude represents the medium's absorption coefficient, which is related to the depth of penetration of the radiation into the medium, and is expressed as:[1]

$$\alpha = k2k = \frac{4\pi}{\lambda}k \qquad \text{Eq. (2.23)}$$

$$and$$

$$\gamma = \frac{1}{\alpha} = \frac{\lambda}{4\pi\kappa} \qquad \text{Eq. (2.24)}$$

where α(γ) is the penetration depth (or photon mean free path) and is the absorption coefficient [1].

“A similar analysis can be performed for current density and pure magnetic materials, yielding”: [1]

$$\sigma = \sigma 1 + i\sigma 2 = \sigma - i\omega\varepsilon_r(\omega) \quad \text{Eq. (2.25)}$$

$$\mu_r(\omega) = \mu 1 + i\mu 2 = \frac{\mu_m}{\mu_o} \quad \text{Eq. (2.26)}$$

where σ1(2) denotes the real and imaginary parts of relative charge density, and μ1(2) denotes the real and imaginary relative permeability of magnetic materials. These real and imaginary components of the relative charge density can be expressed in terms of real and imaginary components of the dielectric response function as follows: [1, 5-15]

$$\sigma 2 = -\omega\varepsilon_o\varepsilon 1 \qquad and \qquad \varepsilon 2 = \frac{\sigma 1}{\omega\varepsilon_o} \quad \text{Eq. (2.27)}$$

with the material's complex index of refraction given by:

$$n\,(\omega) = \sqrt{\varepsilon(\omega)\mu(\omega)} \quad \text{Eq. (2.28)}$$

When incident light strikes a thin film, it undergoes refraction (transmission) and reflection, as illustrated in the fig (4) below:

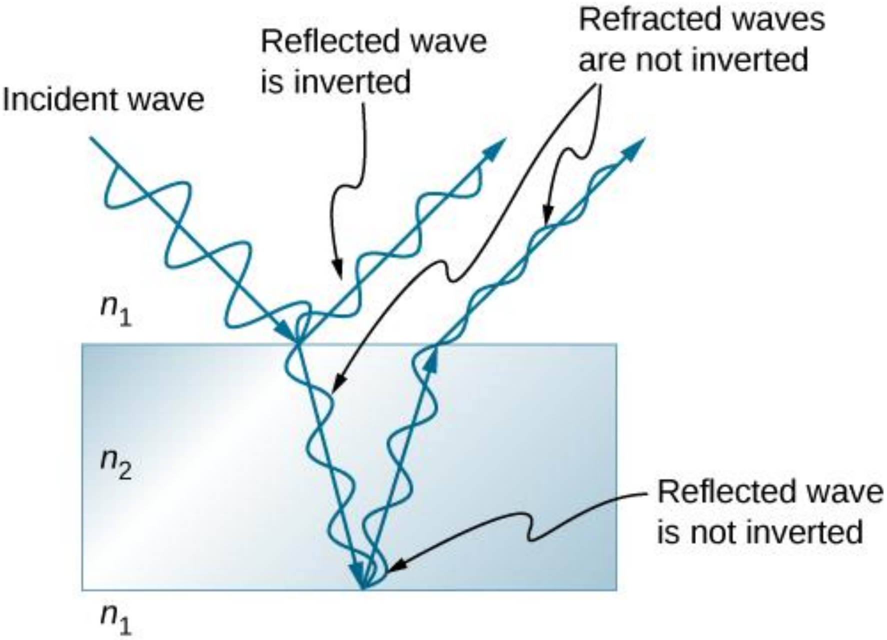

Figure 4: figure depicting the incident, reflected and refracted light waves upon its interaction with medium of the index of refraction n_2 [195]

Using the Fresnel, Snell, and Maxwell equations, along with the boundary (continuity) conditions, one can obtain the reflective, transmission, and absorptivity coefficients for s and p polarized waves: [1, 5-15]

For s-polarized (transverse electric waves) waves: [1, 5 -15]

$$r_s = \frac{\frac{k_{1z}}{\mu_1} - \frac{k_{2z}}{\mu_2}}{\frac{k_{1z}}{\mu_1} + \frac{k_{2z}}{\mu_2}} = \frac{n_1 \cos(\theta_1) - n_2 \cos(\theta_2)}{n_1\, cos(\theta_1) + n_2 cos(\theta_2)} \qquad \text{Eq. (2.29)}$$

$$t_s = \frac{2\frac{k_{1z}}{\mu_1}}{\frac{k_{1z}}{\mu_1} + \frac{k_{2z}}{\mu_2}} = \frac{2n_1\, cos(\theta_1)}{n_1\, cos(\theta_1) + n_2 cos(\theta_2)} \qquad \text{Eq. (2.30)}$$

The absorptivity is expressed as follows:

$$\alpha = \frac{Re(\frac{k_2}{\mu_2})}{Re(\frac{k_1}{\mu_1})}\,|t_s|^2 = \frac{n_2 cos(\theta_2)}{n_1\, cos(\theta_1)}\,|t_s|^2 \qquad \text{Eq. (2.31)}$$

In the case of p-polarized waves (or transverse magnetic waves): [1, 6-16]

$$r_s = \frac{\frac{k_{1z}}{\varepsilon_1} - \frac{k_{2z}}{\varepsilon_2}}{\frac{k_{1z}}{\varepsilon_1} + \frac{k_{2z}}{\varepsilon_2}} = \frac{n_2 \cos(\theta_1) - n_1 \cos(\theta_2)}{n_2\, cos(\theta_1) + n_1 cos(\theta_2)} \qquad \text{Eq. (2.32)}$$

$$t_s = \frac{2\frac{k_{1z}}{\varepsilon_1}}{\frac{k_{1z}}{\varepsilon_1} + \frac{k_{2z}}{\varepsilon_2}} = \frac{2n_2\, cos(\theta_1)}{n_2\, cos(\theta_1) + n_1 cos(\theta_2)} \qquad \text{Eq. (2.33)}$$

The absorptivity is expressed as follows: [1, 5-15]

$$\alpha = \frac{Re(\frac{k_2}{\varepsilon_2})}{Re(\frac{k_1}{\varepsilon_1})}\,|t_p|^2 = \frac{n_2 cos(\theta_1)}{n_1\, cos(\theta_2)}\,|t_p|^2 \qquad \text{Eq. (2.34)}$$

Assuming normal incidence, the above reflective and transmission coefficients for s- polarization and p-polarization are connected with each other as follows:

$$r_s = \frac{n_1 - n_2}{n_1 + n_2} = -r_p \qquad \text{Eq. (2.35)}$$

The reflectivity coefficient is the ratio of the reflected electric wave to the incident wave, and the transmission coefficient is the ratio of the transmitted wave to the incident wave, both of which are expressed as [1, 5 - 15]

$$R(\omega) = r(\omega)e^{i\theta(\omega)} \quad \text{Eq. (2.36)}$$

$$R = \frac{E_{ref}}{E_{in}} \quad \text{Eq. (2.37)}$$

$$T(\omega) = t(\omega)e^{i\theta(\omega)} \quad \text{Eq. (2.38)}$$

$$T(\omega) = \frac{E_{trans}}{E_{in}} \quad \text{Eq. (2.39)}$$

Finally, the reflectivity and transmissivity are calculated as follows:

$$R = |R(\omega)|^2 = rr^* \quad and \qquad T = |T(\omega)|^2 = tt^* \quad \text{Eq. (2.40)}$$

The reflectivity of anisotropic material with normal incidence is given by:

$$R = \left|\frac{n_2 - 1}{n_2 + 1}\right|^2 = \left|\frac{\sqrt{\varepsilon} - 1}{\sqrt{\varepsilon} + 1}\right|^2 \quad \text{Eq. (2.41)}$$

with the reflectivity coefficient denoted by: [1]

$$R(\omega) = \frac{n + ik - 1}{n + ik + 1} \quad \text{Eq. (2.42)}$$

Alternatively, the reflectivity can be expressed as:

$$R(\omega) = \frac{(n-1)^2 + (k_2)^2}{(n+1)^2 + (k_2)^2} \quad \text{Eq. (2.43)}$$

The reflectivity of an unpolarized, circular, or mixed polarized wave is calculated as follows: [5-15]

$$R = \frac{R_s + R_p}{2} \qquad \text{Eq. (2.44)}$$

CHAPTER III

OPTICAL PROPERTIES THEORETICAL BACKGROUND

After introducing the fundamentals of electromagnetic theory in semiconductors, the basic foundation for addressing the optical properties of any semiconductor material has been established. The most important material optical properties for device fabrication and application are the dielectric function and the refractive index. To this end, many models have been proposed and used to calculate and manipulate them. This section introduces, explains and builds some of these models based on classical or semi-classical concepts.

A. Models to calculate Dielectric Function:

1. The Drude model free carriers:

This model simply describes the motion of free carriers within a semiconductor under the influence of an external electromagnetic field. It states that in the absence of this external field, electrons or free carriers within a semiconductor have random motions with zero average velocity (similar to random walk motion), but once the field is turned on or applied, the electrons align themselves in the direction of the external field, resulting in non-zero average velocities, carrying current and heat from which basic semiconductor properties are formed, such as electric and thermal conductivities. The motion of an electron or free carrier can be depicted using the simple concepts and equations derived from Newton's equations of motion as listed below: [1, 5-15]

$$m_e \ddot{x} = -m_e \gamma \dot{x} - eE \quad \text{Eq. (3.1)}$$

where m is the mass of the electron, e is its absolute charge, E is the applied external electric field, γ is the strength of the electron's collision with nearby molecules and atoms (inverse relaxation time or scattering rate).

The applied electric field can be a harmonic field of the form: $E = E_o e^{-i\omega t}$ where E_o is the amplitude of the field and ω its angular frequency. Then the above differential equation has a solution of similar form $x = x_o e^{-i\omega t}$ with following the second derivative $\ddot{x} = -i\omega\dot{x} = -\omega^2 x$ which leads to the following expression for their velocity: [1, 5 -15]

$$\frac{dx}{dt} = \frac{\frac{eE}{m}}{i\omega - \gamma} \quad \text{Eq. (3.2)}$$

Using the relationships $J = \sigma E = -n_e e\dot{x}$ along with Eqs. (2.16) and (2.20), one can calculate the conductivity, dielectric function, and refractive index as follows: [1, 5-15]

$$\sigma(\omega) = \frac{\frac{n_e e^2}{m_e}}{\gamma - i\omega} = \frac{\sigma_o}{1 - i(\frac{\omega}{\gamma})} \quad \text{Eq. (3.3)}$$

$$where$$

$$\sigma_o = \frac{n_e e^2}{m_e \gamma} = \frac{n_e e^2 \tau}{m_e} \quad \text{Eq.(3.4)}$$

with σ_o is the DC electric conductivity.

The dielectric function is defined in the same way:

$$\varepsilon(\omega) = \varepsilon_\infty - \frac{\sigma_o \gamma}{\varepsilon_o(\omega^2 + i\omega\gamma)} = \varepsilon_\infty - \frac{{\omega_p}^2}{\omega(\omega + i\gamma)} \quad \text{Eq. (3.5)}$$

With

$$\omega_p{}^2 = \frac{\sigma_o \gamma}{\varepsilon_o} = \frac{n_e e^2}{m_e \varepsilon_o} \qquad \textit{the plasma frequency} \qquad \text{Eq. (3.6)}$$

If ω>>γ the above dielectric function can be approximated by :

$$\varepsilon(\omega) \approx \varepsilon_\infty - \frac{\omega_p{}^2}{\omega^2}\left(1 - i\frac{\gamma}{\omega}\right) \qquad \text{Eq. (3.7)}$$

Finally, the refractive index and decay coefficient are roughly calculated as follows:

$$n \approx k \approx \sqrt{\frac{\sigma_o}{2\omega\varepsilon_o}} \qquad \text{Eq. (3.8)}$$

The Drude model yields reasonably accurate results at the room, intermediate, and high temperatures but fails to yield accurate results at low temperatures [1, 5-15]. As a result of these factors, new models were proposed, one of which is the Lorentz model, which is described below.

2. The Lorentz or Dipole Oscillator Model:

The Lorentz model provides a classical picture of carrier motion within a material. It resembles carrier motion to a classical damped harmonic oscillator, as shown in Fig (5) below, and it aids our understanding of semiconductor optical properties. The model starts with a damped oscillator's equation of motion with a restoring force provided by an applied external field: [1, 5-15]

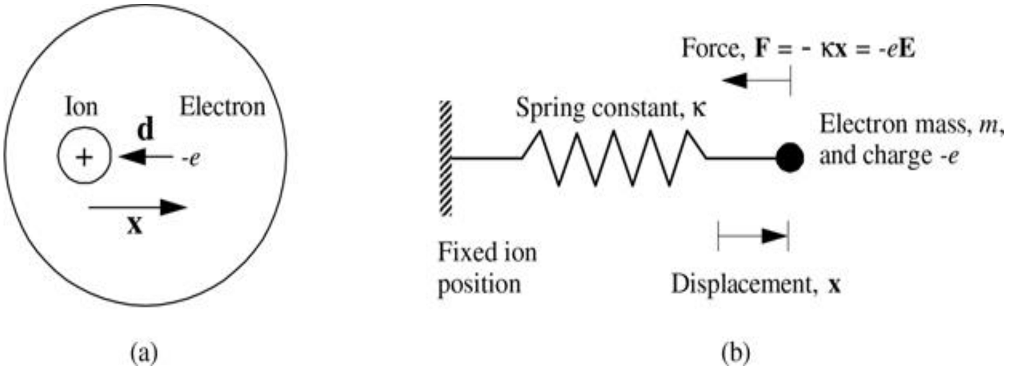

Figure 5: figure (a) showing the motion of electron being scattered with ions, (b) the electron is resembled by damped Lorentz oscillator with restoring force being the field itself [196]

$$\mu\frac{d}{dt}\left(\frac{dx}{dt}\right)+\ \mu\gamma\frac{dx}{dt}+\mu{\omega_j}^2x=\ -eE_oe^{-i\omega t} \quad \text{Eq. (3.9)}$$

where all of the above differential equation's components have the same definition as that in the Drude model, with minor differences such as μ used here denoting the reduced mass of the carriers with index j representing the number of the oscillator. Using the same procedure as described above in the Drude model, the solution is as follows: [1, 5-15]

Eq. (3.10)

$$x = \frac{\frac{e}{\mu}}{{\omega_j}^2 - i\gamma_j\omega - \omega^2} E_o$$

where

$$\omega_j = \sqrt{\frac{K_j}{\mu_j}}$$ *is the resonance frequency* Eq. (3.11)

The preceding equation namely Eq. (3.10) can be used to calculate the total polarization and electric displacement along with the dielectric function:

$$P = \sum_{j=1}^{N} n_j ex = Nex = \frac{\frac{Ne^2}{\mu}}{{\omega_{TO}}^2 - i\gamma\omega - \omega^2} E_o$$ Eq. (3.12)

where T stands for infrared-active transverse phonon. Only the transverse components of the carriers are IR active and can contribute to the optical properties of the semiconductor [1, 5-15]. It is important to note that the summation includes all of the carriers or oscillators. Similarly, the following electric displacement and dielectric functions are provided by: [1, 5-15]

$$D = \varepsilon_o(1 + \chi)E + \frac{\frac{Ne^2}{\mu}}{{\omega_{TO}}^2 - i\gamma\omega - \omega^2} E$$ Eq. (3.13)

$$\varepsilon(\omega) = 1 + \chi + \frac{\frac{Ne^2}{\mu\varepsilon_O}}{{\omega_{TO}}^2 - i\gamma\omega - \omega^2}$$ Eq. (3.14)

For high and low frequencies, equation Eq. (3. 14) reduces to:

$$\varepsilon(\omega) = 1 + \chi \qquad if\ \omega_{TO}{}^2 \ll i\gamma\omega + \omega^2 \to \infty \qquad \text{Eq. (3.15)}$$

$$\varepsilon_s(\omega) = 1 + \chi + \frac{Ne^2}{\mu\varepsilon_O\omega_{TO}{}^2} \qquad if\ \omega_{TO}{}^2 \gg i\gamma\omega + \omega^2 \qquad \text{Eq.(3.16)}$$

The Lorentz equation is reduced to the Lyddane-Sachs-Teller relation for an ideal case with zero dampings, i.e. no friction, which is essential in polar crystals, where the optical phonons split into transverse and longitudinal modes, as shown below: [1, 5 -15]

$$\frac{\omega_{LO}{}^2}{\omega_{TO}{}^2} = \frac{\varepsilon_s}{\varepsilon_\infty} \qquad \text{Eq. (3.17)}$$

$$And$$

$$\frac{\varepsilon(\omega)}{\varepsilon_\infty} = 1 + \frac{\omega_{LO}{}^2 - \omega_{TO}{}^2}{\omega_{TO}{}^2 - i\gamma\omega - \omega^2} \qquad \text{Eq.(3.18)}$$

Finally, we define a set of parameters $S_j = \frac{\omega_{pj}{}^2}{\omega_j{}^2} = \frac{n_j e^2}{\mu_j\varepsilon_o\omega_j{}^2}$ that shows the strength of the oscillation [1, 5 -15]. As a result, in the non-ideal case, the Lorentz model can be written as follows:

$$\varepsilon(\omega) = \varepsilon_\infty + \sum_{j=1}^{N} \frac{S_j\omega_j{}^2}{\omega_j{}^2 - i\gamma_j\omega - \omega^2} \qquad \text{Eq. (3.19)}$$

where ε_∞ denotes the dielectric function at extremely high frequencies, the real and imaginary parts of the dielectric function can be used to calculate the oscillator's index of refraction and decay coefficients. Experiments have revealed that the index of refraction decreases with increasing frequency, a strange result known as the anomalous dispersion relation [1, 5- 15], as illustrated by the graphs in figs 6 to 8. The classical picture approximates the longitudinal and transverse modes, and more accurate results require quantum mechanical description. [1, 5 -15]

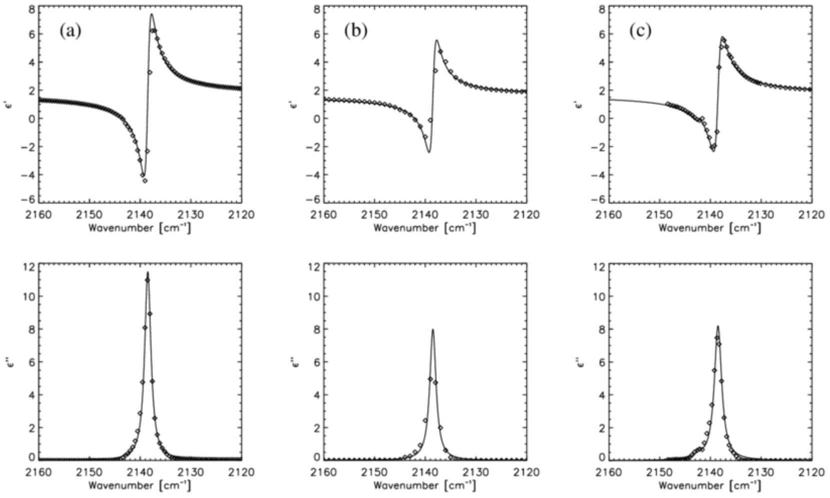

Figure 6: graphs comparing the real and imaginary parts of the dielectric response function by Lorentz method of CO ice of different structures using VLT spectroscopic measurements. [17, 18]

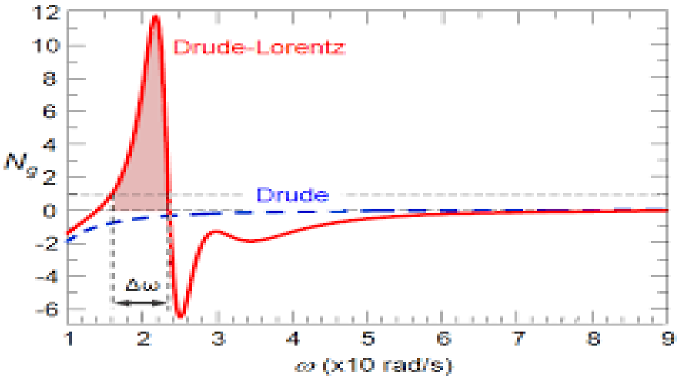

Figure 7: Graph comparing the index of refraction using Drude model (blue) and Lorentz model (red) [18, 19]

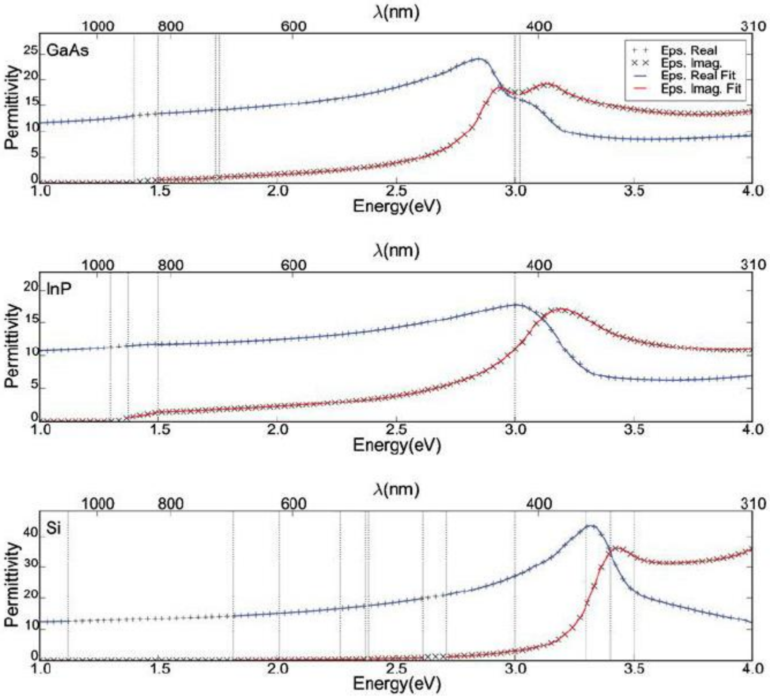

Figure 8: graphs showing the dielectric permittivity versus energy for GaAs, IP, and Si using the Lorentz model [18, 20].

B. Effect Of Point Defect On Free Carriers and Optical Properties:

Experiments and theories revealed that the dielectric functions and related optical property degradation is primarily caused by defects and vacancies during the deposition and post-deposition handling phases. On the other hand, by introducing dopants, efforts were made to improve these optical properties or to mitigate the effects of defects.

Dislocation, antisites, isotopes, are among the aforementioned defects and impurities. All of these flaws and impurities are depicted in Figs (9) and (10). [1, 5-15,118, 119]

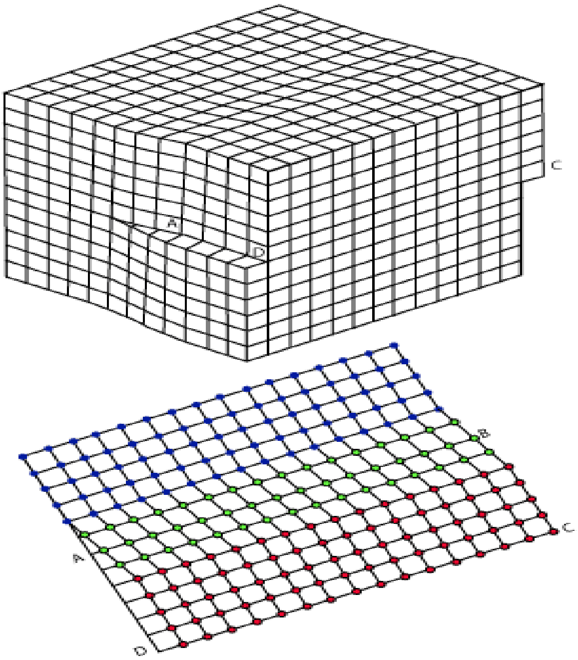

Figure 9: schematic representation of point and planar dislocation in lattice cells [197]

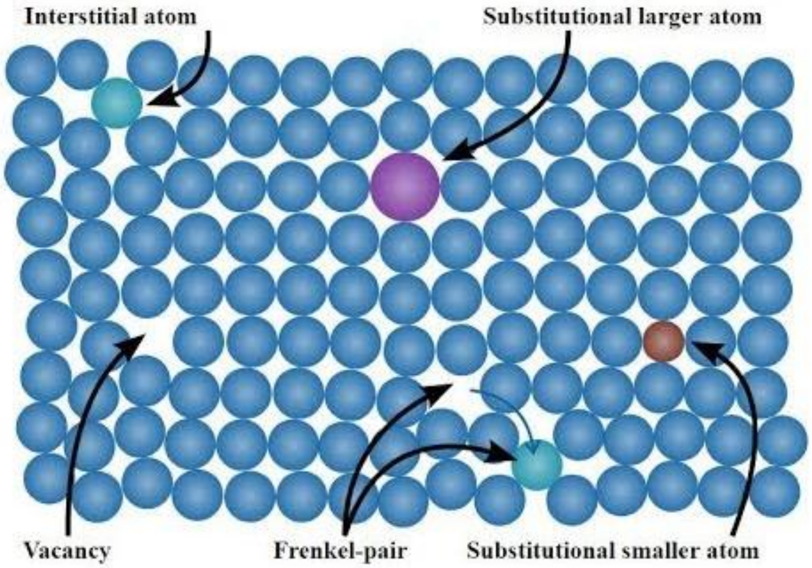

Figure 10:figure summarizing the types of defects originating in crystal lattice cells [198]

These defects and impurities, as described by quantum theory, scatter the free carriers and phonons. As demonstrated by Callaway, Holand, and Klemens [21, 22] in the thermal conductivity of various materials, the scattering process is the primary cause of the degradation of essential semiconducting properties. Second-order processes resulting from anharmonic decay with decreasing phonon energies are the cause of these scattering phenomena [21,22]. The intrinsic anharmonic decay rate can be used to represent the decay rate caused by anharmonic interactions and the scattering processes of point defects or impurities [1, 5 – 15, 24, 25].

The scattering rate is determined by the relaxation time, which is as follows:

$$\frac{1}{\tau} = \sum_{i} \frac{1}{\tau i} \qquad \text{Eq. (3.20)}$$

where τ is the total relaxation time that follows Matthiessen's rule and where “i” is for all scattering/collision processes.

The relaxation time due to point-defect scattering, in this case, is given by: [1, 5-15]

$$\frac{1}{\tau} = g\frac{\pi\omega^2}{12}\, D(\omega) \qquad \text{Eq. (3.21)}$$

where D(ω) denotes the density of modes per unit volume and g denotes the direct measure of the strength and density of point defects in the sample. [1,5-15]

“The total number of modes per unit volume is calculated as follows” [14,15]:

$$n = \frac{1}{V}\int D(q)4\pi q^2 dq = \frac{q^3}{6\pi^2} \qquad \text{Eq. (3.22)}$$

where n denotes the mode concentration.

The zone-center short wavevectors, wavelength is defined by the following expression: [1, 5- 15]

$$\omega = \omega_o\left(1 - \frac{q^2}{k^2}\right) \qquad where\ q^2 = \frac{k^2\Gamma}{\omega} \qquad \text{Eq. (3.23)}$$

where Γ is the inherent anharmonic damping.

The density of states per unit volume can be expressed using the last two equations as follows: [1, 4, 6-16]

$$D(\omega)d\omega = (4\pi q^2 dq) = \left(\frac{1}{6\pi^2}\frac{k^2\Gamma}{\omega}\frac{k}{\sqrt{w}}\frac{d\Gamma}{2\sqrt{\Gamma}}\right) = \left(\frac{1}{6\pi^2}\frac{k^3\Gamma^{\frac{1}{2}}}{\omega^{\frac{3}{2}}}\,d\Gamma\right) = D(\Gamma)d\Gamma$$

As a result, the relaxation time that accounts for anharmonic and defects scattering, as well as the total damping parameter that accounts for the aforementioned scattering processes, is given by: [1, 5-15]

$$\frac{1}{\tau} = \frac{g\pi}{12N}\frac{k^3}{{q_D}^3}\,\omega^{\frac{1}{2}}\,\Gamma^{\frac{1}{2}} \qquad \text{Eq. (3.24)}$$

$$\gamma_{total} = C\omega^{\frac{1}{2}}\,\mathit{\Gamma}^{\frac{1}{2}} \qquad \text{Eq. (3.25)}$$

where N is the total number of modes per unit cell, g is the total number of defects present, q_D is the debye wavevector, and C is a free adjustable parameter. To estimate and study the optical and electronic properties of a given semiconductor, Eqs. (3.24) and (3.25) are usually replaced in equations Eq. (3.12) to Eq. (3.17) given by the Drude model derived in the previous section. [1, 5-15] (Note that m in the Drude model should be replaced by the effective mass of the free carriers).

To visualize the effect of free carriers on the complex dielectric function of symmetrical materials, such as hexagonal structured doped materials, the dielectric response function can be divided into parallel and perpendicular parts, which represent the effect of plasmons or excitons along the symmetry axis and perpendicular to it or in the basal plane, respectively, as shown below: [1,5-15]

$$\varepsilon_{||(\perp),FreeCarrier}(\omega) = -\frac{{\omega_{p,\parallel(\perp)}}^2}{\omega\left(\omega + i\gamma_{free\ carrier,\parallel(\perp)}\right)} \qquad \text{Eq. (3.26)}$$

The following is the complete complex dielectric response function:

$$\varepsilon(\omega) = \varepsilon_\infty + \sum_{j=1}^{N} \frac{S_j {\omega_j}^2}{{\omega_j}^2 - i\gamma_j\omega - \omega^2} - \frac{{\omega_p}^2}{\omega(\omega + i\gamma)} \qquad \text{Eq. (3.27)}$$

The ideal non-damped and non-resonant oscillator equation (3. 27) is reduced to:

$$\varepsilon(\omega) = \varepsilon_\infty - \frac{{\omega_p}^2}{\omega^2} \qquad \text{Eq. (3.28)}$$

The plasma-edged frequency is given by: $\omega_{pe} = \frac{\omega}{\sqrt{\varepsilon_\infty}}\ when\ \varepsilon(\omega) = 0\ in\ equation\ (3.28)$

For Eq. (3.28), the index of refraction is imaginary with a large decay coefficient in low-frequency regions ($\omega \ll \omega_{pe}$), but positive with a low decay coefficient (k tending to zero) in high-frequency regions ($\omega \gg \omega_{pe}$). As a result, materials with low-frequency responses are reflective and the wave cannot propagate within them, whereas materials with positive frequency responses propagate the electromagnetic wave, with decreasing reflectivity that tends to zero at extremely high frequencies, making such materials good absorbers or transmitters. [1, 5-15]

C. Multilayered Systems and Transfer Matrix Method :

The reflectivity and transmissivity derived at the end of the previous chapter, namely equations Eq. (2.27) to Eq. (2.43), are applicable to single coatings or films and are derived from Maxwell equations using boundary-continuity conditions and Fresnel and Snell's laws. However, in multilayered systems where multiple transmission and reflection processes occur between each layer and the end products are the sum of individual processes, as illustrated in fig. (11), the situation becomes complicated and complex. To overcome such obstacles and derive a general method applicable to single and multilayered systems, scientists devised the transfer matrix method, which will be built in this subsection. [1, 5-15, 23]

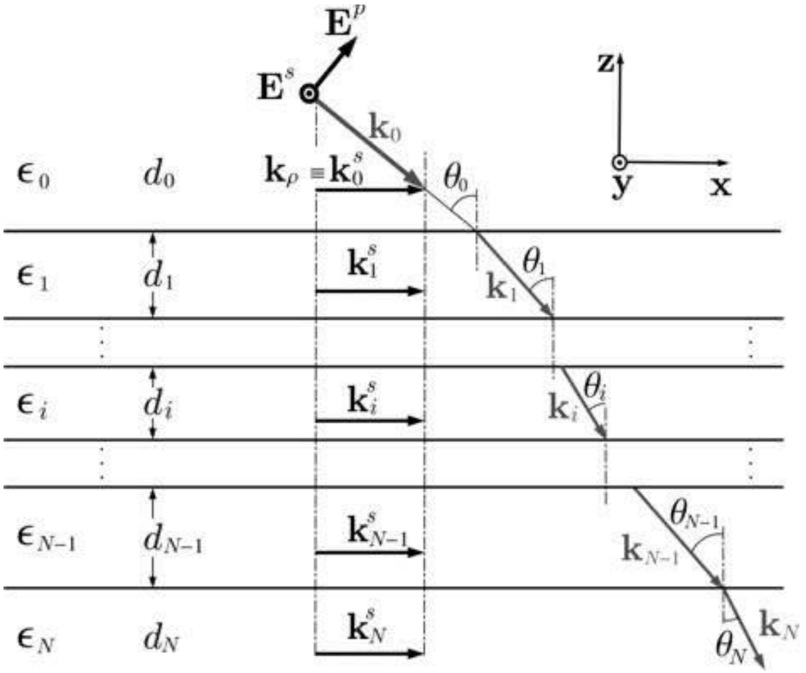

Figure 11: schematic representing the reflection and transmission processes in a multilayered system with varying thicknesses, for s- and p- polarized fields. [5, 192]

Based on the previous chapter's analysis, the reflected and transmitted electric and magnetic fields for single-layered systems can be written as follows:

$$E = Eo\left(e^{i(\omega t \mp K.r)}\right) \qquad \text{Eq. (3.29)}$$

$$H = Ho\left(e^{i(\omega t \mp K.r)}\right) \qquad \text{Eq. (3.30)}$$

Where the sign is determined by the dot product of K and r the direction of wave propagation [1, 5-15, 23]. After removing the time components from equations Eq. (3.29) and Eq. (3.30), the electric field can be written as follows, (the magnetic field can be derived from electric fields using Maxwell's equations) in conjunction with fig 11:

$$E_{i,p} = E_{i+1}\left(e^{i\left(\omega t - \frac{2\pi n_i \sin(\theta_i)}{\lambda} x - \frac{2\pi n_i \cos(\theta_i)}{\lambda} z\right)}\right) \ (reflected) \qquad \text{Eq. (3.31)}$$

$$E_{i,t} = E_{i+1}\left(e^{i\left(\omega t - \frac{2\pi n_{i+1}\sin(\theta_{i+1})}{\lambda}x + \frac{2\pi n_{i+1}cos(\theta_{i+1})}{\lambda}z\right)}\right) \ (transmitted) \qquad \text{Eq. (3.32)}$$

In each medium, we have: [1, 5-15]

$$E_{i,x} = \ {E_i}^{+,p}\, e^{-ix_i z}\cos(\theta_i) \qquad \text{Eq. (3.33)}$$

$$E_{i,y} = \ {E_i}^{-,s}\, e^{-ix_i z} \qquad \text{Eq. (3.34)}$$

where $\mathrm{x_i} = \frac{\delta_i}{d_i} = \frac{2\pi \mathrm{n_i} \cos(\theta_i)}{\lambda}$ where d is the thickness of each layer, and these results are obtained by applying the boundary conditions at z=0 and z=d for each layer. [14]

The relationships found in equations Eq. (2.35), Eq. (2.37), and Eq. (2.40), derived in the previous chapter, can be used to modify the above equations:

$${E_{i-1}}^{+} = \frac{(e^{-i\delta_{i-1}}{E_i}^{+} + r_i e^{-i\delta_{i-1}}{E_i}^{-})}{t_i} \qquad \text{Eq. (3.35)}$$

$${E_{i-1}}^{-} = \frac{(r_i e^{-i\delta_{i-1}}{E_i}^{+} + e^{-i\delta_{i-1}}{E_i}^{-})}{t_i} \qquad \text{Eq. (3.36)}$$

In matrix form, Eq.(3.35) and Eq. (3.36) are as follows:

$$\begin{pmatrix} {E_{i-1}}^{+} \\ {E_{i-1}}^{-} \end{pmatrix} = \frac{1}{t_i}\begin{pmatrix} e^{-i\delta_{i-1}} & r_i e^{-i\delta_{i-1}} \\ r_i e^{-i\delta_{i-1}} & e^{-i\delta_{i-1}} \end{pmatrix}\begin{pmatrix} {E_i}^{+} \\ {E_i}^{-} \end{pmatrix} \qquad \text{Eq. (3.37)}$$

Eq. (3.37) represents the transfer matrix product process for one layer only, with the matrix being for single layer I, and the reflectance and transmittance are given by Eqs. (2.35) – (2.40) in the previous chapter, as: [1, 5-15, 23]

$$R = \frac{({E_i}^-)({E_i}^-)^*}{({E_i}^+)({E_i}^+)^*} \quad and \;\; T = \frac{({E_{i+1}}^+)({E_{i+1}}^+)^*}{({E_i}^+)({E_i}^+)^*} \qquad \text{Eq. (3.38)}$$

We can extend the process to any layered system by using the transfer matrix, for example, for the case of a two-layered system, the transfer-matrix is given by: [1, 5-15, 23]

$$\begin{pmatrix} {E_0}^+ \\ {E_o}^- \end{pmatrix} = \frac{1}{t_1} \begin{pmatrix} 1 & r_1 \\ r_1 & 1 \end{pmatrix} \begin{pmatrix} {E_1}^+ \\ {E_1}^- \end{pmatrix} \qquad \text{Eq. (3.9)}$$

$$\begin{pmatrix} {E_1}^+ \\ {E_1}^- \end{pmatrix} = \frac{1}{t_2} \begin{pmatrix} e^{-i\delta_1} & r_2 e^{-i\delta_1} \\ r_2 e^{-i\delta_1} & e^{-i\delta_1} \end{pmatrix} \begin{pmatrix} {E_2}^+ \\ {E_2}^- \end{pmatrix} \qquad \text{Eq. (3.40)}$$

which can be combined into one product matrix

$$\begin{pmatrix} {E_0}^+ \\ {E_o}^- \end{pmatrix} = \frac{1}{t_1} \frac{1}{t_2} \begin{pmatrix} 1 & r_1 \\ r_1 & 1 \end{pmatrix} \begin{pmatrix} e^{-i\delta_1} & r_2 e^{-i\delta_1} \\ r_2 e^{-i\delta_1} & e^{-i\delta_1} \end{pmatrix} \begin{pmatrix} {E_2}^+ \\ {E_2}^- \end{pmatrix} \qquad \text{Eq. (3.41)}$$

The reflectance and transmittance are given by: $R = \frac{({E_0}^-)({E_o}^-)^*}{({E_o}^+)({E_o}^+)^*} \quad and \;\; T = \frac{({E_2}^+)({E_2}^+)^*}{({E_0}^+)({E_0}^+)^*}$

Using the matrix multiplication laws, the product matrix can be written into a single matrix as follows: [1, 5-15]

$$\begin{pmatrix} 1 & r_1 \\ r_1 & 1 \end{pmatrix} \begin{pmatrix} e^{-i\delta_1} & r_2 e^{-i\delta_1} \\ r_2 e^{-i\delta_1} & e^{-i\delta_1} \end{pmatrix} = \begin{pmatrix} a & b \\ c & d \end{pmatrix} \qquad \text{Eq.(3.41)}$$

with $R = \frac{(c)(c)^*}{(a)(a)^*}$ $and\ T = \frac{(t_1t_2)(t_1t_2)^*}{(a)(a)^*}$

To demonstrate the power of the transfer matrix, the method is applied to a system composed of n-layered thin films deposited on a substrate, as shown in Figs (11) and (12), which are described by the following equations using the same steps as before:

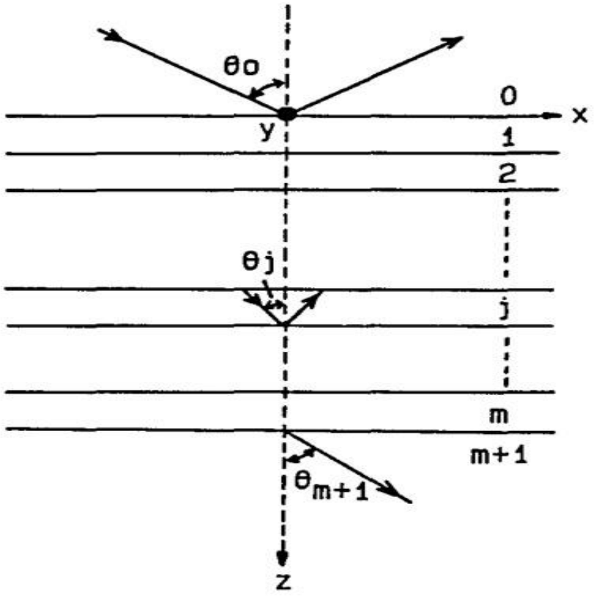

Figure 12: IR light penetrating the multilayered thin films, following the Transfer Matrix method to get the reflectance and transmittance necessary for dielectric function and index of refraction calculations. [5, 192]

On each level, using the transfer matrix, one obtains: [1, 5-15]

$$\begin{pmatrix} {E_0}^+ \\ {E_o}^- \end{pmatrix} = \frac{1}{t_1} \begin{pmatrix} 1 & r_1 \\ r_1 & 1 \end{pmatrix} \begin{pmatrix} {E_1}^+ \\ {E_1}^- \end{pmatrix}$$

$$\begin{pmatrix} {E_1}^+ \\ {E_1}^- \end{pmatrix} = \frac{1}{t_2} \begin{pmatrix} e^{-i\delta_1} & r_2e^{-i\delta_1} \\ r_2e^{-i\delta_1} & e^{-i\delta_1} \end{pmatrix} \begin{pmatrix} {E_2}^+ \\ {E_2}^- \end{pmatrix}$$

……

which can be combined into matrices products

$$\begin{pmatrix} E_0{}^{+} \\ E_o{}^{-} \end{pmatrix} = \frac{1}{t_1}\frac{1}{t_2}\frac{1}{t_3}\frac{1}{t_4}\frac{1}{t_5}\cdots\frac{1}{t_{n+1}}\begin{pmatrix} 1 & r_1 \\ r_1 & 1 \end{pmatrix}\begin{pmatrix} e^{-i\delta_1} & r_2e^{-i\delta_1} \\ r_2e^{-i\delta_1} & e^{-i\delta_1} \end{pmatrix}\ldots.\begin{pmatrix} E_2{}^{+} \\ E_2{}^{-} \end{pmatrix} \qquad \text{Eq.(3.42)}$$

The product matrix can be written into a single matrix using the matrix multiplication laws as [1, 5-15]

$$\begin{pmatrix} 1 & r_1 \\ r_1 & 1 \end{pmatrix}\begin{pmatrix} e^{-i\delta_1} & r_2e^{-i\delta_1} \\ r_2e^{-i\delta_1} & e^{-i\delta_1} \end{pmatrix}\ldots\ldots. = \begin{pmatrix} a & b \\ c & d \end{pmatrix} \qquad \text{Eq. (3.43)}$$

$$with\ R = \frac{(c)(c)^*}{(a)(a)^*} \quad and\ \ T = \frac{(t_1t_2\ldots.t_{n+1})(t_1t_2\ldots.t_{n+1})^*}{(a)(a)^*} \qquad \text{Eq. (3.44)}$$

The index and decay coefficients for each layer can be estimated using this model which is written as $n_{j-1}' = n_{j-1} + ik_{j-1}$ and $n_j' = n_j + ik_j$ respectively. The reflectance and transmittance for each layer can be written using a similar way; $r_j = g_j + ih_j\ \ and\ \ t_j = 1 + r_j$ respectively. [1, 5-15]. where g_j, h_j are the real and imaginary parts of the reflectance and transmittance. Using the relation between reflectivity, transmissivity, and index of reflection derived in the previous chapter we obtain: [5, 14]

$$g_j = \frac{{n_{j-1}}^2 + {k_{j-1}}^2 - {n_j}^2 - {k_j}^2}{(n_j + n_{j-1})^2 + (k_j + k_{j-1})^2} \qquad \text{Eq.(3.45)}$$

$$h_j = \frac{2(n_{j-1}k_j - n_j k_{j-1})}{(n_j + n_{j-1})^2 + (k_j + k_{j-1})^2} \qquad \text{Eq. (3.46)}$$

The absorptivity can be calculated from the complex index of refraction for each layer using the same steps as before.

$$e^{-i(\,\omega t-(n_j+ik_j)d_j\cos(\theta_j)\frac{2\pi}{\lambda})} = (e^{-\alpha_j})\left(\,e^{-i\left(\omega t-(n_j)d_j\cos(\theta_j)\frac{2\pi}{\lambda}\right)}\right) \qquad \text{Eq.(3.47)}$$

where $\alpha_j = (k_j)d_j\cos(\theta_j)(\frac{2\pi}{\lambda})$ which is related to the absorptivity of each layer [5,14]

In addition, the matrix for the single jth layer can be written in a complex form as follows: [5,14]

$$\begin{pmatrix} e^{-i\delta_{j-1}} & r_j e^{-i\delta_{j-1}} \\ r_j e^{-i\delta_{j-1}} & e^{-i\delta_{j-1}} \end{pmatrix} = \begin{pmatrix} p_j + iq_j & r_j + is_j \\ t_j + iv_j & u_j + iw_j \end{pmatrix}$$

Using the complex index of refraction for each medium or the expression Eq. (3.47), with the new elements related to the old ones, we obtain [5,14]

$$p_j = e^{\alpha_{j-1}}\cos\left((n_{j-1})d_{j-1}\cos(\theta_{j-1})\frac{2\pi}{\lambda}\right) \qquad (3.48)$$

$$q_j = e^{\alpha_{j-1}}\sin\left((n_{j-1})d_{j-1}\cos(\theta_{j-1})\frac{2\pi}{\lambda}\right) \qquad (3.49)$$

$$r_j = e^{\alpha_{j-1}} (g_j \cos\left(\left(n_{j-1}\right) d_{j-1} \cos\left(\theta_{j-1}\right) \frac{2\pi}{\lambda}\right) - h_j \sin\left(\left(n_{j-1}\right) d_{j-1} \cos\left(\theta_{j-1}\right) \frac{2\pi}{\lambda}\right)) \tag{3.50}$$

$$s_j = e^{\alpha_{j-1}} (h_j \cos\left(\left(n_{j-1}\right) d_{j-1} \cos\left(\theta_{j-1}\right) \frac{2\pi}{\lambda}\right) + g_j \sin\left(\left(n_{j-1}\right) d_{j-1} \cos\left(\theta_{j-1}\right) \frac{2\pi}{\lambda}\right)) \tag{3.51}$$

$$t_j = e^{\alpha_{j-1}} (g_j \cos\left(\left(n_{j-1}\right) d_{j-1} \cos\left(\theta_{j-1}\right) \frac{2\pi}{\lambda}\right) + h_j \sin\left(\left(n_{j-1}\right) d_{j-1} \cos\left(\theta_{j-1}\right) \frac{2\pi}{\lambda}\right)) \tag{3.52}$$

$$v_j = e^{\alpha_{j-1}} (h_j \cos\left(\left(n_{j-1}\right) d_{j-1} \cos\left(\theta_{j-1}\right) \frac{2\pi}{\lambda}\right) - g_j \sin\left(\left(n_{j-1}\right) d_{j-1} \cos\left(\theta_{j-1}\right) \frac{2\pi}{\lambda}\right)) \tag{3.53}$$

$$u_j = e^{\alpha_{j-1}} \cos\left(\left(n_{j-1}\right) d_{j-1} \cos\left(\theta_{j-1}\right) \frac{2\pi}{\lambda}\right) \tag{3.54}$$

$$w_j = -e^{\alpha_{j-1}} \sin\left(\left(n_{j-1}\right) d_{j-1} \cos\left(\theta_{j-1}\right) \frac{2\pi}{\lambda}\right) \tag{3.55}$$

The above process can be extended to the n-product transfer matrix as shown below: [1,5-15, 23]

$$\begin{pmatrix} 1 & r_1 \\ r_1 & 1 \end{pmatrix} \begin{pmatrix} e^{-i\delta_1} & r_2 e^{-i\delta_1} \\ r_2 e^{-i\delta_1} & e^{-i\delta_1} \end{pmatrix} \dots\dots. = \begin{pmatrix} a & b \\ c & d \end{pmatrix} = \begin{pmatrix} p_{1,n+1} + iq_{1,n+1} & r_{1,n+1} + is_{1,n+1} \\ t_{1,n+1} + iu_{1,n+1} & v_{1,n+1} + iw_{1,n+1} \end{pmatrix}$$

With the new elements connected to the previous elements via the recurrence relations shown below, and each element p,q,r,s,t,v,u, and w having the form shown in equations Eq. (3.56) to Eq. (3.63): [5, 14]

$$p_{1,n+1} = p_{1n}\,p_{n+1} - q_{1n}q_{n+1} + r_{1n}t_{n+1} - s_{1n}u_{n+1} \qquad \text{Eq. (3.56)}$$

$$q_{1,n+1} = q_{1n}\,p_{n+1} + q_{1n}p_{n+1} + s_{1n}t_{n+1} + r_{1n}u_{n+1} \qquad \text{Eq. (3.57)}$$

$$r_{1,n+1} = p_{1n}\,r_{n+1} - q_{1n}s_{n+1} + r_{1n}v_{n+1} - s_{1n}w_{n+1} \qquad \text{Eq.(3.58)}$$

$$s_{1,n+1} = q_{1n}\,r_{n+1} + p_{1n}s_{n+1} + s_{1n}v_{n+1} + r_{1n}w_{n+1} \qquad \text{Eq.(3.59)}$$

$$t_{1,n+1} = t_{1n}\,p_{n+1} - u_{1n}q_{n+1} + v_{1n}t_{n+1} - w_{1n}u_{n+1} \qquad \text{Eq.(3.60)}$$

$$u_{1,n+1} = u_{1n}\,p_{n+1} + t_{1n}q_{n+1} + w_{1n}t_{n+1} + v_{1n}u_{n+1} \qquad \text{Eq.(3.61)}$$

$$v_{1,n+1} = t_{1n}\,r_{n+1} - u_{1n}s_{n+1} + v_{1n}v_{n+1} - w_{1n}w_{n+1} \qquad \text{Eq.(3.62)}$$

$$w_{1,n+1} = u_{1n}\,r_{n+1} + t_{1n}s_{n+1} + w_{1n}v_{n+1} + v_{1n}w_{n+1} \qquad \text{Eq.(3.63)}$$

The reflectance reduces to: [1, 5-15]

$$R = \frac{(c)(c)^*}{(a)(a)^*} = \frac{{t_{1n+1}}^2 + {u_{1n+1}}^2}{{p_{1n+1}}^2 + {q_{1n+1}}^2}$$

The direction-spectral reflectance of a thick layered film with multiple internal reflection processes within a given layer can be calculated as follows: [1, 5-15]

$$\begin{aligned} R &= \rho + \rho(1-\rho)^2\tau^2 + \rho^3(1-\rho)^2\tau^4 + \cdots = \rho + \frac{\rho(1-\rho)^2\tau^2}{1-\rho^2\tau^2} \\ &= \rho\left[1 + \frac{(1-\rho)^2\tau^2}{1-\rho^2\tau^2}\right] \end{aligned} \qquad \text{Eq. (3.64)}$$

where $\tau_\lambda = \tau$ is the internal transmissivity and ρ is the surface reflectivity, and both are wavelength dependent. The direction-spectral transmittance and absorptance are given in the same way by [1, 5-15]

$$T = \frac{(1-\rho)^2\tau}{1-\rho^2\tau^2} \qquad \text{Eq. (3.65)}$$

$$A = \frac{(1-\rho)(1-\tau)}{1-\rho\tau} \qquad \text{Eq. (3.66)}$$

where the internal transmissivity is defined by: $\tau = e^{-\frac{4\pi k_2 d}{\lambda\cos(\theta_2)}}$

It is worth noting that when there is no absorption, the transmissivity and reflectivity are independent of layer thicknesses, and for normal incidence, they decrease for simpler equations. For instance the transmissivity in that case is given by: $T = \frac{2n_2}{{n_2}^2+{n_1}^2} = \frac{2n_2}{{n_2}^2+1}$ if the first medium is vacuum or air with $(n_1 = 1)$ [1, 5-15]

Eqs (3.65) and (3.66), namely the field reflection and transmission, can be expressed for three-layered thin films as follows:

$$r = r_{12} + \frac{t_{12}t_{21}r_{23}e^{2i\beta}}{1-r_{21}r_{23}e^{2i\beta}} \qquad \text{Eq. (3.67)}$$

$$t = \frac{t_{12}t_{23}e^{2i\beta}}{1-r_{21}r_{23}e^{2i\beta}} \qquad \text{Eq. (3.68)}$$

The reflectance can be estimated by: $R' = rr* = \left|r_{12} + \frac{t_{12}t_{21}r_{23}e^{2i\beta}}{1-r_{21}r_{23}e^{2i\beta}}\right|^2$

For an s-polarized or p-polarized electric or magnetic field and a lossless medium, the transmittance in medium 3 can be calculated as follows: [1, 5-15]

$$T' = \frac{n_3\cos(\theta_3)}{n_1 cos(\theta_1)}\, tt* \quad for\ s\ polarization \qquad \text{Eq. (3.69)}$$

$$T' = \frac{n_1 cos(\theta_3)}{n_3 cos(\theta_1)}\, tt* \quad for\ p\ polarization \qquad \text{Eq. (3.70)}$$

If the layer or film is slightly absorbing with low decay coefficients, the transmittance can be approximated by: [1, 5-15]

$$T = \frac{(1-\rho)^2\tau}{1+\rho^2\tau^2-2\rho\tau\cos(2\beta)} \qquad \text{Eq. (3.71)}$$

where $\beta = \begin{cases} m\pi & for\ peaks \\ \left(m+\frac{1}{2}\right)\pi & for\ valies \end{cases}$ with m is a non-negative integer. [1, 5-15]

D. Kramers-Kronig Method and Relations:

The Kramers-Kronig method or relation, which is a linearized simple way of estimating the dielectric response function of various structured materials, including amorphous, polycrystalline, single crystalline, and many others, is another powerful method devised by scientists. This method converts complex relations into linear response functions with real and imaginary parts that can be calculated and related to each other using Cauchy integrals. In recent studies, FTIR spectroscopic analysis was used, which produced acceptable and accurate results when compared to other techniques. The evaluation of Cauchy integrals or the difficulty in developing programs that can estimate such integrals is one limitation of this method or analysis. However, these are technical issues that have been solved or will be resolved as technology advances. This section will construct the Kramers-Kronig analysis. [1, 5-15]

The reflectance of any structured material is made up of amplitude and argument, which can be related to the index of refraction and decay coefficients using Eq. (2.36), Eq.(2.37), and Eq. (2.40). Linearizing the reflectance entails the following steps: [1, 5-15]

$$\ln\big(r(\omega)\big) = \ln\left(\sqrt{|R = rr*|}\right) + i\theta(\omega) \qquad \text{Eq. (3.72)}$$

Let us first introduce the Kramers-Kronig, which will be used to calculate the real and imaginary parts of the reflectance given in the preceding expression Eq. (3.72). As a result of the Kramers-Kronig relation, the response function of a damped harmonic oscillating system is represented by $\alpha(\omega) = \alpha 1(\omega) + i\alpha 2(\omega)$ where α1(2) is the real and imaginary part of the response function respectively, defined by:

$$x(\omega) = \alpha(\omega)F(\omega) \qquad \text{Eq. (3.73)}$$

F(ω) is the total force of the harmonic system given by:

$$m_j \frac{d}{dt}\left(\frac{dx}{dt}\right) + \gamma_j \frac{dx}{dt} + \omega_j{}^2 x = F(\omega) \qquad \text{Eq.(3.74)}$$

Where j denotes the number of oscillators in the system, and m and are the mass and damping coefficients, respectively. As a result, the response function, as in Drude and Lorentz oscillators, can be written as: [1, 5-15]

$$\alpha(\omega) = \sum_{j=1}^{N} \frac{f_j}{\omega_j{}^2 - i\gamma_j\omega - \omega^2} = \sum \frac{f_j\,(\omega_j{}^2 + i\gamma_j\omega - \omega^2)}{(\omega_j{}^2 - \omega^2)^2 + (\gamma_j\omega)^2} \qquad \text{Eq.(3.75)}$$

where $f_j = \frac{1}{m_j}\ is\ a\ constant$, and j runs over the number of oscillators or atoms, assuming there are N atoms represented as oscillators within the given system.

To apply the Kramers-Kronig relation, the function has to satisfy the following conditions: [1, 5- 9, 12-15]

- The poles of the response function should be located entirely below the real axis.
- The integral of $\frac{\alpha(\omega)}{\omega}$ should vanish as ω approaches to ∞ in the upper semi-infinite complex ω-plane, with $\alpha(\omega) \to 0$ as $\omega \to \pm\infty$
- The real and imaginary parts of the response function (namely α1(ω) and α2 (ω)) should be even and odd with respect to ω respectively.

After satisfying the preceding condition, the response function can be evaluated using the Cauchy Integral, as shown below:

$$\alpha(\omega) = \frac{P}{i\pi} \int_{-\infty}^{\infty} \frac{\alpha(s)}{s-\omega}\, ds \qquad \text{Eq.(3. 76)}$$

$$where\ P\ denotes\ the\ principle\ value\ of\ the\ integral\ given\ by:$$

$$\int_{-\infty}^{\infty} \frac{\alpha(s)}{s-\omega}\, ds \ \rightarrow\ \alpha(\omega) \int_{\pi}^{0} \frac{iue^{i\theta}}{ue^{i\theta}}\, d\theta = -i\pi\alpha(\omega) \qquad \text{Eq.(3.77)}$$

$$with\ s = w + ue^{i\theta}$$

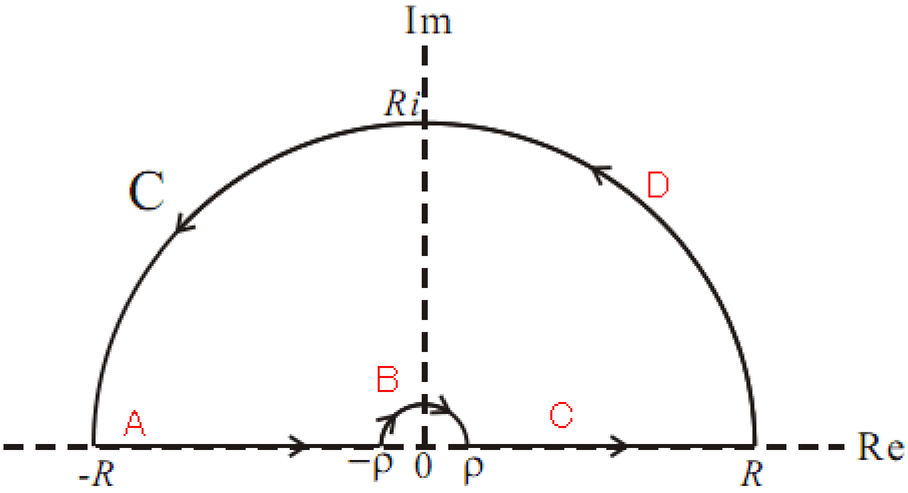

Figure 13: the segments and the upper semi-infinite complex plane for Cauchy integral [9]

$$integrating\ over\ the\ segment\ (1) and\ (3)\ (-R\ to\ R{:}\ ABC\ \ in\ \ figure\ below):$$

$$\int(1) + \int(3) \equiv P\int_{-\infty}^{\infty} \frac{\alpha(s)}{s-\omega}\, dSi\pi\alpha(\omega) \qquad \text{Eq.(3.78)}$$

Using the even and odd properties of the response function's real and imaginary parts, the above Eq. (3.78) integral can be separated into [1, 5-15]

$$\alpha1(\omega) = \frac{P}{\pi}\left(\int_0^{\infty} \frac{\alpha2(s)}{s-\omega}\, ds + \int_0^{\infty} \frac{\alpha2(p)}{p-\omega}\, dp \right) \qquad \text{Eq.(3.79)}$$

$$\alpha2(\omega) = -\frac{P}{\pi}\left(\int_0^{\infty} \frac{\alpha1(s)}{s-\omega}\, ds - \int_0^{\infty} \frac{\alpha1(p)}{p-\omega}\, dp \right) \qquad \text{Eq.(3.80)}$$

In the preceding Eqs. (3.79) and (3.80), p is a dummy variable that can be replaced by s, and the integrals can be further reduced to [1, 5-15]

$$\frac{1}{s-\omega}+\frac{1}{s+\omega}= \frac{2s}{s^2-\omega^2} \qquad \text{Eq.(3.81)}$$

$$\frac{1}{s-\omega}-\frac{1}{s+\omega}= \frac{2\omega}{s^2-\omega^2} \qquad \text{Eq.(3.82)}$$

$$\alpha 1(\omega)=\frac{2P}{\pi}\left(\int_0^\infty \frac{s\alpha 2(s)}{s-\omega}\,ds\right) \qquad \text{Eq.(3.83)}$$

$$\alpha 2(\omega)=-2\omega\frac{P}{\pi}\left(\int_0^\infty \frac{\alpha 1(s)}{s-\omega}\,ds\right) \qquad \text{Eq.(3.84)}$$

Now that the Kramers-Kronig relations have been applied to the reflectivity, we can calculate the phase of the reflectance based on its amplitude, which can be measured experimentally: [1, 5-15]

$$\theta(\omega)=-\omega\frac{P}{\pi}\left(\int_0^\infty \frac{\ln(R)}{s-\omega}\,ds\right)=\frac{-\omega}{\pi}\int_0^\infty \frac{\ln\big(R(s')\big)}{s^2-\omega^2}-\frac{\ln\big(R(s)\big)}{s^2-\omega^2}\,ds$$

$$\theta(\omega)=-\frac{1}{2\pi}\left(\int_0^\infty \ln\left(\left|\frac{s+\omega}{s-\omega}\right|\right)\frac{d\ln\big(R(s)\big)}{ds}ds\right) \qquad \text{Eq.(3.85)}$$

Using the modified equations below, Kramers-Kronig relations have been used to obtain the optical response function for low-dimensional materials such as quantum wells or quantum dots: [13]

$$\sigma 1(\omega)=\frac{2\pi e^2\hbar}{m^2\Omega}\sum\nolimits_{ij}|<j|e.p|i>|^2\frac{f(E_i)-f\big(E_j\big)}{E_j-E_i}\,\delta(E_j-E_i-\hbar\omega) \qquad \text{Eq.(3.86)}$$

And $\sigma 2(\omega) = -\frac{2\pi e^2 \hbar}{m^2 \Omega} \sum_{ij} |< j|e.p|i >|^2 \frac{f(E_i) - f(E_j)}{E_j - E_i} P \frac{1}{(E_j - E_i - \hbar\omega)}$ Eq.(3.87)

The last equations' details can be found elsewhere [14]. Other methods, such as the Kane Model and spin effects on nanomaterials and low-dimensional structures, provide optical properties and demonstrate quantum effects such as magnetic and spin-orbital effects, leading to fascinating technological applications such as spintronics, magnetrons, and many others. They have also found a role in many applications related to nanomaterials, such as lasing materials and plasmonics. [13]

SECTION II

LITERATURE REVIEWS

CHAPTER IV

LITERATURE REVIEWS ZINC OXIDE INTRODUCTION, GROWTH AND ITS OPTICAL PROPERTIES

Zinc Oxide is proposed to be deposited in this thesis as a potential hyperbolic material to be vehicle glasses, to reduce solar radiation heating of the enterior of the vehicle. To that end, this script will introduce the reader to zinc oxide as a nanomaterial, shedding light on its growth techniques as well as its properties, while also serving as a review of previous scholarly work on zinc oxide.

A. Introduction to Zinc Oxide

ZnO is an II-VI semiconducting material having hexagonal, wurtzite, zinc-blende, and rock salt structures, the stability, and formation of these structures depend on deposition conditions and handling processes. For instance hexagonal zinc oxide is reported to have C6mc group structure with lattice parameters a= 0.3296nm and c= 0.52065nm [3]. Zinc oxide is characterized by a relatively large bandgap of 3.37 eV at room temperature, excitonic energies of 65 meV, larger to GaN (26 meV), good electrical and optical properties, high thermal stability, good thermal conductivity [3] compared to indium tin oxide (ITO), and other properties.

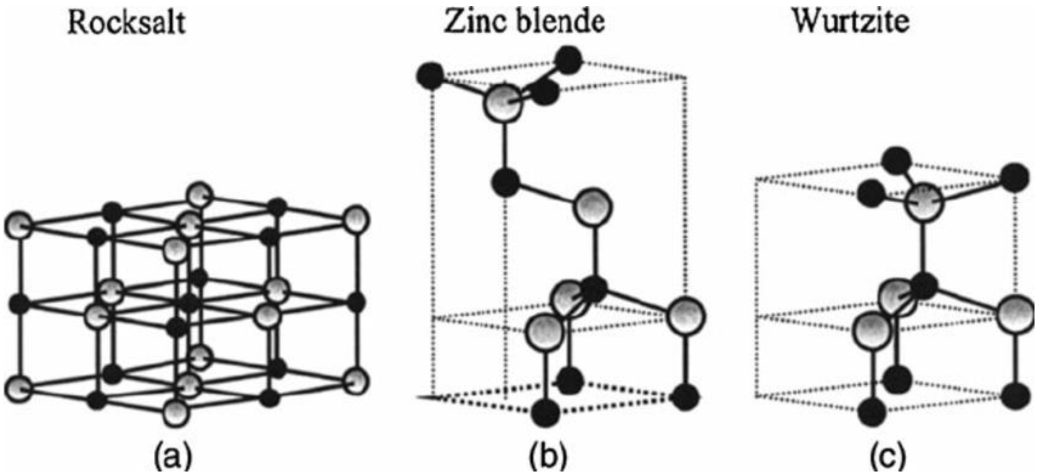

Figure 14: figure illustrating the different crystalline structures of Zinc Oxide namely (a) Rocksalt, (b) Zinc Blende, and (c) Wurtzite crystalline structures [3].

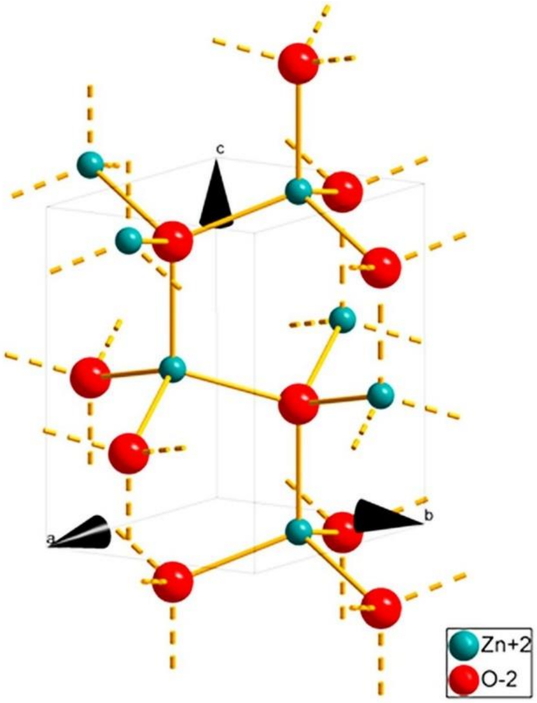

Figure 15: Schematic representation of a crystalline structure of ZnO [26]

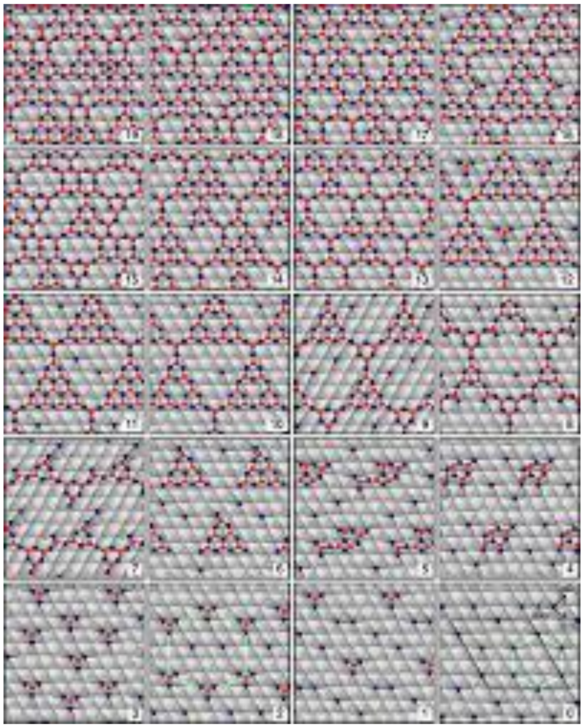

Figure 16: schematic representation of polar crystalline structures of ZnO [27]

Zinc oxide (ZnO), with its unique and promising properties, has been incorporated in optical devices such as light-emitting diodes, optically pumped lasers, transparent conducting oxides, and transparent filmed transistors, among others, as well as piezoelectric devices, sensors, and solar cells, such as gas sensors, biosensors, solar cells, optoelectronic and thermal devices, and surface acoustic wave (SAW) applications, and many other systems and technologies.. [3, 28-31]

B. Growth and Properties of Zinc Oxide:

Transparent conducting oxides (TCO) have attracted scientist interests due to their application in optoelectronics, electronic, and communication devices and technologies.

These properties have been used in different industries such as aircraft and spacecraft coating, optoelectronic, electronic ad surface acoustic wave (SAW) devices. [3, 24-28]

TCO has been fabricated by using various techniques, namely metal-organic chemical vapor deposition (MOCVD), chemical vapor deposition (CVD), physical vapor deposition (PVD), RF and magnetron assisted sputtering, molecular beam epitaxy (MBE), sol-gel, and pulsed laser deposition (PLD). Of all the deposition techniques, it was reported that the PLD is the most efficient, such as Ga_2O_3–In_2O_3, In_2O_3–ZnO, In_2O_3–SnO_2, ZnO–SnO_2, In_2O_3 –$MgIn_2O_4$, $MgIn_2O_4$–$Zn_2In_2O_5$, $ZnSnO_3$–$ZnIn_2O_5$, and $ZnIn_2O_5$–$GaInO_3$ [24, 25], have been manufactured or deposited using the PLD technique.

It is reported that oxides can be deposited at low temperatures, around 300 ºC with good grain size and properties. Moreover, the films deposited under vacuum or low oxygen pressures showed oxygen vacancies. On the other hand, films deposited under high oxygen pressures, up to 100 mbar, solved the issue of oxygen vacancies but showed defects and impurities problems. The thickness of the obtained films depended largely on the type of the laser used, the laser fluence or energy, the density of the materials, and pressure within the chamber. [24, 25]

Because zinc is less expensive and more abundant in nature than indium, many deposition techniques have been proposed to synthesize ZnO nanostructures for various applications and on various substrates, including chemical vapor deposition (CVD) [3, 29], metal-organic chemical vapor deposition (MOCVD) [3,35], laser evaporation, physical vapor deposition (PVD), molecular beam epitaxy (MBE) [3,36], magnetron sputtering (of different types such as RF sputtering methods) [3, 37 – 40, 45], sol-gel [3, 32, 38], pulsed laser deposition (PLD, introduced in the next chapter)[3, 24, 25,44-56, 64-78], and others [3,30, 31, 42].

Much research has been done into depositing ZnO thin films on various substrates and determining their properties to better understand and improve the aforementioned technologies. To that end, this subsection examines some recent publications in which ZnO has been successfully deposited and analyzed.

Valerini and co-workers, [44] deposited ZnO on silicon Si (100), with the following conditions, KrF (248 nm) or ArF (193 nm) excimer lasers, at energies 181 milliJ, with temperature variation ranged between 500-700 ºC, and at oxygen partial pressures of 1,5, 50 and 100 Pa. The obtained samples underwent XRD, SEM, and PL investigations. XRD data showed peaks at (002) and (004) at angles of about 35º, and 72º, respectively, which were attributed to ZnO, and a peak at an angle of about 70º which was attributed to silicon. The obtained nanostructures revealed smooth and rough morphologies, which varied with deposition conditions under SEM analysis. PL investigation revealed a jump or peak in its intensity at energies of 3.0-3.2 eV. This peak was sharp when the PL investigation occurred at temperatures higher than that of Room temperature, which shows the effect of temperature in improving their optical properties.

Zhu and co-workers, [45] studied the effect of thickness on the structural properties of ZnO thin films grown on Glass, with pulsed laser deposition under the following conditions, laser (KrF (248 nm)) energy 348 mJ/pulse, at frequencies of 5 Hz, under oxygen pressure of 12 Pa and at temperatures of 350 ºC, with varying deposition time 1.5 to

20 min. The authors registered highly transparent films, with increasing roughness (exponentially) and thickness (linearly) with increasing time of deposition. All the samples exhibited XRD peaks at 35 º which corresponds to the (002) crystallographic orientation. Moreover, these peaks showed an increase in height and decrease in FWHM with increasing time or thicknesses. The authors also investigated the electrical properties of these samples and analyzed their variation with varying deposition parameters, in particular variations in mobility, charge density, and resistivity were studied with increasing thicknesses. In addition, the authors realized the blueshift of absorption edge with decreasing thicknesses which were speculated to be due to roughness and stress.

Ohshima and co-workers [46] deposited ZnO on different samples namely, Si (100), Silica glass, α-Al_2O_3 (0001), and Corning 7059 Glass, using pulsed laser deposition with energy fluence 2 J/cm^2 , for 15 min, under oxygen environment of pressures $6.67*10^{-3}$ to 26.7 Pa and varying temperatures from room temperature to 700º C. The XRD analysis showed (002) and (004) orientations. . The intensities and widths of the XRD peaks related to these orientations were fount to vary with pressure and temperature. The obtained samples showed high quality when examined with AFM and photoluminescence spectroscopy.

Young Rae Jang and co-workers [47], and Shatha Kassamani and co-workers [14], deposited ZnO on Si (100) and Sapphire substrate respectively. The samples deposited on Si (100) [47], were grown using, Nd Yag laser with an energy fluence of 1 J/cm^2 and frequency of 10 Hz. The system was kept under oxygen partial pressure of 1 mTorr and 1 Torr, with varying temperatures within the range of RT to 800º C. the GIXRD analysis showed strong (002) and (103) peaks with weak ones at (101), (102), (112) and (004) orientations. SEM analysis showed small grains for samples deposited at 1 mTorr and larger gains for those deposited at higher oxygen pressures (1 Torr). XPS and UV PL spectroscopic measurements revealed the visible emission for optimal temperature and pressure, in addition to strong colleration between the (103) peaks and the UV emission intensities. Shatha Kassamani studied the effect of temperature and oxygen pressures on the ZnO films deposited on a sapphire substrate. She deposited samples at 725, 825, and 925 degrees Celsius at oxygen partial pressures of 10, 25, 75, 100, 200, and 500 mTorr with laser energy kept at 400 mJ and repetition frequency of 20 Hz. All deposition were made for 20 min. The deposited samples underwent XRD and SEM analysis and showed (002) peaks depending on the average stain which change with increasing oxygen partial pressures and revealed variation of FWHM with varying temperatures and pressures. SEM analysis showed larger and rougher grains as the pressure of the oxygen increased, revealing the optimal temperature for good quality films. Finally, Uv-Vis and infrared FTIR reflection studies were conducted from which optical properties were deduced.

C. Review on Optical Properties of ZnO

Optical properties and physical processes in zinc oxide were studied extensively over the past few years. The determinants of these properties were found to be related to intrinsic and extrinsic effects in semiconductors, such as the transmission of electrons and holes between the conduction band and valence bands, excitonic formation, and its interaction with electrons and molecules found around it … [3]. Dopants were used to further improve the properties of zinc oxide and manufacturing p-type and n-type zinc oxides. These dopants showed effect on excitonic phenomena leading to new concepts such as bound-accepter excitons, bound-donor excitons….[3]. With the era of lasers and lasing applications, zinc oxide found its role within this community, due to its stimulated, or spontaneous emissions within it. The excitonic, dopants, and emission directly affected the photoluminense properties of zinc oxide, which in turn were dependent on temperature during the experiments. The above-mentioned, properties and phenomena can be found elsewhere [3]. The important properties that this chapter will focus, are the photoluminescence, index of refraction, shifts within the spectrum, and nonlinear susceptibilities and properties.

M. Mosca et al [48] have deposited zinc oxide on different substrates; randomly-oriented quartz (fused silica), sapphire, or GaN templates using PLD techniques. The obtained films were of high crystalline quality and exhibited good photoluminescence and emission properties on sapphire and GaN. The authors realized the effect of oxygen, zinc, and other defects, and dislocations on these properties. The article also reported the improvement of these properties with increasing temperature, in particular at 450, 600, and 675 ºC and 1 Pa of oxygen partial pressure.

Millon et al [49] deposited various structured zinc oxides on various substrates with varying laser type and deposition conditions. The samples with several nanostructures, sizes, and thickness underwent thermal, optical, and electronic investigations. The authors reported on stress and mismatch affecting the optical properties. They further realized that zinc or oxygen vacancies were responsible for absorption and shift in the emission spectrum such as green-level emission that were observed in photoluminescence experiments. The samples underwent a cathodoluminescence experiment which further emphasized the dependence of excitonic emission and optical responses on crystalline quality, defects, and structural imperfections. It also showed improvement in near band edge emission and limited the broadening of excitation level upon annealing the samples under oxygen gas at 800º C [49].

M. Novotny and co-workers, [50] studied the characteristic of zinc oxide thin films grown on various substrates; MgO, polished sapphire, Fused silica by using PLD techniques. The samples were annealed in 10 Pa of oxygen atmosphere at 750 ºC. The structural, optical, mechanical, spectroscopic measurements were conducted on the samples. The authors reported reflectance and transmittance using numerical methods and analyzed them using the Cauchy dispersion relations. The samples showed transparent layers with multiple interferences that varied with film thickness and substrates. Moreover, the refractive and decay coefficients were evaluated using the reflectance and transmittance data. The bandgap was also estimated, using Tauc's plot method, which led to 3.28± 0.05 eV regardless of the substrate type. Corrections on the bandgap energy were done to account for the Coulomb interaction and other effects within the film, which led to 3.38 ± 0.01 eV for MgO and Fused silica and 3.41 ± 0.01 for sapphire. XRD and SEM revealed that ZnO deposited on MgO were single crystallized with basal orientation ZnO (0001) parallel to substrates. On the other hand, the films deposited on sapphire were single crystal but their orientation was not basal and was shifted by 36º to the substrate. Spectroscopic studies were conducted by using slow positron implantation spectroscopy

(SPIS) which showed the defects and their concentration vs thickness, depth, energy, and substrate type. [50].

Lei Zhao and co-workers [51] studied the structural and optical properties on ZnO deposited on quartz-glass, glass and Si (100) and quartz-glass substrates by PLD. In Ref. [51], the obtained samples underwent XRD analysis revealing c-axis (002) peak and peak corresponding to the (103) plane of the hexagonal structure. The temperature increased from 100 to 250 ºC at a step of 50 ºC, which showed an increase in the peaks and decrease of the FWHM. Furthermore, the films showed an increase in thickness with temperature. Photoluminescence spectra revealed UV emission within the range 100 - 250 ºC. This UV emission was speculated to be due to NiO sublayer between sapphire and ZnO. Furthermore, the deep-UV-level emission varied with defects, oxygen and zinc vacancies in particular. The samples were highly transparent with direct bandgap energy of 3.26, 3.26, 3.36, 3.28 eV at deposited temperatures of 100, 150, 200, and 250 ºC respectively. [51]. The obtained samples, after annealing at a high temperature showed a drastic increase in intrinsic defects, which caused violet emission. In Ref [52], the obtained samples showed (002) orientation under XRD analysis. As the annealing temperature increased from 25 to 150 ºC and the deposition time increased from 10 min to 2 hr, the peak intensity and width of (002) plane decreased. Further increasing the annealing temperature to 300 and 450 ºC led to an increase in the (002) peak and decrease in its width. Note that the samples were deposited at a varying temperature within the range of RT to 500 ºC under oxygen partial pressure of 12 Pa). The authors studied the variation of FWHM and grain size with varying deposition temperature as mentioned above. Bandgap energy was measured to be of 3.29, 3.31,3.27, and 3.28 for deposition temperatures of RT, 200, 350. and 500 ºC respectively. Photoluminescence measurements were done with varying deposition temperature and annealing temperature. At RT the near band edge band at 3.18 eV was reported with no other peaks registered. In Ref. [53] the obtained samples showed (002) peaks with varying deposition temperature and oxygen pressures. The obtained samples were of wurtzite crystal structures. The authors also studied the variations of the film thickness versus deposition rate and showed a linear behavior with an average deposition rate of 3.5 nm/min. Optically the samples showed high transmission (of 70%) in the visible range of the spectrum. The authors studied also absorptivity versus photon energy using the Eq. (4.1). [32-56]

$$\alpha^2 = A(h\gamma - Eg) \qquad \text{Eq. (4.1)}$$

where Eg is the optical band gap, A is a constant, hγ is the photon energy,

α is the absorptivity which is related to the transmittance by $T = e^{-\alpha d}$, where d is film thickness. Bandgaps of 3.25-3.27 eV were found, which is in agreement with that of the bulk gap. The temperature and oxygen pressure showed smalled effects on the optical bandgap. On the other hand, the oxygen gas and pressure had a drastic effect on electronic properties, especially with the decrease of oxygen vacancies and hydrogen as an impurity within the film, and the increase of resistivity [53].

In a similar fashion Refs [3, 54-56], studied the relation between conductivity and photoluminescence properties of undoped ZnO grown by PLD on glass at varying pressure [54], and deposition temperature [55]. In Ref [54], the obtained ZnO samples were smooth and showed c-axis orientation under XRD analysis, with high thermal conductivity.

However, the electrical and optical properties, in particular, surface conductivity were affected by oxygen vacancies leading to the formation of n-type ZnO. Photoluminescence measurements revealed near band emission at 2.2-2.5 eV corresponding to green-yellow luminescence which was attributed to deep level excitation, on the other hand, the green-yellow band peaks decreased with increasing oxygen pressures during the deposition phase. The transmission of the samples improves from 60 to 90 % with the increase of oxygen pressures, leading to enhancements in their transparency. Moreover, direct bandgap energy measurement revealed the decrease of band energy from 3.34 to 3.30 eV when the oxygen pressure increased from 40 to 150 mTorr. The Moss-Burstein Shift was realized in these samples due to the widening of the bandgap with varying concentrations of defects [54]. In Ref. [55], apart from measuring the direct bandgap using the above relation, given in Eq. (4.1), the resistivity and refractive index were analyzed numerically using Sellmeir dispersion equations given below: [3, 32-56]

$$\rho = \frac{Rp}{Rs} = Tan(\Psi)e^{i\Delta} \qquad \text{Eq. (4.2)}$$

where Rp and Rs are complex reflection coefficients for p-polarized and s-polarized light waves respectively, Ψ and Δ are ellipsometric parameters that are dependent on photon energy. [2, 32-56]

$$n(\lambda)^2 - 1 = a + \sum_k \frac{b_k\lambda^2}{\lambda^2 - \lambda o^2} \qquad \text{Eq. (4.3)}$$

The Eq. (4.3) is approximated as

$$n(\lambda)^2 = A + B(\frac{\lambda^2}{\lambda^2 - \lambda o^2}) \qquad \text{Eq. (4.4)}$$

where A is the same as the refractive index at long wavelengths, B is the oscillator strength and λo is the resonance wavelength. [3, 32-56]

The measured refractive index of the obtained samples, grown at high temperatures, were within the range of 1.9-2.1, with lower values for the samples grown at low temperature due to their poor crystalline qualities. Near--Band, edge emission was realized with Photoluminescence measurements. The measurements showed small peaks of deep level emission, at higher temperatures and no emission at room temperature, which indicated amorphous ZnO at RT, consistent with XRD analysis. These experiments showed enhancement of optical qualities of ZnO films with varying temperatures, further clarifying the background of these emissions. After annealing, deep level emissions were revealed to be related to the concentration of oxygen vacancies within the samples. With the decrease of oxygen vacancies, deep level emission decreased and the quality of the film improved. Electronic (hall) measurements showed the decrease of resistivity and increase an of the hall mobility with rising temperature [55]. In Ref [56], ZnO was grown on Si, GaAs, corning glass, gold and titanium films, sapphire (c plane) substrates by CO_2 laser evaporation technique with varying oxygen partial pressures. The XRD measurement revealed that most of the grown films are of (0002) orientations, with good crystalline qualities. Apart from electrical, acoustical, and transmission measurements, the samples refractive indices were measured using the following expression:

$$\frac{1}{2nt} = \frac{1}{\lambda i} - \frac{1}{\lambda j}$$ Eq. (4.5)

where λi(j) are the adjacent maxima and minima and t is the thickness measured by profilometric techniques [56]. The recorded value for n was 1.98-2.04 in the range of 550-650 nm. Moreover, thermodynamic measurement allowed the visualization of Zn and O isotopes within the obtained samples, clarifying the stoichiometric ratios of the constituents within the films and their impact on the sample properties with n-type conductivities. Note that for Si (100), infrared transmissivity was measured with an absorption band near 25 μm which was attributed to Zn-O stretching band.

The measurements results will be summarized in the upcoming subsections that cover the optical properties of ZnO nanostructures deposited on various substrates and using different techniques.

1. Refractive index of ZnO and like films:

Experiments conducted on ZnO showed anisotropic optical properties, the dielectric functions were studied using Kramers-Kronig relations. Zinc oxide thin films were deposited on different substrates and their index of refractions for both directions were measured. Numerical and simulations were also performed to better visualize the variation of the index of refraction. The best fit for the ordinary index was obtained using: [3]

$$n(\lambda)^2 = A + \frac{B}{\lambda^2} + \frac{C}{\lambda^4}$$ Eq. (4.8)

where A, B, and C are numerical parameters

The Kramers-Kronig technique has been widely used to deduce the dielectric constants and the index of refraction of ZnO. Some authors used the first-order Sellmeir equation given below: [3]

$$n(\lambda)^2 = A + \frac{B\lambda^2}{\lambda^2 - C^2} \qquad \text{Eq. (4.10)}$$

where A, B, and C are fitting parameters and λ is the wavelength

Many other experiments have been performed in studying and measuring the refractive index of ZnO. In addition, dopants were also added to study their effect on the dielectric and optical properties. [3].

2. Infrared optical properties of ZnO:

Although many studies on ZnO and its optical properties have been conducted, the majority of these studies have focused on UV and visible ranges of the spectrum, with few studies dedicated to mid or far-infrared optical properties. The majority of these infrared measurements were made with spectroscopic ellipsometry, which focuses on measuring equation 4.2 and extracting dielectric function and optical properties [32-43]. According to the literature, zinc oxide deposited on various substrates, most notably glass, sapphire, and silicon, has high UV absorption with almost no or low absorption in the visible and mid-infrared regions; in other words, zinc oxide can be considered transparent or with high transmissivity in the visible and mid-infrared regions. The literature also emphasizes that glass is the best candidate among the other substrates for depositing zinc oxide that possesses interesting properties and for a variety of applications or purposes. [3 ,32 - 43].As a result of reviewing recent articles on the infrared optical properties of zinc oxide, there is still a gap in addressing the infrared dielectric functions using Fourier transform spectroscopy (FTIR) [39], as well as the lack of manufacturing oxide reflectance or oxide hyperbolic metamaterial [57 - 59], and these are the points or research gaps that this thesis attempts to address.

D. Impurities and Dopants in ZnO:

The optical and electrical properties are affected by point defects, vacancies, interstitials, impurities, antisites, dislocations, and other complexes formed during the deposition process. It is reported that the formation of defects can be visualized using the following relation: [3]

$$c = Ne^{-\frac{Ef}{KT}} \qquad \text{Eq. (4.11)}$$

where c: is the concentration of impurities or defects

N: concentration of the sites in the crystal where defects can form

E_f: formation energy of the point defect given by:

$$E_f(q) = E_{\mathrm{tot}}(q) - n_{Zn}\mu_{Zn} - n_O\mu_O - qE_{fer} \qquad \text{Eq. (4.12)}$$

$E_f(q)$: formation energy of a point defect with charge state q

$E_{tot}(q)$: total energy of the system

$n_{Zn(O)}$: number of zinc and oxygen atoms respectively

$\mu_{Zn(O)}$: chemical potential for zinc and oxygen respectively

E_{fer}: fermi energy

K: boltzmann constant

The formation of defects is governed by the chemical potential of zinc and oxygen respectively. It was shown that the most common defects or impurities arising in ZnO-based materials are zinc and oxygen vacancies, sometimes these defects lead to the formation of p-type, or n-type effects, depending on the dominant impurities and their concentration. Experiments have revealed that n-type ZnO contains a high level of Zn leading to oxygen vacancies, on the other hand, p-type showed the opposite trend, i.e. Zinc vacancies are formed. To further understand and reduce these defects or impurities, theoretical methods have been developed. Scientists used the density functional theory with local density approximation and Hubbard models to predict the probability of defect formation, the energy levels of these impurities or defects, and their spread within the materials [3].

First; principle calculations provided data on the mobility of these defects and their flow within the material with changing temperatures. These calculations revealed the introduction of annealing after deposition as a means to reduce these impurities or compensate for the low level of oxygen or zinc. However, not all impurities are related to oxygen or zinc. The optical and electrical properties were majorly affected with oxygen/ zinc vacancies or defects, emphasizing the limited effect of hydrogen or other defects on these properties up to certain concentrations [3,60-63].

Photoluminescence have been widely to study the defects in semiconductors [3]. It showed quantitative and qualitative data on the above-mentioned defects and impurities, in addition, it provided information on quantum efficiency, charge states, excited states ….[3]. These experiments allowed scientists to conclude that oxygen vacancies can lead to a green luminescence band in the emission spectrum of undoped ZnO materials [3].

Dopants have been used to enhance the properties of ZnO, some of these dopants are; Al [3, 66-69], Ti [3], Nb [71, 72], Zr, Sn [69], WO_3, Ga [68], Li [65] , Fl [70], and others [3, 24, 73-78],. However, these dopants in their turn affected the optical properties that led to the emission of green, red, violet, blue and yellow luminescence bands [3, 24, 64-78].

E. Summary

This script introduced the reader to zinc oxide (ZnO), discussing its various crystalline orientations and structures, as well as some of the different deposition techniques. Finally, and perhaps most importantly, it discussed the infrared optical studies of the deposited samples. Therefore, it is, a brief review of recent research on this fascinating material and its applications. The review also discussed some of the defects that may be present in most zinc oxide nanostructures, as well as dopants that can reduce these defects and even improve the ZnO film properties, particularly their optical properties.

SECTION III

EXPERIMENTAL TECHNIQUES, INSTRUMENTS AND PROCEDURES

CHAPTER V

INTRODUCTION TO PULSED LASER DEPOSITION TECHNIQUE AND DEPOSTION CONDITIONS

Technological advances and developments in the solid state, materials, electronics, and energy delivery sectors have led to a renewed interest in the deposition of nanoscale and nanostructured materials for a wide range of applications. As a result, new deposition techniques have emerged, including the pulsed laser deposition technique. The rediscovery of PLD in the 1970s and 1980s paved the way for new scientific discoveries, advances, and new branches in physics, chemistry, materials science, and other fields. Therefore, this chapter will focus on the introduction of this technique while ignoring the theoretical concepts underlying sputtering and deposition, which can be found elsewhere [3,15,16, 24, 25, 79-85]. It will begin by introducing the pulsed laser deposition system and its various components, which are the building blocks of PLD, followed by brief historical overviews and the majority of the achievements of this technique. In the following sections, the review will focus on the deposition of oxides, particularly transparent conducting oxides (TCO) such as indium tin oxide (ITO) and ZnO thin films and nanostructures [24,25]. To provide insight into the optimal functional and experimental parameters for achieving efficient oxide deposits. This will lead to a comparison of PLD with other deposition techniques, revealing some of the advantages and disadvantages of PLD. Finally, the chapter anticipates future areas and developments that may result from the use of pulsed laser ablation techniques

A. Pulsed Laser Deposition - introduction and equipment:

The emergence and acceptance of pulsed laser deposition, PLD, as one of the efficient deposition techniques are based on its applicability and versatility in comparison to other techniques. PLD is defined as “a physical vapor deposition process that is performed in a vacuum system and shares some process characteristics with molecular beam epitaxy and some with sputter deposition” [24]. As shown in the figs (17) and (18) below, a system consists of lasers and chambers where deposition takes place under high vacuum atmospheres or using high purity gases.

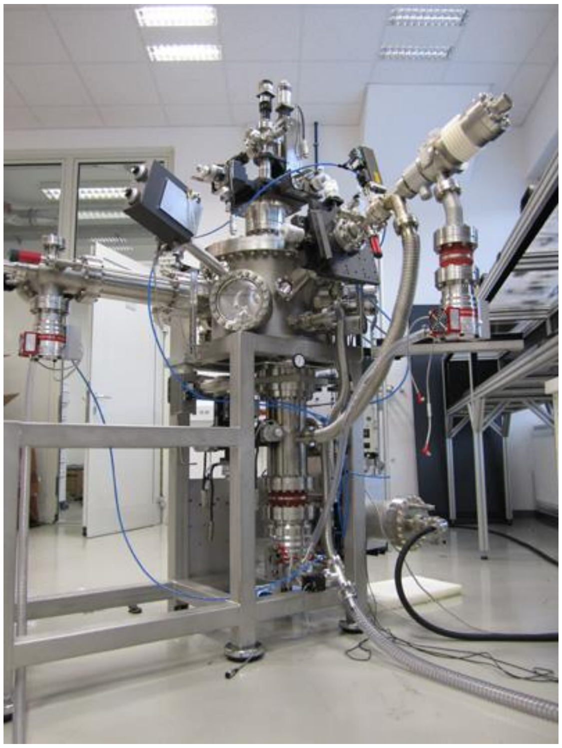

Figure 17 : figure showing pulsed laser deposition (PLD) apparatus [191]

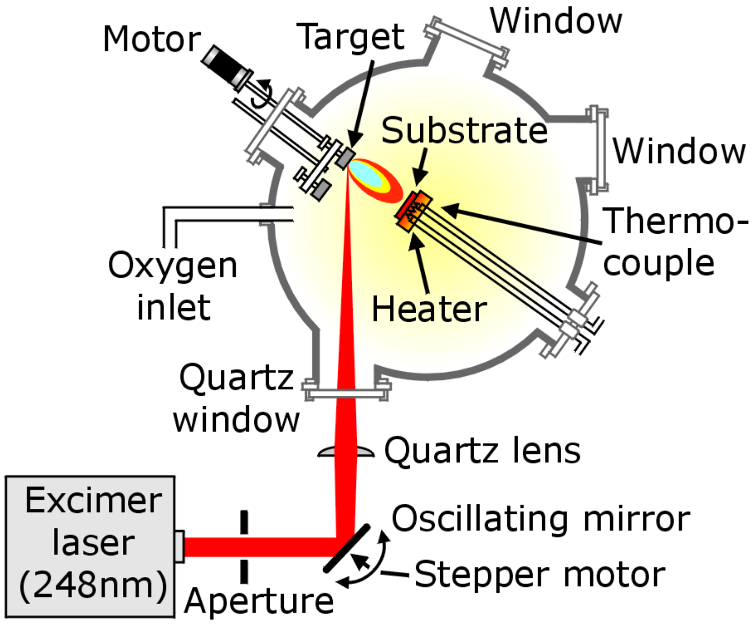

Figure 18: schematic representation of PLD system and deposition process [190]

The PLD apparatus consists of the following main parts or components:

1. Laser: It plays a significant role in depositing high crystalline and efficient films. Lasers impinging on the targets provide the surface of the target with suitable vaporizing energy. The vaporized or ablated energetic particles, forming the plume, tend to spread within the chamber. The evaporation and the kinetic distribution of the ejected particles or plume, highly depend on the wavelength of the incoming photons or lasing light, to that end different types can be used for different material deposition. The choice of the laser type depends on many factors, such as target type, target-laser interaction [15, 16, 24,25], energy fluence, the density of the material, and flow fluency within the chamber… each

of these underwent thoroughly investigation [15, 16, 24,25]. Some of the available and used lasers are ND-YAG (1064 nm, 533 nm), XeCl (308 nm), KrF (248nm), and ArF (193 nm) excimer lasers reaching UV and high energy lasers. [15, 16, 24,25].

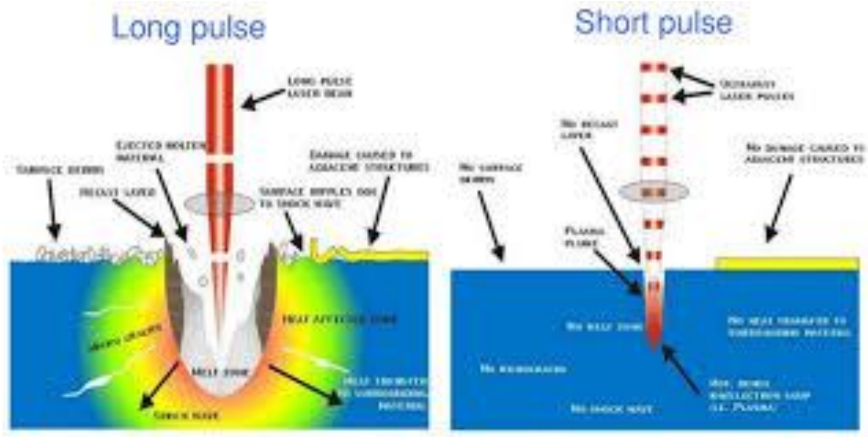

Figure 19: schematic showing the different pulsed lasers and their effect on the target. [188]

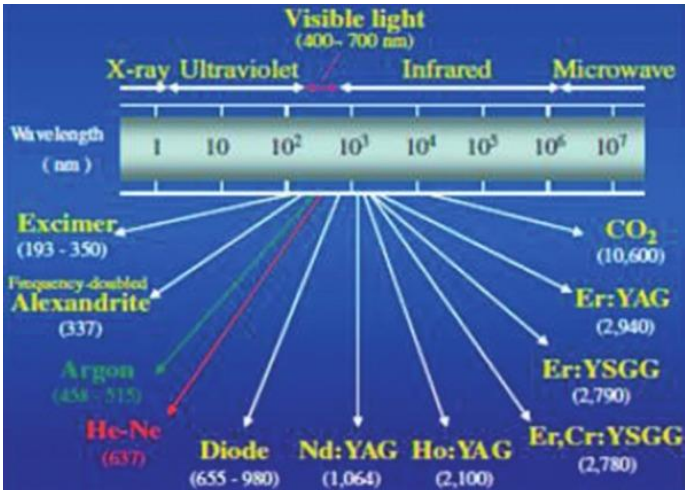

Figure 20: figure showing the different laser types that can be used in PLD along the spectrum. [189]

2. Optics: including lenses, mirrors, laser windows, quartz and beam splitters, and apertures. They aim to direct the lasing light, with minimum absorption and distortion, onto the targets. In some PLD apparatus, these lenses and apertures can be adjusted at suitable angles to align the laser onto the target, providing the most efficient alignments. [24, 25]

3. Chamber: It is one of the main PLD parts, where the majority of the deposition process takes place. Starting with the ablation of the targets that forms a directed forward plume of ejected particles, which is deposited on the substrate. To that end, the chamber should be clean and sealed to avoid contaminants and wastes from entering within the film. Moreover, the chamber can handle high vacuum pressures or high pressures, this gives the privilege to deposit at ultra-high vacuum (10^{-7}-10^{-6} mbar) or under a gaseous atmosphere with pressures reaching 200 mbar. [15, 16, 24,25]

4. Target holder: this includes manipulators or carousals capable of holding several targets, for multi-component deposition. The target can be rotated to avoid damaging or piercing from the energetic laser light and to obtain a uniform plume or homogeneous target vaporization. [15, 16, 24,25]

5. **Substrate holder and heaters:** this includes manipulators or holders, where the substrate(s) is (are) attached. In our case, the substrate is either held by Aluminum strips or using glues that can sustain high temperatures. The heater is attached to the substrate by non-oxidizing tubes and plates that radiate heat thus raising the temperature of the substrate up to 1000ºC. In addition, a substrate shutter is also attached to this holder, to seal the substrate from contaminants during the target-cleaning phase or protect it from any scratch or damage during alignment or target placement phases. The substrate can be moved vertically, thus changing the target-substrate distance.[15, 16, 24,25]
6. **Pumps:** one of the advantages of PLD is to deposit thin films under ultra-high vacuum or gaseous atmospheres of high purity, with varying pressures. To that end, turbo-pump are used to pump the chamber down to 10^{-7}-10^{-6} mbar and to introduce the adequate gases with controllable and varying pressures, some reaching up to 200 mbar. [15, 16, 24,25]

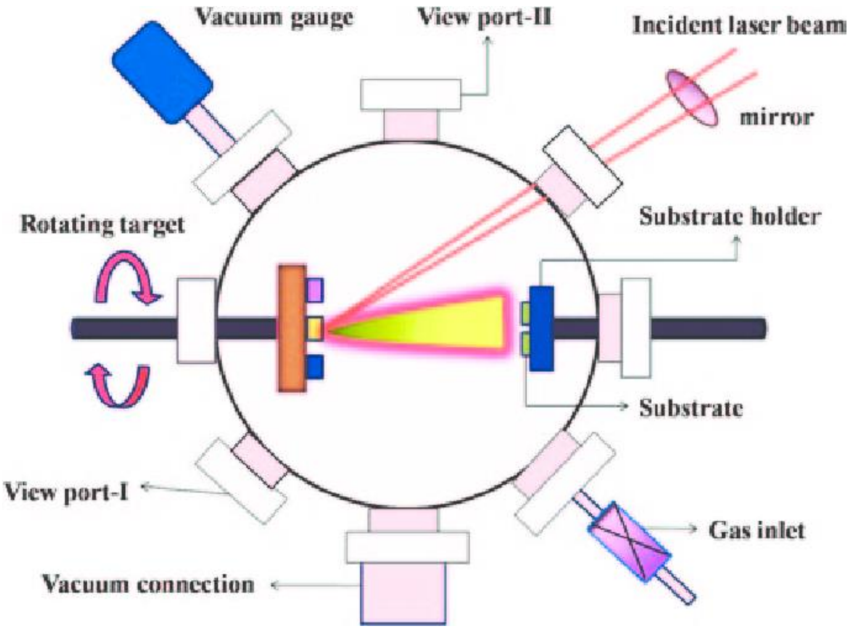

Figure 21: schematic shown PLD apparatus along with its equipment and deposition process [187]

B. Historical Overview of Pulsed laser deposition:

The historical developments of pulsed laser deposition both theoretical and experimental, are divided into three chronological periods: [16, 25]

The 1960s: Rudimentary experimental work was conducted during this period because the technology base for PLD was in its initial phase and not fully developed. For example, some of the lasers available during this period were ruby lasers, Nd glass lasers, and CO2 lasers used at the end of this period. Even with low power and primordial lasers, thin films, on various substrates, semiconductors, insulators, dielectrics, chalcogenides and organic materials were deposited. However, PLD has remained in the laboratories and is being researched for further improvements and developments. [24,25]

The 1970s: a major advancement occurred during this period due to the electronic development and availability in further improving this system and incorporating it into new areas. Another advancement in the technical areas is the development of highly efficient second harmonics used for short wavelength radiation, further improving the deposition by reducing splashing and obtaining congruent evaporations. These further improved film qualities, and opened doors for new films deposition on various materials, such as III-V semiconducting thin films and high T superconductors. [16, 24,25]

The 1980s: major improvements were done during this period with the discovery and availability of laser, which improved the quality of films drastically and opened the door for new material deposition. As such, II-VI compound semiconductors were deposited using ND-YAG laser. In addition, single crystal and heteroepitaxial growth of thin films was performed, compared to molecular beam epitaxy (MBE) and other available deposition techniques. Superlattices, silicon semiconductor films and III-V semiconductor films continued to be studied and deposited. In summary, during this period, a large number of films and nanostructures were prepared, such as nitrides, oxides, and fluorides to name a few, with improved crystalline, mechanical and optical properties. [16, 24, 25]

From the 1990s to the present day, PLD saw drastic improvements both theoretically and experimentally. New complex materials with high purity were deposited such as Nitrides, Oxides, superconductors, optoelectronic devices, Perovskite, and biological materials. Moreover, with the technological development, these PLD-deposited materials led to the development of LEDs, OLEDs, nanowires, nanotubes, Single and multi-wired nanotubes, protecting coatings, wideband gap dielectrics, and hybrid systems. In addition, the PLD system was improved further, with the use of plasma and ions leading to Plasma assisted PLD, ion-assisted PLD, and others. These improvements further assisted and facilitated in depositing films that were considered hard or impossible, such as boron nitrides (BN), hexagonal-AlN and super-lattice structures, polymers ceramics, and organic or inorganic materials for biosensors and related nanotechnologies, just to name a few. Theoretically, Monte Carlo and Molecular simulation improved our understanding and vision about thin films and their properties such as solving Green's equation to visualize the thermal conductivity of thin films or related materials, or the Matrix method for detecting optical and electrical properties of various systems [1,3, 81-86]. As we continue to improve our technologies, we will further improve PLD systems and discover new ways of deposition, or even new material depositions, such as room temperature superconductors, ferroelectric and magnetic materials, and nanotechnologies. [4, 15, 16, 24, 25] (and references mentioned in the previous chapter IV)

C. Advantages and disadvantages of Pulsed laser deposition:

PLD, like any other technique, has advantages and disadvantages. To evaluate and improve PLD systems, it was compared to other available deposition techniques, such as Molecular beam epitaxy (MBE), chemical vapor deposition (CVD), Ion beam deposition, physical vapor deposition, ion vapor deposition, metal-organic chemical vapor deposition (MOCVD), physical-chemical vapor deposition (PECVD), and sputtering (RF-sputtering, magnetron, and neutron sputtering technique). This qualitative comparison revealed that PLD has the following benefits: [16, 24, 25]

- Can be used for epitaxial growth
- Can be used for hetero-structural deposition

- Possessed relatively high deposition rates compared to other deposition techniques
- Can deposit material at low temperatures
- Has good adhesion or improved film deposition using energetic deposition processes
- Low cost
- Easy material change during experiments or maintenance
- Efficient deposition of materials on the substrates using different targets

It also reflected the following drawbacks or disadvantages:

- The deposited films by PLD does not have large areas
- Particulates and impurities can be introduced within the film from the chamber, or the gases used during deposition.

However, the disadvantages listed above can be mitigated or controlled by using ultra-pure materials or cleaning techniques. Furthermore, the benefits far outweigh the drawbacks, making it a promising technique for depositing various nanostructures. These disadvantages or drawbacks must be addressed before PLD can be used commercially and industrially to replace other deposition techniques, but for the time being it remains a research and development technique [3, 16 24].

To demonstrate the benefits and drawbacks of PLD in comparison to others, we have summarized all necessary positive and negative points in the table below:

Advantages of PLD	Disadvantages of PLD
The stoichiometric similarity concerning the targets	Splashing or degradation of the film
Low costs	Small area coverage
Controllable temperature, pressure, The energy of the laser and target-substrate distances	Particles, impurities, and defects within the deposited materials
Deposition at lower temperatures	Film fluctuation especially at edges
Easy change of parts	
Various laser types	
High deposition rates	
Multi-layer and hetero-structure deposition	

Table 1: Table summarizing some of the advantages and disadvantages of pulsed laser deposition compared to other deposition techniques [16, 24, 25]

D. Growth and deposition experiments:

As previously stated, PLD is a device that can be used to fabricate and grow various materials and structures. As noted previously, it is a process that has similarities to molecular beam epitaxy and sputtering techniques. To that end, our PLD apparatus, which is depicted below, is made up of a KrF excimer laser (of 248 nm in wavelength, 20 ns pulse duration). The excimer laser energy can be adjusted from 100 to 600 milliJoules, as well as the frequency, which can be set to as low as 1 Hz or as high as 50 Hz. The laser light is focused onto the target ceiled into the ultra-clean chamber via lenses and quartz mirrors.

Figure 22: figure showing our pulsed laser deposition [199]

The Growth of ZnO thin films on glass substrates consists of several stages and phases which are elaborated below: [15, 16]

1. Cleaning and substrate preparation: the glass substrates are cleaned to remove any contaminant present on its surface. The cleaning procedure starts by placing the samples into pure acetone heated to 55 ºC for about 10 min. Afterward, the samples are placed within pure methanol, heated to 55 ºC for about 10 min as well. Then the substrates are rinsed with deionized or distilled water for about 2 min and finally dipped in pure methanol for about 5 seconds. Lastly, the cleaned substrates are removed from the methanol, dried by nitrogen gas, and placed into the chamber, by mounting it onto a silver plate (serving as substrate holder).
2. Target installation and alignment: the laser and PLD system is turned on before the cleaning phase. After placing the substrate, the substrate shutter is closed to avoid contaminants during the alignment from falling on its surface. Plexiglass is replaced

in place of the target, and the laser is adjusted at a maximum HV of 27 kV and a frequency of 1 Hz. The laser hits a point on the plexiglass, which is marked. A needle is placed on this marked spot, showing the position of the plume that hits the substrate, to which the substrate is rotated to maintain maximum alignment between the needle and the target. This alignment is done to maximize the deposition of the target on the substrate. Before replacing the ZnO target, the chamber is cleaned with pure isopropanol and dried with nitrogen gas.

3. Vaccumization: the target is placed into the PLD chamber, after drying the chamber with nitrogen gas. Then the chamber is ceiled by a wooden clamp. The chamber is then pumped, reaching high vacuum pressures up to 10^{-5}-10^{-7} mbar.
4. Heating and pressure adjustment: The thermostat is adjusted to the desired temperature. In our experiment, the substrates are heated to 350 ºC, at a rate of 700. After stabilizing the temperature, oxygen gas is injected into the chamber to reach the required pressures. To maintain these pressures the flow rate of the gas is adjusted. In our procedure, the deposition was performed under a partial oxygen pressure of 0.12 mbarr, with an adjustable flow rate of 315-320 sccm. [45]
5. Cleaning the target: once the required pressure is adjusted and maintained, the laser is set on a maximum HV of 27 kV with a repetition rate (frequency) set at 10 Hz. Then the substrate shutter is closed and the target is cleaned pulsed, for about 5 to 10 mins.
6. Deposition: after pulsed-cleaning of the target, the substrate-to-target distance is set, which in our case is 5 cm. The laser mode is replaced under ENG-NGR mode, which is the energy mode, and through a laser controller, the energy of the laser and

its frequency is adjusted. Finally, the substrate shutter is open, and deposition is executed for a specific period. In our procedure, the samples were deposited with laser energy of 350 mJ at a repetition rate of 5 Hz. The deposition time was varied from 15 min to 2 hour and 30 min, to study the effect of thickness on the properties of zinc oxide. [45]

7. Cooling and characterization: lastly, the samples are cooled down under oxygen partial pressure of 0.12-0.14 mbarr, to room temperature. Afterward, the chamber is ventilated and the samples are extracted to be analyzed. The characterization techniques and experimental devices will be introduced in the upcoming chapters.

Deposition conditions	Sample 2	Sample 3	Sample 4	Sample 5	Sample 6	Sample 7	Sample 8
Laser energy (milliJoules)	340	348	348	348	348	348	348
Repetition frequency (Hz)	5	5	5	5	5	5	5
Vacuum pressure (mbar)	$3*10^{-5}$	$3*10^{-5}$	$3*10^{-5}$	$3*10^{-5}$	$3*10^{-5}$	$3*10^{-5}$	$3*10^{-5}$
Oxygen partial pressure (mbar)	$1.4*10^{-1}$	$1.2*10^{-1}$	$1.2*10^{-1}$	$1.2*10^{-1}$	$1.2*10^{-1}$	$1.2*10^{-1}$	$1.2*10^{-1}$
Oxygen flow rate (sccm)	332 - 334	315 - 322	315 - 320	315 – 320	314 - 320	315 - 325	310 - 320
Temperature (ºC)	350	350	350	350	350	350	350
Deposition duration (min)	About 30	About 35	About 40	About 45	About 50	About 60	About 75

Table 2: Table summarizing the conditions used for depositing samples 9 to 11 and 17 to 19 by pulsed laser deposition

Deposition conditions	Sample 9	Sample 10	Sample 11	Sample 17	Sample 18	Sample 19
Laser energy (milliJoules)	348	348	348	348	348	348
Repetition frequency (Hz)	5	5	5	5	5	5
Vacuum pressure (mbar)	$3*10^{-5}$	$3*10^{-5}$	$3*10^{-5}$	$3*10^{-5}$	$3*10^{-5}$	$3*10^{-5}$
Oxygen partial pressure (mbar)	$1.2*10^{-1}$	$1.2*10^{-1}$	$1.2*10^{-1}$	$1.2*10^{-1}$	$1.2*10^{-1}$	$1.2*10^{-1}$
Oxygen flow rate (sccm)	319 - 325	319 - 325	319 - 325	150 - 160	150 - 160	150 - 160
Temperature (ºC)	350	350	350	350	350	350
Deposition duration (min)	About 55	About 15	About 120	About 90	About 115	About 150

Table 3: Table summarizing the conditions used for depositing samples 9 to 11 and 17 to 19 by pulsed laser deposition

E. Summary and future trends of PLD:

PLD has been and will be used for the future deposition of oxides, nitrides, and other complex nanostructures. Anticipated application areas for PLD include nano-sized wires, large-area coatings, multilayer and heteroclastic structures, and p-type and n-type doped oxides. Not to mention biological materials, ferroelectric and magnetic oxides and similar materials. Plasma-assisted PLD and ion-assisted PLD promise a reduction in film inhomogeneity, film fluctuation, and an improvement in film quality by avoiding or further reducing impurities and particles that reach the substrate during the deposition phase. As the technology develops, new accessories will be manufactured to further enhance the PLD system and make it available to commercial and industrial markets.

CHAPTER VI

X-RAY DIFFRACTION (XRD)

X-ray diffraction (XRD) is a technique used to characterize the crystal structure of various nano/micromaterials, as well as to study the size of particles and deduce some of their properties. It can also be used to characterize electrical and liquid solutions. When electromagnetic radiation falls on any periodic structure with a specific orientation and geometric variation, diffraction patterns and effects are visualized. This diffraction phenomenon is affected by the interatomic distance between the crystals or planar arrays that form the geometric structure under study, which is usually between 0.15 and 0.4 nm, corresponding to an electromagnetic spectrum with energies ranging from 3 to 8 keV, and therefore the use of X-ray diffraction [16, 120,127-129]. To this end, after defining X-ray diffraction, this section will focus on the phenomenon and techniques of diffraction, mentioning the different types of radiation used, concisely covering the theoretical background necessary to understand the X-ray diffraction process, and finally covering the experimental procedures followed during our characterization measurement and X-ray diffractometry apparatus. Finally, the script will provide a summary of the descriptive analysis as well as a list of references used.

A. Types of radiation used in diffraction

Three types of radiation are commonly used in diffraction processes and characterization: X-rays, electrons, and thermal neutrons. [9, 96 , 118-120]

X-rays with photon energies ranging from 10 to 100 KeV can penetrate the crystal and are easily scattered by electrons. X-rays can determine a variety of characteristics and structural studies, but they can't pinpoint the location of light atoms like hydrogen or helium, and they can't tell the difference between different isotopes. The X-ray diffraction mechanism focuses on scattered radiations that are coherent and in phase with the incidence radiation, with no significant changes in its wavelength.[9, 96 , 118, 119]

Electrons' interactions with interatomic particles and molecules are highly dependent on the charge of the molecules that make up the investigated samples, so electrons can only penetrate a few Angstroms within crystal layers. Thus, the use of electron diffraction is well-known for the surface layer and surface crystalline studies; typical applications for such surfaced analysis include thin films. [10, 96 , 118, 119]

Slow-moving neutrons (typically thermal neutrons) with wavelengths compatible with interatomic distances can interact with the investigated samples in a variety of ways. It can penetrate deep into non-magnetic materials, reaching the nuclei. Furthermore, neutron elastic and inelastic scattering can provide a wealth of information about the samples being studied and can distinguish between isotopes of the same element. Because neutrons have no charge, their interaction is highly dependent on their energy; thus, measurements registering any change in neutron energy and direction of its inelastic scattering are commonly used in studying and characterizing that are based on neutrons. Materials with magnetic fields, on the other hand, can affect the depth and interaction with the incoming neutrons; for example, a neutron scattered elastically can provide data on the magnetic moment distribution within the examined samples. [9, 96]

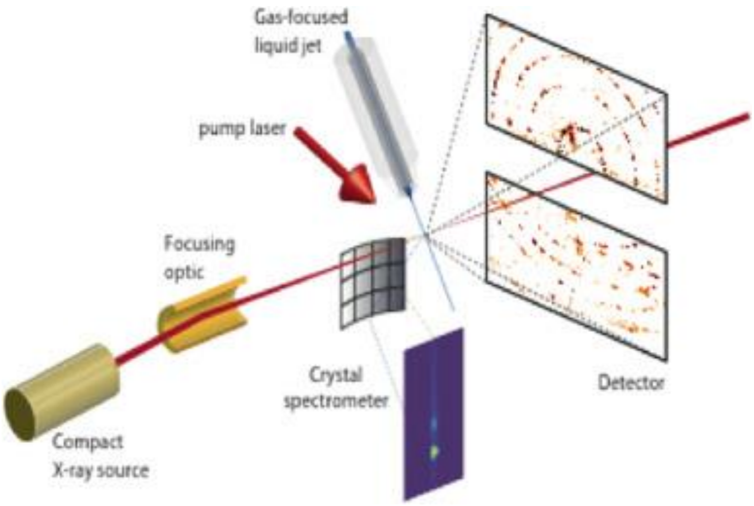

Figure 23: Sketch showing X-ray diffraction process [123]

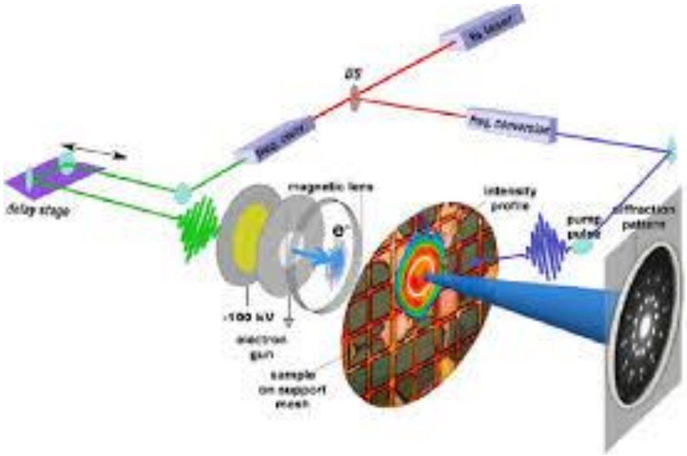

Figure 24: Sketch showing electron diffraction process [121]

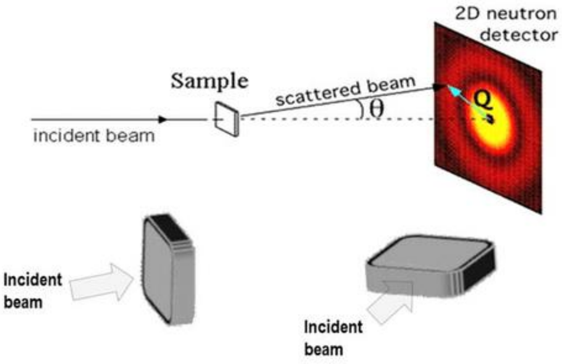

Figure 25: Sketch depicting Neutron Diffraction process [124, 125]

Figure 26: Figure illustrating the difference of X-ray, electron, and neutron diffraction patterns [130]

B. Bragg Diffraction Law

The reflected diffraction of monochromatic rays incident on a crystalline sample's surface is highly dependent on the wavelength and geometric structure of this surface. W.L.Bragg proposed and presented a simple picture and a simple equation describing these diffraction conditions in the 1913s to establish the conditions where diffraction is noticed. As a result, the crystalline structure is represented by a set of planes containing the crystal's atoms, with each plane separated by a distance known as interatomic or interplanar distances, as shown in the fig. (27) below. [9, 96, 118-120]

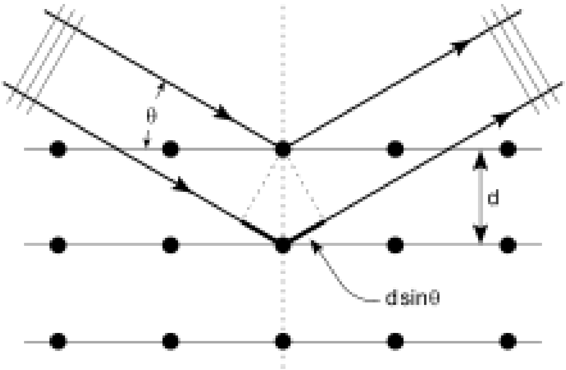

Figure 27: Sketch depicting the diffraction process from a set of planes arranged along with the crystalline samples [9, 118]

The incident radiation is reflected from the set of planes that make up the samples, as shown above, much like a light ray is reflected from a mirror surface!! The reflection in this Bragg's image is specular, which means that the incident angle of the incoming rays must be equal to the reflected angles. The reflected rays continue along their path and are interfered with each other at the detector. According to the interference phenomenon, only constructive interference can attribute to physical reflection patterns, whereas destructive interference will prevent any reflected beam from appearing. As a result, constructive interference necessitates that the path difference between the rays is an integer multiple of the wavelength, as shown in the Eq. 6.1 below: [9, 96, 118-120]

$$2d\sin(\theta) = n\lambda \qquad \text{Eq. (6.1)}$$

Where d denotes the interplanar distance, n denotes the order of reflection, λ is the wavelength of the incoming x-rays, and θ is the angle between the plans and the incident or reflected rays, as shown in fig. 28 above. This is Bragg's equation for diffraction, which holds for all wavelengths up to and including to $\lambda \leq 2d$. [9, 96, 118-120]

As previously stated, the Bragg conditions show that the diffraction is heavily influenced by the wavelength and angle, i.e. the geometric structure of the sample. As a result, either the wavelength or the angle can be varied until the above condition is met, providing new information about the structure and crystallinity of the samples under investigation. Typically, for a given set of incident wavelengths, the angle is varied by rotating the sample, revealing previously unseen features that are revealed by crystal symmetries and satisfying diffraction conditions. [9, 96, 118-120]

Finally, the Bragg diffraction conditions are a simple and crude model that explains the diffraction process without mentioning anything about scattering phenomena, and structure factor of the atoms that compose the crystal, which must have a high influence on the diffraction patterns or must have information about the various crystalline-properties under examination. [9, 96, 118-120]

C. Diffraction Condition and Scattering Factor

The crystal properties are invariant under translation of the form T=ua+vb+wc, where (u,v,w) are integers and (a, b, c) are unit vectors along the axes of the crystal. Since any physical property of any crystal can be deduced from the electronic density of states, then the density of states should be invariant as well under this translation. [9, 96, 118-120]

$$n(r+T) = n(r) \quad [9] \qquad \text{Eq. (6.2)}$$

where n is the density of states and r is a vector represented in Cartesian coordinates by r=xa+yb+zc. For the sake of simplicity, we will limit ourselves to one dimension and then generalize it to higher dimensions. One can demonstrate that the density of states can be expanded in a Fourier Series with the Reciprocal Space (Refer to the Appendix A) as follows: [9, 96, 118-120]

$$n(x) = \sum_p n_p e^{i\frac{2\pi p}{a}x} \quad [9] \qquad \text{Eq. (6.3)}$$

Here the density of state was expanded over the Reciprocal Space using the Complex Fourier Series, with $\frac{2\pi}{a}$ denoting the length of the Brillouin Zones (also refer to the Appendix A). Since n is used to derive the physical properties of the crystal as mentioned, it should denote a real function. Thus, it should satisfy the following condition: [9, 118]

$$n_p = n_{-p}^{*} \quad [9] \qquad \text{Eq. (6.4)}$$

where the * denotes for complex conjugate. This can be extended to high dimension as follows: [10]

$$n(r) = \sum_{G} n_G e^{iGr} \quad [9] \qquad \text{Eq. (6.5)}$$

where G denote the lattice vectors in the reciprocal space or Fourier Space (Refer to the Appendix A) [9, 118].

Consider the incident x-rays falling on the sample, which are represented by e^{ik1r} where k1 is the incident wavevector (where the amplitude and time component of the incoming beams or waves, are dropped for the sake of simplicity). Similarly, scattered waves are denoted by e^{ik2r} where k2 represents the scattered wavevector. [9, 118]

Given that the amplitude of a wave scattered from a space within a volume V sample is proportional to the electron local density of states, it can be demonstrated that the amplitude of theelectromagnetic scattered waves is proportional to the following: [9, 118]

$$F = \int n(r)\, e^{i(k1-k2)r} dV = \int n(r)\, e^{-i\Delta kr} dV \quad [9] \qquad \text{Eq. (6.6)}$$

where Δk = k2-k1 or k1+Δk = k2 [9, 118], and is defined as the change in the scattered wavevector or changes to the wavevector caused by scattering processes. By plugging equation Eq. (6.5) into equation Eq. (6.6), one obtains:

F= $\sum_G \int n_G e^{i(G-\Delta k)r} \ dV$ [9] Eq. (6.7)

The above equation should satisfy the following $G = \Delta k$, and Eq. (6.7) reduces to $F = Vn_G$ [9], showing that the scattering factor is independent of the directional charge distribution, and the magnitude of the wavevector reduces to:

$$(k1 + G)^2 = \ k2^2 \qquad \text{Eq.(6.8)}$$

The conservation of energy must be satisfied during the scattering process, which means that the incident and reflected or scattered rays must have the same energy. As a result, the incident and scattered wavevectors must have the same wavevector, in other words, k1=k2=k. This reduces the above equation, Eq. (6.8) into:[9, 96, 118-120]

$$2K.G = G^2 \text{ [9]} \qquad \text{Eq. (6.9)}$$

Note that –G and G both represent the same reciprocal lattice vectors and their amplitudes are the same. As a result, G can be denoted as G = $hb_1 + kb_2 + lb_3$, where (b_1, b_2, b_3) are the reciprocal unit vector and (h,k,l) are integers known as miller indices, which are the indices of the crystallographic plane where the diffraction processes take place. Having the angle between k and G to be θ, the above last equation reduces to the Bragg Diffraction law, with d representing the interatomic distance along the [hkl] direction or parallel to the plane (h/n, k/n, l/n) and n here being the integer denoting the order of the diffraction. [9, 118]

The classical scattering theory predicts that as the angle 2θ between the incident and scattered waves increases, the scattering efficiency decreases, which is attributed to the electron distribution over a volume with a diameter compatible with the x-ray wavelength [118]. As a result, the scattering radiation of a single electron or particle after accounting for the surrounding interferences is of the form

$$f_i = \int n_i(r) e^{-iGr} dV \quad [118] \qquad \text{Eq. (6.10)}$$

where index “i” refers to the i-th atoms within the crystal.

Assuming that α is the angle between r and G, one obtains for f_i expressed in Eq. 6.10 considering spherical coordinates within the integration:

$$f_i = 2\pi \int n_i(r) e^{-iGrcos(\alpha)} r^2 dr d(\cos(\alpha)) \quad [9,118] \qquad \text{Eq. (6.11)}$$

$$f_i = 4\pi \int n_i(r) r^2 dr \, \frac{\sin(Gr)}{Gr} \quad [9,118] \qquad \text{Eq. (6.12)}$$

with $Gr = \frac{4\pi \sin(\theta)}{\lambda}$

Finally, upon performing the integration the atomic scattering factor reduces to:

$$f_i = Z \frac{\sin(Gr)}{Gr} \; [9,118] \qquad \text{Eq. (6.13)}$$

where Z is the number of the atomic electrons within the crystal. [9, 96, 118-120]

For small Gr, which is often the case, the atomic scattering factor reduces to the electron number. As a result, the atomic scattering factor can be calculated using the charge density distribution, as demonstrated by the Hartree-Fock self-consistent distribution function [118]. Although atomic bonding can change the electron charge distribution, the scattering is close to the Hartree-Fock expression, which can be investigated by changing the angle in the Bragg Law without changing the X-ray wavelength. Because mass is in the denominator in the scattering theory, and because neutrons are heavier than electrons, X-ray scattering by neutrons is usually negligible and will not influence the electronic x-ray data.[118]

The diffraction theory that is expressed as Δk = G may further be restricted by the geometrical representation, which is expressed through the Laue Eqs. (6. 14) as shown below:

$$\begin{aligned} a.\Delta k &= 2\pi u \\ b.\Delta k &= 2\pi v \\ b.\Delta k &= 2\pi w \end{aligned} \qquad \text{Eq. (6.14)}$$

where again (a, b, c) are the unit vectors along the axis, and (u, v, w) are integers presenting the magnitude of the vector. [9, 118]

The first equation of the preceding expression, namely Eq. (6.14), confines Δk within a cone along the direction a. Similarly, the second and third equations of the preceding expression limit the Δk within a cone along b and c, respectively. As a result, Δk must satisfy the three previously stated conditions, which are maintained by varying and searching for an appropriate wavelength or crystal orientation, the latter by rotating the samples or changing the angle θ. [9, 118]

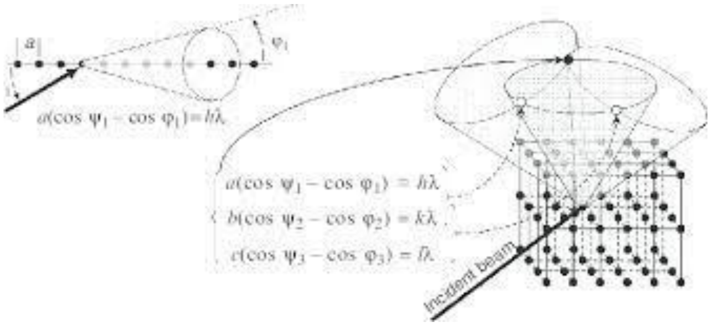

Figure 28: sketch illustrating the Laue diffraction conditions, showing the cones along the different orientations [126]

D. Structure Factor

The structure factor considers the impact of the various types of atoms and molecules present in the crystal, as well as defining the positions of the atoms within the unit cell. Defects or different atoms within the crystal can scattered incoming radiation out of phase with that scattered by the main atoms composing the crystal, along with certain (hkl) directions. [9, 96, 118, 119]

Consider a solid with N atoms in its basis. Assume that all of these atoms are placed along the (hkl) plane, with no atoms above or below these planes, and are separated by d_{hkl}. The first-order x-ray reflection has the highest and maximum efficiency; however, all remaining planes reflect with an angle of 2π lag in phase compared to the prior plane. However, in practice, some atoms usually occupy positions along with the above and below (hkl) planes, resulting in scattered waves from each atom that are out of phase with each other. [9, 96, 118, 119]

As the diffraction condition codified as $\Delta k = G$ is satisfied the scattering factor, mention in the previous section, for such crystal with N atoms or cells can be written in the following manner:

$$\mathrm{F} = F_G = N \int n(r) e^{-iGr} \; dV = NS_G \quad [9] \qquad \text{Eq. (6.15)}$$

In the above equation, the integration runs over a single cell, and S_G is the structure factor. As can be seen, the scattering factor from each atom or cell is proportional to the structure factor, which is coded in the preceding expression [9, 118]. The structure factor further reduces the intensities of the scattered rays in various materials by imposing additional restrictions in addition to the diffraction conditions, for example, for the BCC lattice the structure factor is zero when the sum (h+k+l) is an odd integer, whereas for the FCC lattice the structure factor is non-zero when h, k, and l are either all even or all odd. [9, 96, 118, 119]

E. Our X-ray Diffractometer and Experimental procedure

Figure 29: figure showing our Bruker AXS D-8 Advance Bragg Brentano diffractometer [129, 199]

The X-ray measurements and analysis were carried out using the D-8 Advanced AXS Bruker Bragg-Brentano available at our CRSL labs, with an analysis mode-locked at θ/2θ mode, which corresponds to the variation of the output beam angle coupled at the same time with the incident angle, in other words, the incident and scattered angles are equally varied, with a constant specified wavelength at all times during the measurement. The D-8 Advance AXS XRD diffractometer is outfitted with a copper x-ray tube that emits K_α and K_β radiations, the latter is eliminated using Nikel filters, and the former includes $K_{\alpha1}$ and $K_{\alpha2}$ which is removed by the EVA software. After passing through Nickel filters and focusing mirrors, x-rays with wavelengths of 1.5418 Angstrom are directed towards the samples under investigation. The scans were carried out using Bragg-Brentano geometry and the following experimental parameters: The copper tubes were set to 40 KV voltage and 40 milliAmpere current, and the angle 2θ was varied in increments of 0.02 degrees from 5 to 90 degrees, with scan speed for each step set to 1 sec. [16, 129]

Following the measurement, the obtained data is collected by the detector and analyzed by the EVA software, displaying the crystallinity and any defects found within the sample. A search and match analysis performed by the EVA software and the International Center for Diffraction Data (ICDD) identifies the XRD patterns [16, 129]. XRD measurements were performed separately on the ZnO targets, the substrates used, and the various thin films deposited on the substrates to assess the crystallinity and to compare the XRD patterns of the samples with those of the target and substrate. It should be noted that the obtained XRD patterns were normalized, which eliminated the background noise present during the experiment, and that the total width at half maximum (FWHM) was calculated by selecting an area in the EVA software that contained the required peak. [16, 129]

Figure 30: figure showing sample holder used in our XRD measurements [129]

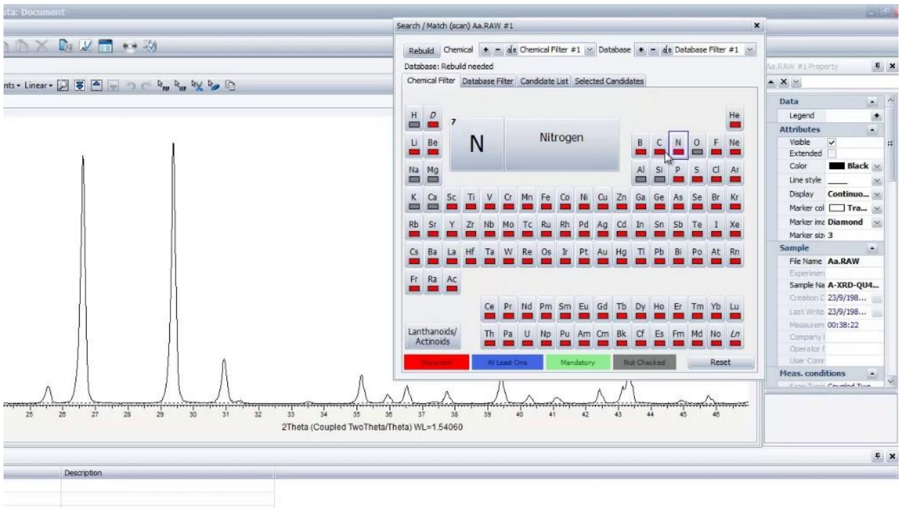

Data
Legend

Attributes

Visible	☑
Extended	☐
Color	Black
Line style	
Display	Continuo...
Marker col	Tra...
Marker ima	Diamond
Marker siz	3

Sample

File Name	Aa.RAW
Experimen	
Sample Na	A-XRD-QU4...
Creation C	23/9/198...
Last Write	23/9/198...
Measurem	00:38:22
Company I	
Operator I	
User Com	

Meas. conditions

Figure 31: figure representing the EVA software used in identifying the obtained peaks [129]

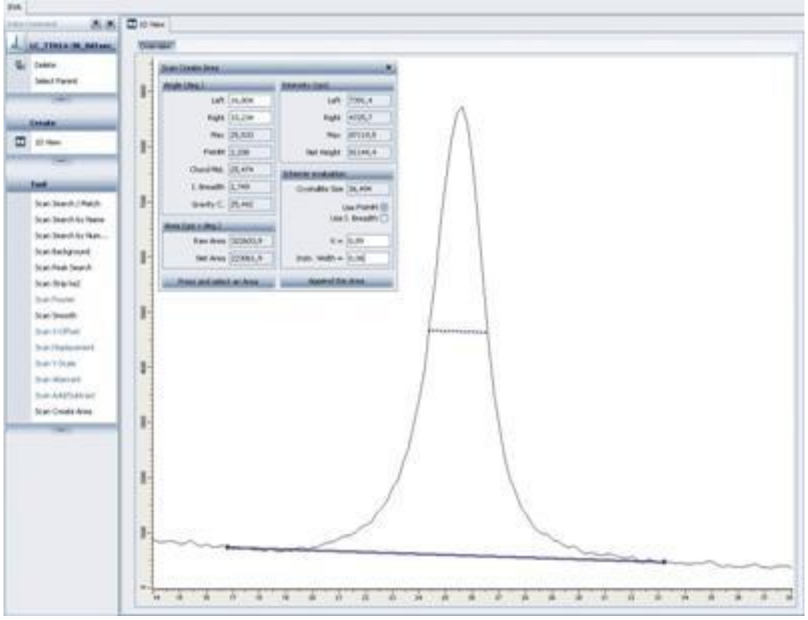

Figure 32: Figure showing an example of FWHM measurement with EVA software [129]

F. Summary

This chapter introduced the reader to the technique of X-ray diffraction (XRD), covering the different types of radiation used for diffraction and diffractometers, as well as some of the theoretical underpinnings of the apparatus, such as Bragg diffraction conditions, Laue equations, structural and scattering factors. Finally, and perhaps most importantly, this chapter described the experimental procedures and steps we followed during our experiments, as well as our X-ray diffractometer (Bruker apparatus).

CHAPTER VII

SCANNING ELECTRON MICROSCOPY (SEM)

Scanning electron microscopy (SEM) is a technique that uses electron beams to scan the surface of nanomaterials and produce an image of the sample surface. SEM can provide a three-dimensional perspective as well as a morphological view of the samples being studied. Therefore, SEM can be used to visualize small samples with nanometer scales ranging from 10 to 20 nm in diameter [96]. This section will start by presenting the scanning electron microscopy system, briefly introducing its different parts, and then it will present some of the applications in which the SEM plays a crucial role; moreover, it will predict the future areas and developments that could follow the incorporation of the SEM or similar devices [99, 113].

A. Scanning Electron Microscopy - introduction and equipment:

The advent of electron optics in the 1930s prompted the search for new electron-optical instruments of various types [87-99]. Transmission and scanning electron microscopy were some of these devices. The word microscope is etymologically derived from the Greek words micros, which means small, and skopeo, which means to look at [87]. As the name implies, electron-scanning microscopy examines or enlarges materials or devices that are invisible to the naked eye [87-99]. Because electrons have shorter wavelengths than optical lights, they can be focused or impinged on materials at nanometer scales, revealing more material features than optical microscopes [87-89, 92, 96]. Images or features are obtained in a scanning electron microscope (SEM) by analyzing a high-energy electron beam on the sample surface, thus the name scanning electron microscope (SEM) [87, 88-98]. Modern SEMs can enlarge or magnify the investigated objects to the point where they can resolve or reveal features smaller than one nm in dimension. Furthermore, the impinging electrons emit x-rays with specific energies that can be used to detect the composition of the investigated materials. In summary, "SEM is a material characterization tool that provides information about surface or near-surface structure, composition, and defects in bulk materials" [87]. To that end, it has accompanied scientists in their experimental work since its inception, and with its continued advancement, the SEM is now used in a wide range of disciplines and industries. [87-98]

Figure 33: figure showing scanning electron microscopy apparatus [108, 114]

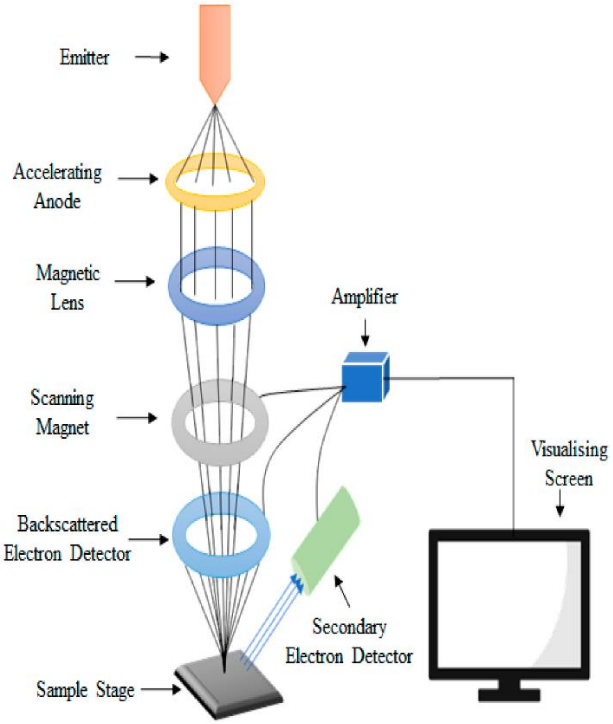

Figure 34: schematic representation of scanning electron microscopy [108]

The electron column, chamber, and controlling system are the main components of SEM, as shown below, in addition to other instruments or parts, such as optical lenses, apertures, aberration systems of various types, Stigmators, scanning coils, magnifiers, chambers, pumps, heaters, chillers, stages, sample holders, infrared cameras and detectors, that function as basic but play an important role in achieving highly demanding microscopic applications [16, 87-98, 115, 116]. As a result, this script will summarize the essential components and parts of the SEM system: [87-98]

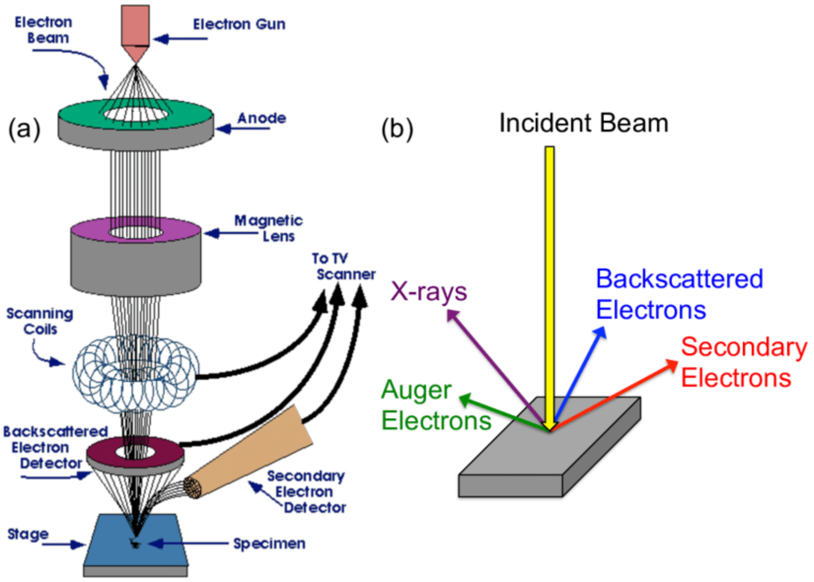

Figure 35: Sketch showing the constituent parts of an SEM [114]

1. Electron Column: it is a long cylindrical body located above the chamber that contains electron guns or sources, lenses, coils, and apertures to focus the incoming electron on the investigated samples [87-98].

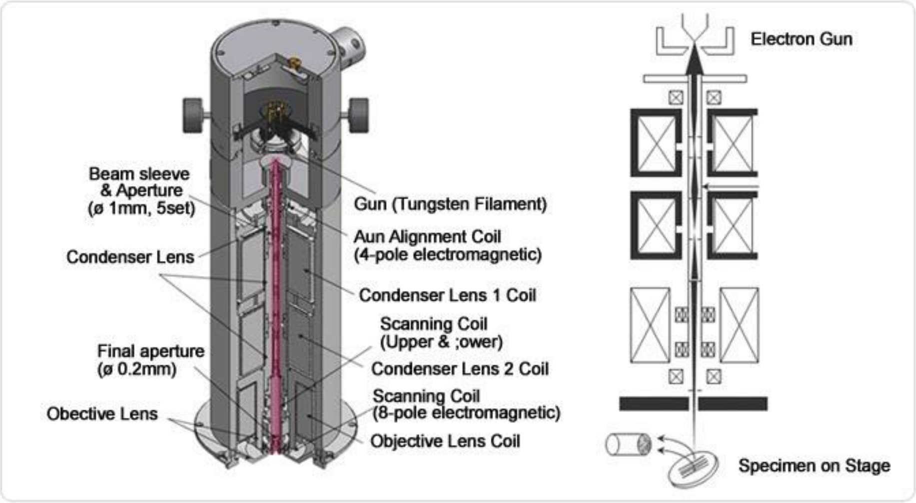

Figure 36: figure showing electron column located in an SEM along with its constituting parts. [200]

2. Electron Guns or Sources: The primary function of electron sources is to generate electrons and accelerate them towards samples for various applications. Electrons are aligned towards the investigated samples by electromagnetic forces using voltages ranging from 2 to 30 kV depending on the type of investigation and required parameters. To ensure that a large number of electrons reach the samples, the electron gun is usually stored in a highly vacuumed environment to avoid electron interaction with molecules in the ambient air [1]. Various types of electron guns used in SEM, which are usually classified as thermionic emission or field emission, and are briefly summarized here; further information on electron guns can be found elsewhere [87-98]:

   2.1- Tungsten Filament: The emitting filaments in such guns are made of tungsten wires that have been annealed strain-free and have a V-shaped "Hairpin" shape. The use of tungsten wires is attributed to its properties, most notably its high melting points, low vapor pressure, low thermal coefficient of expansion, and high tensile strength, which allow tungsten to withstand extreme heat and pressure. Tungsten electron thermionic emitters are low-cost and dependable, making them popular for low-magnification imaging and micro-chemical analysis. On the other hand, it has some disadvantages, such as a short lifetime (depending on the emission current used, it can last up to 100 hours for moderate currents), oxidation of tungsten wires, which can drastically hinder electron production; however, this can be avoided by storing such guns or systems at low vacuums of 10^{-3} Pa. Furthermore, tungsten electron guns require a high working function (typically 4.5 eV), low brightness, and a large energy spread (1.5-2.5 eV). All of these characteristics make tungsten guns unsuitable for low-energy microscopy applications (1-5 kV). [87, 88-99]

2.2- Lanthanum Hexaboride emitters: Lanthanum Hexaboride (LaB_6), emitting filaments in such guns, have a purple-violet color and a high melting point. Similarly, such sources are chosen due to properties such as low working function, high melting points, low vapor pressure, chemical, and thermal stability. Because of the aforementioned properties, lanthanum hexaboride is brighter than tungsten filaments and has a longer lifetime, which improves the quality of microscopic images. However, such systems are expensive and require a high vacuum (typically of 10^{-5} Pa) to prevent the oxidation of lanthanum hexaboride, which prompted the search for alternative sources of LaB6 that are low oxidizing in nature. Finally, because tungsten filaments and Lanthanum hexaboride are thermionic emitters, they are unsuitable for low voltage and low energy imaging or microscopic applications [87, 88-99].

2.3- Cold Field Emission Guns: As an electron emitter, these guns employ single crystallized tungsten cathode tips through which electrons are emitted via quantum-mechanical tunneling without the use of thermal sources, and which are controlled by electric fields that extract and direct the electron towards the investigated samples. Because they operate at a lower temperature, such systems have a longer lifetime, higher brightness, and a smaller energy spread than thermionic systems. These characteristics allow such systems to be used for low-energy microscopic imaging and applications**.** However, such systems are chemically unstable due to their sensitivity to chemical interaction, and their application is limited to lower current. Furthermore, it necessitates a high vacuum environment at all times to maintain its stability, and lower demagnification degrees make it susceptible to fluctuations in electromagnetic fields from sources outside the system. All of these disadvantages make scanning electron microscopies complex in structure and design, but they are used for high-resolution measurements. [87, 88-99].

2.4 – Schottky Field emitters: This emitter is a combination of field and thermionic emissions, in which the applied electric field is used to reduce the working function of tungsten wire or tungsten filament, which emits electrons via thermionic processes as described for tungsten filament guns. The tungsten filament is sometimes coated to further reduce its high working function. To avoid contamination and to maintain stable current and high brightness, such emitters must be kept in clear and high vacuum environments, extending their lifetime. However, because of thermionic processes, it has a higher energy spread, larger tungsten filament tip radius, larger areas, and lower spatial resolution or limited resolution with low voltages. Schottky emitters are typically associated with applications that require large stable currents, such as backscattered diffraction and x-ray dispersive spectroscopy, but they can also be used in other microscopic applications [87, 88-99].

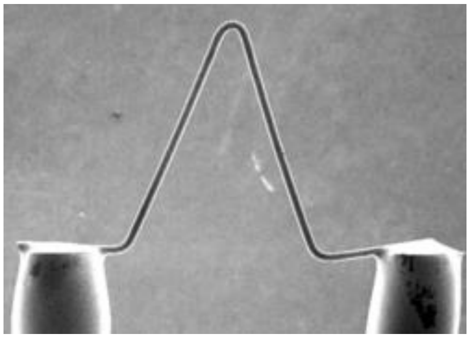

Figure 37: figure showing tungsten filament used in SEM [87-98]

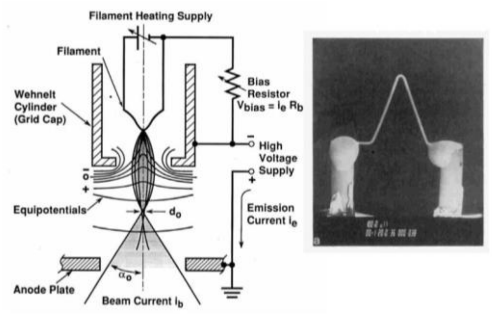

Figure 38: schematic representation of tungsten filament guns used in some SEM systems [87]

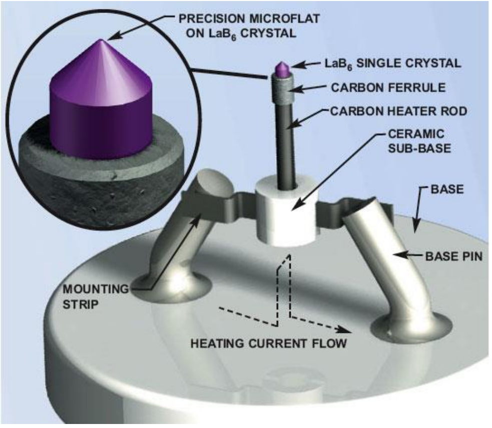

Figure 39: Figure representing LaB_6 electron emitters used in some SEM systems [87]

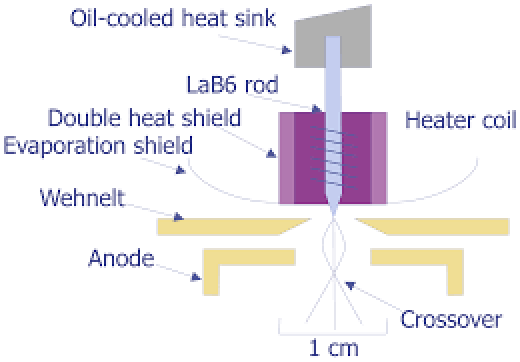

Figure 40: schematic representation of LaB_6 electron gun [87]

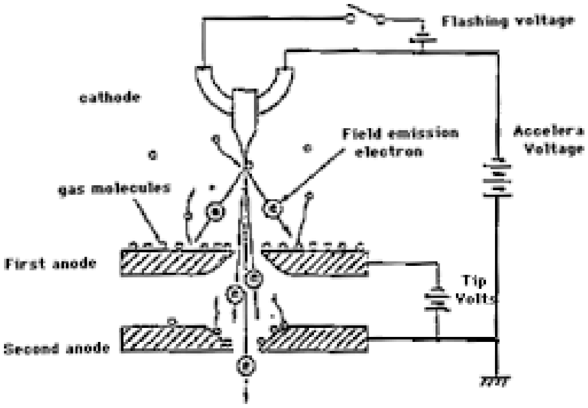

Figure 41: schematic representation of cold field emitters used in some SEM [104]

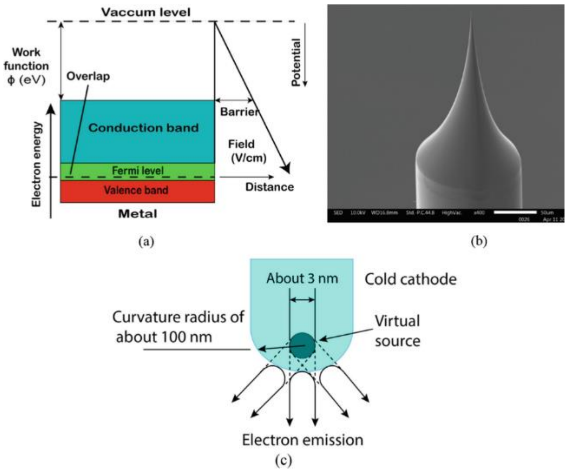

Figure 42: Schematic representation of (a) quantum-mechanical tunneling process, (b) the tungsten sharp tip used in cold field emitters, and (c) electron emission process with virtual source [87]

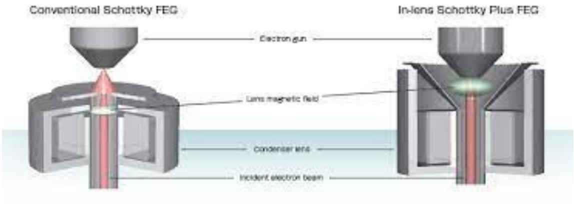

Figure 43: schematic representation of Schottky Field emitters used in some SEM [87]

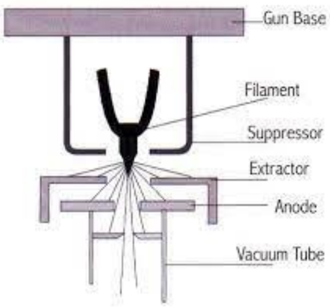

Figure 44: Schematic representation of Shottky field electron emitter set up [104].

3. Chambers: a chamber located at the base of an SEM in which samples can be stored and which contains many important types of equipment such as infrared cameras, sample stages and holders, and others required for microscopic analysis and imaging. During SEM operations, the chamber can be vacuumed to high pressures. [87, 88-99]
4. Vacuum Pump: attached to the SEM to keep the system under high vacuum while also keeping the chamber and samples clean of any impurities from the samples or the ambient environment. In addition, the electron beam's path must be cleared of any molecules or particles that may interact with it that can avoid or obstruct as it approaches the samples or the detectors. [87, 88-99]
5. Detectors: The detectors collect the signal that leaves the investigated samples and converts it into electrical pulses, which are processed and displayed as an image on SEM computers or EDX. SEM can use a variety of detectors, some of which are permanently attached to it while others can be dislocated or replaced. The primary function of all of these detectors is to collect incoming signals, process or analyze them,

and then display them to users. To that end, different detectors use different constituents of the incoming electron beams, such as secondary or backscattered beams, or x-rays, to analyze the desired different required features found on the surface of samples. Everhart-Thornley, Through the Lens, Backscattered electron, Scintillator Backscattered electron, and channel plate detectors are examples of these detectors [87]. We will concisely focus on Everhart-Thornley and Backscattered electron detectors, as they are widely used in most modern SEMs, the details of these and other detectors can be found elsewhere [87, 88-112].

5.1- Everhart-Thornley detectors: This type of detector can detect both secondary and backscattered electrons, but it is best known for detecting secondary electrons. These are scintillator photomultipliers named after their creators, Thomas E. Everhart and Richard F. M. Thornley. These detectors are popular among SEM users and installers due to their efficiency and benefits. The large solid angle of collection of secondary electrons, amplified signals, low noise, high signal efficiency collection even at low incident beam energies, low cost, and long working hours are some of the advantages of such a detector. [87, 88-112]

5.2- Backscattered Electron detector: These detectors, as the name implies, collect backscattered electrons, which have higher energies than secondary electrons. However, a large proportion of backscattered electrons are scattered, and only a small proportion of them reach the detector. As a result, it is recommended to have such detectors in addition to the Everhart-Thornley detector to increase its efficiency and improve the results obtained. These detectors have several advantages, including low cost, small and simple designs, low sensitivity to low energy backscattered electrons, which improves image resolution, and fast response. [87, 88-112]

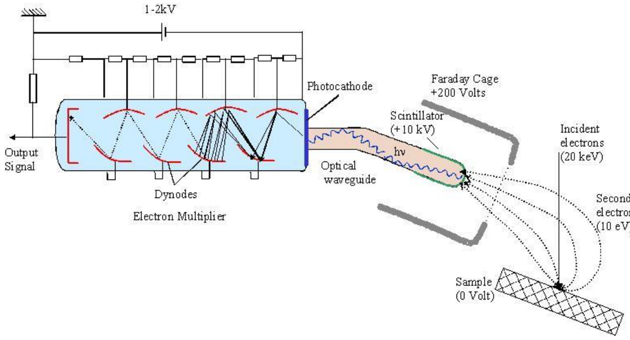

Figure 45: schematic representation of Everhart-Thornley detector collecting and processing secondary electrons leaving the sample surface [87].

Figure 46: Thomas Everhart one of the founding fathers of the E-T detector [201]

Figure 47: figure showing the Everhart-Thornley detector set up [87]

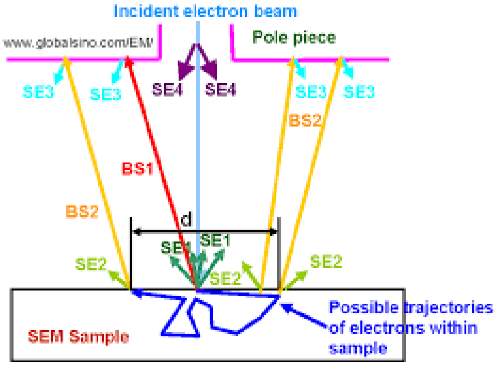

Figure 48: Sketch showing the different types of electron beams leaving the sample surface [87]

B. Energy Dispersive X-ray Spectroscopy (EDX):

The energy-dispersive x-ray spectroscopy (EDX) technique, which is attached to the SEM, is used to perform molecular analysis, or to identify the chemical components that make up or are present in the samples under examination. The electrons with specific energies that fall on the surface of the samples interact with the atoms present in the shells or energy levels of the compounds that make up the samples, causing energy to be transferred to the electrons present in these shells. When the electrons absorb this energy, they either jump into higher shells or escape from the atoms, leaving holes in their wake. After a while, these electrons return to lower levels or shells by emitting photons with specific energies, typically x-rays, which are accelerated and collected by the EDX detector for analysis. The detector counts or monitors the number and energies of incoming photons and provides a qualitative prescription to the atomic and molecular distribution on the samples' surface. It is worth noting that EDX fails or is inaccurate in determining hydrogen, helium, or lithium that may be present in the samples, as well as failing to provide quantitatively those compositions that have less than 0.2 wetting percent. As a result, the obtained results are quantitatively dependent on the initial energy of the electron, the electron composition and electronic bonding found on the surface of the samples, and their interaction with the incoming electrons. Thus, the results of the EDX analysis can only be trusted on a qualitative level. [16, 91, 93, 115, 116]

The INCA energy system, which is used by our computer software, is a module that controls and monitors the x-ray acquisition and an EDX detector aimed at detecting these x-rays, which then analyzes the data or spectrum obtained and provides the users with the necessary information or data, which included the elemental composition of the samples, as well as their atomic percentage presence. It is worth noting that the EDX system is sensitive to infrared light, and all infrared LEDs within the SEM chamber should be turned off at all times during EDX analysis, as mentioned above (infrared cameras bulletin). Furthermore, x-ray lights have short lifetimes and can interact with the environment present within the chamber; thus, the EDX detector should be placed at a certain distance from the sample to collect these x-rays before decaying; additionally, the detector should not be placed too close to the sample surfaces, where energetic photons and electrons may damage it. As a result, it is recommended that the working distance, or the distance between the EDX detector and the samples, be set to 15 mm to ensure the system's safety and the quality of the results obtained. [16, 115, 116]

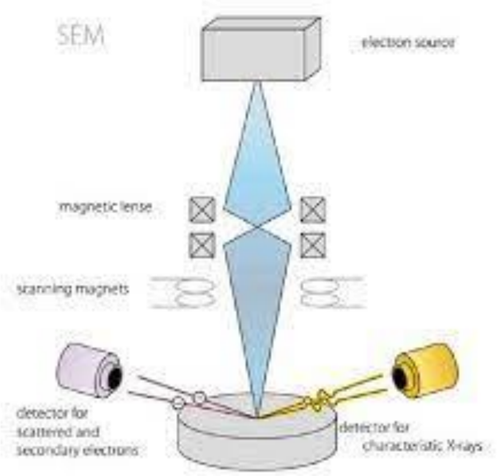

Figure 49: Sketch showing the principle of EDX analysis [113]

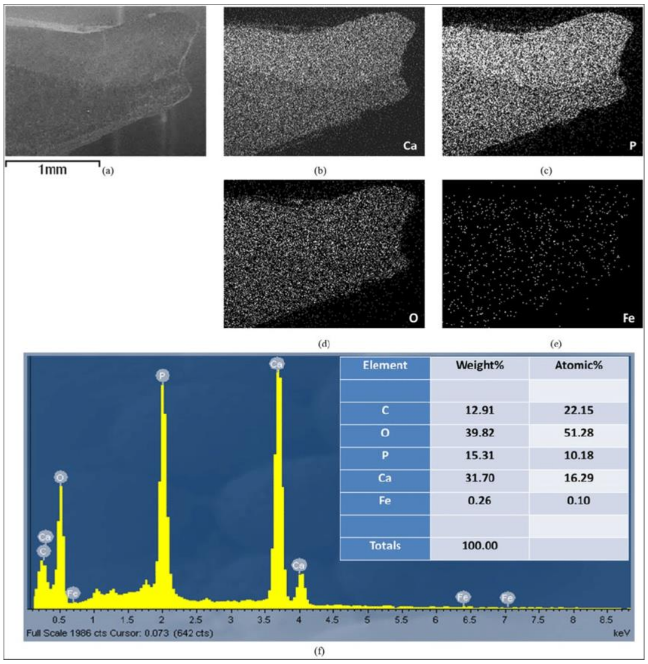

Element	Weight%	Atomic%
C	12.91	22.15
O	39.82	51.28
P	15.31	10.18
Ca	31.70	16.29
Fe	0.26	0.10
Totals	100.00	

Figure 50: An example of EDX result obtained by INCA software [116, 117]

C. Experimental Procedure:

The samples were placed in the chamber, which was then evacuated by pumping them up to $5*10^{-3}$ Pa pressures. The beam of electrons emitted by Schokty Electron guns is then accelerated and guided towards the samples by a high-accelerated voltage, assigned by the users and set at 5 KV. As a first step, the electron gun is automatically centered to improve the quality of the images obtained. The type electron beam was used to emit and generate an electron gun, which was alternated between Secondary Electron (SE) and In-beam Secondary Electrons, depending on which produced better images. After selecting the resolution mode, which is distinguished by high resolution and low depth focusing, the image is magnified by adjusting the magnification and working distance using the adjustable knobs found on the SEM's controlling box. By carefully adjusting the stigmators, brightness, and working distance, you can improve the working distance, magnifications, and image quality on the computer screen. Following that, the spot is localized and focused on the samples by correcting the wobbling of the image that was detected during the previously mentioned adjustments. Finally, the high-quality image obtained is ready for analysis, such as thickness measurement or EDX analysis to determine its constituents. It is worth noting that our samples were non-conductive, and we used a carbon tap to eliminate or reduce the charging issue. Another method involves coating the samples with conducting film of pre-registered thicknesses, such as gold or platinum, to be observed under the electron beam and reduce the charging effects. Furthermore, in addition to the previously mentioned steps, the image quality can be improved by tilting or rotating the samples or sample stage, allowing to visualize the different faces or surfaces of the samples from various angles. The SEM Mira 3 Computer software controls all of these operations and analysies. [16, 115, 116]

Figure 51: Figure showing controlling system via computer and our SEM [199]

Figure 52: figure showing sample holder and stabs on which the sample is attached used in SEMs [199]

Figure 53: figure showing an example of vertical sample holder (vertical stab) used in SEMs [199]

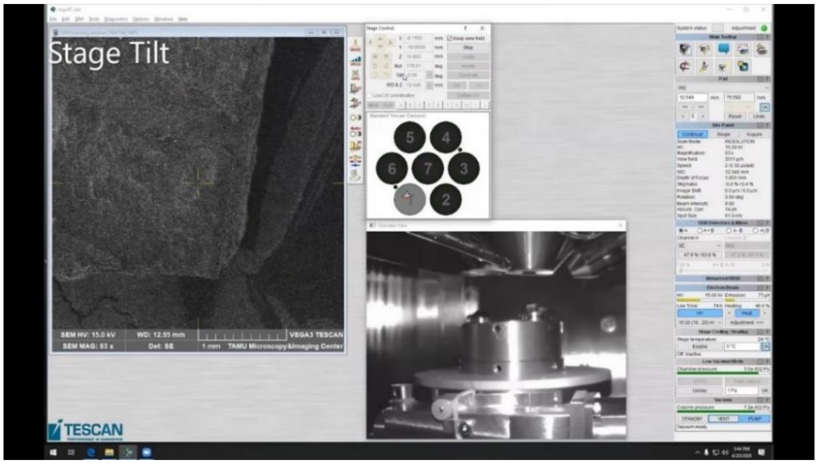

Figure 54: figure showing the Mira 3 software used in our SEM [186]

D. Summary and Application of SEM:

This text has introduced the reader to scanning electron microscopy, covering in detail its experimental setup and mentioning the advantages and disadvantages of some of the instruments or parts of it that have been used. It also highlighted and introduced the reader to the fathers of modern SEM, those who contributed to its development and advancement, and the phases of evolution that SEM went through from its conception to its commercialization. Finally, but importantly, it discussed the experimental procedures and steps we followed during our experiments. In addition to imaging and microanalysis of physical properties, for semiconductors, superconductors or power devices [107], SEM is now an essential part of almost every laboratory, contributing to and participating in a variety of experiments in different fields and disciplines, such as imaging and microanalysis of biological cells, tissues, or bacteria [95], identification of chemicals and liquids, determination of the composition of dental products [117], food products [108], and micropaleontological products [101], to name a few. Finally, SEM will continue to advance and develop and, as previously stated, may contribute to new projects or ideas, leading to new experimental devices, such as the point-projection microscope [113], proposed for future generations.

CHAPTER VIII

UV-VIS-NIR SPECTROSCPY

UV-VIS spectroscopy is a technique for studying and examining the optical properties of a wide range of materials in the ultraviolet, visible and sometimes near-infrared regions of the electromagnetic spectrum. These optical properties are derived from the analysis and study of the transition of electrons between the energy levels of the molecules, ions and atoms that make up the sample being studied. The technique has been improved to more efficiently estimate the band gap of the samples and to derive other optical properties such as the dielectric function, refractive index, and dispersion relation [16, 134, 144-146]. To this end, after introducing UV-VIS spectroscopy, this text will briefly focus on the theoretical phenomenon behind these techniques. It will then expand on the experimental procedures used in our measurements. Finally, the script will provide a summary of the descriptive analysis as well as a list of references used.

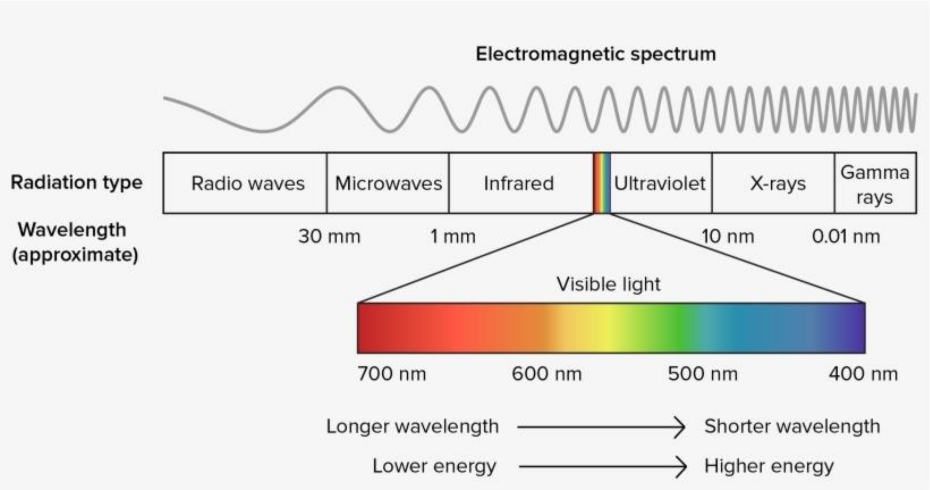

Figure 55: Figure introducing the electromagnetic Spectrum [202]

A. Theoretical Background and Principles:

When electromagnetic radiation, i.e. a photon, strikes a molecule or an atom, it either collides or interacts with them, elastically a process known as Rayleigh scattering, and where the conservation laws are maintained. Alternatively, when photons are collided inelastically, they exchange energy with the particles present in the samples. Inelastic collisions can cause Raman scattering, which is similar to vibrational spectroscopy and will be briefly discussed in the chapter on Fourier transform infrared spectroscopy. Finally, the incoming photon may be absorbed by the molecules or particles that comprise the sample in a process known as absorbance, which is characterized by total inelastic collision or scattering [131,132, 135-138].

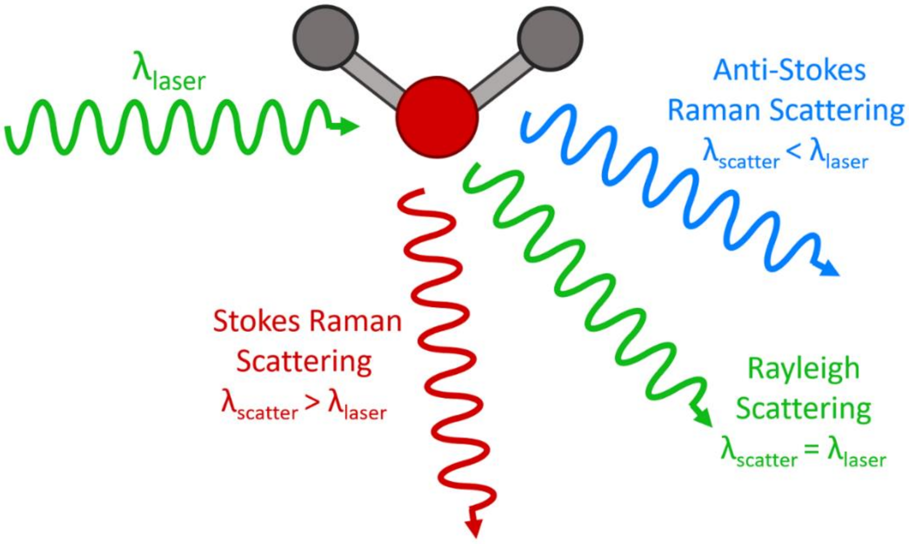

Figure 56: Sketch illustrating the different scattering processes described above [203]

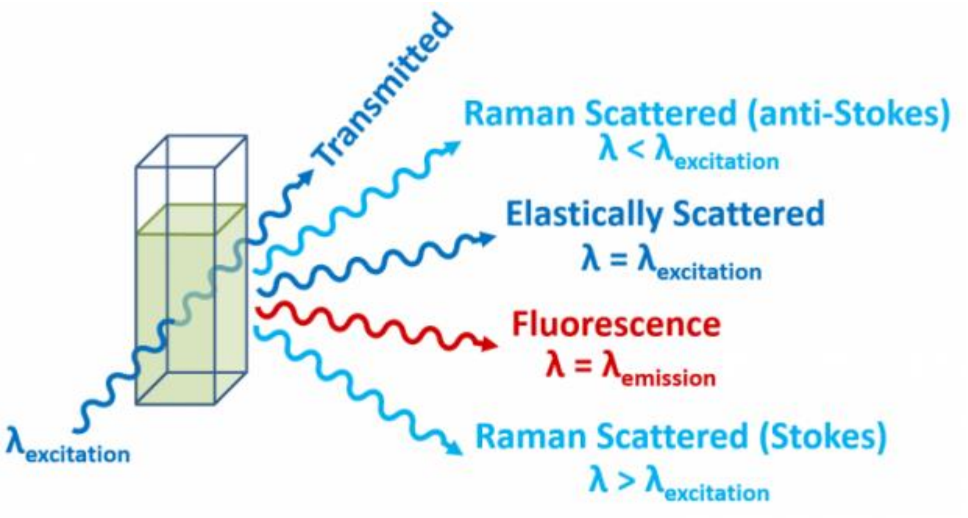

Figure 57: Sketch illustrating the various spectroscopic scattering processes [204]

The photon entering with an intensity Io interacts inelastically with the particles present in the samples, causing a variation in intensity that is related to the number of photons initially arriving, the number of different molecules, atoms or species present in the sample, and the thickness of the sample, as expressed Eq. (8.1) below: [131-133, 135-138]

$$dI = -\varepsilon c I dl \quad [131, 132] \qquad \text{Eq. (8.1)}$$

where I is the intensity of the incoming photons, dI is the change in intensity after the scattering process, c is the sample concentration; comprising the number of different species found in the sample, and dl is the infinitesimal part of sample thickness, or the thin slab containing the sample (for liquids or gases) [131-133]. The symbol ε denotes the amount of radiation absorbed by a sample at a specific wavelength or the probability of photon-matter undergoing total inelastic collision [132], which is commonly referred to as absorptivity. The minus sign in front of the above equation depicts the decrease in the light or photon intensity as it passes or interacts with the matter present [132].

Integrating the above equation leads to the following solution:

$$\log\left(\frac{I}{I_o}\right) = -\varepsilon c l \quad [131, 132] \qquad \text{Eq. (8.2)}$$

The absorbance is defined as the logarithm of the ratio of the initial intensity to the scattered intensity and is a measure of the amount of radiation or light a sample absorbs within a wavelength range of the electromagnetic spectrum as described by the famous Bouguer-Lambert-Beer law, which is givenin Eq. (8.3) below:

$$A = \log\left(\frac{I_O}{I}\right) = \varepsilon c l \quad [131, 132] \qquad \text{Eq. (8.3)}$$

Similarly, the Lambert-Beer equation can be used to estimate the transmission of the sample, typically measured in percentage, which is defined as the amount of light that passes through the sample and is the ratio of the scattered or transmitted intensity to the initial intensity of the incident beam, as expressed below:

$$\%T = \frac{I}{I_O} * 100 \qquad [131\text{-}133] \qquad \text{Eq. (8.4)}$$

$$A = \log\left(\frac{1}{T}\right) = \varepsilon c l \qquad [131\text{-}133] \qquad \text{Eq. (8.5)}$$

Most UV-VIS spectrometers used for quantitative analysis are theoretically based on this. Typically, such experiments focus on estimating the physical or optical properties of unknown samples by estimating their transmission or absorption. As a result, care should be taken to properly calibrate the parameters such as temperature, standard samples chosen, reduction of Stray light, and many others that, if not handled properly, can lead to incorrect conclusions and analysis. [132, 133]

The Kubelka-Munk equations are used for reflectance measurement because the Lambert-Beer equation assumes that the samples do not scatter or reflect light and that the intensity of the light is not lost during scattering or reflection processes. The Kubelka-Munk function, which is shown in the equations below, correlates between the diffuse reflecting power, absorption coefficient, and scattering coefficients of the samples under investigation.[133]

$$F(R_\infty) = \frac{(1-R_\infty)^2}{2R_\infty} = \frac{K}{S} \text{ [133]} \qquad \text{Eq. (8.6)}$$

where R_∞ implies for a sample of infinite thickness and zero background reflectance, and the factor 2 in the denominator is attributed to the absorption in the scattering expression of K and S for a finite path length d as depicted in Eqs. 8.7 and 8.8 below:

$$S = \frac{2.303}{d} * \frac{R_\infty}{2-R_\infty^2} * \log(\frac{R_\infty(1-R_0R_\infty)}{R_\infty - R_0}) \qquad \text{[133]} \qquad \text{Eq. (8.7)}$$

$$K = \frac{2.303}{2d} * \frac{1-R_\infty}{1+R_\infty} * \log(\frac{R_\infty(1-R_0R_\infty)}{R_\infty - R_0}) \qquad \text{[133]} \qquad \text{Eq. (8.8)}$$

where R_0 is the diffuse reflecting power of the sample for an ideal black non-reflecting background; however, there is no such thing as an ideal white background, and the R_∞

measured differs from that deduced from the above equation. As a result, R_∞ is always measured with standard samples, which serve as a white reflecting background:[133]

$$R_\infty = \frac{R_{sample}}{R_{standard}} \quad [133] \qquad \text{Eq. (8.9)}$$

The Kubelka-Munk function is also affected by the absorption coefficient, molar extinction coefficient, and concentration of the samples under investigation. Finally, this function is influenced by the wavelength and angle of the incidence, which can be changed with different experimental setups and tools to investigate their effects on the reflectance.

$$F(R_\infty) \cong \frac{\varepsilon c}{S} \quad [133] \qquad \text{Eq. (8.10)}$$

where ε is the molar extinction coefficient or the absorption coefficient, c denotes the concentration and S is the Kubelka-Munk scattering function as defined in Eq. (8.7) and $F(R_\infty)$ is the Kubelka-Munk function. [133]

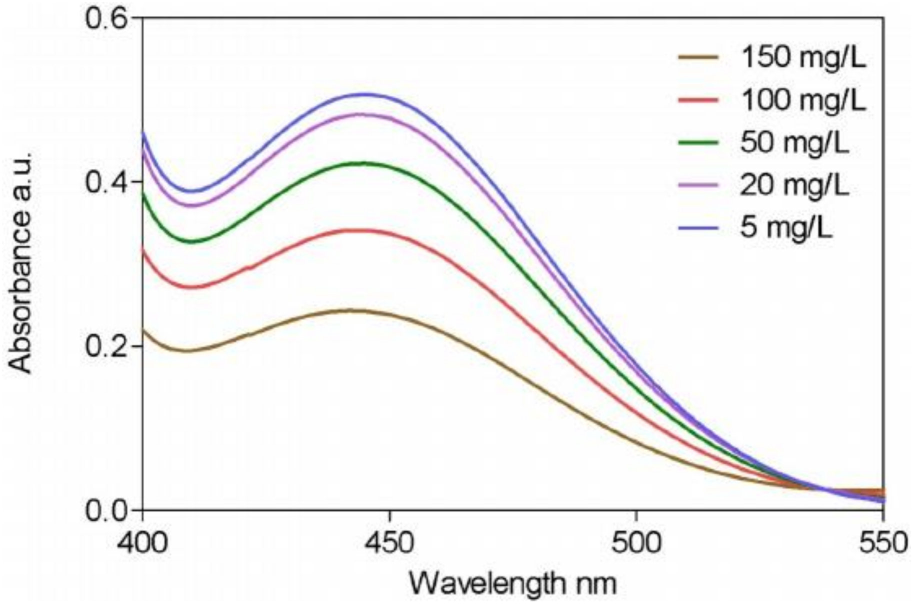

Figure 58: Figure showing an example of absorption spectrum measured by UV-VIS spectrometer [141]

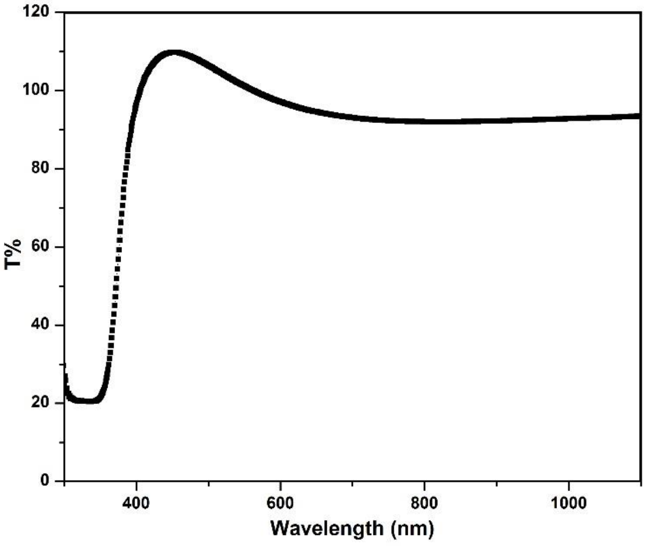

Figure 59: Figure showing an example of ZnO UV-VIS transmission spectrum

B. Our Experimental apparatus and Procedures:

Figure 60: figure showing our UV-VIS-NIR spectrophotometer [185]

Figure 61: Figure showing our Reflection measurement apparatus that attaches to our UV-VIS-NIR spectrometer [185]

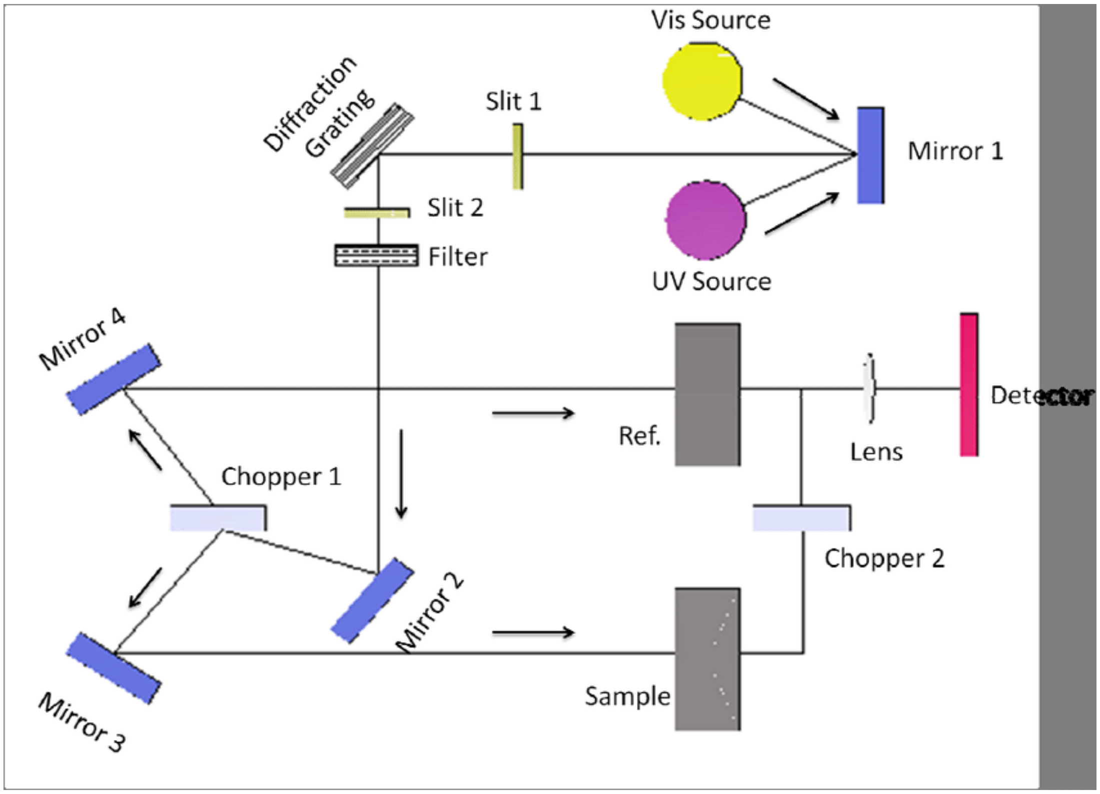

Figure 62: Sketch illustrating Double Beam UV-VIS detection system [142]

All of our measurements are carried out with the ARN-475 model Jasco UV-VIS-NIR spectrometer, which is available at CRSL labs and measures in the range of 200nm to 2000nm of the electromagnetic spectrum. As previously stated, the light emitted by the tungsten-deuterium lamps is polarized by monochromators and grating, and then split into two parts, one of which passes through the sample under investigation and the other through the reference used. Finally, the lights are measured by PMT detectors one after the other, like the procedure of the Double beam detector as depicted in Figs 60 to 62. As the acronym UV-VIS-NIR spectrometer suggests, this spectrometer measures absorbance, transmittance, absolute and relative reflectance in the ultraviolet, visible, and near-infrared regions. [16, 147]

In our case, we measured the transmittance and relative reflectance. During the transmittance measurement phase, the following procedure was followed. To begin, the transmittance of the empty container, where the target and reference samples are placed, is measured using baseline correction to account for all environmental fluctuations that affect the rays and thus influence the experimental results. The percent transmittance of the bare substrate, in this case, glass, is then measured using the ambient environment within the container as a reference sample. Finally, the transmittance of ZnO deposited on glass samples is measured one after the other, with the ambient environment serving as a reference. [16]

Figure 63: figure showing sample holder for solids used in our UV-VIS transmittance measurements [185]

The apparatus for measuring reflectance consists of integrating spheres, sample holders, and detectors. Depending on the investigated samples and goals, absolute and relative reflectance can be measured. In the former, the angle of incidence is usually varied manually between 5 and 90 degrees, whereas in the latter, the angle is usually fixed at 90 degrees, to which the sample and detectors are attached. [16, 133, 147]

Figure 64: figure showing the adjustment of the container ARN 915 Mode used for reflectance measurements [185]

Figure 65: ARN 915 modeled container used for reflectance measurements [185]

Figure 66: figure depicting the mode of attachment of the ARN 915 container to the spectrometer and the software used for reflectance measurements [185]

The following procedure was followed during the reflectance measurement phase. First, the ARN 915 modeled container is properly attached to the UV-VIS spectrometer, and the angle of incidence is kept constant at 90 degrees throughout the measurements. On a white mirror-like sample with 100 percent reflectance in the UV-VIS-NIR spectrum, the baseline correction was performed. The reflectance of the substrates and that of the deposited samples are then measured one after the other using the white mirror as a reference; all of our samples were measured in the range of 200 to 2500 nm. [16, 147]

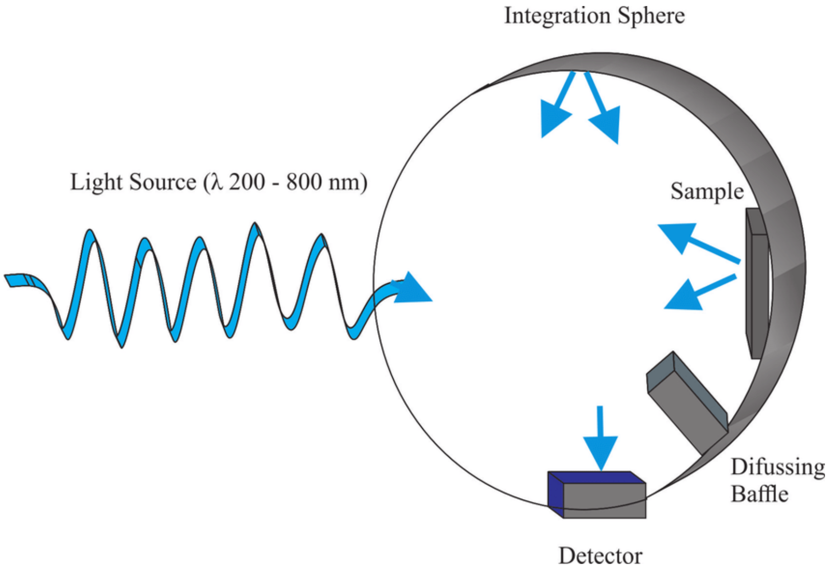

Figure 67: Sketch illustrating the relative reflectance measurement process [145]

C. Summary

The Lambert-Beer equation, scattering types, absorbance, transmittance, and reflectance were all covered in this script, which introduced the reader to the UV-VIS-NIR Spectroscopic technique. It also emphasized and introduced the reader to the spectrometer's various experimental components graphically. Finally, and perhaps most importantly, it discribed our experimental procedures and steps, as well as our Jasco UV-VIS-NIR spectrometer.

CHAPTER IX

FOURIER TRANSFORM INFRARED SPECTROSCOPY THEORY & EXPERIMENTAL PROCEDURES

A. Introduction

The introduction of interferometers into the scientific communities, initially as a means of studying light and investigating its properties [148], has been one of the greatest experimental achievements of recent decades. Michaelson's experiment estimated the speed of light in a vacuum and demonstrated the absence of the aether. The Michelson interferometer was used to study the wave aspect of light particles, opening the way to new research in the world of optics. Spectrometry is a recently established experimental field in which the Michelson interferometer has seen rapid application. Infrared spectrometry, in particular, has spread to other fields such as organic chemistry, biology and medicine, to name a few. Primary infrared spectrometry has been used to study and examine bonding within organic or complex compounds and molecules; it has also been used by pharmacists and veterinarians to identify specific types of drugs or components of certain drugs [149]. Finally, spectroscopy has paved the way for new experimental techniques such as X-ray diffraction, magnetron resonance, and ellipsometry, to name a few, that have paved the way for the world of nanoscale. After establishing the use of infrared spectroscopy, this chapter focuses on Fourier transform interferometry, its advantages and disadvantages, as well as the mathematical background of this technique, while also reflecting some experimental procedures or processes that can validate the experimental measurements.

Infrared spectroscopy is based on sendings electromagnetic energy with sufficient energy to excite the atoms, causing them to vibrate. This vibration generates a wave that propagates throughout the system and contains information that is specific to the system from which it originated. As a result, infrared spectroscopy ties to decipher these waves, providing us with the properties of the molecules, which can later be used in device application and technology.

B. Fundamentals of Vibrational Spectroscopy:

1. Simple Harmonic approximation and phonon modes

a. Classical picture :

To start with a traditional classical image, let's consider a one-dimensional image of molecules, just to simplify the mathematics but this can be generalized to any dimension. The harmonic approximation assumes that these molecules are placed on points connected by oscillators capable of vibrating at specific frequencies, as shown in the fig (68) below.

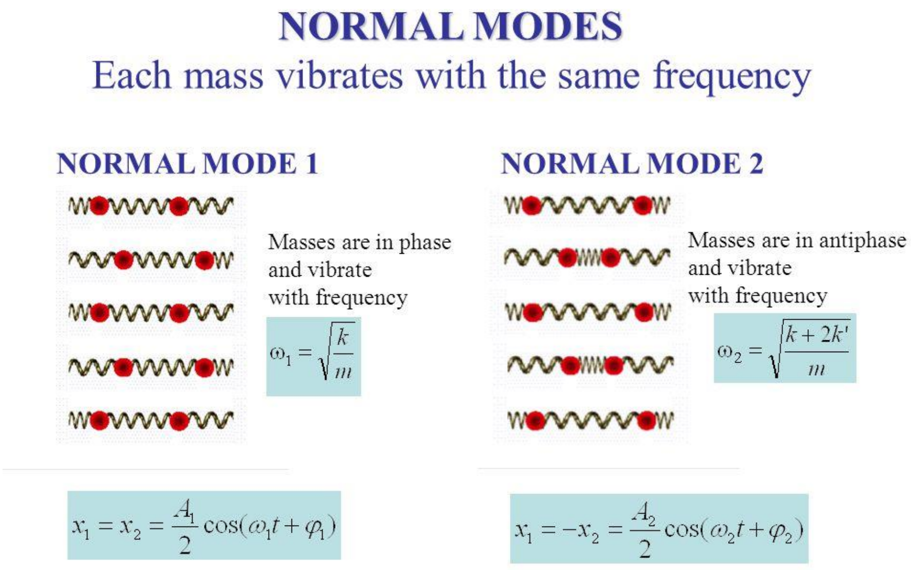

NORMAL MODES

Each mass vibrates with the same frequency

NORMAL MODE 1

Masses are in phase
and vibrate
with frequency

$$\omega_1 = \sqrt{\frac{k}{m}}$$

$$x_1 = x_2 = \frac{A_1}{2}\cos(\omega_1 t + \varphi_1)$$

NORMAL MODE 2

Masses are in antiphase
and vibrate
with frequency

$$\omega_2 = \sqrt{\frac{k+2k'}{m}}$$

$$x_1 = -x_2 = \frac{A_2}{2}\cos(\omega_2 t + \varphi_2)$$

Figure 68: harmonic representation of atom within diatomic molecules.

The masses classically are attached by a spring having spring constant K with the following potential:

$$V(x) = \frac{1}{2}Kx^2 \qquad \text{Eq. (9.1)}$$

Where x represents the position of the moving particle, in the same fashion the kinetic energy can be defined by:

$$KE = \frac{1}{2}\mu\dot{x}^2 \qquad \text{Eq. (9.2)}$$

Where m is represented by μ defined as the reduced mass of the particles expressed as:

$$\mu = \frac{m_1 m_2}{m_1 + m_2}$$ Eq. (9.3)

The center of mass's position is given by: [149, 150]

$$x = \frac{m_1 x_1 + m_2 x_2}{m_1 + m_2}$$ Eq. (9.4)

The equation of motion of the particle attached to a spring follows the differential equation Eq. 9.5: [149, 150]

$$\mu \frac{d}{dt}\left(\frac{dx}{dt}\right) = Kx$$ Eq. (9.5)

The solution to the above differential equation is in the form:

$$x = Acos\,(\omega t + \varphi)$$ Eq. (9.6)

where A is the Amplitude, ω = 2πf is the angular frequency and φ is the phase shift determined from initial conditions. Let us now return to our system of diatomic molecules attached by a spring, the energy of such a system can be represented by:

$$E = \frac{\mu}{2}\dot{Q}^2 + \frac{K}{2}Q^2 + \frac{M}{2}\dot{x}^2$$ [150] Eq.(9.7)

Here Q represents the position of the particle and x is the position of the center of mass, and $M=m_1 + m_2$, here the speed of the center of mass is in inertial reference meaning $\ddot{x} = 0$, the motion of the particle can be described by Eq. (9.6), differentiating Eq. (9.6), and replacing it in Eq. (9.5) gives us: [149, 150]

$$[\omega^2 - \frac{K}{\mu}]Q(t) = 0$$ Eq. (9.8)

Eq. (9.8) gives us:

$$4\pi^2 f^2 = \frac{K}{\mu} \quad leading\ to\ f = \frac{1}{2\pi}\sqrt{\frac{K}{\mu}} \qquad \text{Eq. (9.9)}$$

“Since the frequency of the spring corresponds to the frequency of the molecular vibrations and the spring constant corresponds to the force constant of the chemical bond one can get from Eq. 9.8 that the frequency of the molecular vibration is proportional to the ratio of spring constant to the reduced mass of the atoms raised to the power half. [150].

The energy of the atoms can be reduced to:

$$E = \frac{\mu}{2}\dot{Q}^2 + \frac{K}{2}Q^2 = \frac{1}{2}A^2\mu\omega^2 \qquad \text{Eq. (9.10)}$$

The kinetic, potential, and total energy in this classical simple model are shown in the fig. 69 below, however, this model does not show the vibrational states shown by experiments, therefore the need for quantum mechanics.

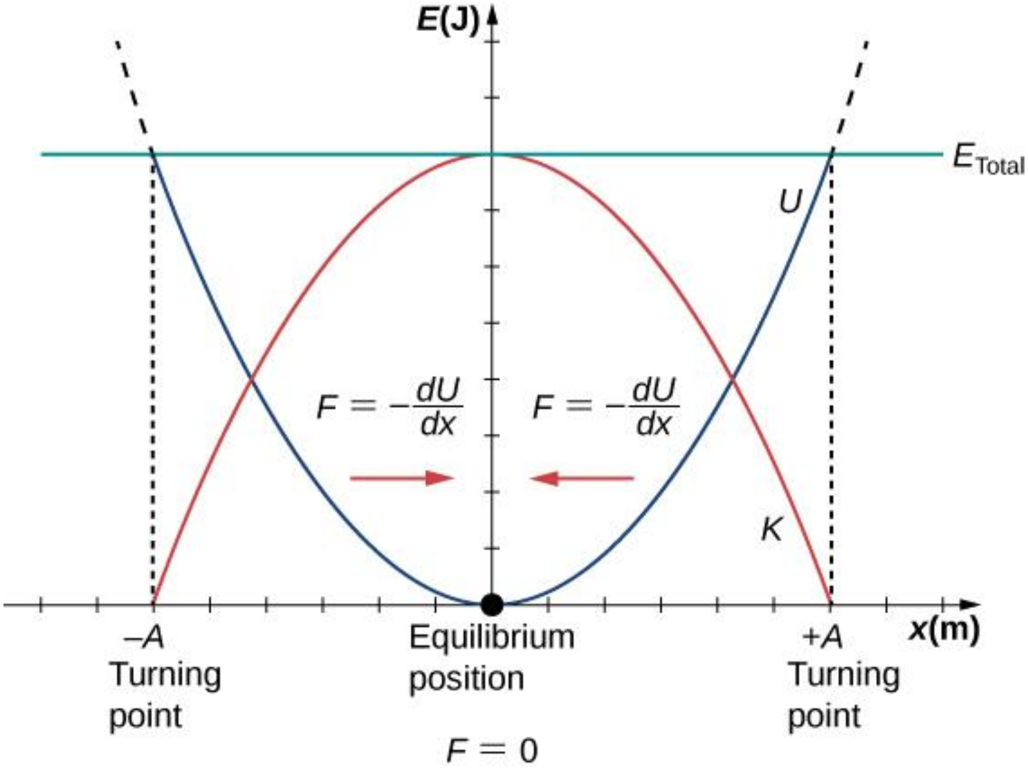

Figure 69: graph showing the kinetic, potential, and total energies of simple harmonic spring. [149,150]

Quantum mechanical treatment:

The hamiltonian of the system can be written as: [149,150,151-155]

$$H = T + V = \frac{\mu}{2}\dot{Q}^2 + \frac{K}{2}Q^2 \qquad \text{Eq. (9.11)}$$

where the quantities in the above equation hold the same meanings as in the classical picture.

Applying the Schrodinger equation to find eigenvalues and eigenvectors which represent the energies and wave function of the system respectively. [149,150 -155]

$$H\Psi = E\Psi = \left(\frac{p}{2} + \frac{K}{2}Q^2\right)\Psi \qquad \text{Eq. (9.12)}$$

where E is the energy operator, p is the momentum operator $p = -i\hbar\frac{\partial}{\partial x}$, ψ are the eigenfunctions or the wavefunctions. [149,150 -155]

Solving the Schrodinger equation, Eq. 9.12, gives the energy and eigenfunctions:[149,150 -155]

$$E = \left(n + \frac{1}{2}\right)h\upsilon \qquad \text{Eq. (9.13)}$$

where n is the principal quantum number (integer), υ is the frequency where ω=2πυ,

The eigenfunctions are: [149,150,151-155]

$$\Psi = A\, H\left(\sqrt{\alpha}Q\right)e^{-\frac{\alpha}{2}Q^2} \qquad \text{Eq. (9.14)}$$

where $\alpha = \frac{4\pi^2\mu\upsilon}{h},\ the\ constant$ H is the Hermite polynomials and A is the normalization factor [150].

The plot of the potential and eigenfunctions of this system is shown in the figure 70 below. The quantum mechanical picture has resolved all the issues raised by the classical picture. It also describes the discrete and allowed energy states of the vibrating diatomic or polyatomic systems.

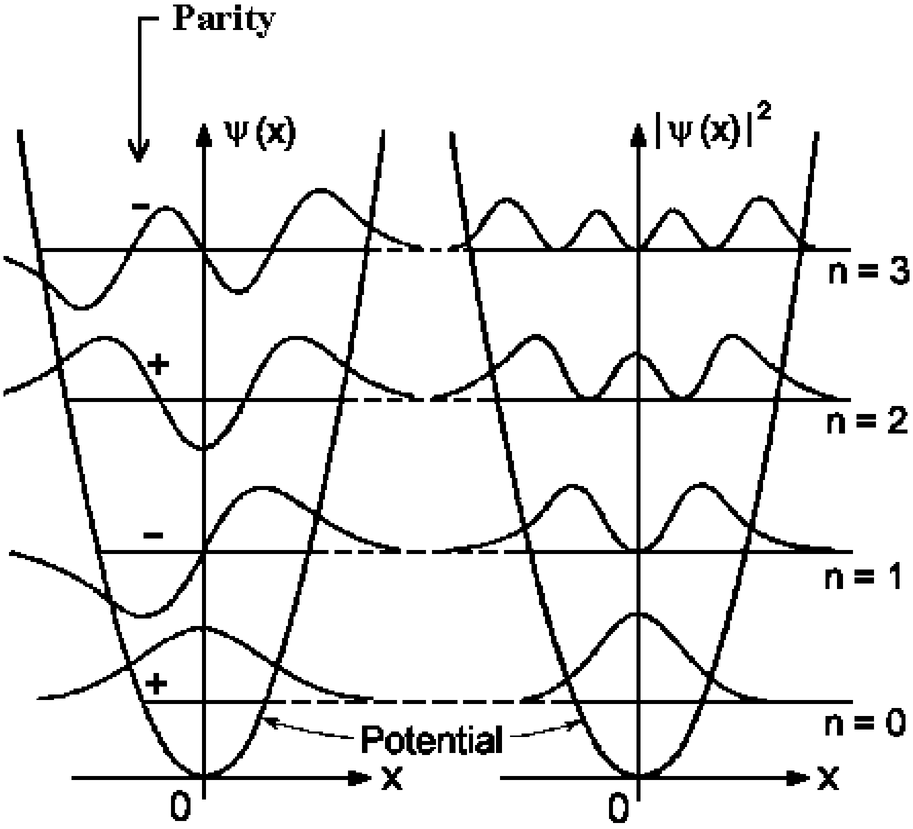

Figure 70: figure showing the potential, eigenvector, and probabilities of the eigenstates (square of wavefunctions) for the simple harmonic approximation to diatomic molecules. [149, 150, 193]

b. Anharmonic terms in the potential and their effects:

In the previous section, the potential energy was considered parabolic, however, Taylor expanding around the minimum x=0 results in higher terms that may contribute to the analysis: [149,150 -155]

$$V(x) = V(0) + x\frac{\partial V}{\partial x}(x=0) + \frac{1}{2}x^2\frac{\partial}{\partial x}\left(\frac{\partial V}{\partial x}\right)(x=0) + \frac{1}{6}x^3\frac{\partial}{\partial x}\frac{\partial}{\partial x}\left(\frac{\partial V}{\partial x}\right)(x=0) + ..$$

In the above Eq., V(0) is constant and can be absorbed into V(x). Since the expansion is at the minimum point, the first derivative is zero and; the second derivative is equal to a constant, which compared to the previous section is the spring constant or strength. These notions reduces this last equation to [149,150 -155]

$$V(x) - V(0) = \frac{1}{2}x^2 \frac{\partial}{\partial x}\left(\frac{\partial V}{\partial x}\right)(x=0) + \frac{1}{6}x^3 \frac{\partial}{\partial x}\frac{\partial}{\partial x}\left(\frac{\partial V}{\partial x}\right)(x=0) + \cdots \qquad \text{Eq. (9.15)}$$

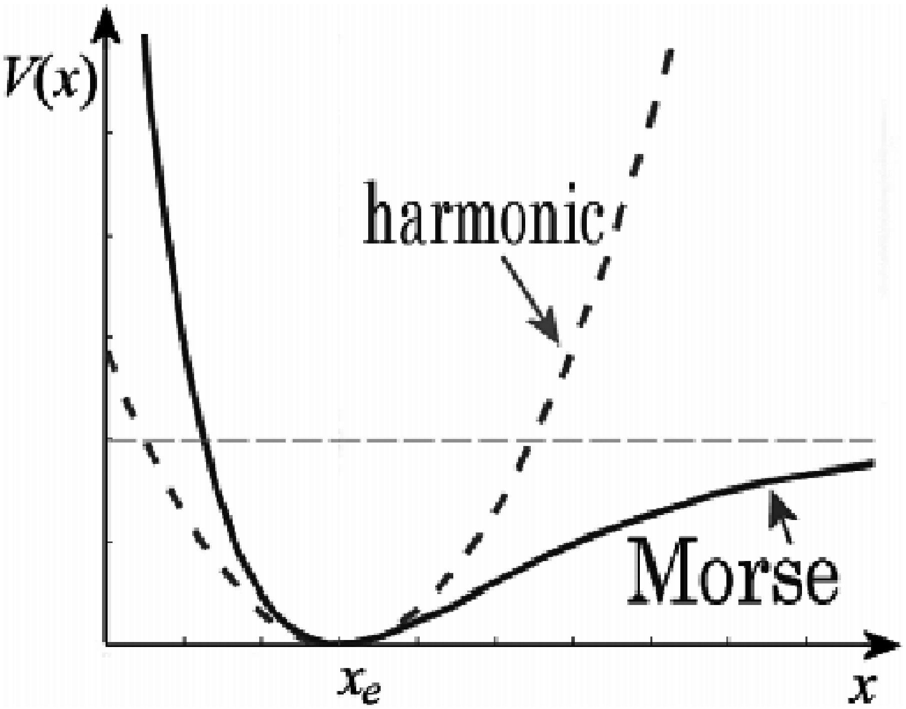

Figure 71: schematic comparing the harmonic and Morse's potential energies [149, 151]

The Morse's function $V(r) = D_e[1 - e^{-a(r-r_e)}]^2$, $where\ r_e$ is the equilibrium position, and D_e is the Dissociation energy, as depicted in Figures 9.5, 9.6, and 9.8, expressed the harmonic potential at regions closer to the equilibrium, denoted by $r=x_e$ in the above graph namely fig. 71. However, it deviates as one gets away from the equilibrium point. Usually, the potential is reduced to [149,150-155]

$$V = K_2 x^2 + K_3 x^3 + \cdots \qquad \text{Eq.(9.16)}$$

Using Time-independent perturbation theory, and solving the Schrodinger equation one obtains the energy in the form:

$$E' = \left(V + \frac{1}{2}\right) h r_e - \left(V + \frac{1}{2}\right)^2 h \nu_e x_e \; [150] \qquad \text{Eq.(9.17)}$$

where the potential is considered up to the third term, and where $\nu_e = \frac{a}{\pi}\sqrt{\frac{D_e}{2\pi}}$ and x_e is a constant known as the anharmonic constant given by $x_e = \frac{h\nu_e}{4D_e} = \frac{ha}{4\pi\sqrt{2\mu D_e}}$. Finally, V and V+1 are the vibrational quantum numbers [150]:

$$\Delta E = h\nu_e - 2h\nu_e x_e (V + 1) \;\; [150] \qquad \text{Eq.(9.18)}$$

Overtones and combination modes are produced as a result of the anharmonic terms. Overtone levels are levels where two or more normal vibrations are excited, and combination modes are modes resulting from the excitation of two or more normal vibrations modes. Even though anharmonicity prohibits combinational modes and forbidden transitions, figs (72) and (77) show that weak combinational modes can result in spectroscopic data. Overtones and combinational modes are typically weak; however, when Fermi resonance occurs, they become equally strong and visible in comparison to the fundamentals (fig (77)). This last case demanded that the frequencies of overtones and combinations be equal to the frequencies of the fundamentals (fig (77)); the theoretical background of Fermi Resonance is beyond the scope of this script and can be found elsewhere [150].

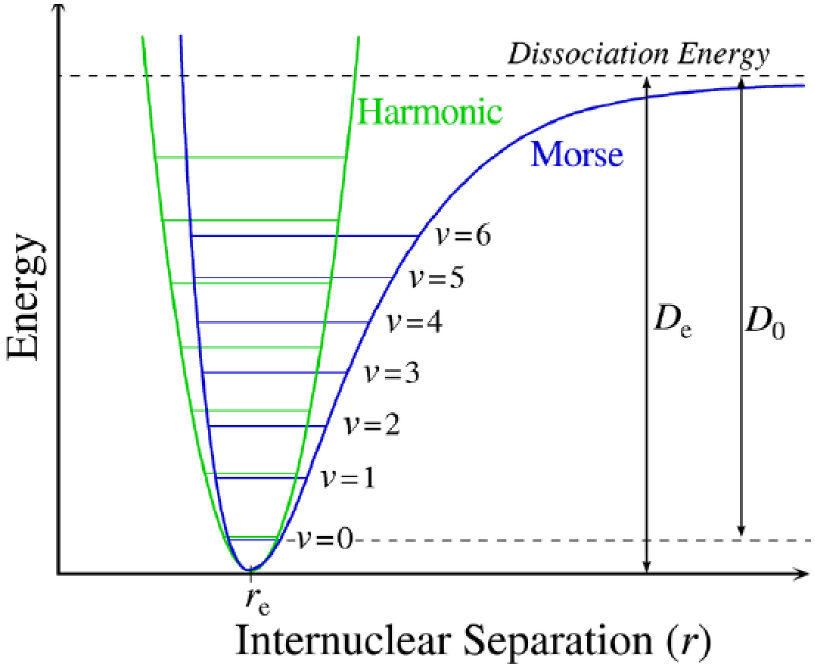

Figure 72: figure showing the harmonic and anharmonic potential energies.[150]

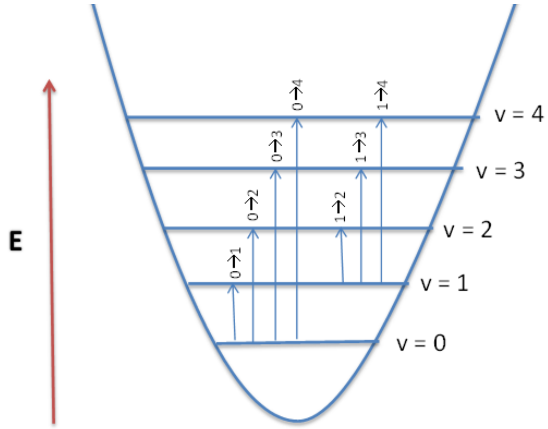

Figure 73: figure showing potential energy along with fundamental transitions [193]

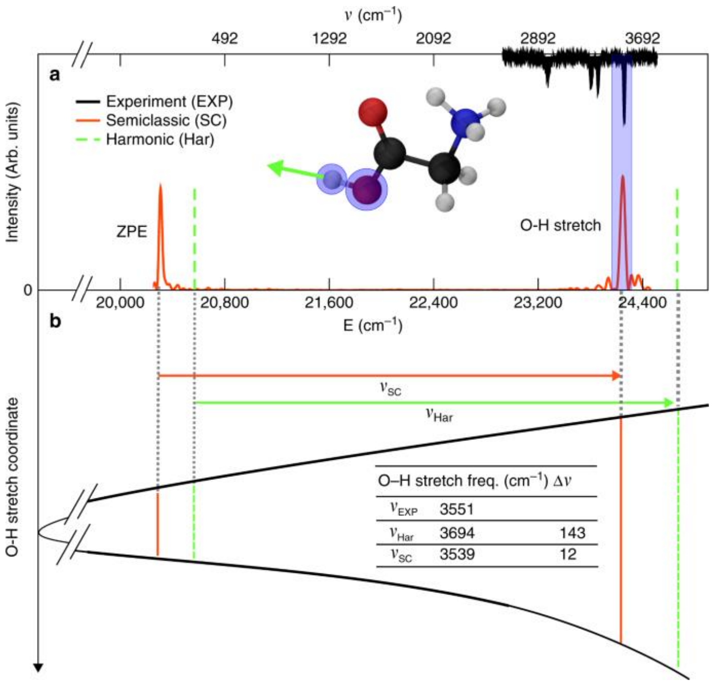

O–H stretch freq. (cm−1)		Δν
ν_{EXP}	3551	
ν_{Har}	3694	143
ν_{SC}	3539	12

Figure 74: Anharmonic potential along with the spectroscopic spectrum of O-H stretched molecule [158].

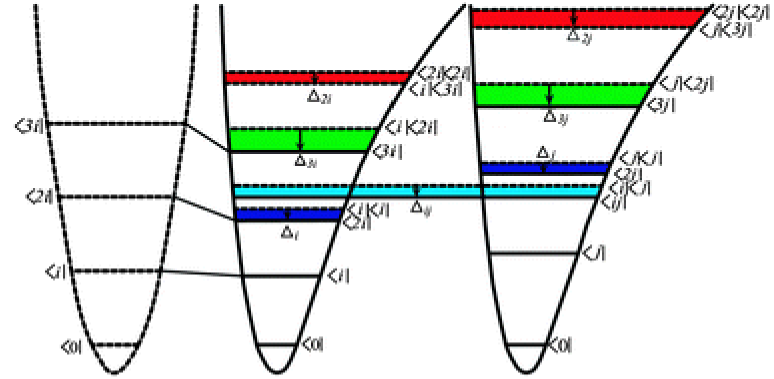

Figure 75: Figure depicting Anharmonic, overtone, and combinations level along with allowed transitions [168].

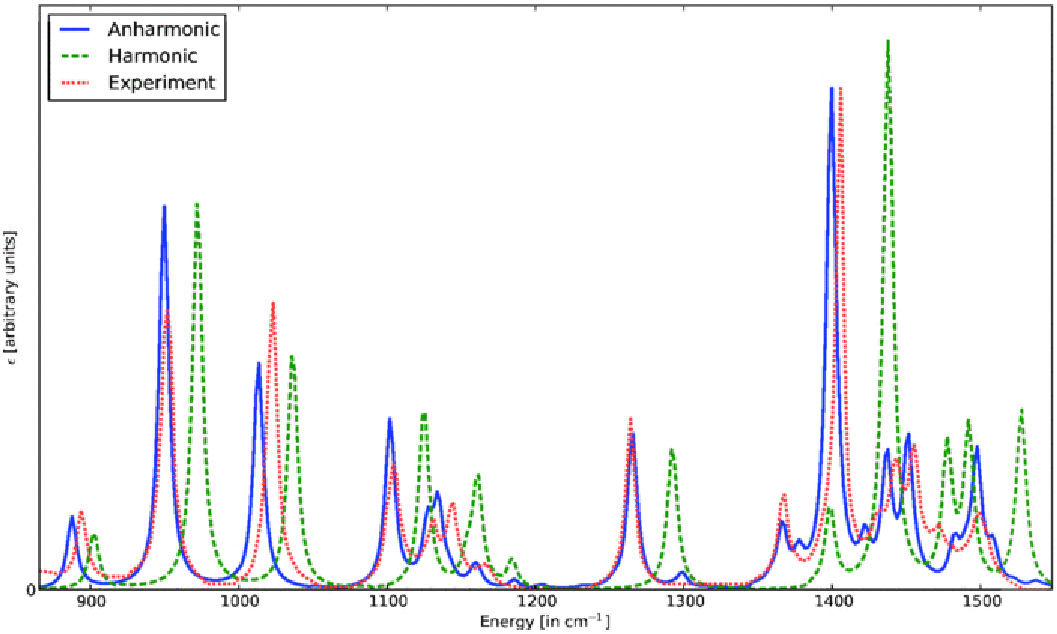

Figure 76: figure comparing the spectroscopic spectrum of harmonic, anharmonic deciphered by second perturbation and that of experimentally realized [156,158,159,169].

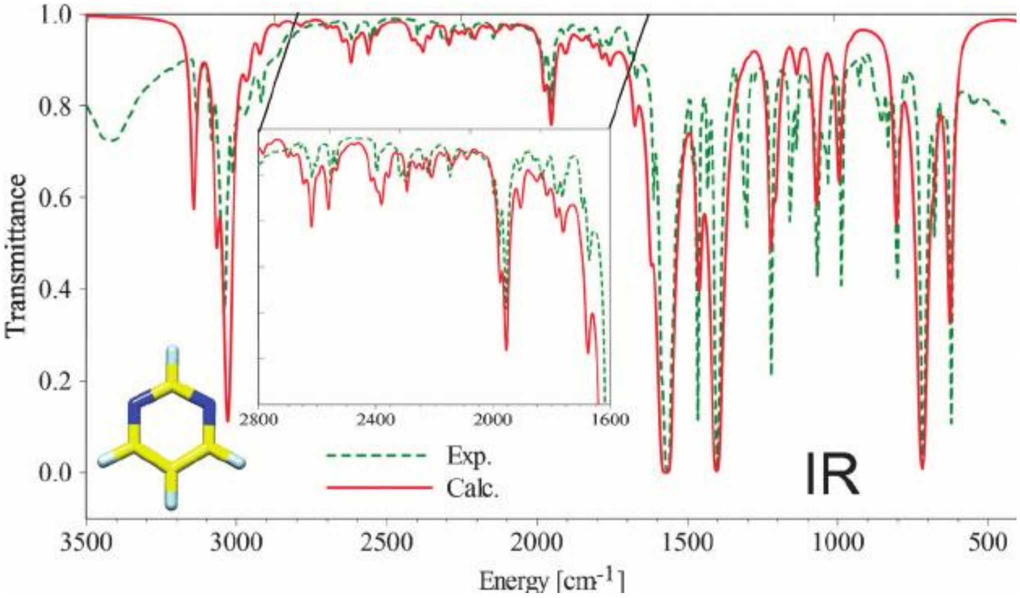

Figure 77: estimated and experimental infrared spectrum of a molecule [160].

C. Infrared Spectroscopy and instruments:

1. Infrared Spectroscopy

Sir William Herschel's discovery of infrared radiation in the early 1800s [150] paved the way for the development of theoretical and experimental techniques to better understand the properties of this radiation [150]. Lambert-Beer established the fundamental law for spectroscopic analysis. The Lambert-Beer law, as it was later named, relates the sample's transmittance to the intensity of the radiation that interacts with the sample, as stated in Eq (9.19):

$$T\ (v) = \frac{I}{I_O} = \ e^{-\alpha(v)b} \qquad \text{Eq.(9.19)}$$

where T is the transmittance, with percentage transmittance given by $T = 100T\ (v) = 100\frac{I}{I_O}$, I is the intensity reflected from the surface of the sample, I_O is the intensity of the radiation before interacting with the samples or background spectrum’s intensity, b is the thickness of the sample and α is the absorption coefficient of the sample at a certain wavenumber. Note that other than the thickness, the quantities in equation (Eq. 9.19) depend on υ, which is the wavenumber expressed as $v = \frac{1}{\lambda}$, where λ is the wavelength of the radiation. Linearizing the above equation facilitates the investigation, and leads to the reduced equation:

$$A = \log\left(\frac{1}{T}\right) = \alpha(v)b = acb \qquad \text{Eq.(9.20)}$$

where a is the absorptivity, b is the thickness and c is the density of the sample or the component of interest. Moreover, the radiation showed two important parameters, which was established by electromagnetism, namely the complex index of refraction n’ of the sample and the penetration depth that is given by the Eqs. (9.21) and (9.22):

$$n'(v) = n(v) + ik(v) \qquad \text{Eq. (9.21)}$$

$$\delta = \frac{\alpha(v)}{4\pi v} \qquad \text{Eq. (9.22)}$$

where k is the decay coefficient in the above Eq. (9.21).

Scientists constructed experiments and devices aimed at studying the characteristics of infrared radiation and its effects when interacting with different samples. The first mid-infrared spectrometer was devised by Melloni in 1833 that led to the discovery of infrared transparency of NaCl [150]. The first interferometer was constructed by Michelson in the 1890s, which measured the speed of light and verified the non-existence of either or difference between lights traveling in different directions. With the integration of Fourier Transform into physics, Fourier transforms infrared spectrometers were established in the 1950s and 1960s. Beyond this point, scientists fabricated beamsplitters, mirrors, and many other elements that improved and commercialized interferometers. In the 1970s and 1980s, programs and softwares were devised to facilitate the measurement and analysis provided by interferometers and spectrometers.

Therefore infrared spectrometers focus on deciphering the infrared radiation, where the latter i.e. the radiation interacted with the samples. The characteristics and some properties of the samples are predicted throughout the transmittance, absorptance, or reflectivity measurements by infrared spectrometers [132, 157, 160]. Infrared spectroscopy can measure spectra of almost all molecules making it universally used. The obtained spectra contain a lot of information that is unique for each molecule or material, applying it to detect various properties and characteristics. Instruments, devices, and detectors used in any brand of infrared spectroscometers are easy to handle and operate with. Moreover, they are relatively fast, which can measure a spectrum of a high quality and accuracy within a few minutes depending on the complexity of the measured materials. Most of these instruments and devices are relatively cheap or inexpensive which facilitates maintenance and replacements. Finally, most infrared spectrometers are sensitive, meaning they can measure accurately and produce spectrum even with a minimum amount of a molecule or material. Despite all the mentioned advantages, infrared spectrometers sometimes fail to detect certain constituents or materials, especially those that do not vibrate or interact under infrared radiations. Moreover, it sometimes fails to distinguish between certain samples within a complex material or mixtures of materials. However, techniques have been established to overcome such types of obstacles and disadvantages. All the above-mentioned advantages and disadvantages are summarized in table 4 below. [131, 149, 150].

Advantages	Disadvantages
Universal	Fails to detect certain types of molecules and materials
Inexpensive	Fails to distinguish between components within complex mixtures
Relatively fast easy handling and measurements	Sensitive to water or liquids
Spectrum rich of sample properties	
sensitive to a minimum amount of samples	

Table 4**:** Table showing the advantages and disadvantages of infrared spectroscopy and spectrometers [131].

2. Michelson Interferometers and FTIR:

Most modern interferometers are reminiscent of Michelson interferometer named after Albert Michelson who first devised it in the 1880s [131, 149]. Michelson interferometer, as depicted in the fig. 78 below, consists of the laser source, collimating mirrors, beam splitters, two reflecting mirrors one fixed and the other moving, and finally detectors.

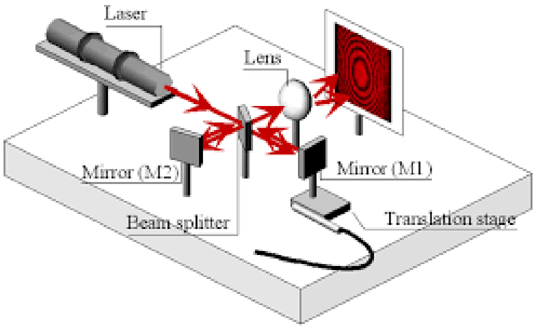

Figure 78: A 3D image of Michelson interferometer used in FTIR [184]

The laser light emitted from the infrared or laser sources after being collected by collimating mirrors is directed toward the beam splitter which is situated usually at 45 ° or bisecting angles with respect to the fixed and moving mirrors. The beamsplitter is an optical device designed to split the incident light into reflected and transmitted parts. The reflected beam is directed towards the fixed mirrors and the transmitted one towards the moving mirror. Both beams are then reflected and combined at the detector which transmits the data to a computer to be analyzed by the user. The transmitted and reflected beams interfere at the detecting point forming bright and black patterns as shown in fig (80), corresponding to constructive and destructive interferences. The constructive and destructive interferences depend on optical path difference expressed as [131, 149-155]

$$\delta = \begin{cases} m\lambda & for\ constructive \\ \left(m + \frac{1}{2}\right)\lambda & for\ destructive \end{cases} \qquad \text{Eq. (9.23)}$$

where m is an integer

If the optical path difference is an integer multiple of the wavelength, the two beams interfere constructively, on the other hand, if its an odd multiple of the wavelength they interfere destructively. [131, 149-155]

Fourier transform infrared interferometer is an infrared spectrometer based on Michelson interferometer. As its name suggests, the obtained data by the detector are Fourier Transformed usually by using appropriate computational software and programs, and then they are left to be analyzed and investigated. Moreover, the light sources used in this type of experimental apparatus are infrared radiation that interacts with the atoms at specific frequencies causing them to vibrate. The vibrated waves carry important information about the absorptivity or transmissivity of the samples which provides crucial information about the samples. Therefore the main objective of such a system is to facilitate the analysis of the detected signals or waves by the mathematical tools provided by Fourier Transform, to be introduced later, and then extract from it the properties of the sample required by the users, i.e. reflectivity, transmittance or absorbance. [131, 149-155]

FTIR advantage over infrared spectrometers is their high signal-to-noise ratio. The signal to noise ratio is given by: [131, 149-155]

$$SNR = \frac{Signal}{Noise} \qquad \text{Eq.(9.24)}$$

The signal-to-noise ratio gives the quality of the measurement performed. The higher the SNR or the lower the noise is the more the accuracy of the obtained results. The amount of signal to noise ratio depends on the amount of light hitting the detectors. In most infrared spectrometers light passes through mirrors, lenses, collimators, and other components that absorb or deflects the beam, decreasing its intensity. However this is not the case in FTIR. The high-intensity infrared beam hitting the detector gives high SNR values improving the quality of the measurements. [131, 149-155]

Another advantage of FTIR is its multiplex. Experiments have shown that SNR is directly proportional to the time required during scanning and also is proportional to the number of scans performed. These proportionalities are given by Eqs. (9.25) and (9.26): [131, 149-155]

$$SNR \approx t^{\frac{1}{2}} \qquad \text{Eq.(9.25)}$$

$$SNR \approx N^{\frac{1}{2}} \qquad \text{Eq.(9.26)}$$

where t is the time taken by each scan, and N is the number of scans added together to give the spectrum [131].

The advantage of multiplex is that increasing by the number of scans improves the SNR enhances and the quality of obtained spectrum enhances. However, caution should be made to the resolution, since the abrupt increase in the number of scans may affect the resolution. However, in most modern FTIR this increase is controlled by software improving signal qualities. Another advantage is the precision of FTIR measurements giving rise to quantitative and qualitative spectroscopic analysis [132]. Hence, most FTIR measurements are reproducible. It is important here to mention the advantages of high SNR. Reducing the noise within the spectrum leads to accurate concentration measurements and quantitative accuracy of the analyzed results. Despite these mentioned advantages of FTIR, one of the disadvantages of these devices is the presence of artifacts within the spectrum. Although background spectrum and corrections have been made to get rid of these artifacts, some may still be present. The most common artifacts present in the most spectrum are the contribution of CO_2, and water to the measured spectrum. However, this disadvantage can be resolved by comparing the obtained data with those found in the libraries for CO2 and water [131]. The mentioned advantages and disadvantages are summarized in table (5) below [4].

Advantages	Disadvantages
High and better SNR	Artifacts present in the samples and spectrums
Multiplex advantage	
Throughput advantages	
High precision and reproducibility of the results	

Table 5: Table showing the advantages and disadvantages of FTIR [131].

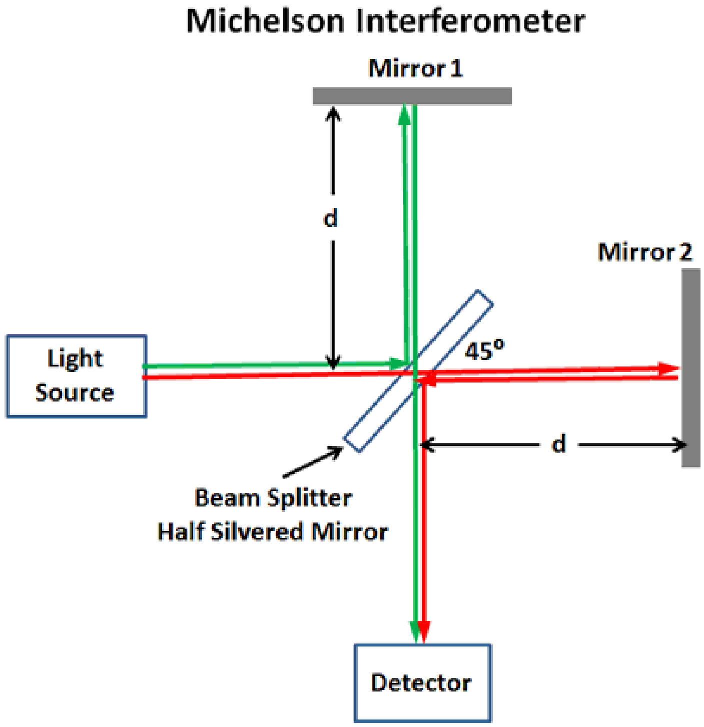

Figure 79: Illustration showing Michelson interferometer [183]

D. Mathematical background: The Fourier Transform:

The background of most Michaelson interferometers used today in our daily lives is the Fourier transforms, which transforms from the original time domain to the frequency domain, thus facilitating the analysis and handling of interferograms. This section will introduce this transform, mentioning its properties, as well as covering some important functions used in interferograms, and finally mentioning some software and computational programs that make these calculations easier, less time consuming and efficient. [131, 149-155]

The Fourier transform is defined by the following pair integrals:

$$H(s) = \int_{-\infty}^{\infty} h(t) e^{-i2\pi st} dt \qquad \text{Eq. (9.25)}$$

$$h(t) = \int_{-\infty}^{\infty} H(s)\, e^{i2\pi st}\, ds \qquad \text{Eq. (9.26)}$$

where Eqs. (9.25) and (9.26) are the Fourier Transform Integral and the Inverse Fourier Transform Integral respectively.

Mathematically any function to have Fourier transform must satisfy the following conditions: [152-155]

1. The function must be finite and defined at every point within the domain of interest.

2. The function must be absolute integrable; meaning $\int_{-\infty}^{\infty}|h(t)|dt$ must exist and be a definite value less than infinity.[152-155]
3. H(s) and h(t) should be differentiable and their derivatives should exist at every point within the domain of interest, especially within the left and right of a given point of interest.[152 - 155]

The properties of the Fourier transform are summarized in Appendix B.

This section presents this transformation, mentioning its properties, as well as some important functions used in interferograms, and finally mentioning some software and computational programs that make these calculations easier, less time consuming and efficient. Here we establish the background of most of these computational tools, by discretizing the Fourier integral and it's inverse: [151,152,154,155]

$$H(s) = \Delta t \sum_{j=0}^{N-1} h(j\Delta t)e^{-i2\pi s j\Delta t} \qquad \text{Eq. (9.27)}$$

$$h(t) = \Delta s \frac{1}{N} \sum_{j=0}^{N-1} H(j\Delta s)e^{i2\pi t j\Delta s} \qquad \text{Eq. (9.28)}$$

where N is the number of sampled points.

All the properties for the continuous Fourier transform, mentioned in the Appendix B, still hold for the discrete. Most of the established programs focus on estimating the summations found in either Eqs. (9.27) and (9.28). However, sometimes the truncation applied for discrete one does not match with the continuous cases. Such effects result in side lobes and other artifacts known as spectral leakages, which are due to most of the case errors that may alter the estimations performed as shown in the fig. 80 below. [151- 155]

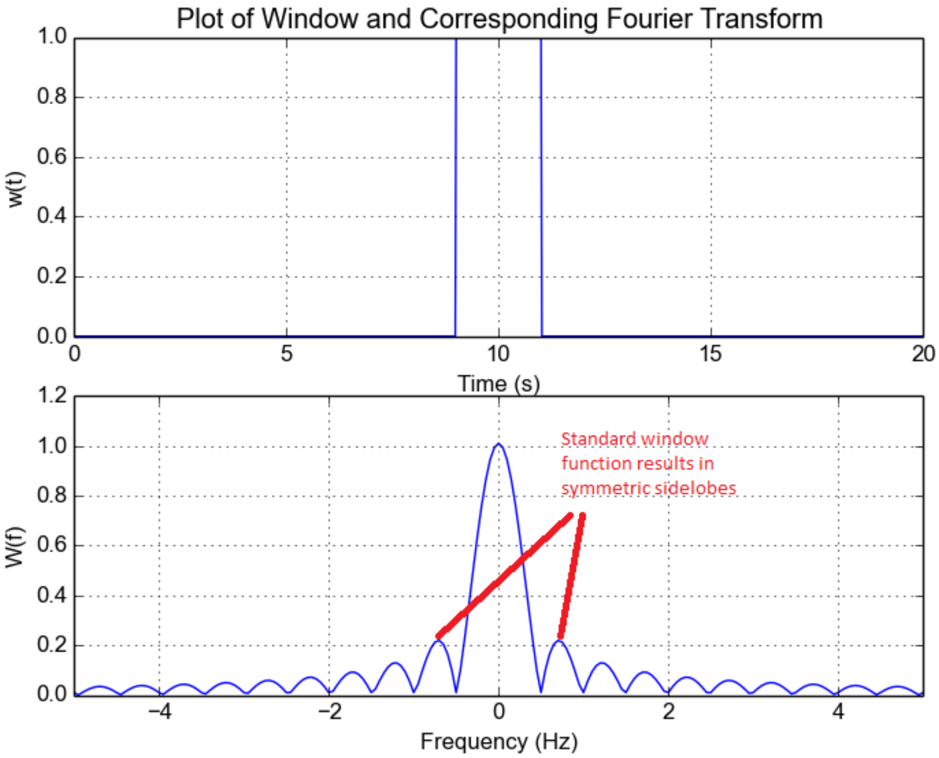

Figure 80: graph showing the truncated effect on the Fourier transform and the formation of sidelobes [151,152,154,155]

To resolve these issues, the spectral lines are convoluted with various functions given in Appendix C. This convolution process is known as " Apodization" which is simply an optical technique in filtering out the sidelobes and leakages from artifacts or instrumental errors. Apodization is a useful and powerful technique in minimizing the effect of sidelobes and truncation effects, leading to more certain calculations. An example of apodizations is shown in the figs 81 and 82 below.

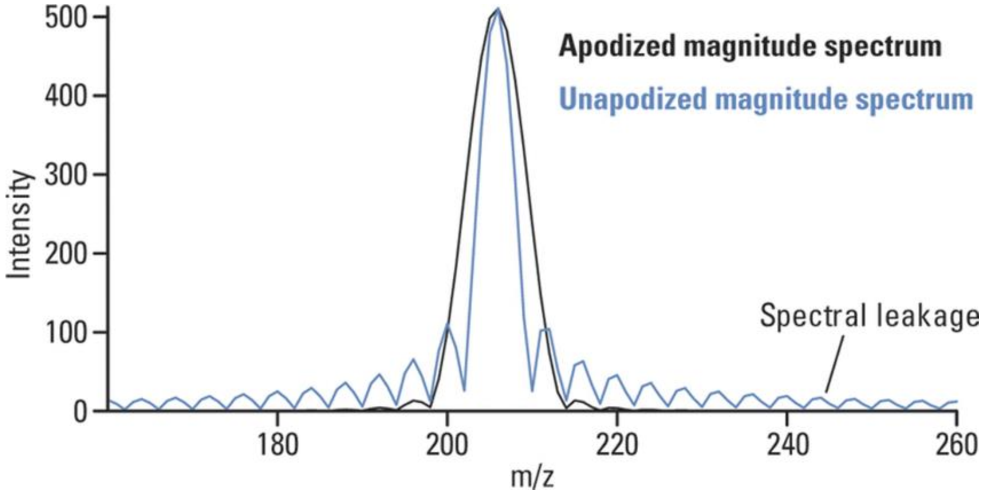

Figure 81: figure showing the effect of apodization process as an attempt of reducing artifacts [205]

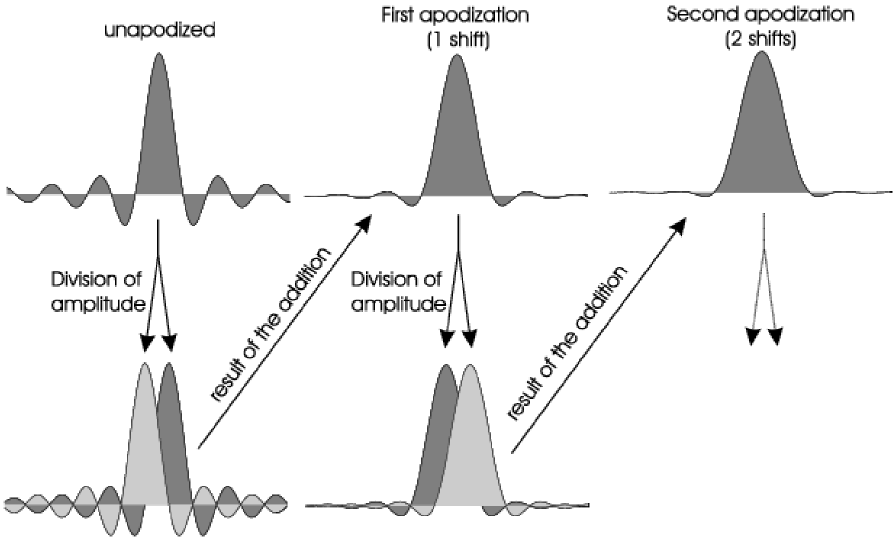

Figure 82: figure showing the reduction of spectral leakages and sidelobes within the spectrum after being Apodized [149]

To further distinguish between signals from the sample and artifacts, aliasing is applied or introduced upon the signal. Aliasing is the multiplication of the signal with specific functions, (see in the appendix C), which corresponds to the convolution of the Fourier transformed spectrum. Its basic aim is to reduce instrumental effects, distortions and artifacts found in the signal, or, in other words, reducing the obstacles present that can alter or complicate the analysis of the spectrum. Examples of aliasing also referred to as sampling are represented in the few figures, namely figs (83) to (85) below.

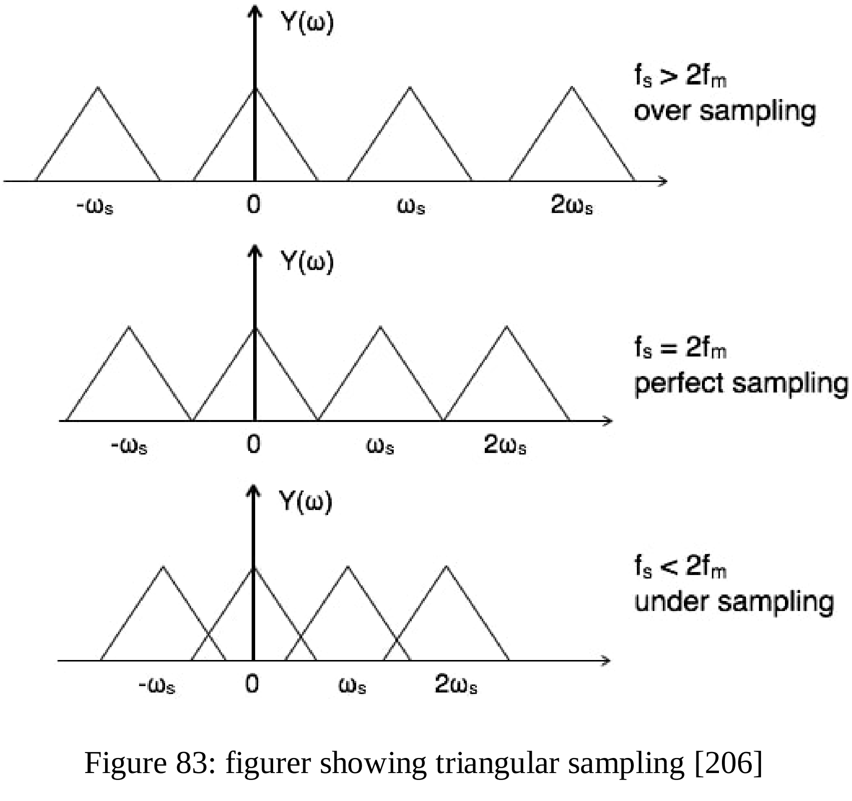

Figure 83: figurer showing triangular sampling [206]

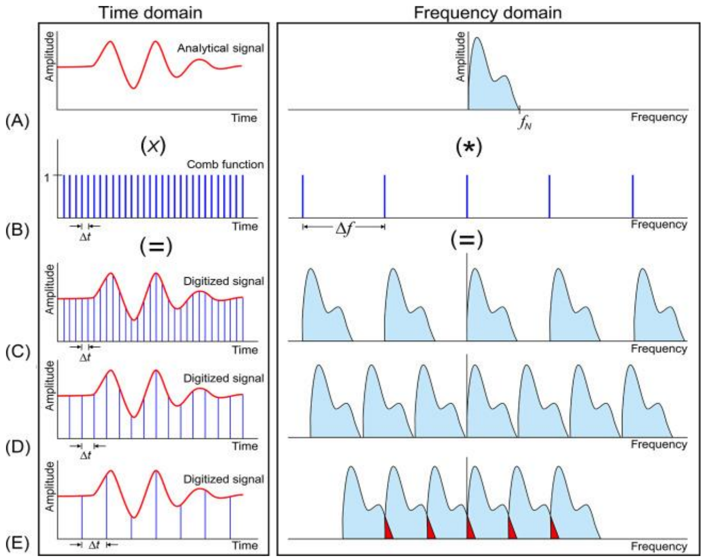

Figure 84: figure showing the aliasing process in time and frequency domains

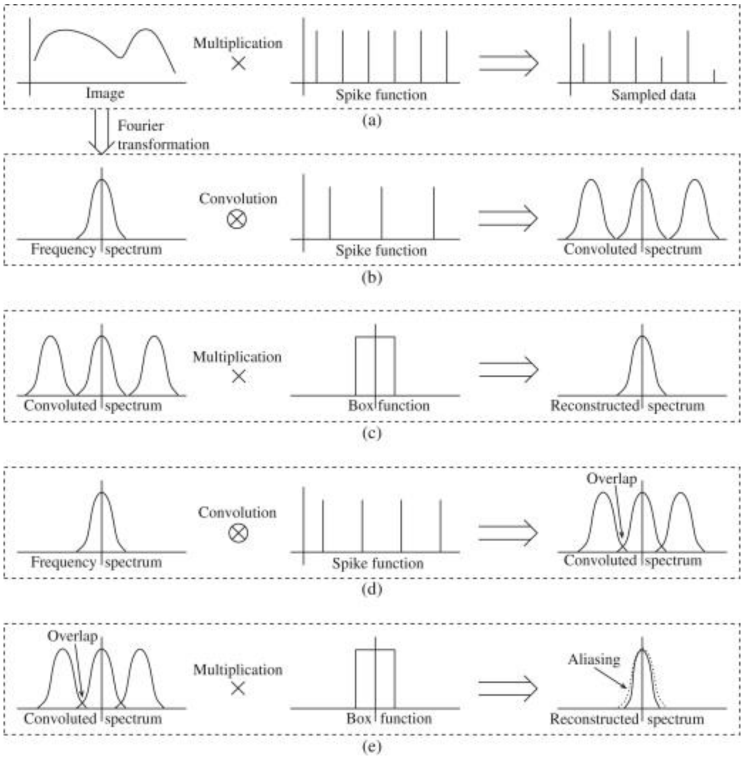

Figure 85: figure showing the sample aliasing using different functions

As depicted in figs (83) to (85) , sampling requires a critical frequency given by:

$$f = \frac{1}{\Delta t} = 2fmax \qquad \text{Eq. (9.29)}$$

which is known as Nyquist frequency or condition. Any sampling at frequencies less than the critical Nyquist frequency results in overlaps between the sampled intervals, this is known as undersampling as shown in fig 83 (c). Also, any sampling at frequencies above Nyquist frequnecy results in sampled domains separated by empty intervals which are referred to as oversampling as depicted in fig 83 (a). Therefore the proper sampling or aliasing is done by satisfying the critical Nyquist frequency given above as clearly seen in fig 83 (b). A similar condition applied for the discrete analysis. The number of points within each interval to be sampled is given by: $N = \frac{2v_{max}}{\Delta v} \quad where\ v = \frac{1}{\lambda}$.

Once these conditions are satisfied we can continue the discrete Fourier analysis. The discrete Fourier series can be written by using the Nyquist condition given as $f = \frac{n}{\Delta t} = \frac{nk}{Nt}$:

$$H(s) = \sum_{j=0}^{N-1} h(jtmax)jtmax\, e^{-i2\pi nj/N} \ ) \qquad \text{Eq. (9.30)}$$

$$h(t) = \frac{n}{N} \sum_{j=0}^{N-1} 2fmaxH(jfmax)e^{i2\pi jnN} \qquad \text{Eq. (9.31)}$$

Taking W=$e^{-i2\pi/N}$, Eqs. (9.30) and (9.31) reduce to [151, 154, 155]

$$H(s) = \Delta t \sum_{j=0}^{N-1} h(jtmax)\, W^{jn} \qquad \text{Eq. (9.32)}$$

Eq (9.32), as illustrated above, can be written in a matrix form:

$$\left[H^{(j)}(s)\right] = \Delta t \begin{bmatrix} W_0^{(0)} & \cdots & W_n^{(0)} \\ \vdots & \ddots & \vdots \\ W_0^{(n)} & \cdots & W_n^{(n)} \end{bmatrix} [h(jt)] \qquad \text{Eq. (9.33)}$$

where [H(s)] and [h(jt)] are column vectors containing the elements of fourier transformed (frequency domained)and non-transformed (time-domained) values, respectively.

Therefore, the discrete Fourier transform facilitates solving the matrix relation given in Eq. (9.33). Most devised software and programs, such as the Cooley-Tukey algorithm [154, 155], resides in solving Eq. (9.33), using different techniques such as neural network [164-166], fast Fourier transform [154,155,19] just to name a few.

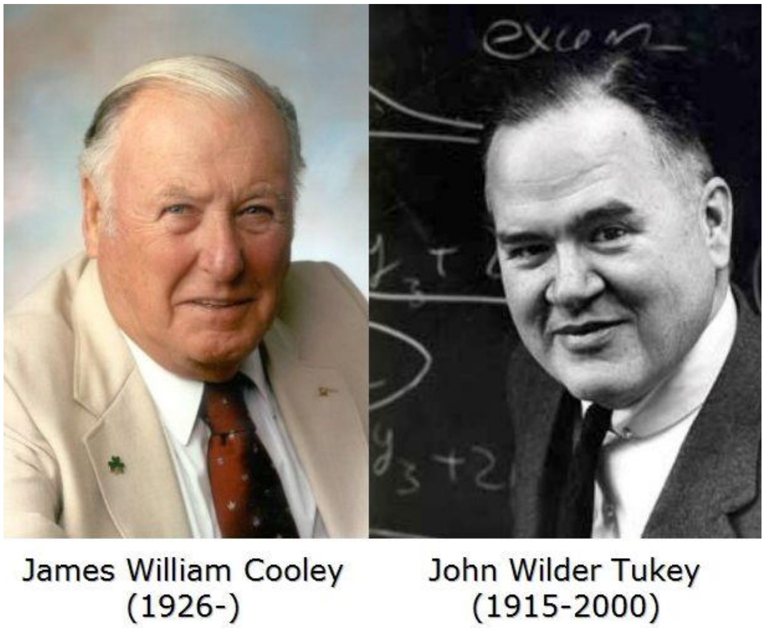

Figure 86: James Cooley and John Tukey who established the FFT Cooley-Tukey algorithm [207]

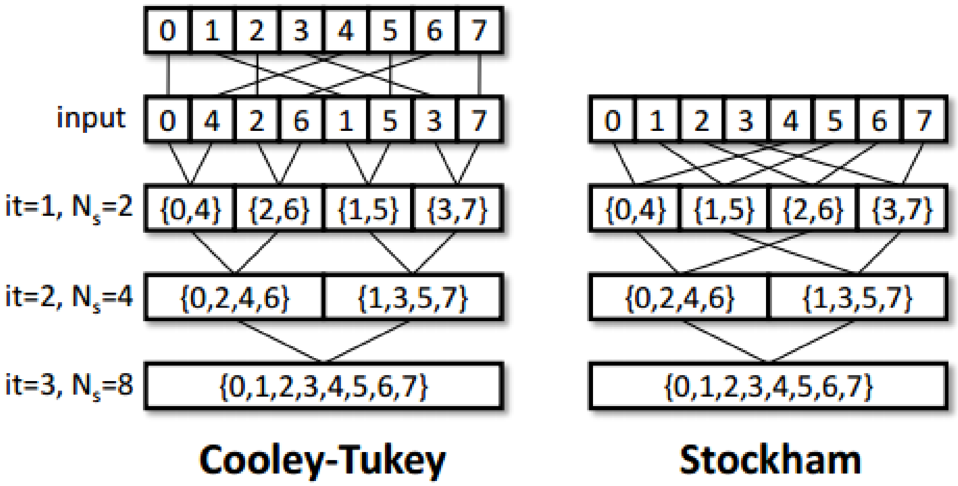

Figure 87: figure showing Cooley-Tukey and Stockham algorithms performing calculations [182]

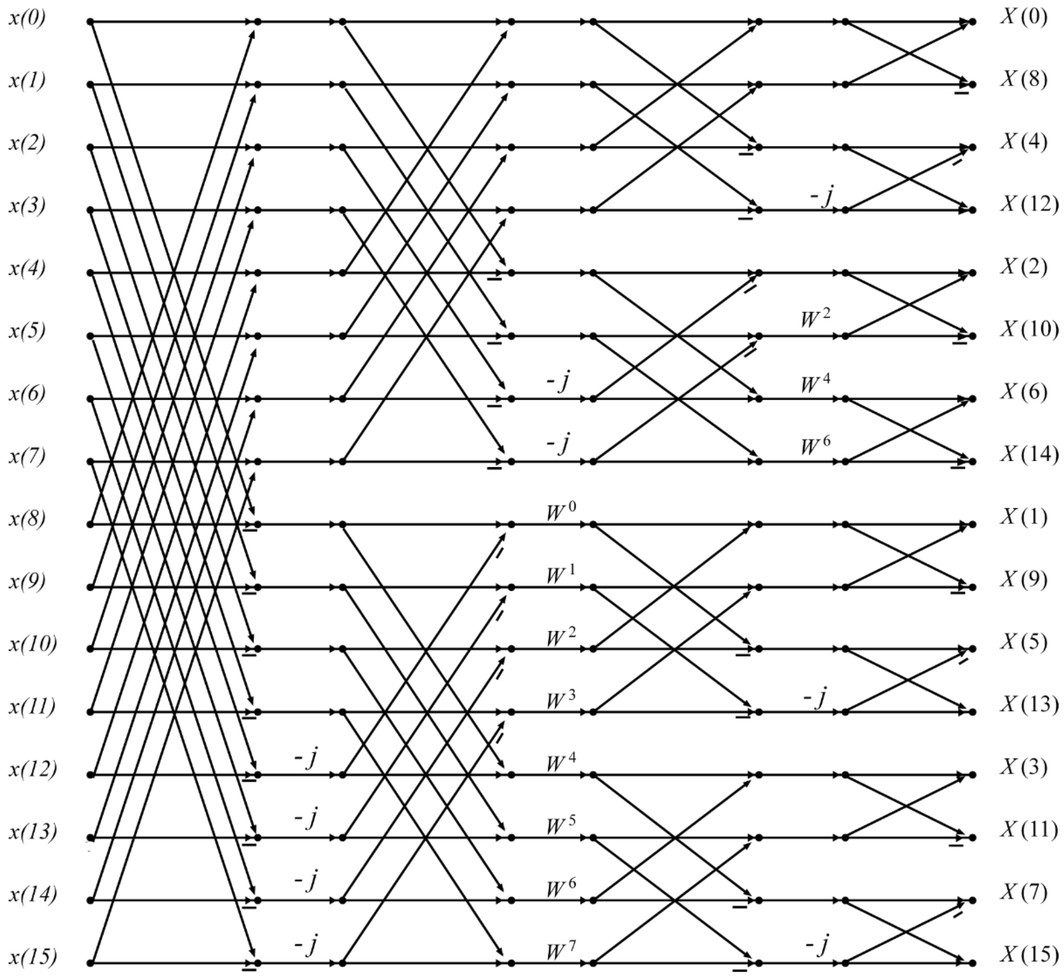

Figure 88: illustration showing the FFT Cooley-Tukey algorithm process and procedures followed during calculations [154, 155].

E. Experimental Spectrum Processing and Handling :

Experimentalists devised procedures and processes to facilitate sample handling and reduce artifacts altering the spectrum analysis. Some of these experimental tools and guidelines are recommended and advisable to follow or apply:[131]

- Have a clear idea about the algorithm to be applied and which algorithm is the most efficient
- It is crucially advised to have a copy of the original data or spectrum.
- Spectral subtraction is the process of subtracting the spectrum of artifacts and impurities from the original spectrum. This allows to get rid of CO_2 and water and other impurities that alter our data as mentioned above. In most modern interferometers, this subtraction can be performed and controlled by adequate software and algorithm.[131].
- Baseline corrections are another type of process in getting rid of drifts and problems appearing at the level of the base. This process allows one to regulate and re-calibrate the baseline reducing defects introduced by experimental instruments and fluctuations caused by software and programs. In modern interferometers, baseline corrections are available within the experimental procedures.
- Smoothing is another method developed by spectroscopists and experimentalists to reduce the amount of noise in the spectrum, facilitating and easing the analysis. Various functions are found in the literature that can be applied to reduce and smoothen the spectrum. However smoothing is not advisable as it can alter and affect the spectrum leading to loss of information. Therefore, smoothing should be applied cautiously.
- A better way of reducing noise and defects is derivating the spectrum. The first derivative removes offsets, artifacts within the baseline, on the other hand, the second derivation regulates the slope and further reduces offsets. Most modern

interferometers contain algorithms that can derivate the spectrum accurately within a few minutes. One problem arising from derivation is that sometimes the derivative curves contain higher noises. However, these problems can be easily solved by smoothing or using good and efficient algorithms [131,163]. Finally, the derivation is a good process to reduce noises and offsets that can ease the results being detected and analyzed especially in quantitative spectroscopic analysis. [132].

- Deconvolution is a process of splitting two or more peaks that come on top of each other. This process is also known as Fourier self deconvolution (FSD [151-155, 161]). Deconvolution results in cepstrum as depicted in the figure below, making broad bands look like narrow bands enhancing the quality of the information, and reducing the noise.
- Library searching is a useful process in identifying the appearance of the interferogram. Due to the effect of deconvolution on the resolution, or the limitations and constraints imposed on the above-mentioned processes, library search perhaps is the most powerful technique in identifying artifacts, noise, and components related to water or CO_2 or any other impurities. [131].

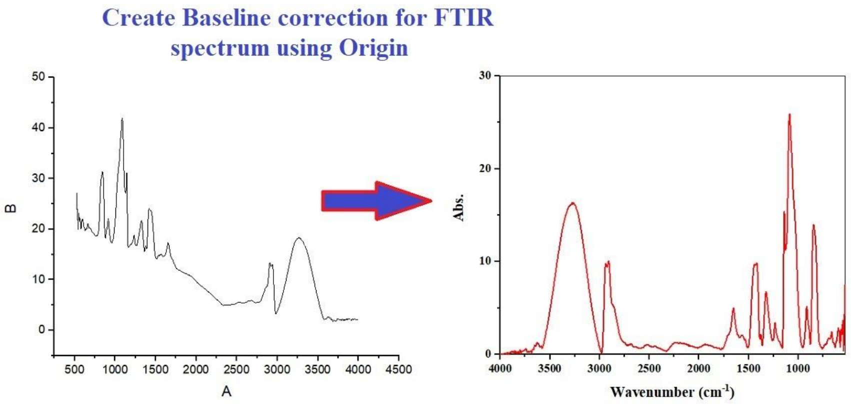

Figure 89: figure demonstrating baseline correction for FTIR spectrum. [209]

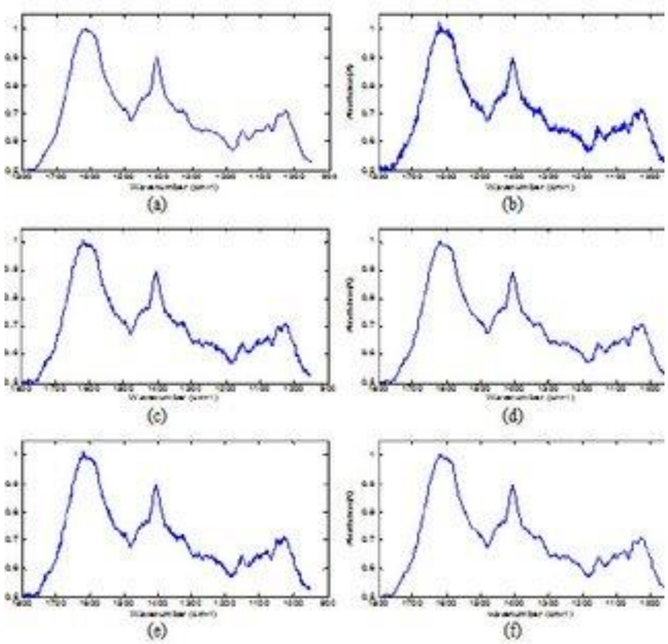

Figure 90: figure clarifying the effect of smoothing on FTIR spectrum [162].

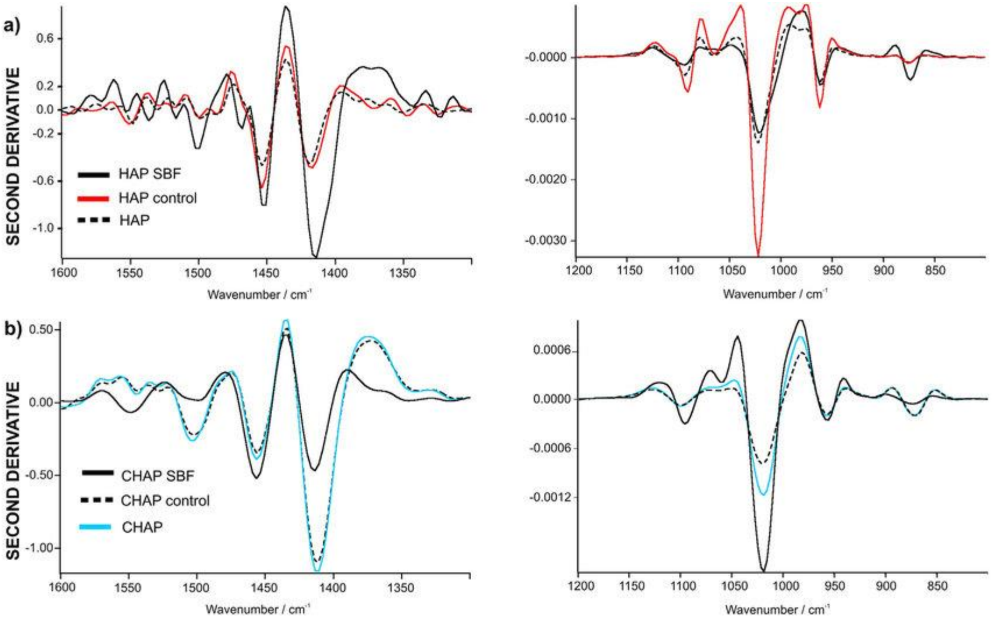

Figure 91:figure exemplifying the effect of derivatives on FTIR spectrums [157].

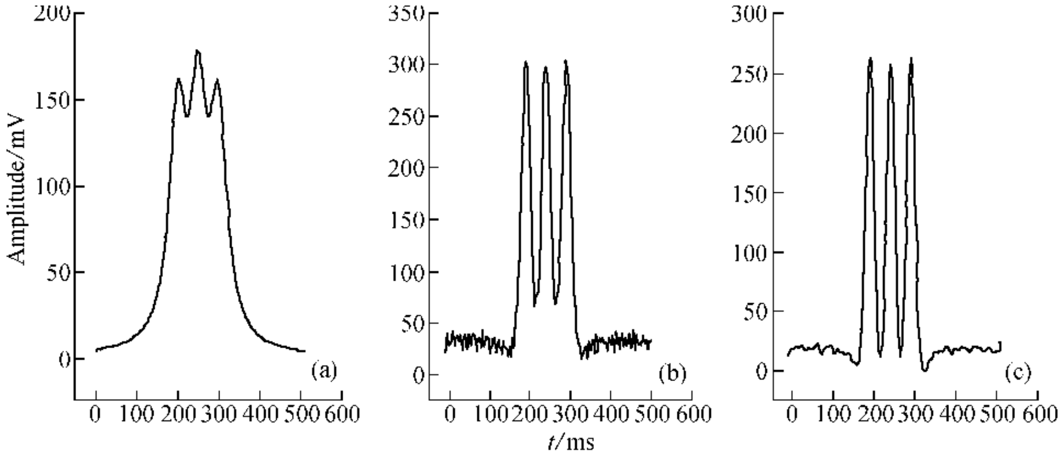

Figure 92: figure illustrating the Fourier self deconvolution on FTIR spectrums [161]

F- Our FTIR Set up and Experimental procedure

Figure 93: figure showing our FTIR system [180]

All necessary infrared measurements were performed on our FTIR system modeled after Thermo Electron Corporation's Nicolet 4700 spectrometer of the 560/760 spectrometer systems as shown in the figure above. This spectrometer can measure transmission, reflectivity, or absorption spectra in the range of the 400 -4000 cm^{-1} spectral range. As mentioned earlier, most modern FTIRs in general, and our system in particular, incorporate a Michelson interferometer, which has advantages over other spectrometers and also offers higher accuracies, especially in frequency measurements, due to its high throughput. [16, 131, 149]. Our FTIR system consists of the following main components:

- Infrared Source: consists of a heated filament that emits infrared radiation, as shown in the fig (94) below.

Figure 94: figure depicting te IR source used in our FTIR system. [180]

- Optics: These are made up of parabolic mirrors, lenses, and collimators that align the incoming radiation and direct it into the Michelson interferometer in unison. Lenses and parabolic mirrors are also used to focus the aligned rays that have passed through the Michelson interferometer onto the samples and, later, to the detectors.
- Michelson interferometer: as previously stated, this consists of a KBr beam splitter, as shown in the figs 95 and 96, as well as, moving and fixed mirrors...
- Sample and sample holders: the beams that enter this compartment are focused on the sample, from which the reflected or transmitted rays are focused on the detectors via lenses and mirrors, depending on the purpose of the investigation.

- Detectors: Finally, the reflected or transmitted beams are focused on the detector, where they are displayed and stored by software, in our case OMNIC software, ready for the investigator to analyze and decode.

Figure 95: figure showing the KBr beam splitter used in our FTIR system [180]

Figure 96: figure depictng the Michelson interferometer attached to our FTIR [180]

Figure 97: figure showing the DTGS-KBr detector used in our system [180]

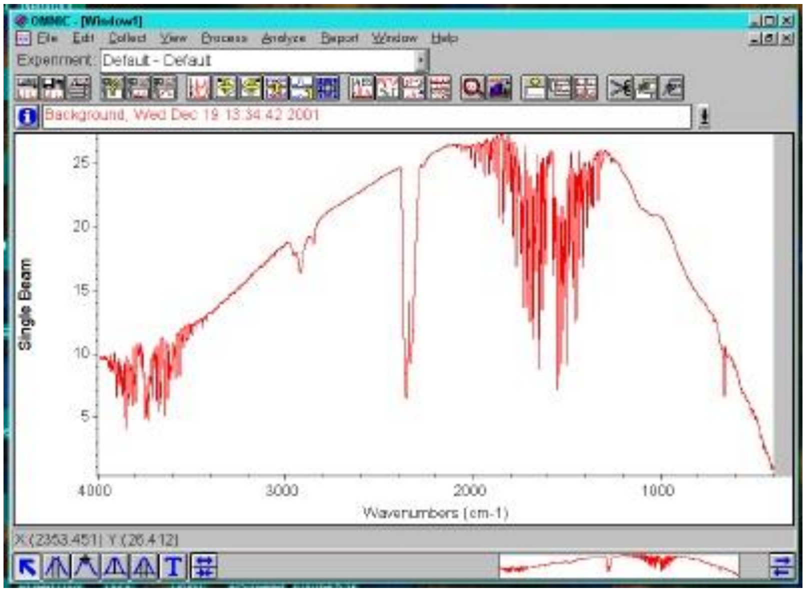

Experiment: Default - Default

Background, Wed Dec 19 13:34:42 2001

X:(2353.451) Y:(26.412)

Figure 98: Figure depicting an example of OMIC software displaying background measurement in our system. [181]

The measurements begin with the selection of the necessary parameters, such as setting the number of scans and, selecting an appropriate resolution. A background collection is performed in the compartment to account for the effect of the environment and components or instruments that will be extracted from those of signals measured using samples. Typically, background data is collected before each measurement. A golden mirror-like object is used for reflectivity, and ambient air within the compartment for transmission measurements, as depicted in figure (98). Finally, the spectrum of each sample is measured sequentially, and analyzed by the OMNIC software, where the displayed data shows the ratio of the spectrum of the samples to that of the background, thus eliminating the instrumental and environmental effects surrounding the samples. Hence the obtained signals and data contain the necessary optical information specific to the samples, which are stored and ready to be analyzed by the users.

G. Summary:

In this chapter, we have discussed the background of vibrational spectroscopy, highlighting infrared spectroscopy, mentioning its applications and drawbacks. We also introduced Fourier transform infrared spectroscopy, covering its versatility and superiority over other infrared spectroscopy techniques and available devices. Finally, we discussed the Fourier transform, considered the backbone of Fourier transform infrared spectroscopy, detailing its properties, discretization and sampling techniques, and mentioning the computational tools available to solve the matrix form of the Fourier analysis. After covering the theoretical basis of FTIR, we have detailed the experimental procedures and guidelines that can be used to process and facilitate the analysis of data obtained from FTIR measurements.

SECTION IV

THESIS OUTCOME

CHAPTER X

RESULTS AND DISCUSSIONS

Pulsed laser deposition was used to deposit zinc oxide on glass. The resulting samples were measured by XRD, SEM, UV-Vis spectroscopy and FTIR to investigate the suitability of ZnO as a hyperbolic material with the potential to control the direction of incident solar infrared radiation on vehicle glass. This chapter begins by introducing hyperbolic metamaterials, including their types, designs, basic properties, and applications. It then summarizes and discusses the results obtained using the experimental techniques highlighted in the previous chapter, as well as the analytical methods used in this research and analysis.

A. Hyperbolic Metamaterials: basic properties, fundamentals, and applications

Hyperbolic metamaterials are anisotropic materials that function as metals in one direction and as dielectrics in the other, and are therefore defined by a permittivity tensor of the form .

$$\varepsilon = \begin{bmatrix} \varepsilon_{xx} & 0 & 0 \\ 0 & \varepsilon_{yy} & 0 \\ 0 & 0 & \varepsilon_{zz} \end{bmatrix} \qquad \text{Eq. (10.1)}$$

where at leat one of its components has a different sign from the others.

Naturally, any material is defined by a dispersion relation for the propagation of extraordinary or ordinary waves through it. This dispersion can be obtained from Maxwell's equations given in chapter II of this text, and expressed as: [58, 59, 171-178]

$$k_x^2 + k_y^2 + k_z^2 = \frac{\omega^2}{c^2} \qquad \text{Eq. (10.2)}$$

where the propagative wave is represented by the wavevectors components k_x, k_y, and k_z, and produces a closed isofrequency spherical or ellipsoidal shell surfaces in the momentum space, as illustrated in the fig (99 (a)) below. However, in a hyperbolic metamaterial Maxwell-Garnett approximation predicts a dispersion of the form: [58, 59, 171,-178]

$$\frac{k_x^2 + k_y^2}{\varepsilon_{zz}} + \frac{k_z^2}{\varepsilon_{xx}} = \frac{\omega^2}{c^2} \qquad \text{Eq. (10.3)}$$

As mentioned earlier, the hyperbolic metamaterial has dielectric components that are opposite in sign. To put it another way, $\varepsilon_{||}.\varepsilon_{\perp} < 0$, this results in open isofrequency surfaces in the momentum space, as seen in figs (99 (b) and (c)) below. [58, 59, 171-178]

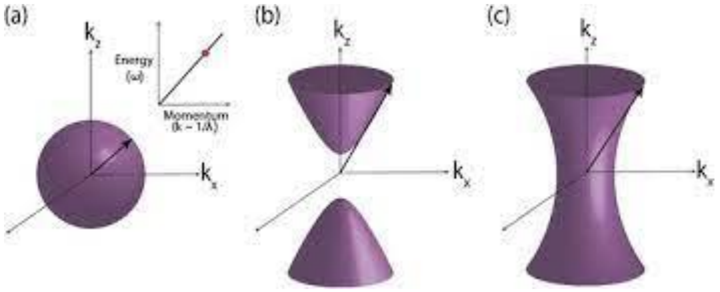

Figure 99: schematic illustration of isofrequency surfaces of extraordinary wave propagation in (a) real materials, (b)&(c) for hyperbolic metamaterials respectively [58, 172-176]

It is worth noting that the negative components result in a metal-like surface, whereas the positive components results in a dielectric-like surfaces. We can distinguish two forms of hyperbolic metamaterials [58, 59, 171-178]

- Type 1 hyperbolic metamaterials have just one negative component of their dielectric tensor $\varepsilon_{zz} < 0, and\ \varepsilon_{xx} = \varepsilon_{yy} > 0,$. These produce symmetric hyperbolic isofrequency surfaces of the form illustrated in fig (99 (b)).[58, 59, 172-176]
- Type 2 hyperbolic metamaterials have two components of their dielectric tensor negative$\varepsilon_{zz} > 0, and\ \varepsilon_{xx} = \varepsilon_{yy} < 0$ . . These produce a continous hyperbolic surface as the one shown in fig (99 (c)). [58, 59, 172-176]

Hyperbolic metamaterials are created in one, two, or three dimensions utilizing nanofabrication and engineering processes such as top-to-down or bottom-to-up stacking, milling, and other depositional techniques, some of them are discussed in Chapter 5. In general, such metamaterials can be multilayer films consisting of silver, gold, or transparent oxide and nitrides, such as TiO2, SiN, and SiC [58, 174, 176], to name a few, or they can be built into nanowires or tubes, for example, by metal factor filling inside a dielectric material. [58, 59, 171-178]

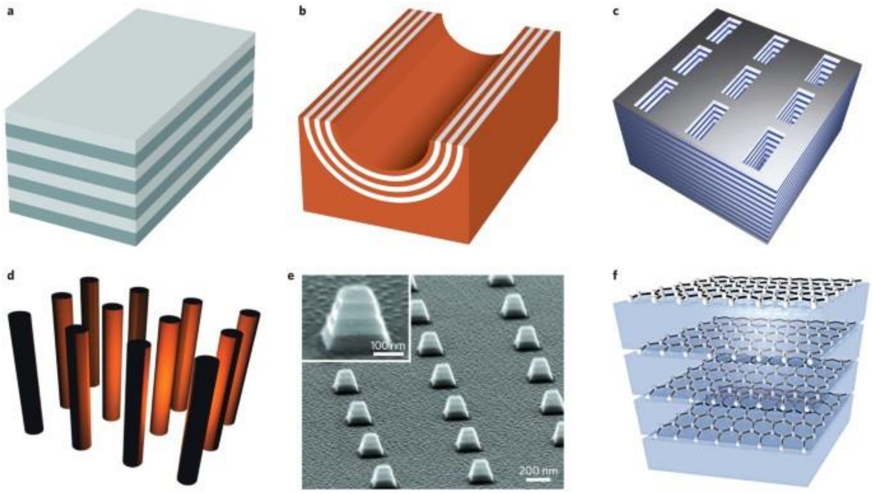

Figure 100: figure depicting different hyperbolic metamaterials fabricated shapes and designs [59]

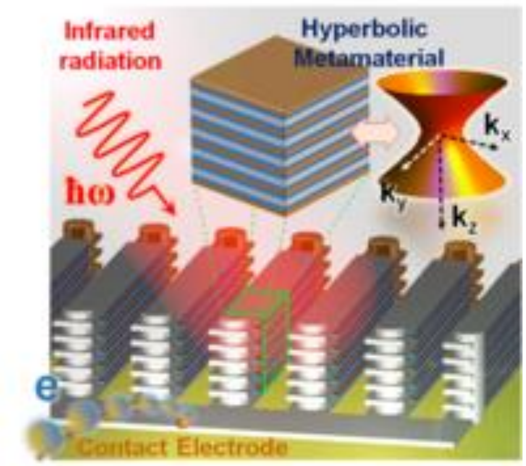

Figure 101:Schematic representing metal-insulator-metal junction made up of hyperbolic metamaterial and interacting with IR radiation [179]

The in-plane and cross-plane dielectric functions of the multilayered metal-dielectric material are given by the following relationships: [58, 59, 171-178]

$$\varepsilon_{||} = \rho\varepsilon_m + (1-\rho)\varepsilon_d \qquad \text{Eq. (10.4)}$$

$$\varepsilon_\perp = \frac{\varepsilon_m \varepsilon_d}{= \ \rho\varepsilon_m + (1-\rho)\varepsilon_d} \qquad \text{Eq. (10.5)}$$

with

$$\rho = \frac{d_m}{d_m + d_d} \qquad \text{Eq. (10.6)}$$

Here $d_{m(d)}$ is the metal (dielectric)thickness, $\varepsilon_{m(d)}$is the dielectric constant for metal (dielectric). Thus one can realize that the optical constant of the hyperbolic metamaterial is highly dependent or influenced by the thickness of the thin layers, which we intend to investigate in this script for ZnO thin film layers deposited on glass.

One can distinguish between the dielectric near zero, defined as the dielectric function passing through the value zero, and the dielectric near the poles, defined as the recording poles of the dielectric [58]. Although these values are represented as singularities in the phonon density of states, the density of states remains a hyperboloid at infinity, which has intriguing applications [58].

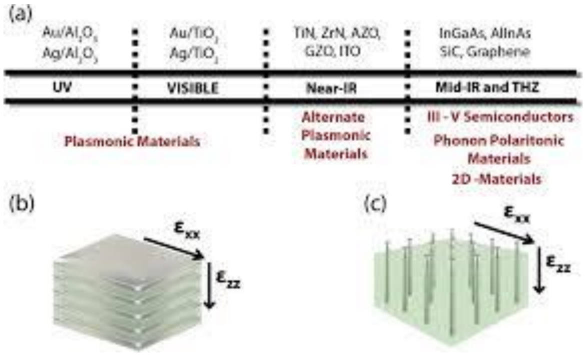

Figure 102: figure showing different hyperbolic metamaterial along with their resonant frequency [58].

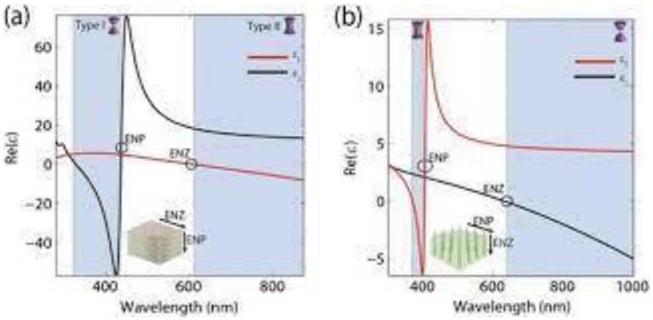

Figure 103: Schematic illustrating epsilon near zero and poles in different typed hyperbolic metamaterial [58]

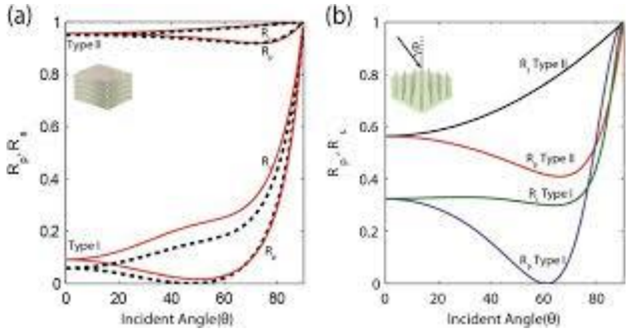

Figure 104: figure depicting the epsilon near zero and poles effects in the reflectivity spectrum in different typed hyperbolic metamaterial [58]

Hyperbolic metamaterials with broadband singular behavior in their density of states, as well as infinite phonon density of states, have found applications in superlenses [57], super-resolution imaging [57-59, 171, 176], enhanced quantum [176, 178] effects surpassing classical electrodynamical dynamical phenomena [177], advanced thermal systems [176, 177] and managements, new stealth technologies [171-173, 176] , gravitational and cosmological phenomena [175,176] and beyond [176, 179].

The major interest of hyperbolic materials lies in the fact that they can be used to control the direction of light. The direction of light incident on a hyperbolic material is determined by the sign and magnitude of the two principal components (in-plane and across-plane) of the dielectric permittivity tensor. The propagation angle θ (e.g., the angle between the Poynting vector and the z-axis) of the hyperpbolic polaritons (HPs) in hyperbolic media can be approximated by the following formula

$$\theta = \frac{\pi}{2} - argtan\left(\frac{\sqrt{\varepsilon_z(\omega)}}{i\sqrt{\varepsilon_t(\omega)}}\right) \qquad \text{Eq. (10.7)}$$

where$\varepsilon_z = \varepsilon_{zz}$ and $\varepsilon_t = \varepsilon_{xx} = \varepsilon_{yy}$. Thus, materials exhibiting hyperbolic behavior over a broad infrared spectral range, and in which the ratio of the in-plane dielectric constant to the cross-plane dielectric constant remains unchanged in the spectral range in which the material is hyperbolic, are of particular interest because they can control the direction of a large part of the solar infrared radiation. Coating the vehicle glasses with this type of material would deflect the incident solar infrared rays and avoid heating the interior of the vehicle. As such, broad-band infrared hyperbolic materials would minimize the risk on children on board because each year, children die from heatstroke after being left unattended in motor vehicles.

A potential candidate for this application is ZnO. As mentioned previously, ZnO is transparent in the visible spectrum and, when grown by PLD, it forms well-oriented gains having a columnar/conical structure with a high concentration of defect-induced free electrons. These electrons will be confined in the direction perpendicular to the grain axis, while remaining nearly free along the grain axis. This effect would increase the anisotropy of the ZnO structure and induce very different plasma oscillation frequencies parallel and perpendicular to the grain axis. Therefore, the dielectric tensor of ZnO films obtained by PLD may have two principal components with different signs due to the different oscillation of the plasma parallel and perpendicular to the grain axis. Furthermore, the grain shape, and hence the optical anisotropy of the ZnO film, can be controlled by the film thickness. This offers the possibility to control the ratio of the in-plane dielectric constant to the cross-plane dielectric constant, and thus allows to control the propagation direction of the HPs. In this chapter, we investigate the hyperbolicity of the polaritons in ZnO films grown by PLD on glass substrates. We use XRD experiment to demonstrate the well orientation of the grains along the c-axis and the SEM technique to show the columnar shape of the grains. The transparency of the films in the visible spectral range is assessed by reflection measurements in the visible and near-UV spectral ranges. The signs of the in-plane and cross-plane dielectric constants and their ratio in the entire infrared spectral range beyond the phonon resonance are evaluated from an accurate analysis of the infrared reflectivity measurements.

B. XRD measurements

ZnO thin films obtained by PLD with different deposition times were first examined by XRD. The spectrometer used and the measurement setup are given in Chapter VI. The results are shown below in Fig 105.

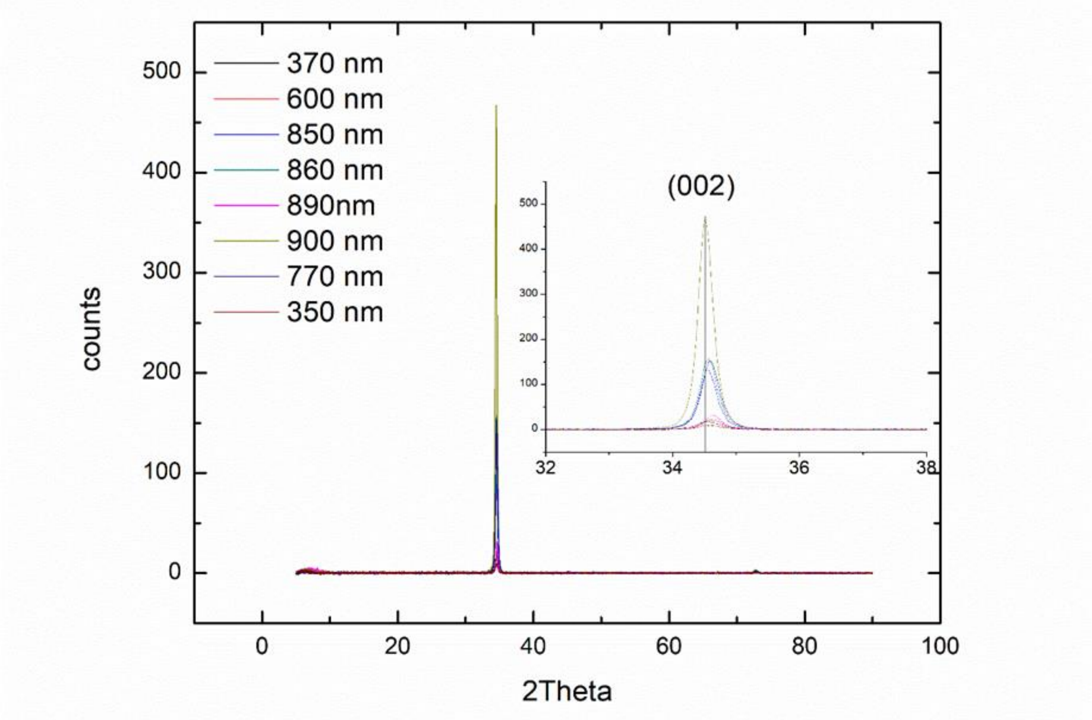

Figure 105: XRD patterns of the grown films

The XRD spectra show only one peak related to the (002) plane, which is perpendicular to the c-axis of the ZnO Wurtzite structure. This peak broadens and shift slightly with changing the film thickness due to a change in the crystallinity or the strain field in the film. However, the occurance of a single peak related to the (002) plane clearly demonstrates that all grains are oriented along the c-axis.

C. SEM Measurements:

The cross-sections of the ZnO films were imaged using SEM to observe the grain shape. The details of the SEM used and the technical procedure that was adopted to measure the cross-sections of the films are given in Chapter VII. All the measured films showed columnar grains. The SEM image of the cross-section of a ZnO film deposited on glass by PLD for one hour is shown below in Fig 106.

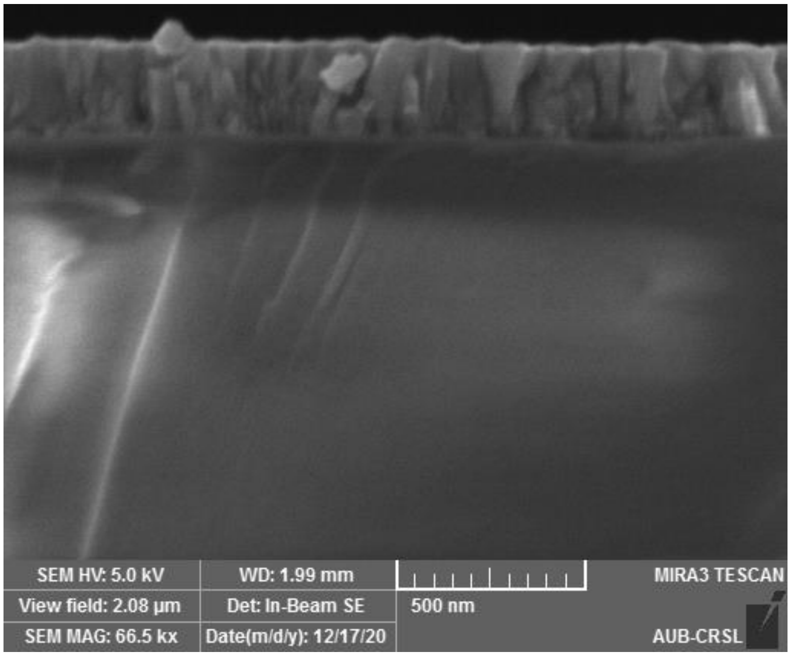

Figure 106: SEM micrographe of the cross-section of ZnO film grown on glass by PLD for one hour. The columnar nature of the grains is clearly seen.

In addition, to the shape of the grains in the films, the SEM measurements were used to deduce the thickness of the films, which is needed for precise analysis of the FTIR spectra that will be presented later in the discussion of the results.

D. Measurement of Transmittance in the Visible Spectral Range

The transparency of the grown samples in the visible spectral range was assessed using a UV-Vis spectrometer operating with optical gratings. Detailed description of the specrometer used and the measurement setup is provided in Chapter VIII. The measured transmittance spectra of the samples are shown in Fig 107 together with the transmittance of glass.

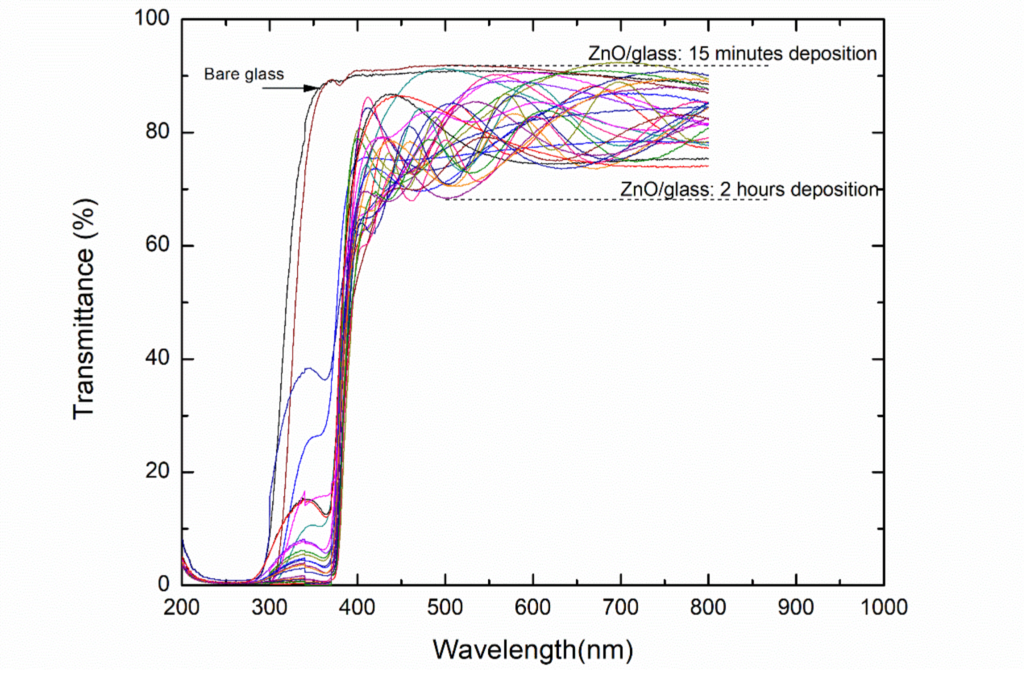

Figure 107:Transmittance of the grown samples in the visible spectral range.

These spectra show that the transmittances of the grown samples are wavelength dependent due to interference phenomena. The measured transmittance spectra also show that the transmittance of the samples decreases slightly with increasing film thickness. However, in general, glass coated with ZnO films remains transparent even for thick films deposited for about 2 hours by PLD. These results show that ZnO does not significantly impair the visibility of the passengers in the vehicle.

E. Measurement of Reflectivity in The Infrared Spectral Range

The infrared reflectivity spectra of the developed samples were measured using the Fourier transform infrared spectrometer described in Chapter IX. The angle of incidence was set $\pi/4$ in all measurements.

The dielectric properties of the glass substrate, which are necessary for accurate analysis of the dielectric properties of ZnO films deposited on glass, were first obtained from the Kramers-Kronig analysis of a bare glass substrate. The Kramers-Kronig conversion technique is detailed in Chapter III, and the dielectric properties obtained for the glass substrate used in this study are shown in Fig 108.

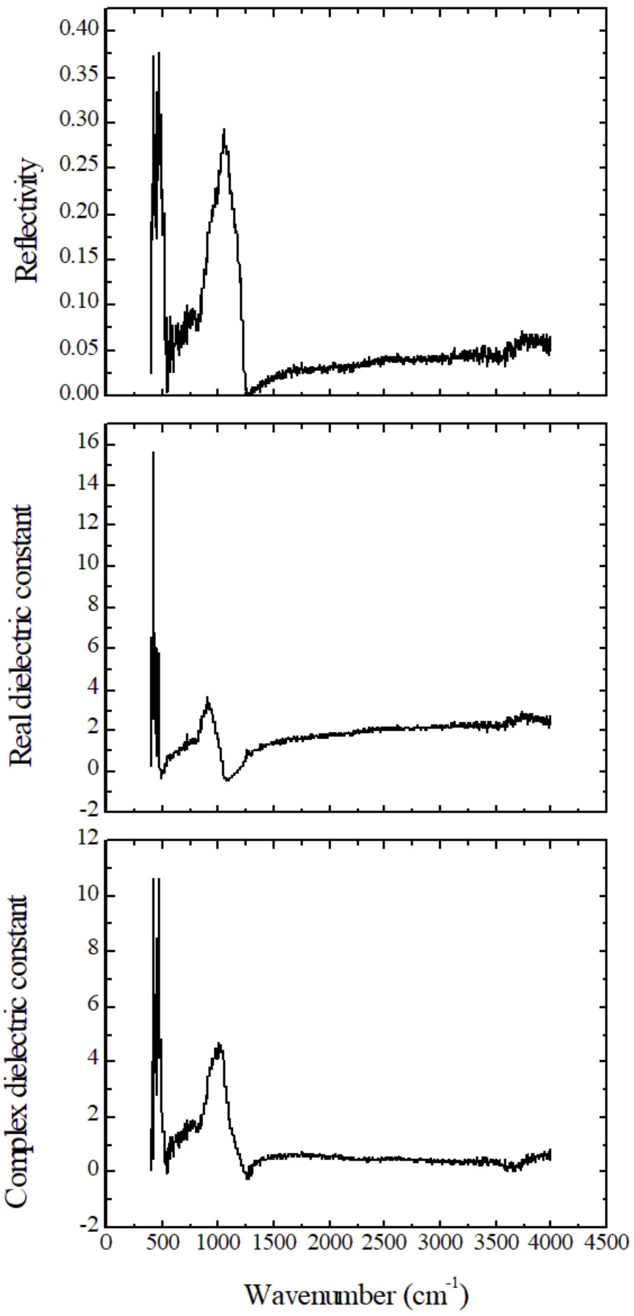

Figure 108:infrared reflectivity and complex dielectric function of the glass substrate used in the present study.

To deduce the complex dielectric functions of the films deposited on glass, we considered an anisotropic permittivity tensor of the form given in Eq 10.1. Now, if we consider the direction of the incoming electric field with respect to (x, y, z) is defined by

$$\hat{E} = \begin{pmatrix} sin\,\theta\, cos\,\varphi \\ sin\,\theta\, sin\,\varphi \\ cos\,\theta \end{pmatrix} \qquad \text{Eq.(10.8)}$$

where θ is the angle between the electric field and the z-axis and φ is the azimuthal angle, we find that the electric displacement vector is given by

$$\vec{D}(\omega) = \varepsilon(\omega)\hat{E}.|\vec{E}| \qquad \text{Eq. (10.9)}$$

Upon using Eqs 10.1 and 10.8 in Eq. 10.9, we find that the magnitude of the displacement vector is given by

$$D(\omega) = \left(\varepsilon_{xx} sin^2\theta cos^2\varphi + \varepsilon_{yy} sin^2\theta sin^2\varphi + \varepsilon_{zz} cos^2\theta\right)E(\omega) \qquad \text{Eq. (10.10)}$$

Since the angle of incidence is equal to $\pi/4$ and the incident light was unpolarized (i.e.$\langle cos^2\varphi\rangle = \langle sin^2\varphi\rangle = \frac{1}{2}$), and the basal plane of the wurtzite structure is isotropic (i.e. $\varepsilon_{xx} = \varepsilon_{yy}$), the overall dielectric function of the films for the measurement configuration is given by

$$\varepsilon_{effective} = \frac{\varepsilon_{xx}}{2} + \frac{\varepsilon_{zz}}{2} \qquad \text{Eq. (10.11)}$$

The in-plane and cross-plane dielectric constants in Eq 10.11 can be written according to the Drude-Lorentz model given by Eq 3.27. Upon using these dielectric functions and the glass dielectric function derived from the Kramers-Kronig analysis of the glass reflectivity spectrum in the Tansfer-Matrix method introduced in Chapter III, the overall reflectivity from the samples investigated can be calculated.

To obtain the parameters of the in-plane and cross-plane Drude-Lorentz oscillators (Eq 3.27), we have fitted the measured reflectivity to the model for the reflectivity from a two-layer system described above. The fitting results are given in Table 6.

Samples	Thickness (nm)	$\varepsilon_{\infty s}$	$\varepsilon_{\infty c}$	ωp_s (cm^{-1})	ωp_c (cm^{-1})	τ_s	τ_c	$\frac{\gamma_s}{\omega \tau_s}$	$\frac{\gamma_c}{\omega \tau_c}$	S_s	S_c
2	370	1.4	0.0	50000	850000	5.5e-9	2.0e-9	0.02	0.01	0.35	1.65
3	600	1.3	-0.2	210000	930000	5.0e-9	2.0e-9	0.05	0.01	0.70	0.40
4	850	1.1	-0.6	210000	930000	4.0e-9	2.0e-9	0.01	0.03	0.80	0.05
5	690	1.3	-0.5	250000	1010000	4.0e-9	2.0e-9	0.02	0.03	1.00	0.0
6	800	1.4	-0.9	210000	1050000	3.5e-9	2.0e-9	0.03	0.01	0.80	0.0
7	860	1.5	-0.9	290000	1090000	4.0e-9	2.0e-9	0.06	0.02	0.95	0.0
8	860	1.6	-1.0	290000	1050000	4.0e-9	2.0e-9	0.03	0.03	1.10	0.0
9	770	1.9	2.4	330000	10000	3.5e-9	5.0e-9	0.06	0.01	0.65	0.3
10	350	1.7	-0.7	10000	2970000	0.5e-9	10.5e-9	0.15	0.09	0.55	0.0
11	1770	1.4	-0.2	250000	610000	5.5e-9	2.0e-9	0.01	0.01	0.95	0.80
17	1940	1.3	0.2	370000	53000	3.5e-9	2.0e-9	0.21	0.01	0.35	0.25
18	2000	1.4	0.2	330000	530000	3.5e-9	2.0e-9	0.21	0.01	0.4	0.25

Table 6: Summary of the samples vibrational obtained by fitting the measured infrared reflectivity spectra to Eq. 10.11.

- $\varepsilon_{\infty s(c)}$ is the high-frequency dielectric constant in perpendicular to the palne of incidence (along the c-axis);
- $\omega p_{s(c)}$ is the plasma frequencies perpendicular to the plane of incidence (along the c-axis)
- $\tau_{s(c)}$ is the free-electrons relaxation time perpendicular to the plane of incidence (along the c-axis)
- $\gamma_{s(c)}$ is the phonon damping factor perpendicular to the plane of incidence (along the c-axis)
- $S_{s(c)}$ is the oscillator strength perpendicular to the plane of incidence (along the c-axis).

The in-plane and cross-plane dielectric constants and plasma frequencies obtained by fitting the reflectivity spectra to the theoretical model for the reflectivity of a two-layer system are shown in Fig 109 and the high quality of the spectra fitting is shown in Apendix D.

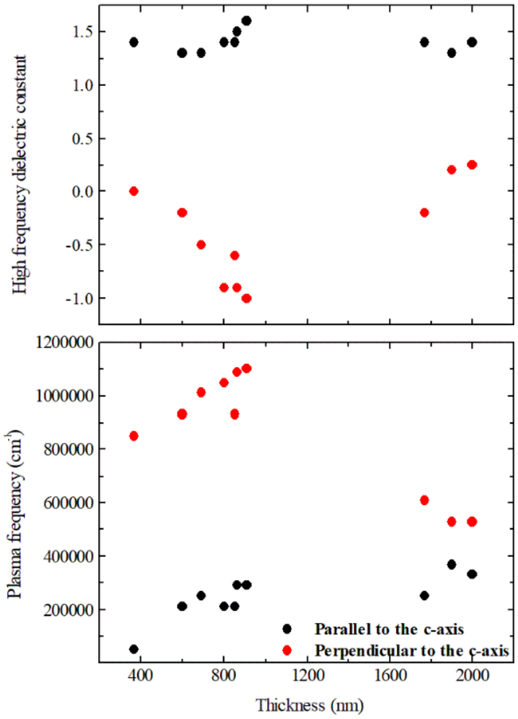

Figure 109: in-plane and cross-plane high-frequency dielectric constants and plasma frequencies as a function of the film thickness

It is very interesting to note that the in-plane and cross-plane dielectric constants show opposite signs and a ratio that depends on the film thickness. Furthermore, the in-plane and cross-plane plasma frequencies of the developed films appear to follow the same trend as the high-frequency dielectric constants, reinforcing the hypothesis that the columnar nature of the ZnO grains causes high optical anisotopy in the film with dielectric behavior in one direction and metallic behavior in another. As the high-frequency dielectric constant determines the response of the material from the edge of the phonons resonnace band (the Reststrahlen band) to infinity, these results demonstrate that polaritons in thin ZnO films deposited on gless are hyperbolic over a wide spectral range, and the ratio of the in-plane to cross-plane dielectric constant is controllable through the film thickness. Therefore, we believe that coating the class with ZnO films would allow controlling the direction of propagation of solar infrared radiation and help reduce the heat absorbed by the vehicle interior.

F. Summary:

In this chapter, we presented the characterization techniques we employed in this thesis to examine the structural and optical characteristics of ZnO films grown on glass and to examine the signs and anisotropy of the dielectric constants. By fitting the measured infrared reflectivity spectra to a theoretical model for reflectivity, we demonstrated that ZnO thin films on glass are hyperbolic materials over a broad infrared spectrum from the edge of the phonon resonance band to infinity. We have also shown that the ratio of the in-plane dielectric constant to the cross-plane dielectric constant can be controlled by the film thickness.

CHAPTER XI

CONCLUSION AND FUTURE ROADMAPS

This thesis investigated the infrared optical properties of thin ZnO films deposited on glass. The manuscript begins by a chapter presenting James Maxwell's electromagnetic theory, describing the interaction of the electromagnetic wave with materials, particularly polar crystals such as zinc oxide. The derivation of the characteristics of a material by examining its interaction with electromagnetic radiation is also presented in this chapter. The next chapter introduces the Drude and Lorentz models. The theory is expanded to be applied to multilayer materials by employing the T-matrix approach, which extracts the optical characteristics of the end layers by a recursive method starting from the first layer. The Kramers-Kronig theory, which serves to extrcat imaginary quantities from the real ones is also presented in this chapter.

The next chapters discusses the propertes of the material investigated in this thesis and presented the deposition technique used as well as many characterization techniques we employed to probe important characteristics of the material investigated .

The last chapter summarizes the results obtained in this thesis. It reveales that the in-plane and ocross--plane dielectric constants of zinc oxide exhibit opposing signs throughout a large range of the infrared region of the electromagnetic spectrum. In this chapter, we demonstrate that ZnO thin films on glass are hyperbolic materials over a broad infrared spectrum from the edge of the phonon resonance band to infinity. We also show that the ratio of the in-plane dielectric constant to the cross-plane dielectric constant can be controlled by the film thickness. As a future research studies or works, we consider the following possible roadmaps

- Investigation of the optical characteristics of a comparable zinc oxide filmsmaterial produced on different substrates and using different deposition processes. Thus, examining the influence of deposition and its parameters approaches on optical characteristics.
- According to the literature, dopants improve some of the optical characteristics of the materials while also disclosing new features. To that purpose, one possibility is to investigate the alteration in optical characteristics of zinc oxide by doping it, maybe with Al or Ga.

The results of this thesis reveal a prospective use of hyperbolic metamaterials in general, and our samples in particular, in safety and thermal management applications (as reported in Ref [176]). However, they still need to undergo vehicle testing and address essential modifications before they can be transitioned or adopted at the industrial level. That said, this thesis has also demonstrated a new type of application for hyperbolic metamaterials, providing a new avenue in exploring the characteristics of metamaterials and their applications.

APPENDIX A

The Bragg condition and crystal properties were defined in the Fourier space or the Reciprocal space, which is defined as the space accompanying the ordinary space in which the crystal is represented in real life, and is translated to by the Fourier transform, hence the name Fourier space or the Reciprocal Space. Thus the primitive lattice vectors (a, b, c) of the real space are related to the reciprocal lattice vectors by the following expressions [9,118]

$$a^* = 2\pi \frac{b \times c}{a.(b \times c)}$$

$$b^* = 2\pi \frac{c \times a}{a.(b \times c)} \qquad \text{Eq. (A.1)}$$

$$c^* = 2\pi \frac{a \times b}{a.(b \times c)}$$

where a, b, and c are the lattice vector in the ordinary space and a*, b* are and c* is the reciprocal lattice vectors, with $a.(b \times c)$ representing the volume of the unit cell in the ordinary space and $V = \frac{2\pi}{a.(b\times c)}$ representing the volume of the reciprocal unit cell. Thus one can realize that in ordinary space the vector has a dimension of length whereas in the reciprocal space a vector has a dimension $(\text{length})^{-1}$. [9, 118]

As defined previously, G represents a reciprocal lattice vector having components satisfying equation (15), to that end the equation of (hkl) planes must satisfy the following expressions:

$$d_{hkl} = r.n = \frac{r.G}{|G|} = \frac{2\pi}{|G|} \text{ [118]} \qquad \text{Eq. (A.2)}$$

where |G| is the magnitude of the reciprocal lattice vector G = Δk with the following Laue conditions:

$$\begin{aligned} a.\Delta k &= 2\pi h \\ b.\Delta k &= 2\pi k \\ b.\Delta k &= 2\pi l \end{aligned} \qquad \text{Eq. (A.3)}$$

where h, k, and l are the miller indces. [9, 118]

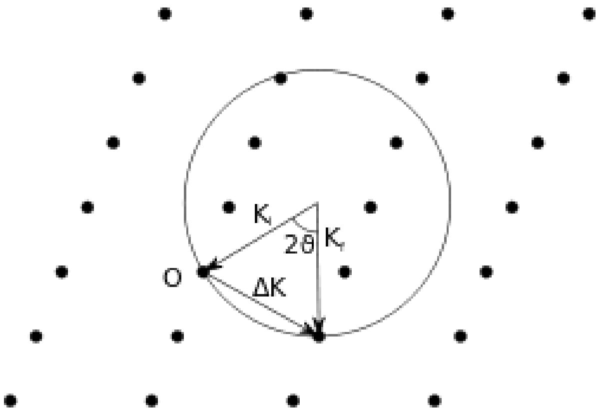

Figure 110: Sketch showing the Ewald construction used to interpret vectors for diffraction [9, 96, 118-120]

“ The Brillouin zone is defined as the smallest volume enclosed by the planes that are perpendicular bisectors to the reciprocal lattice vectors ” [9]. They are essential components in the analysis of any crystalline property and can be defined or represented by Wigner-Seitz primitive cell within the reciprocal space, as shown in the figures below. [9, 118]

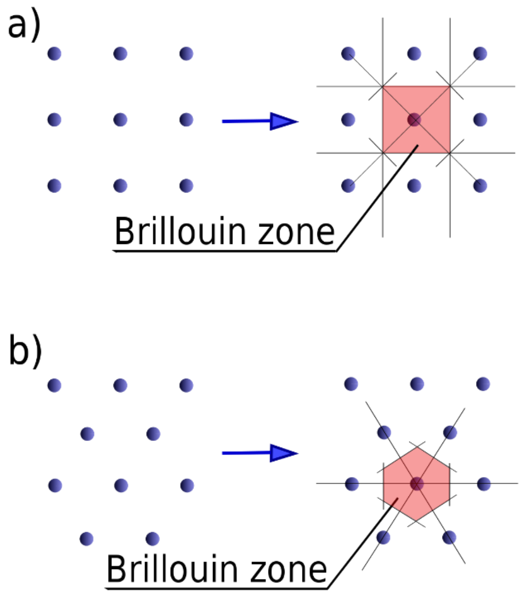

Figure 111: Sketch showing Brillouin zones within different crystalline arrangements [9, 210]

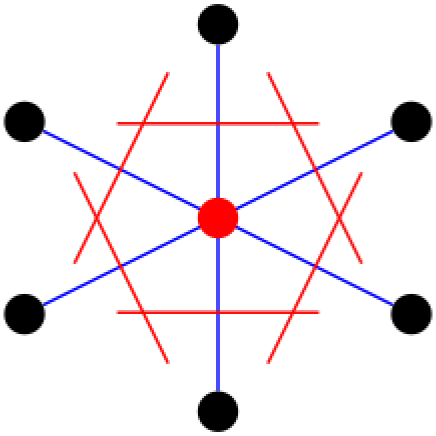

Figure 112: Sketch elaborating Wigner-Seitz primitive cell construction [9, 209]

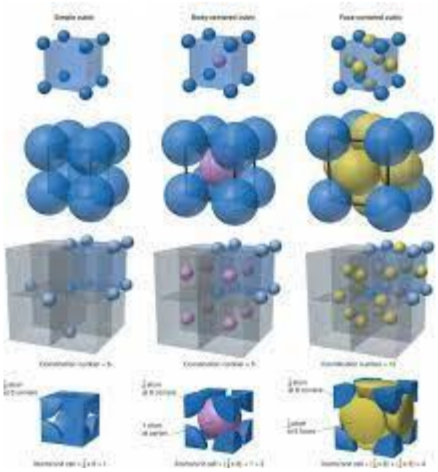

Figure 113: Sketch representing the different crystalline structures [9, 211]

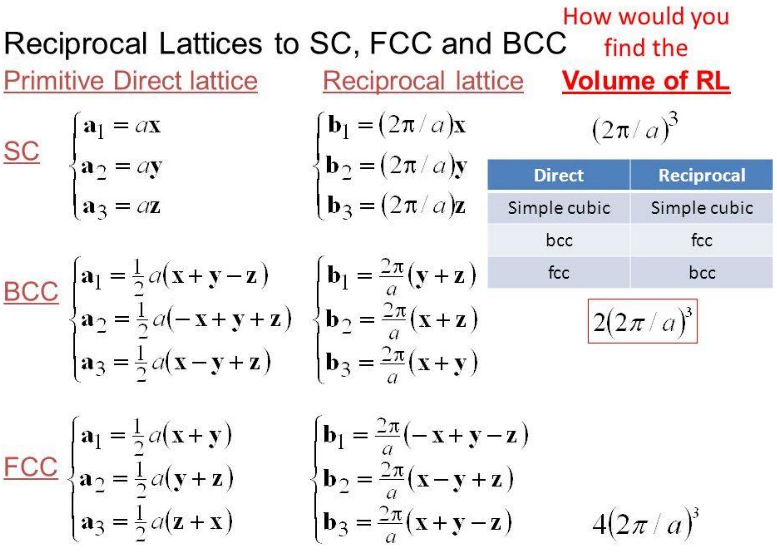

Reciprocal Lattices to SC, FCC and BCC

How would you find the **Volume of RL**

Primitive Direct lattice — Reciprocal lattice

SC

$$\begin{cases}\mathbf{a}_1 = a\mathbf{x}\\ \mathbf{a}_2 = a\mathbf{y}\\ \mathbf{a}_3 = a\mathbf{z}\end{cases} \qquad \begin{cases}\mathbf{b}_1 = (2\pi/a)\mathbf{x}\\ \mathbf{b}_2 = (2\pi/a)\mathbf{y}\\ \mathbf{b}_3 = (2\pi/a)\mathbf{z}\end{cases} \qquad (2\pi/a)^3$$

Direct	Reciprocal
Simple cubic	Simple cubic
bcc	fcc
fcc	bcc

BCC

$$\begin{cases}\mathbf{a}_1 = \frac{1}{2}a(\mathbf{x}+\mathbf{y}-\mathbf{z})\\ \mathbf{a}_2 = \frac{1}{2}a(-\mathbf{x}+\mathbf{y}+\mathbf{z})\\ \mathbf{a}_3 = \frac{1}{2}a(\mathbf{x}-\mathbf{y}+\mathbf{z})\end{cases} \qquad \begin{cases}\mathbf{b}_1 = \frac{2\pi}{a}(\mathbf{y}+\mathbf{z})\\ \mathbf{b}_2 = \frac{2\pi}{a}(\mathbf{x}+\mathbf{z})\\ \mathbf{b}_3 = \frac{2\pi}{a}(\mathbf{x}+\mathbf{y})\end{cases} \qquad \boxed{2(2\pi/a)^3}$$

FCC

$$\begin{cases}\mathbf{a}_1 = \frac{1}{2}a(\mathbf{x}+\mathbf{y})\\ \mathbf{a}_2 = \frac{1}{2}a(\mathbf{y}+\mathbf{z})\\ \mathbf{a}_3 = \frac{1}{2}a(\mathbf{z}+\mathbf{x})\end{cases} \qquad \begin{cases}\mathbf{b}_1 = \frac{2\pi}{a}(-\mathbf{x}+\mathbf{y}-\mathbf{z})\\ \mathbf{b}_2 = \frac{2\pi}{a}(\mathbf{x}-\mathbf{y}+\mathbf{z})\\ \mathbf{b}_3 = \frac{2\pi}{a}(\mathbf{x}+\mathbf{y}-\mathbf{z})\end{cases} \qquad 4(2\pi/a)^3$$

Figure 114: figure showing the primitive lattice vectors and their transformation within the reciprocal space for different crystal structures [9]

APPENDIX B

The general properties of Fourier Transform:

(Refer for this Appendix to Refs[151-155])

Shift theorem: for the Fourier transform and its inverse:

$$H1(s) = \int_{-\infty}^{\infty} h(t \mp t_o) e^{-i2\pi st} dt = e^{\pm i2\pi st_o} \int_{-\infty}^{\infty} h(t) e^{-i2\pi st} dt$$

$$= e^{\pm i2\pi st_o} H(s) \qquad \text{Eq. (B.1)}$$

$$h1(t) = \int_{-\infty}^{\infty} H(s \mp s_o) e^{i2\pi st} ds = e^{\mp i2\pi ts_o} \int_{-\infty}^{\infty} H(s) e^{i2\pi st} ds$$

$$= e^{\mp i2\pi ts_o} h(t) \qquad \text{Eq. (B.2)}$$

Similarity/Scaling Theorem: for the Fourier Transform and its inverse:

$$H1(s) = \int_{-\infty}^{\infty} h(at) e^{-i2\pi sat} dt = \frac{1}{a} \int_{-\infty}^{\infty} h(t) e^{-i2\pi st} dt = \frac{1}{a} H(s) \qquad \text{Eq. (B.3)}$$

where a is a constant such that $a \neq 0$

Similarly, we have:

$$h1(t) = \int_{-\infty}^{\infty} H(as)e^{i2\pi ast}ds = \frac{1}{a}\int_{-\infty}^{\infty} H(s)e^{i2\pi st}ds = \frac{1}{a}h(t) \qquad \text{Eq. (B.4)}$$

Cosine/Sine relations: in this section, we will introduce the Fourier transform when a function is mutilated or contains any trigonometric function. We will limit ourselves for cosine but the theory remains valid for any other trigonometric relations. Sometimes this relationship is referred to as a modulation theorem or property of Fourier transform and its inverse. It is expressed as:

$$H1(s) = \int_{-\infty}^{\infty} h(t)cos(2\pi ts_o)e^{-i2\pi st}dt = \int_{-\infty}^{\infty} h(t)\left(\frac{e^{i2\pi ts_o} + e^{-i2\pi ts_o}}{2}\right)e^{-i2\pi st}dt$$

$$= \frac{1}{2}(H(s+s_o) + H(s-s_o))$$

$$h1(t) = \int_{-\infty}^{\infty} H(s)\cos(2\pi st_o)\, e^{i2\pi st}ds = \int_{-\infty}^{\infty} H(s)\left(\frac{e^{i2\pi st_o} + e^{-i2\pi st_o}}{2}\right)e^{i2\pi st}ds$$

$$= \frac{1}{2}\big(h(t+t_o)\ + h(t-t_o)\big)$$

Convolution relation: the convolution relation of two functions f(x) and g(x) is defined by:

$$f(x) * g(x) = \int_{-\infty}^{\infty} f(u)g(x-u)\, du \qquad \text{Eq. (B.5)}$$

The Fourier transform of a convolution function is defined by :

$$\int_{-\infty}^{\infty} f(t) * g(t)e^{-i2\pi st}\, dt = F(s)G(s) \qquad \text{Eq. (B.6)}$$

where F(s) and G(s) are the Fourier transform of f(t) and g(t) respectively [151-155]

Similarly.

$$\int_{-\infty}^{\infty} F(s) * G(s)e^{i2\pi st}\, ds = f(t)g(t) \qquad \text{Eq. (B.7)}$$

Product relation: let h(t) be the product of two functions f(t) and g(t), the Fourier transform and its inverse of h(t) and H(s) are expressed:

$$H(s) = \int_{-\infty}^{\infty} h(t)e^{-i2\pi st} dt = \int_{-\infty}^{\infty} f(t)g(t)e^{-i2\pi st} dt = F(s) * G(s) \qquad \text{Eq. (B.8)}$$

$$h(t) = \int_{-\infty}^{\infty} H(s)e^{i2\pi st} ds = \int_{-\infty}^{\infty} F(s)G(s)e^{i2\pi st} ds = f(t) * g(t)$$

linearity relation: let h(t) be the sum of two functions f(t) and g(t), the Fourier transform and its inverse of h(t) and H(s) are expressed as:

$$\begin{aligned} H(s) &= \int_{-\infty}^{\infty} h(t)e^{-i2\pi st} dt = \int_{-\infty}^{\infty} (f(t) + g(t))e^{-i2\pi st} dt \\ &= F(s) + G(s) \end{aligned} \qquad \text{Eq. (B.10)}$$

$$h(t) = \int_{-\infty}^{\infty} H(s)e^{i2\pi st}ds = \int_{-\infty}^{\infty} (F(s)+G(s))e^{i2\pi st}ds = f(t) + g(t)$$ Eq. (B.11)

Complex functions: let z(t) be a function defined by z(t) = f(t) +ig(t), where f(t) and g(t) are real and imaginary parts of z(t) respectively. The fourier transform of z(t) is given by:

$$H(s) = \int_{-\infty}^{\infty} z(t)e^{-i2\pi st}dt = \int_{-\infty}^{\infty} (f(t) + ig(t))e^{-i2\pi st}dt = F(s) + iG(s)$$

$$= Re\big(H(s)\big) + i\, Im(H(s))$$

where Re(H(s)) and Im(H(s)) are the real and imaginary parts of H(s) defined by; Re(H(s))=F(s) and Im(H(s))= G(s). This relation holds for the inverse fourier transform.

An interesting relation of fourier transform for an even and odd function are summarized in the following equations:

$$F(s) = \int_{-\infty}^{\infty} f(t)e^{-i2\pi st}dt = \int_{0}^{\infty} f(t)\cos(2\pi st)dt = Re(s)$$ Eq. (B.12)

where f(t) is an even function and:

$$G(s) = \int_{-\infty}^{\infty} g(t)e^{-i2\pi st}dt = i\int_{0}^{\infty} g(t)\sin(2\pi st)dt = iIm(s)$$ Eq. (B.13)

with g being an odd function. The above equations hold for inverse Fourier transform. Moreover, it states that the Fourier transform of an even and odd function is real and imaginary respectively.

The above complex relation gives power relation of a Fourier transform:

Let f(t), f(s) and g(t) and G(s) be Fourier transformed pairs, the power relation is stated by:

$$\int_{-\infty}^{\infty} h(t)g^{*}(t)dt = \int_{-\infty}^{\infty} H(s)G^{*}(s)ds \qquad \text{Eq. (B.14)}$$

where * in the above equation is the complex conjugation of g(t).

Parseval’s Theorem: the Parvesal’s theorem is derived from equation (43), and it simply states that the area under the curve h(t) is the same as the area under the Fourier transformed curves, which implies that the Fourier transform does not change or alter the area covered by any given function. Parseval’s theorem is given by:

$$\int_{-\infty}^{\infty} |h(t)|^{2}\, dt = \int_{-\infty}^{\infty} |H(s)|^{2}\, ds \qquad \text{Eq. (B.15)}$$

Correlation relation: just like convolution relation, the correlation theory is defined by;

Let f(t) and g(t) be two functions, the correlation or cross-correlation relation is given by:

$$f(t) \circledast g(t) = \int_{-\infty}^{\infty} f^{*}(u-t)g(u)du = \int_{-\infty}^{\infty} f^{*}(u)g(u+t)du \qquad \text{Eq. (B.16)}$$

where * is the complex conjugation, as similar relation holds for the Fourier transformed functions:

$$F(s) \circledast G(s) = \int_{-\infty}^{\infty} F^*(v) G(v + s) dv \qquad \text{Eq. (B.17)}$$

On the other hand, the Fourier transform of the correlation relation is:

$$F\{f(t) \circledast g(t)\} = \int_{-\infty}^{\infty} \int_{-\infty}^{\infty} f^*(u) g(u + t) e^{-i2\pi st} du\, dt = F(s) G^*(s) \qquad \text{Eq. (B.18)}$$

A special case of the correlation relation is where f(x) =g(x), this is sometimes named as autocorrelation relation, and the above equations reduce in this case to :

$$f(t) \circledast f(t) = \int_{-\infty}^{\infty} f^*(u - t) f(u) du = \int_{-\infty}^{\infty} f^*(u) f(u + t) du$$

$$F\{f(t) \circledast f(t)\} = \int_{-\infty}^{\infty} \int_{-\infty}^{\infty} f^*(u) g(u + t) e^{-i2\pi st} du\, dt = F(s) F^*(s) = |F(s)|^2$$

$$F(s) \circledast F(s) = \int_{-\infty}^{\infty} F^*(v) F(v + s) dv$$

Derivative and integral Theorems: the Fourier transform like any function can be differentiated and integrated. These properties of the Fourier transform are given by the equations B.19 below. Note that we presented here the result The derivation of these properties are found elsewhere [151-155].

$$\frac{d^k}{dt^k} f(t) = \int_{-\infty}^{\infty} H(s)\, e^{i2\pi st}\, (i2\pi s)^k\, ds \qquad \text{Eq. (B.19)}$$

$$\ldots.. \iiint F(s) ds = \int_{-\infty}^{\infty} h(t)\, e^{-i2\pi st}\, \frac{1}{(i2\pi t)^k}\, dt \qquad \text{Eq. (B.20)}$$

Here the derivative and integration are applied k times.

APPENDIX C

Details for this Appendix, can be found in Refs [151-155]

The Boxcar Function:

$$\Pi(t) = \{ \begin{matrix} 1 & if\ |t| \leq T \\ 0 & if\ \ |t| > T \end{matrix} \qquad \text{Eq. (C.1)}$$

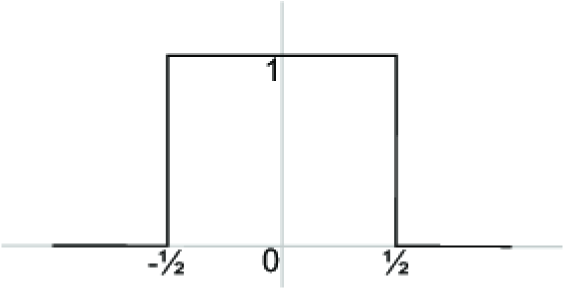

Figure 115: figure showing the plot of Boxcar rectangular function with period T=1.

The Fourier transform of this function is:

$$F(\Pi) = \int_{-\infty}^{\infty} \Pi(\mathrm{t}) e^{-i2\pi f t} dt = 2T \frac{sin(2\pi f T)}{2\pi f T} = 2T sinc(2\pi f T) \qquad \text{Eq. (C.2)}$$

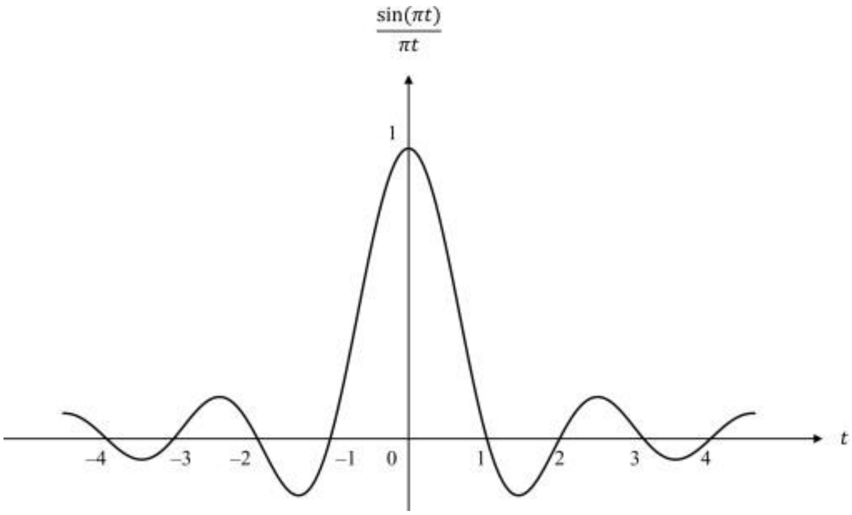

Figure 116: figure showing the plot of sinc(x) Fourier transform of Π (x)

The triangular function is defined as:

$$\Lambda = \begin{cases} 1 - \frac{L}{|x|} & if\ |x| \leq L \\ 0 & if\ |x| > L \end{cases} \qquad \text{Eq. (C.3)}$$

The Fourier transform of the triangular function is:

$$F(\Lambda) = \int_{-\infty}^{\infty} \Lambda(\mathrm{t}) e^{-i2\pi f t} dt = T sinc^2(\pi f T) \qquad \text{Eq. (C.4)}$$

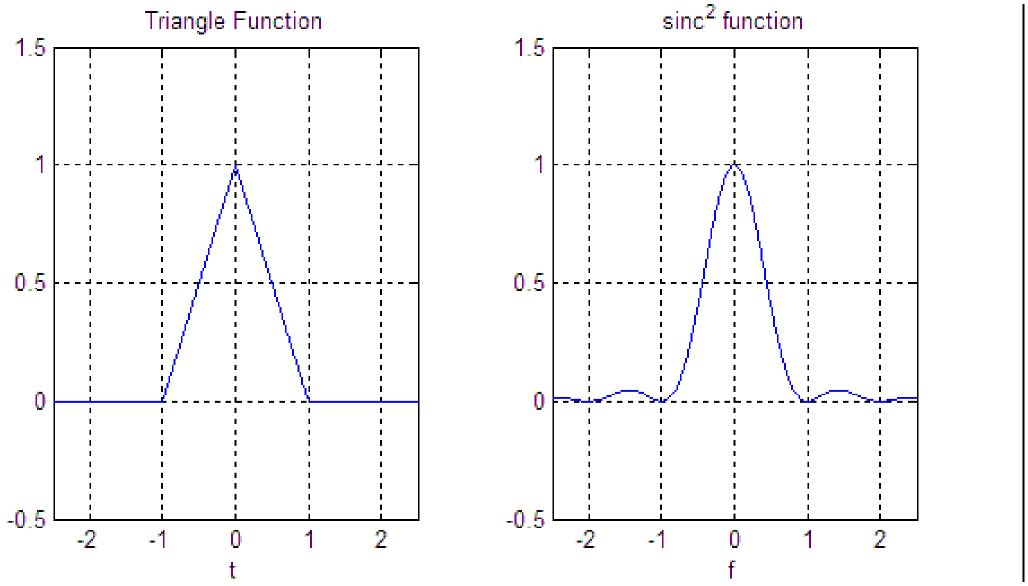

Figure 117: figure showing the plot of triangular (with period L=1) and its Fourier transform

Heaviside unit function is defined by:

$$H(x) = \{ \begin{matrix} 1 & if\ x \geq 0 \\ 0 & otherwise \end{matrix} \qquad \text{Eq. (C.5)}$$

and its Fourier transform:

$$F(\mathrm{H}) = \int_{-\infty}^{\infty} \mathrm{H(t)} e^{-i2\pi f t} dt = \frac{1}{2\pi f i} \qquad \text{Eq. (C.6)}$$

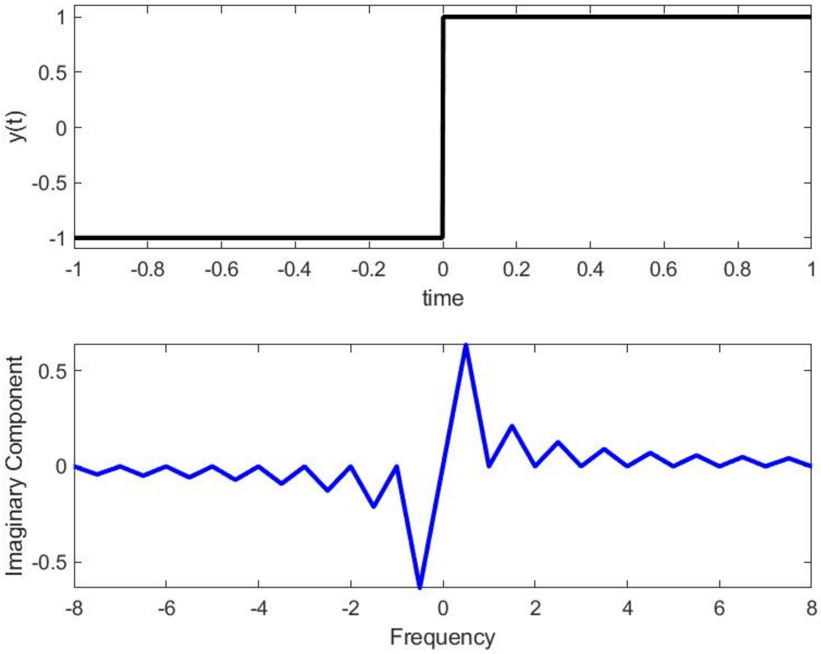

Figure 118: figure showing the plot of Heaviside Unit Step Function and its Fourier transform

Sign function defined by:

$$sgn(x) = \begin{cases} 1 & if\ x > 0 \\ -1 & if\ x < 0 \end{cases} \qquad \text{Eq. (C.7)}$$

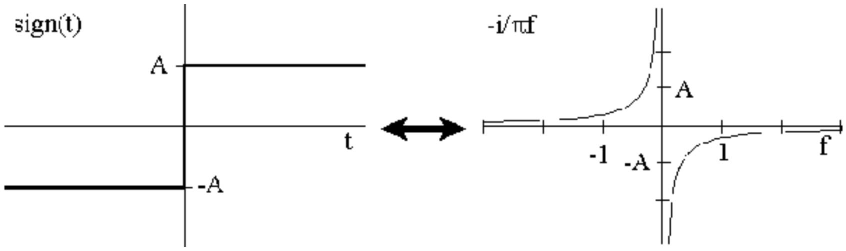

Figure 119: figure showing the plot of Sgn (x) and its Fourier transform

Dirac delta function defined by:

$$\delta(x) = \begin{cases} \infty & if\ x = 0 \\ 0 & otherwise \end{cases} \qquad \text{Eq. (C.8)}$$

with $\int_{-\infty}^{\infty} \delta(x)dx = 1$

Figure 120: figure showing the plot of Dirac delta function (a) and its Fourier transform (b)

Shah Function defined as:

$$\text{ш}\,(x) = \sum_{n=-\infty}^{\infty} \delta(x-n) \qquad \text{Eq. (C.9)}$$

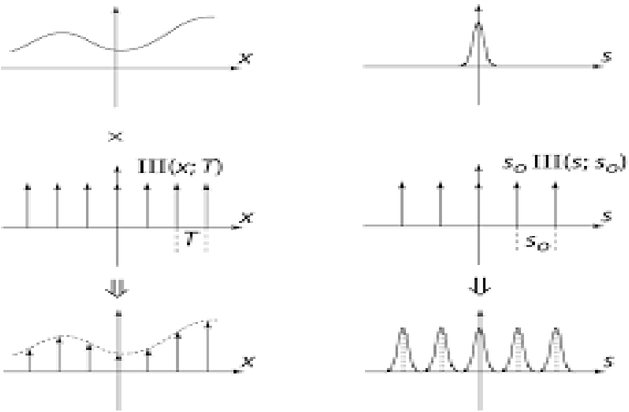

Figure 121: figure showing the plot of Shah function and its Fourier transform along with its effect when acted on a function

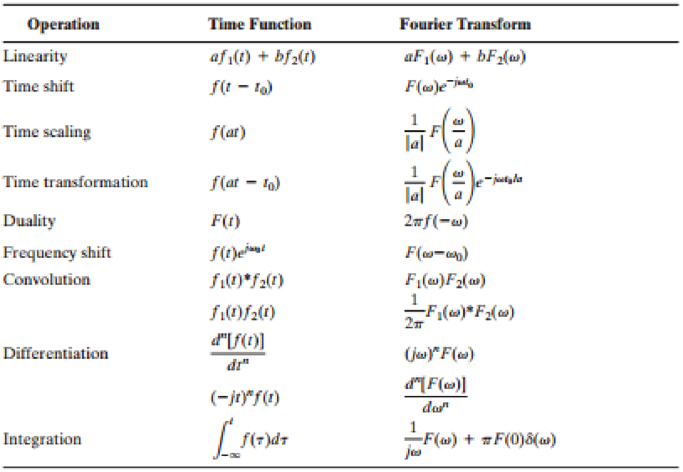

Operation	Time Function	Fourier Transform
Linearity	$af_1(t) + bf_2(t)$	$aF_1(\omega) + bF_2(\omega)$
Time shift	$f(t - t_0)$	$F(\omega)e^{-j\omega t_0}$
Time scaling	$f(at)$	$\frac{1}{\lvert a\rvert} F\left(\frac{\omega}{a}\right)$
Time transformation	$f(at - t_0)$	$\frac{1}{\lvert a\rvert} F\left(\frac{\omega}{a}\right)e^{-j\omega t_0/a}$
Duality	$F(t)$	$2\pi f(-\omega)$
Frequency shift	$f(t)e^{j\omega_0 t}$	$F(\omega-\omega_0)$
Convolution	$f_1(t)*f_2(t)$	$F_1(\omega)F_2(\omega)$
	$f_1(t)f_2(t)$	$\frac{1}{2\pi}F_1(\omega)*F_2(\omega)$
Differentiation	$\frac{d^n[f(t)]}{dt^n}$	$(j\omega)^n F(\omega)$
	$(-jt)^n f(t)$	$\frac{d^n[F(\omega)]}{d\omega^n}$
Integration	$\int_{-\infty}^{t} f(\tau)d\tau$	$\frac{1}{j\omega}F(\omega) + \pi F(0)\delta(\omega)$

Figure 122: figure summarizing the properties of Fourier Transform [151, 155]

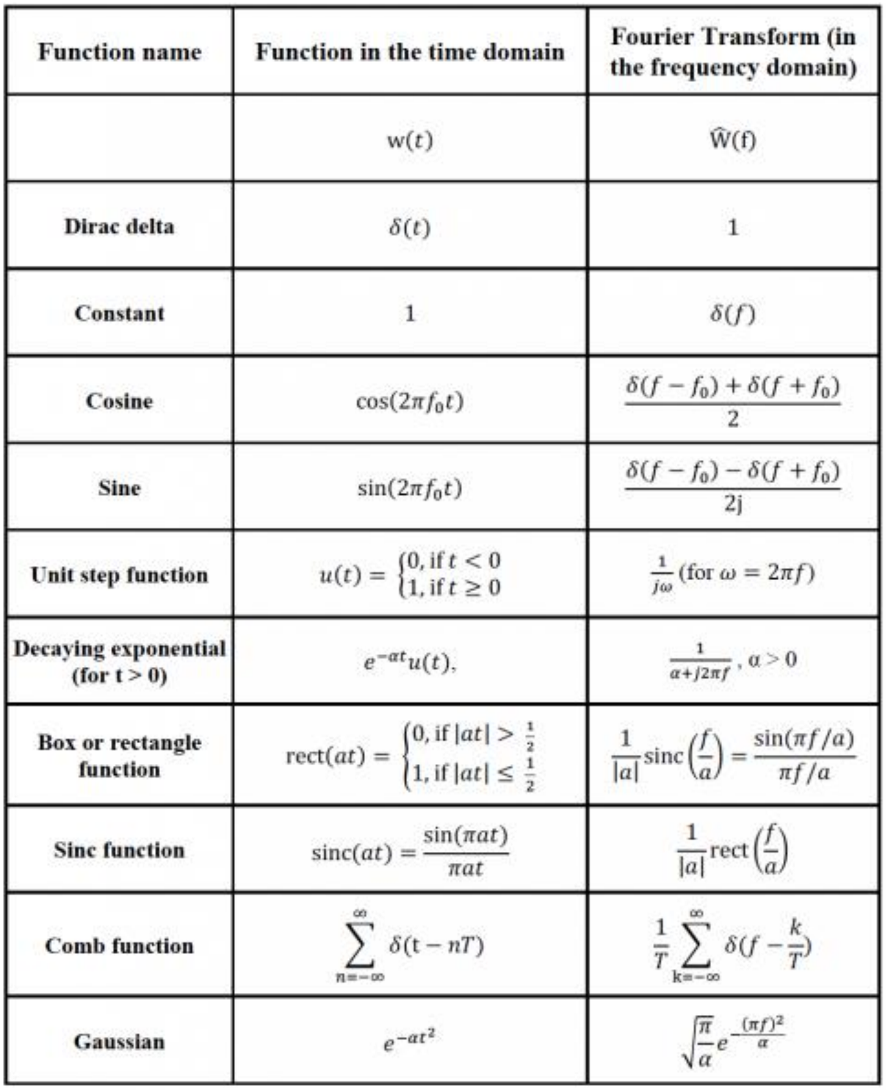

Function name	Function in the time domain	Fourier Transform (in the frequency domain)
	$\mathrm{w}(t)$	$\widehat{\mathrm{W}}(\mathrm{f})$
Dirac delta	$\delta(t)$	1
Constant	1	$\delta(f)$
Cosine	$\cos(2\pi f_0 t)$	$\dfrac{\delta(f-f_0)+\delta(f+f_0)}{2}$
Sine	$\sin(2\pi f_0 t)$	$\dfrac{\delta(f-f_0)-\delta(f+f_0)}{2\mathrm{j}}$
Unit step function	$u(t) = \begin{cases} 0, \text{if } t < 0 \\ 1, \text{if } t \geq 0 \end{cases}$	$\frac{1}{j\omega}$ (for $\omega = 2\pi f$)
Decaying exponential (for t > 0)	$e^{-\alpha t}u(t),$	$\frac{1}{\alpha+j2\pi f}$, $\alpha > 0$
Box or rectangle function	$\operatorname{rect}(at) = \begin{cases} 0, \text{if } \lvert at\rvert > \frac{1}{2} \\ 1, \text{if } \lvert at\rvert \leq \frac{1}{2} \end{cases}$	$\dfrac{1}{\lvert a\rvert}\operatorname{sinc}\left(\dfrac{f}{a}\right) = \dfrac{\sin(\pi f/a)}{\pi f/a}$
Sinc function	$\operatorname{sinc}(at) = \dfrac{\sin(\pi at)}{\pi at}$	$\dfrac{1}{\lvert a\rvert}\operatorname{rect}\left(\dfrac{f}{a}\right)$
Comb function	$\sum_{\mathrm{n}=-\infty}^{\infty} \delta(\mathrm{t}-nT)$	$\dfrac{1}{T}\sum_{\mathrm{k}=-\infty}^{\infty} \delta(f-\dfrac{k}{T})$
Gaussian	$e^{-\alpha t^2}$	$\sqrt{\dfrac{\pi}{\alpha}}e^{-\frac{(\pi f)^2}{\alpha}}$

Figure 123: figure summarizing the most sampling functions and their Fourier Transforms [151, 155]

APPENDIX D

In this appendix, we show the infrared reflectivity spectra from the samples ellaborated as well as their best fit to the model for infrared reflectivity detailed in the body of the manuscript.

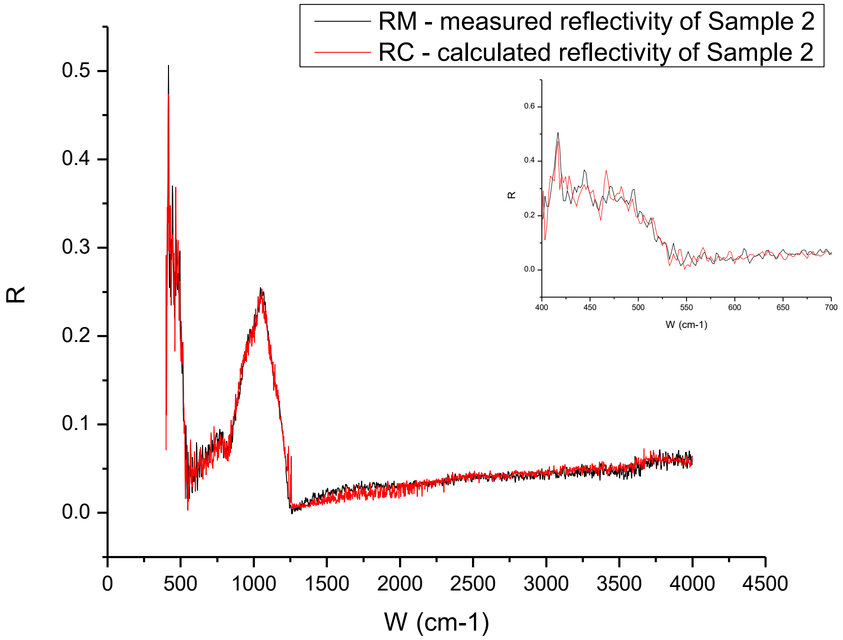

Figure 124: Measured and calculated IR reflectivity spectra from Sample 2. The inset shows the reflectivity band of the ZnO film.

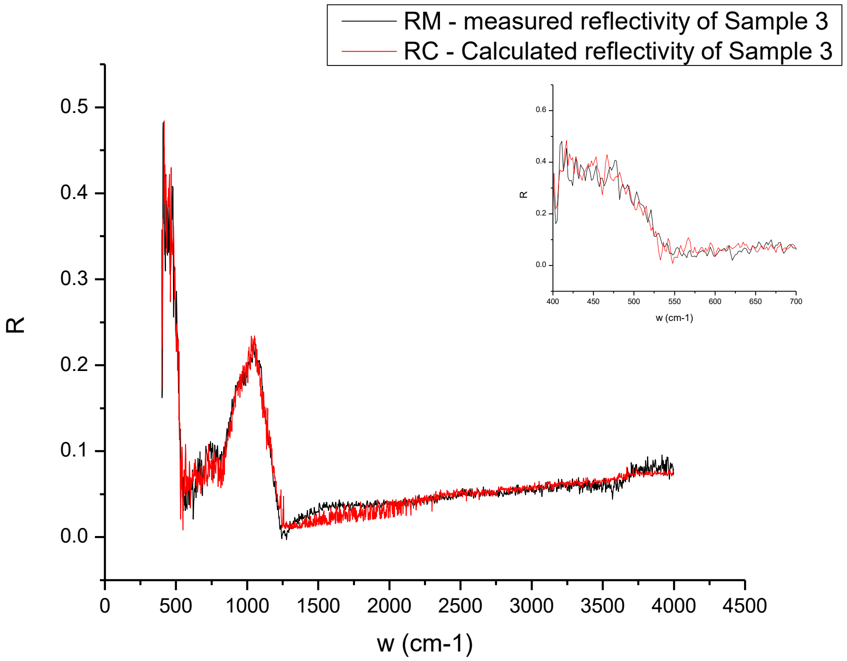

Figure 125: Measured and calculated IR reflectivity spectra from Sample 3. The inset shows the reflectivity band of the ZnO film.

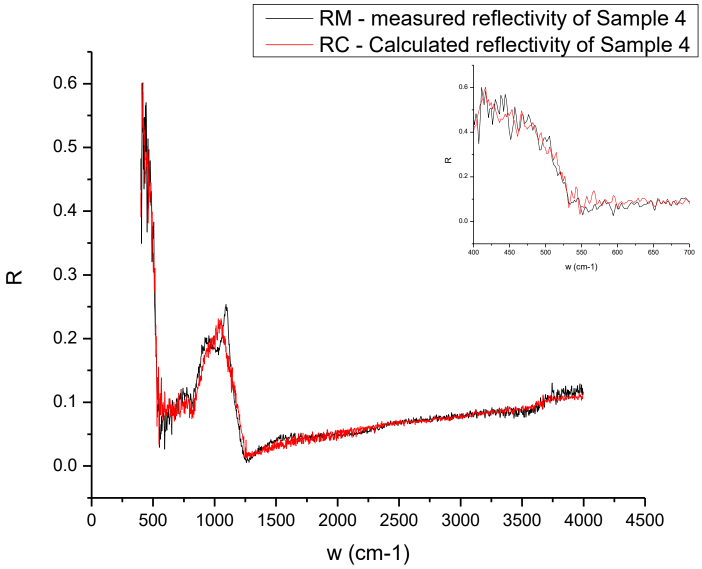

Figure 126: Measured and calculated IR reflectivity spectra from Sample 4. The inset shows the reflectivity band of the ZnO film.

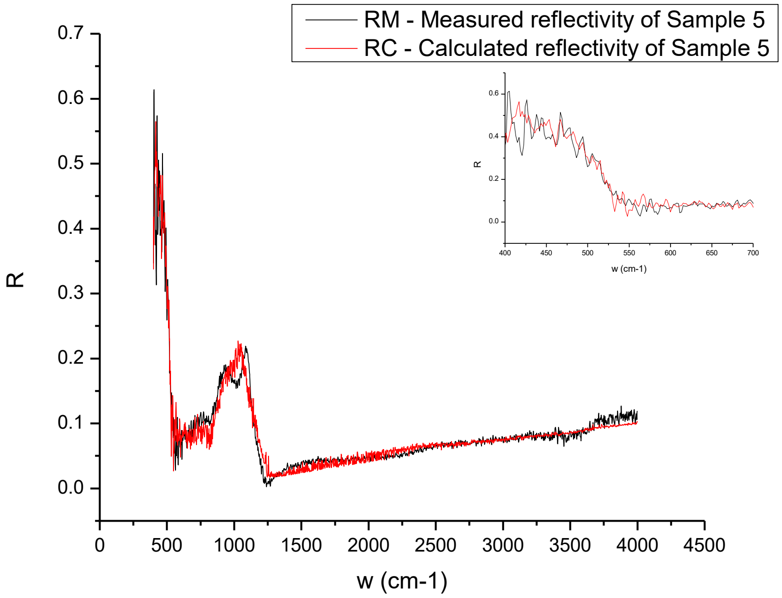

Figure 127: Measured and calculated IR reflectivity spectra from Sample 5. The inset shows the reflectivity band of the ZnO film.

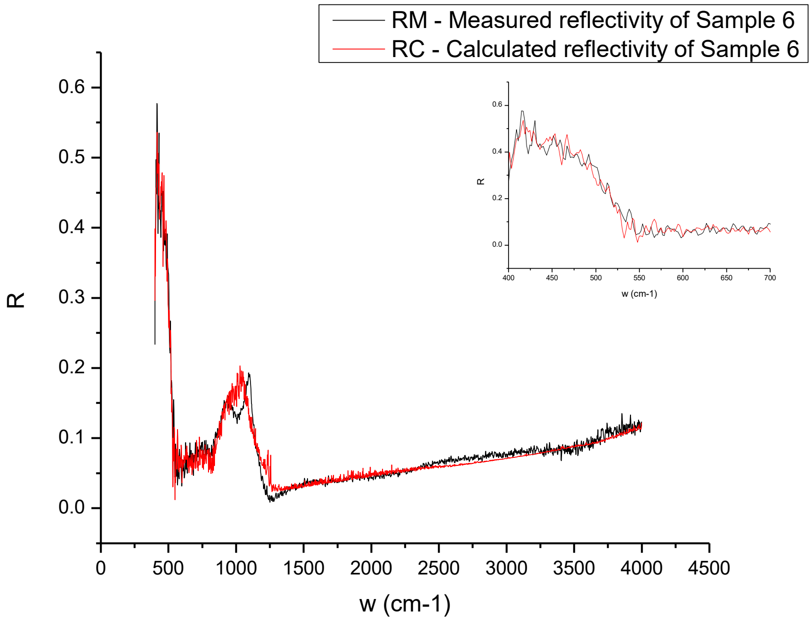

Figure 128: Measured and calculated IR reflectivity spectra from Sample 6. The inset shows the reflectivity band of the ZnO film.

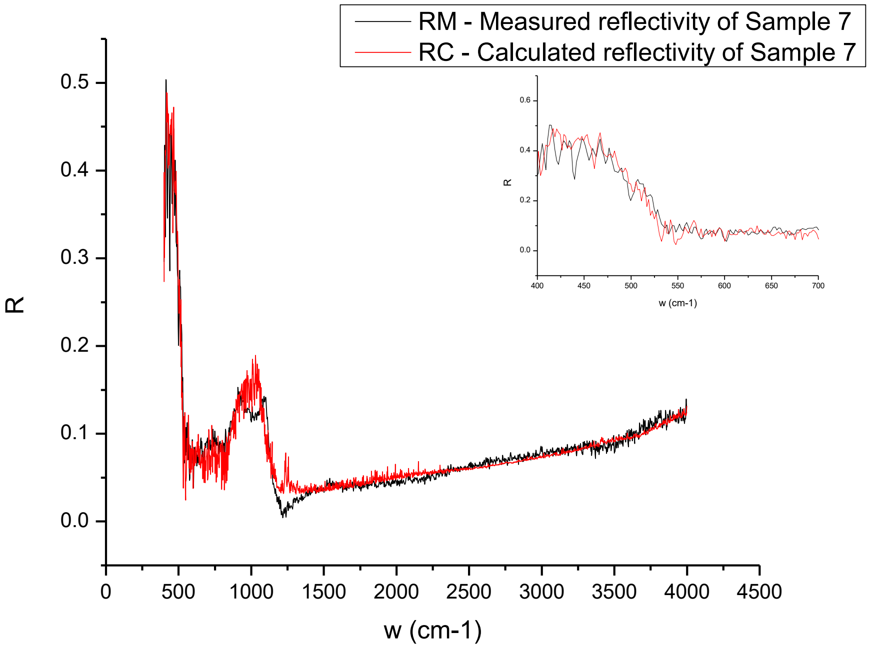

Figure 129: Measured and calculated IR reflectivity spectra from Sample 7. The inset shows the reflectivity band of the ZnO film.

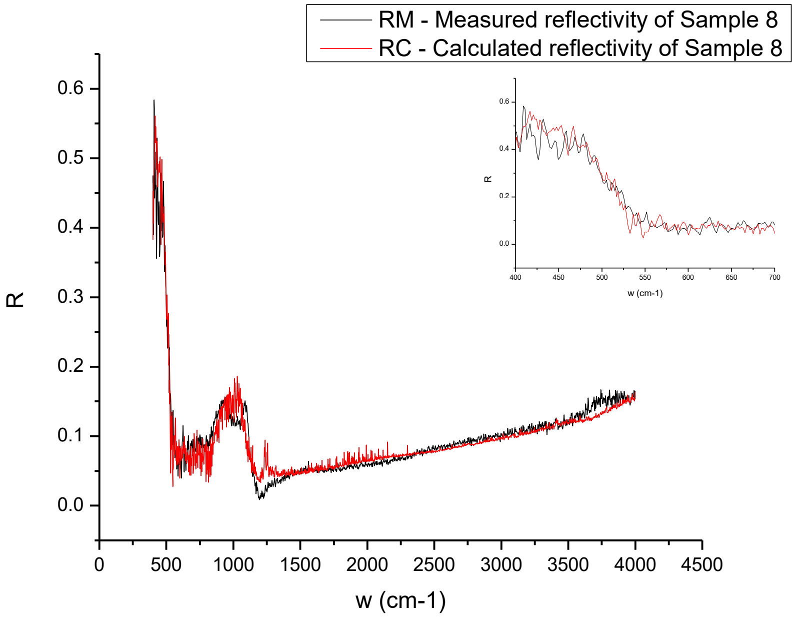

Figure 130: Measured and calculated IR reflectivity spectra from Sample 8. The inset shows the reflectivity band of the ZnO film.

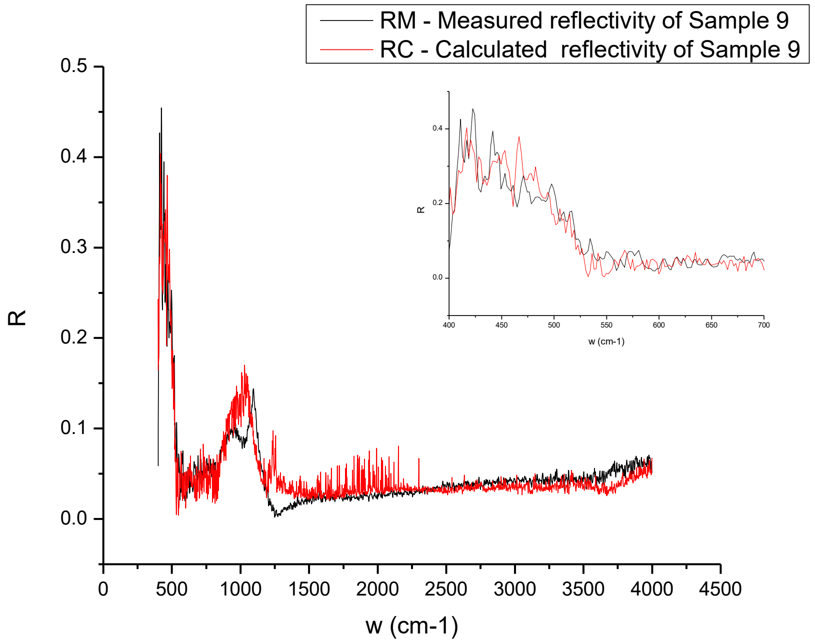

Figure 131: Measured and calculated IR reflectivity spectra from Sample 9. The inset shows the reflectivity band of the ZnO film.

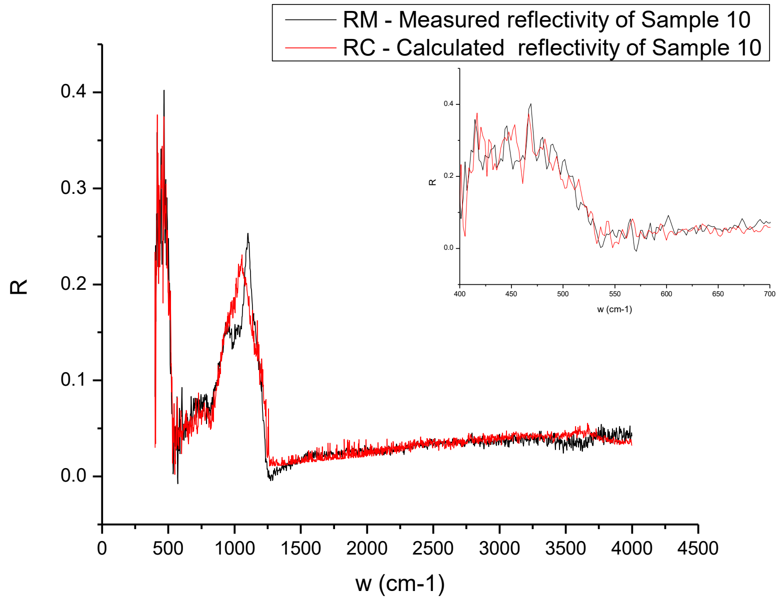

Figure 132: Measured and calculated IR reflectivity spectra from Sample 10. The inset shows the reflectivity band of the ZnO film.

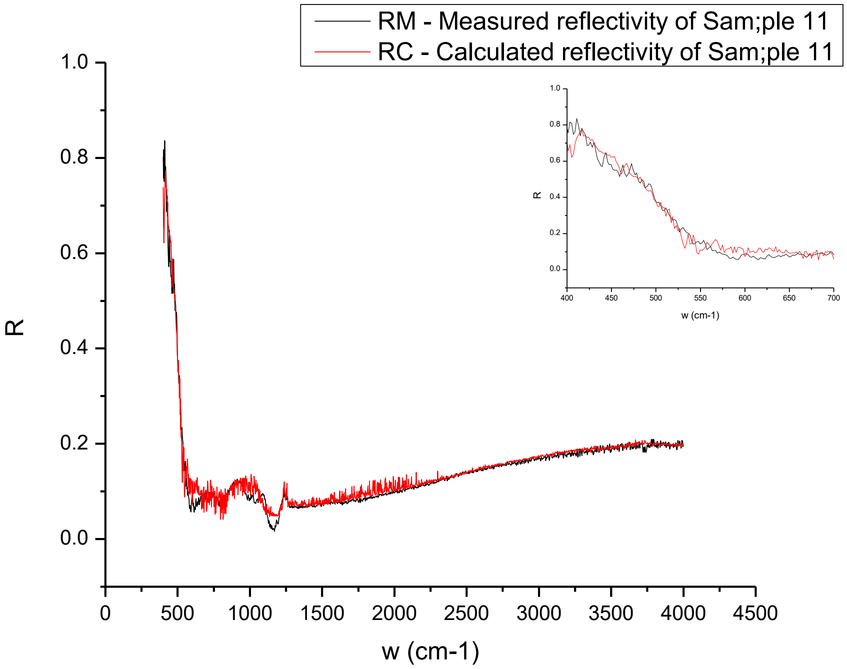

Figure 133: Measured and calculated IR reflectivity spectra from Sample 11. The inset shows the reflectivity band of the ZnO film.

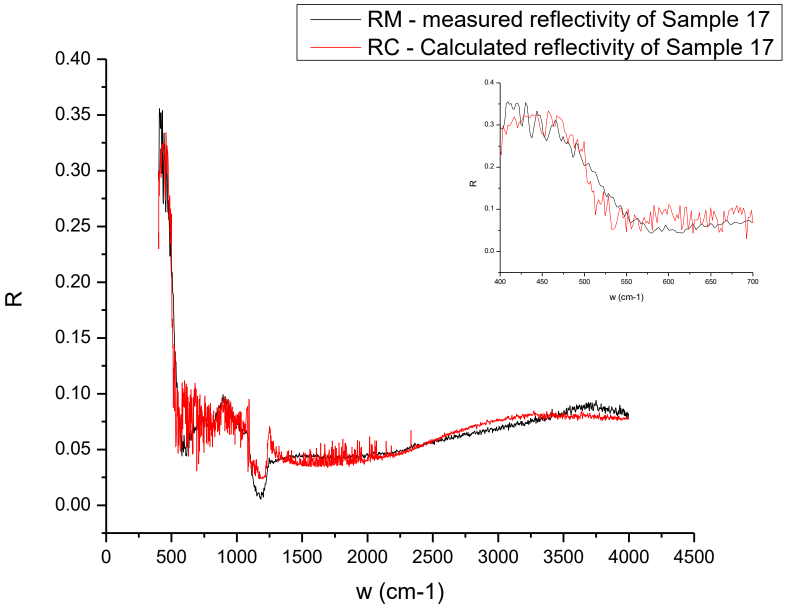

Figure 134: Measured and calculated IR reflectivity spectra from Sample 17. The inset shows the reflectivity band of the ZnO film.

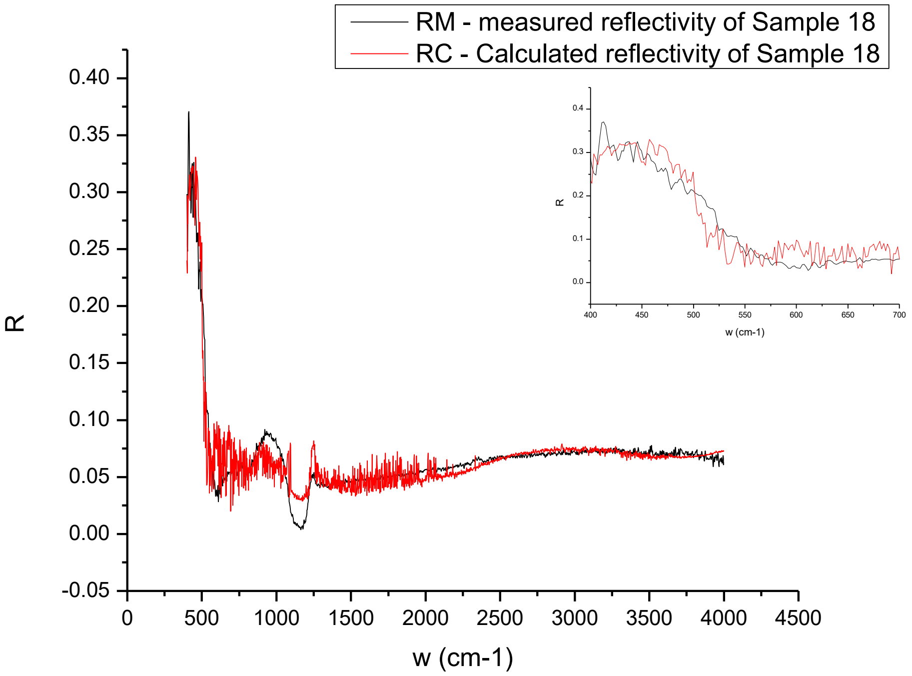

Figure 135: Measured and calculated IR reflectivity spectra from Sample 18. The inset shows the reflectivity band of the ZnO film.

REFERENCES

[1]- Zhang, Z. M. (2007). Nano/Microscale Heat Transfer. The McGraw-Hill Companies.

[2]- Tong, Z., & Liu, H. (2020, July 08). Modeling in-vehicle VOCS distribution from CABIN interior Surfaces under solar radiation. Retrieved April 17, 2021, from https://www.mdpi.com/2071-1050/12/14/5526/htm

[3]- Morkoç, H., & Özgür, U. (2009). Zinc oxide: Fundamentals, materials and device technology. Weinheim: Wiley-VCH Verlag GmbH & KGaA.

[4]- Wu, X., Lee, J., Varshney, V., Wohlwend, J., Roy, A., & Luo, T. (2016, March 01). Thermal conductivity of Wurtzite zinc-oxide from First-Principles Lattice dynamics - a comparative study with gallium nitride. Retrieved, from https://ui.adsabs.harvard.edu/abs/2016NatSR...622504W/abstract

[5] - Heavens, O. S. (1991). Optical properties of thin solid films. New York: Dover.

[6]- Shenzel, O., & Ohlidal, M. (2018). Optical characterization of thin solid films (Vol. 64). SPRINGER.

[7]- Locharoenrat, K. (2016). Optical properties of solids: An introductory textbook. Singapore: Pan Stanford Publishing.

[8] - Fox, M. (2010). Optical properties of solids (Second Ed.). Oxford England: Oxford University Press.

[9] – Kittel, C. (2005). Introduction to Solid State Physics (eighth Ed.). John Wiley & Sons.

[10] - Bansal, N. P., & Doremus, R. H. (1986). Handbook of glass properties. Orlando, Florida: Academic Press.

[11] - Bach, H., Dr., & Neuroth, N., Dr. (1998). The Properties of Optical Glass. Berlin Heidelberg: Springer-Verlag.

[12] - Perkowitz, S. (1994). Optical characterization of semiconductors: Infrared, Raman, and photoluminescence spectroscopy. Acad. Press.

[13] - Davies, J. H. (1998). The physics of low-dimensional semiconductors: An introduction. Cambridge: Cambridge Univ. Press.

[14] - Shamseddine, M. O. (2012). Optical Analysis of Boron Nitride thin films. American University of Beirut Department of Physics.

[15] - Dakik, M. Y. (September 2020). Method for Deriving the Complex Infrared Dielectric Function of Amorphous Thin Films from the Infrared Reflectivity Spectroscopy American University of Beirut.

[16] - Kaassamani, S. T. (2017). Highly crystallized zinc oxide thin films grown by pulsed laser deposition (Unpublished master's thesis). The American University of Beirut.

[17]- Pontoppidan, K., Fraser, H., Dartois, E., Thi, W., Van Dishoeck, E., Boogert, A. . . . Bisschop, S. (2003, July 04). A 3-5 Mu M Vlt Spectroscopic survey of embedded young low mass stars I - Structure of the CO ice. Retrieved from arXiv.org Astro-ph arXiv:Astro-ph/0307097v1

[18]- Oughstun, K., & Cartwright, N. (2003, June 30). On the Lorentz-Lorenz formula and the LORENTZ model of Dielectric dispersion. Retrieved from https://www.osapublishing.org/oe/abstract.cfm?uri=oe-11-13-1541

[19]- Nunes, F. D., Borges, B. V., & J., Weiner. (2012, July 2). Analysis of dispersive and dissipative media with optical resonances.

[20]- Buencuerpo, J., Munioz-Camuniez, L., Dotor, M., & Postigo, P. (2012, May 10). Optical absorption enhancement in a hybrid system photonic crystal–thin substrate for photovoltaic applications. Retrieved from https://www.osapublishing.org/oe/abstract.cfm?uri=oe-20-S4-A452

[21]- Callaway, and Joseph. "Model for Lattice Thermal Conductivity at Low Temperatures." NASA/ADS, ui.adsabs.harvard.edu/abs/1959PhRv..113.1046C/abstract.

[22]-Holland, M. G. "Analysis of Lattice Thermal Conductivity.

" NASA/ADS,ui.adsabs.harvard.edu/abs/1963PhRv..132.2461H/abstract.

[23]- Quigley, K. (May 3, 2018). Physical Amplification of Chemical Colorimetric Sensing and a Transfer Matrix Analysis (Unpublished master's thesis). Department of Physics Brown University.

[24] - Eason, R. W. (2007). Pulsed laser deposition of thin films: Applications-led growth of functional materials. Hoboken, NJ: Wiley.

[25] - Chrisey, D. B., & Hubler, G. K. (1994). Pulsed laser deposition of thin films. New York: Wiley.

[26] - Wang, Z. L. (2004). Zinc oxide nanostructures: growth, properties, and applications. Journal of Physics: Condensed Matter, 16(25). doi:10.1088/0953-8984/16/25/r01

[27] - Özgür, Ü, Hofstetter, D., & Morkoç, H. (2010). ZnO Devices and Applications: A Review of Current Status and Future Prospects. Proceedings of the IEEE, 98(7), 1255-1268. doi:10.1109/jproc.2010.2044550

[28] - Espitia, P. J. P., Soares, N. de F. F., Coimbra, J. S. dos R., de Andrade, N. J., Cruz, R. S., & Medeiros, E. A. A. (2012, February 22). Zinc oxide nanoparticles: Synthesis, antimicrobial activity, and food packaging applications. Food and Bioprocess

Technology. Retrieved November 6, 2021, from https://link.springer.com/article/10.1007/s11947-012-0797-6.

[29] - Natsume, Y., Sakata, H., Hirayama, T., & Yanagida, H. (1992). Low-temperature conductivity of ZnO films prepared by chemical vapor deposition. Journal of Applied Physics, 72(9), 4203-4207. doi:10.1063/1.352231

[30] - Sandana, V. E., Rogers, D. J., Teherani, F. H., Mcclintock, R., Bayram, C., Razeghi, M., . . . Falyouni, F. (2009). Comparison of ZnO nanostructures grown using pulsed laser deposition, metal-organic chemical vapor deposition, and physical vapor transport. Journal of Vacuum Science & Technology B: Microelectronics and Nanometer Structures, 27(3), 1678. doi:10.1116/1.3137990

[31] - Heo, Y. W., Norton, D. P., & Pearton, S. J. (2005). Origin of green luminescence in ZnO thin film grown by molecular-beam epitaxy. Journal of Applied Physics, 98(7), 073502. doi:10.1063/1.2064308

[32] - AGHGONBAD, M. A. R. Y. A. M. M. O. T. A. L. L. E. B. I., & SEDGHI, H. A. S. S. A. N. (2018, February). Spectroscopic ellipsometry studies on zinc oxide thin films deposited by sol-gel method with various precursor concentrations: Request PDF. ResearchGate. Retrieved from https://www.researchgate.net/publication/323151970_SPECTROSCOPIC_ELLIPSOMETRY_STUDIES_ON_ZINC_OXIDE_THIN_FILMS_DEPOSITED_BY_SOL-GEL_METHOD_WITH_VARIOUS_PRECURSOR_CONCENTRATIONS.

[33] - Aghgonbad, M. M., & Sedghi, H. (2018, April 12). Influence of annealing temperature on optical properties of zinc oxide thin films analyzed by spectroscopic ellipsometry method. Chinese Journal of Physics. Retrieved from https://www.sciencedirect.com/science/article/pii/S0577907318300856.

[34] - Das, S., Das, S. K., Chakraborty, S. R., & Deb, A. K. (2018, June 12). Investigation of Optical Properties of Zinc-Oxide Thin Films Deposited on Various Substrates: A Simulation Study. ResearchGate. Retrieved from https://www.researchgate.net/publication/325710766_Investigation_of_Optical_Properties_of_Zinc-Oxide_Thin_Films_Deposited_on_Various_Substrates_A_Simulation_Study.

[35] - Sharma, S., Periasamy , C., & Chakrabarti, P. (2015, November 10). Thickness dependent study of RF sputtered ZnO thin films ... ResearchGate. Retrieved from https://www.researchgate.net/publication/279837829_Thickness_Dependent_Study_of_RF_Sputtered_ZnO_Thin_Films_for_Optoelectronic_Device_Applications.

[36] - Khoshman, J. M., Manda, A. A., & Kordesch, M. E. (2015, February 19). Near-infrared optical constants and optical polarization properties of ZnO thin films. Thin Solid Films. Retrieved from https://www.sciencedirect.com/science/article/pii/S0040609015001546.

[37] - Dinh, N. N., Trung, T. Q., Binh, L. K., khoa, N. dang, & Thuan, V. T. M. (2015, February 24). Investigation of zinc oxide thin film by spectroscopic ... ResearchGate. Retrieved from https://www.researchgate.net/publication/268302607_Investigation_of_zinc_oxide_thin_film_by_spectroscopic_ellipsometry.

[38] - Hlaing Oo, W. M., Mccluskey, M. D., Huso, J., & Bergman, L. (2014, June 6). (PDF) infrared and Raman spectroscopy of ZnO nanoparticles ... ResearchGate. Retrieved from https://www.researchgate.net/publication/234891970_Infrared_and_Raman_spectroscopy_of_ZnO_nanoparticles_annealed_in_hydrogen.

[39] - Noei, H., Qiu, H., Wang, Y., Löffler, E., Wöll, C., & Muhler, M. (2014, May 23). (PDF) the identification of ZnO nanoparticles by infrared spectroscopy.

ResearchGate. Retrieved from https://www.researchgate.net/publication/23503113_The_identification_of_ZnO_nanoparticles_by_infrared_spectroscopy.

[40] - Mammadov, E., Naghavi, N., Jehl, Z., Renou, G., Tiwald, T., Mamedov, N., Lincot, D., & Guillemoles, J.-F. (2014, February 12). Dielectric function of zinc oxide thin films in a broad spectral range. Thin Solid Films. Retrieved from https://www.sciencedirect.com/science/article/pii/S0040609014001370.

[41] – Liu, Y. C., Hsieh, J. H., & Tung, S. K. (2006, March 3). Extraction of optical constants of zinc oxide thin films by ellipsometry with various models. Thin Solid Films. Retrieved from https://www.sciencedirect.com/science/article/pii/S0040609006001775.

[42] - Bundesmann, C., Ashkenov, N., Schubert, M., Rahm, A., Wenckstern, H., Kaidashev, E. M., Lorenz, M., & Grundmann, M. (2004, February 12). Infrared dielectric functions and crystal orientation of A-plane ZnO thin films on R-plane sapphire determined by generalized ellipsometry. Thin Solid Films. Retrieved from https://www.sciencedirect.com/science/article/pii/S0040609003018285.

[43] - Ashkenov, N., Mbenkum, B. N., Bundesmann, C., Riede, V., Lorenz, M., Spemann, D., Kaidashev, E. M., Kasic, A., Schubert, M., Grundmann, M., Wagner, G., Neumann, H., Darakchieva, V., Arwin, H., & Monemar, B. (2003, January 1). Infrared dielectric functions and phonon modes of high-quality ZnO films. AIP Publishing. Retrieved from https://aip.scitation.org/doi/10.1063/1.1526935.

[44] -Valerini, D., Caricato, A. P., Lomascolo, M., Romano, F., Taurino, A., Tunno, T., & Martino, M. (2008). Zinc oxide nanostructures grown by pulsed laser deposition. Applied Physics A, 93(3), 729-733. Doi: 10.1007/s00339-008-4703-z

[45]- Zhu, B. L., Sun, X. H., Guo, S. S., Zhao, X. Z., Wu, J., Wu, R., & Liu, J. (2006). Effect of Thickness on the Structure and Properties of ZnO Thin Films Prepared by

Pulsed Laser Deposition. Japanese Journal of Applied Physics, 45(10A), 7860-7865. doi:10.1143/jjap.45.7860

[46]- Ohshima, T., Thareja, R., Ikegami, T., & Ebihara, K. (2003). Preparation of ZnO thin films on various substrates by pulsed laser deposition. Surface and Coatings Technology, 169-170, 517-520. Doi: 10.1016/s0257-8972(03)00164-6

[47] - Jang, Y. R., Yoo, K.-H., & Park, S. M. (2010, December 23). Properties of ZnO thin films grown on si (100) substrates by pulsed laser deposition. Journal of Materials Science & Technology. Retrieved from https://www.sciencedirect.com/science/article/pii/S1005030210601582.

[48]- Mosca, M., Macaluso, R., Calì, C., Butté, R., Nicolay, S., Feltin, E. . . . Grandjean, N. (2013, May 16). Optical, structural, and morphological characterization of epitaxial ZnO films grown by pulsed - laser deposition, from https://www.sciencedirect.com/science/article/pii/S0040609013008122

[49] - Millon, E., Perrière, J., Tricot, S., & Boulmer-Leborgne, C. (2008, May 12). Pulsed-laser deposition of ZnO and related COMPOUND thin films for optoelectronics, from https://www.spiedigitallibrary.org/conference-proceedings-of-spie/7005/1/Pulsed-laser-deposition-of-ZnO-and-related-compound-thin-films/10.1117/12.785499.full

[50] - Novotny, M., Cizek, J., Kuzel, R., Bulir, J., Lancok, J., Connolly, J. Brauer, G. (2012). Structural characterization of ZnO thin films grown on ..., from https://physics.mff.cuni.cz/kfnt/pas/files/publications/2012/papers/Novotny_J-Phys-D_45_225101_2012.pdf iop.org/JPhysD/45225101

[51] - Zhao, L., Lian, J., Liu, Y., & Jiang, Q. (2005, December 27). Structural and optical properties of ZnO thin films deposited on quartz glass BY pulsed laser deposition, from https://www.sciencedirect.com/science/article/pii/S0169433205016156

[52]- Zhu, B., Zhao, X., Su, F., Li, G., Wu, X., Wu, J., & Wu, R. (2010, February 04). Low-temperature Annealing effects on the structure and optical properties of ZnO films grown BY pulsed laser deposition from https://www.sciencedirect.com/science/article/abs/pii/S0042207X10000862

[53] - Zhao, J., Li, X., Bian, J., Yu, W., & Gao, X. (2004, December 30). Structural, optical and electrical properties of ZnO films grown BY pulsed laser deposition (PLD), from https://www.sciencedirect.com/science/article/pii/S0022024804019153

[54] - Yu, C. F., Sung, C. W., Chen, S. H., & Sun, S. J. (2009). Relationship between the photoluminescence and … from https://www.researchgate.net/publication/229323756_Relationship_between_the_photoluminescence_and_conductivity_of_undoped_ZnO_thin_films_grown_with_various oxygen pressures

[55] - Shan, F., Liu, G., Lee, W., Lee, G., Kim, I., Shin, B., & Kim, Y. (2005, February 09). Transparent conductive ZnO thin films on glass substrates deposited by pulsed laser deposition from https://www.sciencedirect.com/science/article/pii/S0022024805000369

[56]- Sankur, H., & Cheung, J. (1983, October 01). Highly oriented ZnO films grown by laser evaporation from https://avs.scitation.org/doi/abs/10.1116/1.572219

[57] - Li, P., Lewin, M., Kretinin, A. V., Caldwell, J. D., Novoselov, K. S., Taniguchi, T., Watanabe, K., Gaussmann, F., & Taubner, T. (2015, June 26). Hyperbolic phonon-polaritons in boron nitride for near-field optical imaging and focusing. Nature News. Retrieved from https://www.nature.com/articles/ncomms8507.

[58] - Shekhar, P., Atkinson, J., & Jacob, Z. (2014, June 11). Hyperbolic metamaterials: Fundamentals and applications - nano convergence. SpringerOpen. Retrieved from https://nanoconvergencejournal.springeropen.com/articles/10.1186/s40580-014-0014-6.

[59] - Poddubny, A., Iorsh, I., Belov, P., & Kivshar, Y. (2013, November 28). Hyperbolic metamaterials. Nature News. Retrieved from https://www.nature.com/articles/nphoton.2013.243.

[60] - Lavrov, E. V. (2009, September 2). Hydrogen in ZnO. Physica B: Condensed Matter. Retrieved from https://www.sciencedirect.com/science/article/pii/S0921452609010102.

[61] - Lavrov, E. V. (2010, February 15). Hydrogen in ZnO. Spie digital library. Retrieved November 6, 2021, from https://www.spiedigitallibrary.org/conference-proceedings-of-spie/7603/1/Hydrogen-in-ZnO/10.1117/12.846018.full?SSO=1.

[62] - Van de Walle, C. G. (2000, August 1). Hydrogen as a cause of doping in zinc oxide. ResearchGate. Retrieved, from https://www.researchgate.net/publication/12332596_Hydrogen_as_a_Cause_of_Doping_in_Zinc_Oxide.

[63] - Lavrov, E. V., Herklotz, F., & Weber, J. (2009, April 28). Identification of hydrogen molecules in ZnO. ResearchGate. Retrieved from https://www.researchgate.net/publication/26285008_Identification_of_Hydrogen_Molecules_in_ZnO.

[64] - Drmosh, Q., Rao, S., Yamani, Z., & Gondal, M. (2013, January 02). Crystalline nanostructured Cu doped ZnO thin films grown at room temperature by pulsed laser deposition technique and their characterization from https://www.sciencedirect.com/science/article/pii/S016943321202291X

[65]- Zhang, Y., Lu, J., Ye, Z., He, H., Zhu, L., Zhao, B., & Wang, L. (2007, August 10). Effects of growth temperature on Li–n dual-doped p-type ZnO thin films prepared BY pulsed laser deposition from https://www.sciencedirect.com/science/article/pii/S0169433207011749

[66] - Kaur, G., Mitra, A., & Yadav, K. L. (2015, February 21). Pulsed laser deposited AL-DOPED ZnO thin films for optical application from https://www.researchgate.net/publication/272625105_Pulsed_laser_deposited_Al-doped_ZnO_thin_films_for_optical_applications

[67]- Shan, F., & Yu, Y. (2003, April 26). Optical properties of pure and Al DOPED ZnO thin films fabricated with PLASMA produced by excimer laser from https://www.sciencedirect.com/science/article/pii/S0040609003003432

[68]- Li, Z., Chen, Z., Huang, W., Chang, S., & Ma, X. (2011). The transparency comparison of Ga- and Al-doped ZnO thin films. Applied Surface Science, 257(20), 8486-8489. doi:10.1016/j.apsusc.2011.04.138

[69]- Sofiani, Z., Sahraoui, B., Addou, M., Adhiri, R., Lamrani, M., Dghoughi, L. . . . Bala, W. (2007, March 15). Third harmonic generation in Undoped and X DOPED ZnO Films (X: Ce, F, Er, Al, Sn) deposited by SPRAY PYROLYSIS, from https://aip.scitation.org/doi/full/10.1063/1.2711143

[70]- Cao, L., Zhu, L., Jiang, J., Zhao, R., Ye, Z., & Zhao, B. (2010, December 08). Highly transparent and conducting fluorine-doped ZnO thin films prepared by pulsed laser deposition, from https://www.sciencedirect.com/science/article/pii/S0927024810006550

[71]- Shao, J., Dong, W., Li, D., Tao, R., Deng, Z., Wang, T. . . . Fang, X. (2010, May 01). Metal-semiconductor transition in nb-doped ZnO thin films prepared by pulsed laser deposition, from https://www.sciencedirect.com/science/article/pii/S0040609010006012

[72] - Lin, J., Zhang, Y., Ye, Z., Gu, X., Pan, X., Yang, Y., . . . Zhao, B. (2009). Nb-doped ZnO transparent conducting films fabricated by pulsed laser deposition. Applied Surface Science, 255(13-14), 6460-6463. DOI: 10.1016/j.apsusc.2009.01.002

[73] - Ngom, B., Mpahane, T., Manyala, N., Nemraoui, O., Buttner, U., Kana, J. . . . Beye, A. (2008, November 14). Structural and optical properties of nano-structured tungsten-doped ZnO thin films grown by pulsed laser deposition, from https://www.sciencedirect.com/science/article/pii/S0169433208022721

[74]- Zhao, S., Zhou, Y., Zhao, K., Liu, Z., Han, P., Wang, S. . . . Yang, G. (2006, January 09). Violet luminescence emitted from Ag-nanocluster doped ZnO thin films grown on fused quartz substrates by pulsed laser deposition, from https://www.sciencedirect.com/science/article/pii/S0921452605013335

[75] - Shan, F., Kim, B., Liu, G., Liu, Z., Sohn, J., Lee, W., . . . Yu, Y. (2004, May 01). Blueshift of near band edge emission in Mg DOPED ZnO thin films and aging, from https://aip.scitation.org/doi/10.1063/1.1690091

[76]- Kim, H., Horwitz, J., Kim, W., Mäkinen, A., Kafafi, Z., & Chrisey, D. (2002). Doped ZnO thin films as anode materials for organic light-emitting diodes. Thin Solid Films, 420-421, 539-543. Doi: 10.1016/s0040-6090(02)00836-2

[77] - Park, S., Ikegami, T., Ebihara, K., & Shin, P. (2006). Structure and properties of transparent conductive-doped ZnO films by pulsed laser deposition. Applied Surface Science, 253(3), 1522-1527. doi:10.1016/j.apsusc.2006.02.046

[78] - Alsaad, A. M., Ahmad, A. A., Al-Bataineh, Q. M., Bani-Salameh, A. A., Abdullah, H. S., Qattan, I. A., Albataineh, Z. M., & Telfah, A. D. (2020, April 8). Optical, structural, and crystal defects characterizations of dip synthesized (Fe-Ni) co-doped ZnO thin films. MDPI. Retrieved from https://www.mdpi.com/1996-1944/13/7/1737.

[79]- Francombe, M. H., & Vossen, J. L. (1995). Thin films: Advances in research and development. San Diego, CA: Academic Press.

[80]- Berakdar, J., & Kirschner, J. (2004). Correlation spectroscopy of surfaces, thin films, and nanostructures. Weinheim: Wiley-VCH.

[81]- Cao, Z. (2011). Thin-film Growth: Physics, materials science, and applications. Oxford: Woodhead Pub.

[82]- Chopra, K. L. (1985). Thin film phenomena. Malabar, FL: R.E. Krieger.

[83]- Oechsner, H., & Etzkorn, H. W. (1984). Thin Film and Depth Profile Analysis. Berlin: Heidelberg.

[84]- Wandelt, K. (2014). Surface and interface science. Weinheim: Wiley-VCH Verlag GmbH & KGaA.

[85]- Prasad, P. N. (2004). Growth and characterization of Nanomaterials, in Nanophotonics. Hoboken, NJ: Wiley.

[86]- Willmott, P. R., & Huber, J. R. (2000). Pulsed laser vaporization and deposition. Reviews of Modern Physics, 72(1), 315-328. doi:10.1103/revmodphys.72.315

[87] - UL-HAMID, A. N. W. A. R. (2019). Beginners' guide to scanning electron microscopy. SPRINGER.

[88] - Breton, B. C., Oatley, C., McMullan, D., & Smith, K. C. A. (2004). Sir Charles Oatley and the scanning electron Microscope: A tribute published to coincide with the centenary of the birth of Charles William Oatley O.B.E., f.r.s., 14 February 1904-11 March 1996. Elsevier, Academic Press.

[89] - Kazmiruk, V. (2012, March 9). Scanning electron microscopy. IntechOpen. https://www.intechopen.com/books/1505.

[90] - Pennycook, S. J., & Nellist, P. D. (2011). Scanning transmission electron microscopy - imaging and Analysis: Stephen J. Pennycook. Springer. https://www.springer.com/gp/book/9781441971999.

[91]- Goldstein, J. I., Michael, J. R., Scott, J. H. J., Newburry, D. E., Ritchie, N. W. M., & Joy, D. C. (2018). Scanning electron microscopy and x-ray microanalysis (Fourth Edition). SPRINGER-VERLAG NEW YORK.

[92] - Reimer, L. (2011). Scanning electron microscopy: Physics of image formation and microanalysis (Second Edition, Vol. Volume 45). Springer.

[93] - Goldstein, J. I., Newburry, D. E., Lyman, C. E., Lifshin, E., Echlin, P., Joy, D. C., Sawyer, L., & Michael, J. R. (2003). Scanning electron microscopy and x-ray microanalysis (Third Edition). Springer.

[94] - Brodusch, N., Demers, H., & Gauvin, R. (2018). Field emission scanning electron microscopy: New perspectives for materials characterization. Springer.

[95]- Schatten, H., & Pawley, J. B. (2008). Biological low-voltage scanning electron microscopy. Springer.

[96] - Prasad, P. N. (2004). Nanophotonics. John Wiley & Sons.

[97] - Michler, G. H. (2008). Electron microscopy of polymers. Springer.

[98] - Goldstein, J. I., Yakowitz, H., Everhart, T. E., Newbury, D. E., Lifshin, E., Colby, J. W., & Coleman, J. R. (1977). Practical scanning electron microscopy: electron and ion microprobe analysis. Plenum Press, New York.

[99] - McMullan, D. (2006, December 7). Scanning electron microscopy 1928–1965. Wiley Online Library. https://onlinelibrary.wiley.com/doi/abs/10.1002/sca.4950170309. (1995)

[100] - Pease, R. F. W., & Nixon, W. C. (1964, August 25). high resolution scanning electron microscopy. https://iopscience.iop.org/article/10.1088/0950-7671/42/2/305/pdf.

[101] - Hay, W. W., & Sandberg, P. A. (1967, October). The Scanning Electron Microscope, a Major Break-through for Micropaleontology. https://www.researchgate.net/publication/257246284_The_Scanning_Electron_Microscope_a_Major_Break-through_for_Micropaleontology.

[102] - Oatley, C. W. (1966, October). The scanning electron microscope. https://www.jstor.org/stable/43419587.

[103] - Zworykin, V. K. (1942, September). The scanning electron microscope. https://www.jstor.org/stable/24967890.

[104] - ADVANCED FE Applications COURSE. (n.d.). https://www.utoledo.edu/engineering/cmsc/pdfs/SEM%20Workshop%20presentation%201.pdf.

[105] - Ponce, A., Mejía-Rosales, S., & José-Yacamán, M. (2012, July). Scanning Transmission Electron Microscopy Methods for the Analysis of Nanoparticles (chapter 37). https://www.researchgate.net/profile/Sergio-Mejia-Rosales/publication/229082469_Scanning_Transmission_Electron_Microscopy_Methods_for_the_Analysis_of_Nanoparticles/links/58078a2d08ae07cbaa541e8a/Scanning-Transmission-Electron-Microscopy-Methods-for-the-Analysis-of-Nanoparticles.pdf.

[106]- Lu, Y., Zhang, X., & Li, H. (2018, January 22). (PDF) A Simplified focusing and astigmatism correction method for a scanning electron microscope. ResearchGate. https://www.researchgate.net/publication/322650174_A_simplified_focusing_and_astigmatism_correction_method_for_a_scanning_electron_microscope.

[107] - Ma, H., Mikmekova, S., Konvalina, I., Yin, X., Sun, F., Pinos , J., Vaskovicova, N., Prucha , L., Mullerova , I., Mikmekova , E. M., & Chen, D. (2021, April 3). (PDF) imaging Ferroelectric nanodomains in Strained BIFEO ... https://www.researchgate.net/publication/350595704_Imaging_Ferroelectric_Nanodo

mains_in_Strained_BiFeO_3_Nanoscale_Films_Using_Scanning_Low-Energy_Electron_Microscopy_Implications_for_Low-Power_Devices.

[108] - Sharma, S., Jaiswal, S., Duffy, B., & Jaiswal, A. K. (2019, March 19). Nanostructured materials for food applications: Spectroscopy, Microscopy, and physical properties. https://www.mdpi.com/2306-5354/6/1/26/pdf.

[109] - Montreux, M., Houdelier, F., Masseboeuf, A., & Hytch, M. J. (2011, January). Highly coherent electron gun with cold field emission from carbon nano-cone tips. ResearchGate. https://www.researchgate.net/publication/268367204_Highly_coherent_electron_gun_with_cold_field_emission_from_carbon_nano-cone_tips.

[110]- The scanning electron microscope: a small world of possibilities (poster). (n.d.). https://www.sciencemag.org/sites/default/files/custom-publishing/documents/SEM%20poster_front_0.pdf.

[111] - EVERHART, T. E., & Thornley, R. F. M. (1960, July). Wide-band detector for micro-microampere low-energy ... https://iopscience.iop.org/article/10.1088/0950-7671/37/7/307.

[112] - H., W. I. N. S. O. N. C., BRICENO, MARTHA, OZKAYA, DOGAN, & KUO. (2014, May). (Pdf) characterization of catalysts using secondary and Backscattered Electron In-lens Detectors. https://www.researchgate.net/publication/266970280_Characterisation_of_Catalysts_Using_Secondary_and_Backscattered_Electron_In-lens_Detectors.

[113] - Joy, D. C., & Frost, B. G. (2001, March 28). Scanning electron microscopy: Present capability, future improvements, and potential replacements. AIP Publishing. https://aip.scitation.org/doi/abs/10.1063/1.1354456.

[114] - Walock, M., Nouveau, C., Stanishevsky, A. V., Martin, N., Imhoff, L., Mark L., Catledge, S. A., & Vohra, Y. K. (2012). Nanocomposite coatings based on quaternary metal nitrogen (thesis). HAL, Paris.

[115] - Oxford Instruments Analytical Halifax Road High Wycombe HP12 3SE, UK. (2006). INCA energy dispersive X-ray spectrometer Operator Manual. (from American University of Beirut – CRSL lab manuals – PDF)

[116] - Brno: TESCAN, Czech Republic . (2011/2013). user manual for MIRA 3 series scanning electron microscope. (from American University of Beirut – CRSL lab manuals – PDF)

[117] - Sui , T., Korsunsky, A. M., Ying, S., & Landini, G. (2015, April 11). (Pdf) x-ray study of human dental tissues affected by Erythroblastosis Fetalis ... ResearchGate. https://www.researchgate.net/publication/274713390_X-ray_Study_of_Human_Dental_Tissues_Affected_by_Erythroblastosis_Fetalis.

[118] - Blakemore, J. S. (1988). Solid-state physics (Second). Univ. Pr

[119] - Omar, M. A. (2008). Elementary solid state physics: Principles and applications. Addison Wesley publishing company. (chapter 2: X-Ray, Neutron, and Electron Diffraction In Crystals)

[120]- Birkholz, M., Fewster, P. F., & Genzel, C. (2006). Thin-film analysis by X-ray scattering. WILEY-VCH.

[121] - Sciaini, G. (2019, April 4). (PDF) recent advances in ultrafast structural techniques. ResearchGate. https://www.researchgate.net/publication/332215023_Recent_Advances_in_Ultrafast_Structural_Techniques.

[122] - Chen, Y., Morris, M. F., Obradovic, B., Wang, G., Li, D., Tasch, A. F., & Swinnea, J. S. (2000, May 2). The impact of crystal cut error on the measured impurity ... ResearchGate. https://www.researchgate.net/profile/Yang-Chen-45/publication/3283803_The_impact_of_crystal_cut_error_on_the_measured_impurity_profiles_resulting_from_ion_implantation/links/561bf85008aea80367243505/The-impact-of-crystal-cut-error-on-the-measured-impurity-profiles-resulting-from-ion-implantation.pdf.

[123] - Kärtner, F. X., Ahr, F., Calendron, A.-L., Çankaya, H., Carbajo, S., Chang, G., Cirmi, G., Dörner, K., Dorda, U., Fallahi, A., Hartin, A., Hemmer, M., Hobbs, R., Hua, Y., Huang, W. R., Letrun, R., Matlis, N., Mazalova, V., & Fromme, P. (2016, February 27). AXSIS: Exploring the frontiers IN Attosecond X-ray Science, imaging, and spectroscopy. Nuclear Instruments and Methods in Physics Research Section A: Accelerators, Spectrometers, Detectors, and Associated Equipment. https://www.sciencedirect.com/science/article/pii/S0168900216002564.

[124] - Yushin, G. (2013, February 28). The neutron scattering technique provides new data on ... Phys.org. https://phys.org/pdf281259376.pdf.

[125] - Gallego, N. C., Burchell, T. D., He, L., Kirkham, M. J., & Contescu, C. I. (2016, January). Neutron Irradiation Effects on the Structure of Highly Oriented Graphite: A XRD and SANS Study. ResearchGate. https://www.researchgate.net/publication/312118366_Neutron_Irradiation_Effects_on_the_Structure_of_Highly_Oriented_Graphite_A_XRD_and_SANS_Study.

[126] - Zavalij, P. Y. (2014, May 16). (Pdf) properties, sources, and detection of radiation. ResearchGates. https://www.researchgate.net/publication/226416238_Properties_Sources_and_Detection_of_Radiation.

[127] - Connolly, J. R. (2005). Introduction to x-ray powder diffraction. http://www.xray.cz/xray/csca/kol2011/kurs/dalsi-cteni/connolly-2005/01-xrd-intro.pdf.

[128] - Rachwal, J. D. (2010). X-ray diffraction applications in thin films And (100) silicon substrate stress analysis (thesis). The University of South Florida, Tampa, Fla.

[129] – D8 advance | Bruker. (n.d.). https://www.bruker.com/en/products-and-solutions/diffractometers-and-scattering-systems/x-ray-diffractometers/d8-advance-family/d8-advance.html. (User's Manual for Bruker AXS D8 Advance/D 8 Discover diffractometers. Germany, Karlsruhe: Bruker AXS GmbH (2010) – from American University of Beirut with all related documents)

[130] - Lecture 22: Matter waves. LECTURE 22 MATTER WAVES - UW Canvas. (n.d.). https://canvas.uw.edu.

[131]- Smith, B. C. (2011). Fundamentals of Fourier transform infrared spectroscopy. CRC Press.

[132]- Smith, B. C. (2002). Quantitative Spectroscopy: Theory and practice. Academic Press.

[133] - Perkampus, H.-H., Grinter, C. H., & Threlfall, T. L. (1992). Uv-vis spectroscopy and its applications. Springer-Verlag.

[134] - R., K. C. S. S. (2013). Uv-Vis and Photoluminescence spectroscopy For Nanomaterials Characterization. Springer Berlin Heidelberg.

[135]- Forster, H. (2004). UV/VIS Spectroscopy. Springer-Verlag. Springer-Verlag Mol. Sieves (2004)4:337-426.

[136] - Caro, C. A. D., & Claudia, H. (2017, November 12). (PDF) UV/VIS Spectrophotometry - fundamentals and applications. ResearchGate.

https://www.researchgate.net/publication/321017142_UVVIS_Spectrophotometry_-_Fundamentals_and_Applications.

[137] - Picollo, M., Aceto, M., & Vitorino, T. (2018, November 16). Marcello Picollo / maurizio Aceto / TATIANA VITORINO UV ... Physical Sciences Reviews. https://run.unl.pt/bitstream/10362/107857/1/_Physical_Sciences_Reviews_UV_Vis_spectroscopy.pdf.

[138] - Altemose, I. R. (1986, September 1). Evolution of instrumentation for UV-visible spectrophotometry. part I. Journal of Chemical Education. https://pubs.acs.org/doi/pdf/10.1021/ed063pA216.

[139] - Fournier-Salaun, M.-C., & Salaun, P. (2007). Quantitative determination of hexavalent chromium in aqueous solutions by UV-vis spectrophotometer. Central European Journal of Chemistry. https://link.springer.com/article/10.2478/s11532-007-0038-4.

[140]- Kumar, A., Deval, V., Tandon, P., Gupta, A., & D’silva, E. D. (2014, April 8). Experimental and theoretical (FT-IR, Ft-Raman, Uv–vis, NMR) spectroscopic analysis and first-order hyperpolarizability studies of non-linear OPTICAL material: (2e)-3-[4-(methyl sulfanyl) PHENYL]-1-(4-NITROPHENYL) Prop-2-en-1-one using density functional theory. Spectrochimica Acta Part A: Molecular and Biomolecular Spectroscopy. https://www.sciencedirect.com/science/article/pii/S1386142514004831.

[141] - Bessonneau, V., & Thomas, O. (2012, March 13). (Pdf) assessment of exposure to alcohol vapor from alcohol-based hand rubs. ResearchGate. https://www.researchgate.net/publication/225293966_Assessment_of_Exposure_to_Alcohol_Vapor_from_Alcohol-Based_Hand_Rubs.

[142] - Gao, X., Buckley, D. N., & Leahy, M. J. (2017). Vanadium Redox Flow Batteries For Large-Scale Energy Storage (thesis).

https://www.researchgate.net/publication/320902604_VANADIUM_REDOX_FLOW_BATTERIES_FOR_LARGE-SCALE_ENERGY_STORAGE.

[143] - Jiulong, S. (2017, February 27). (Pdf) development of inorganic-organic hybrid materials ... ResearchGate. https://www.researchgate.net/publication/314081363_Development_of_Inorganic-Organic_Hybrid_Materials_for_Waste_Water_Treatment. (thesis)

[144] - Bordoloi, A., & Mohanta, D. (2019, February 13). (PDF) a detailed study on optical and physical properties ... ResearchGate. https://www.researchgate.net/publication/327623886_A_DETAILED_STUDY_ON_OPTICAL_AND_PHYSICAL_PROPERTIES_OF_RICE_AND_ITS_BY-PRODUCTS. (thesis)

[145] - Cordero, E., Sivakov, V., & Ploss, B. (2016, March). (PDF) hydrogen generation on SILICON NANOSTRUCTURES. Researchgate. https://www.researchgate.net/publication/319036561_Hydrogen_Generation_on_Silicon_Nanostructures. (thesis)

[146] - Soliman, D. M., Ntziachristos, V., Westmeyer, G. G., & Ziegler, S. (2017). Augmented microscopy: Development and application of high-resolution optoacoustic and multimodal imaging techniques for label-free biological observation (thesis).

[147] - V-730 routine UV-visible SPECTROPHOTOMETER: JASCO: JASCO. JASCO Inc. (2021, July 14). https://jascoinc.com/products/spectroscopy/uv-visible-nir-spectrophotometers/models/v-730-uv-vis-spectrophotometer/. (User manual from American University of Beirut CRSL labs)

[148] - Flora, A. P., Rex, A. F., & Thornton, S. T. (2013). student solutions manual for Thornton & Rex's Modern physics, fourth edition (Third Ed.). Boston, MA: Brooks / Cole Cengage Learning.

[149] - Griffiths, P. R., & DeHaseth, J. A. (2007). Fourier transform infrared spectrometry (Second Ed.). New York: Wiley.

[150] - Christy, A. A., Ozaki, Y. & Gregoriou, V. G. (2001). Modern Fourier transforms infrared spectroscopy. Amsterdam: Elsevier.

[151]- Kauppinen, J., & Partanen, J. (2002). Fourier transforms in spectroscopy (First Ed.). Berlin: Wiley-VCH.

[152]- Bell, R. J. (1972). Introductory Fourier transform spectroscopy. New York: Acad. Pr.

[153] - Gaskill, J. D. (1978). Linear systems, Fourier transforms, and optics. United States: John Wiley & Sons.

[154]- Brigham, E. O. (1974). The fast Fourier transform. Englewood Cliffs, NJ: Prentice-Hall.

[155]- Bracewell, R. N. (2000). The Fourier transform and its applications (Third ed.). Boston: McGraw-Hill.

[156]- Bloino, J., & Barone, V. (2012, March 28). A second-order perturbation theory route to Vibrational averages and transition properties of molecules: General formulation and application to infrared and VIBRATIONAL Circular DICHROISM SPECTROSCOPIES. Retrieved from https://aip.scitation.org/doi/10.1063/1.3695210

[157]- Sroka-Bartnicka, A., Borkowski, L., Ginalska, G., Ślósarczyk, A., & Kazarian, S. (2016, August 02). Structural transformation of SYNTHETIC hydroxyapatite under simulated in VIVO conditions studied WITH ATR-FTIR SPECTROSCOPIC IMAGING. Retrieved from https://www.sciencedirect.com/science/article/pii/S1386142516304425

[158] - Aieta, C., Micciarelli, M., Bertaina, G., & Ceotto, M. (2020, August 28). Anharmonic quantum nuclear densities from full-dimensional vibrational eigenfunctions with application to protonated glycine. Retrieved, from https://www.nature.com/articles/s41467-020-18211-3

[159]- Ju, W., Lu, C., Liu, C., Jiang, W., Zhang, Y., & Hong, F. (2020, January 22). Rapid identification of atmospheric gaseous pollutants using Fourier-transform infrared spectroscopy combined with independent component analysis. Retrieved from https://www.hindawi.com/journals/jspec/2020/8920732/

[160] - Barone, V., Baiardi, A., Biczysko, M., Bloino, J., Cappelli, C., & Lipparini, F. (2012, June 13). Implementation and validation of a multi-purpose virtual spectrometer for large systems in complex environments. Retrieved from https://pubs.rsc.org/en/content/articlelanding/2012/cp/c2cp41006k

[161]- Jianbin, Z., Z., Hongquan, & G., Hong. (2000, February). Wavelet-Fourier self-deconvolution. Retrieved, from https://www.researchgate.net/publication/225766590_Wavelet-Fourier_self-deconvolution

[162]- Jusman, Y., Isa, N., Ng, S., Kanafiah, S., & Osman, N. (2015, August 19). Quadratic of Half ELLIPSE smoothing technique for Cervical CELLS FTIR spectra in a screening system. Retrieved, from https://www.sciencedirect.com/science/article/pii/S1877050915020530

[163]- Schmitt, M., Biemann, L., Meerts, W., & Kleinermanns, K. (2009, July 01). Analysis of the FTIR spectrum Of PYRAZINE using evolutionary algorithms. Retrieved from https://www.sciencedirect.com/science/article/pii/S0022285209001519

[164]- Highlander, T., & Rodriguez, A. (2016, January 25). Very efficient training of convolutional neural networks using fast Fourier transform and overlap-and-add. Retrieved, from https://arxiv.org/abs/1601.06815

[165]- Cecotti, H., & Graeser, A. (2008). Convolutional neural network with embedded Fourier transforms for EEG classification. Retrieved from https://ieeexplore.ieee.org/document/4761638/

[166]- R., Velik. (n.d.). Discrete Fourier transforms computation using neural networks. Retrieved from https://www.researchgate.net/publication/221175373_Discrete_Fourier_Transform_Computation_Using_Neural_Networks

[167]- Martin, M., & Hynes, J. T. (2004). Femtochemistry and femtobiology: Ultrafast events in molecular science. Amsterdam: Elsevier.

[168]- Meng, K., & Wang, J. (2010, December 20). Anharmonic overtone and combination states of glycine and two MODEL peptides examined by VIBRATIONAL SELF-CONSISTENT field theory. Retrieved, from https://pubs.rsc.org/en/content/articlelanding/2011/cp/c0cp01177k

[169] -Anharmonic vibrational spectroscopy http://kkrk.chem.elte.hu/molim/lectures/Electronic_vibrational_line_shape_Part2.pdf

[170]- Margenot, A., Parikh, S., & Calderón, F. (2019, January 10). Improving infrared spectroscopy characterization of soil organic matter with spectral subtractions: Protocol. Retrieved February 14, 2021, from https://www.jove.com/v/57464/improving-infrared-spectroscopy-characterization-soil-organic-matter.

[171] - Smolyaninov, I. I., & Smolyaninova, V. N. (2017, June 20). Hyperbolic metamaterials: Novel physics and applications. Solid-State Electronics. Retrieved

from https://cpb-us-w2.wpmucdn.com/wp.towson.edu/dist/d/225/files/2016/05/Solid-State-Electronics-2017-Hyperbolic-metamaterials-trq3wc.pdf

[172] - Smolyaninov, I. I. (2018). Hyperbolic metamaterials. Morgan & Claypool Publishers.

[173] - Maier, S. A., & Smolyaninov, I. I. (2018). Chapter 3 - Hyperbolic Metamaterials. In World Scientific Handbook of Metamaterials and Plasmonics (Vol. Volume 1). essay, World Scientific.

[174] - Guo, Z., Jiang, H., & Chen, H. (2020, February 21). Hyperbolic metamaterials: From dispersion manipulation to applications. AIP Publishing. Retrieved from https://aip.scitation.org/doi/10.1063/1.5128679

[175] - Smolyaninov, I. I. (2011, January 24). Virtual Black Holes in Hyperbolic Metamaterials. aXriv.org. from https://arxiv.org/abs/1101.4625

[176] - Urbas, A. M. (2016, August 9). Roadmap on optical metamaterials - iopscience. iopscience/Journal of Optics. Retrieved from https://iopscience.iop.org/article/10.1088/2040-8978/18/9/093005/meta or Augustine M Urbas et al 2016 J. Opt. 18 093005

[177] - Pendharker, S., Hu, H., Molesky, S., Starko-Bowes, R., Poursoti, Z., Pramanik, S., Nazemifard, N., Fedosejevs, R., Thundat, T., & Jacob, Z. (2017, March 31). Thermal graphene metamaterials and epsilon-near-zero high-temperature plasmonics. iopscience.iop.org/ Journal of Optics. Retrieved from https://iopscience.iop.org/article/10.1088/2040-8986/aa6010

[178] - Chen, P.-Y., Hajizadegan, M., Sakhdari, M., & Alù, A. (2016, April 28). Giant photoresponsivity of mid-infrared hyperbolic metamaterials in the quantum regime. PHYSICAL REVIEW APPLIED. Retrieved from https://journals.aps.org/prapplied/abstract/10.1103/PhysRevApplied.5.041001

[179] - Chen, Y., Zhang, R.-Y., Xiong, Z., Hang, Z. H., Li, J., Shen, J. Q., & Chan, C. T. (2019, July 16). Non-abelian gauge field optics. Nature Communications. Retrieved January 9, 2022, from https://www.nature.com/articles/s41467-019-10974-8

[180] - Nicolet Magna Ftir Thermo FT-IR Spare Parts. (n.d.). Retrieved from http://www.ir-spectra.com/services/magna.htm

[181] - Omnic software free download FTIR 16 . Wakelet. (n.d.). Retrieved January 29, 2022, from https://wakelet.com/wake/WHqc9-0pKV52IoPjXGc7B

[182] - BettinaBettina 7111 silver badge22 bronze badges, EvilEvil 9, & Yuval FilmusYuval Filmus 263k2525 gold badges280280 silver badges460460 bronze badges. (1964, January 1). How does the stockham FFT work? Computer Science Stack Exchange. Retrieved from https://cs.stackexchange.com/questions/51742/how-does-the-stockham-fft-work

[183] - Yeragi, E., Nalawad, K. P., Gotmare, S., Yeragi, P., & Prabhu, V. (2019, August 7). Iosr-JDMS   volume-18 ~ issue-8 ~ August-2019. IOSR Journal. Retrieved January 29, 2022, from https://iosrjournals.org/iosr-jdms/papers/Vol18-issue8/Series-5/A1808050108.pdf

[184] - Lin, H.-H., Hung, K.-K., Wang, L.-Y., & Su, W.-H. (2016, September 7). A 3D translation stage calibrated with Michelson interferometers. SPIE Digital Library. Retrieved January 29, 2022, from https://www.spiedigitallibrary.org/conference-proceedings-of-spie/9958/1/A-3D-translation-stage-calibrated-with-Michelson-interferometers/10.1117/12.2240068.full

[185] - Applications and solutions 2012 - jasco inc.. (n.d.). Retrieved from http://jascoinc.com/docs/application-notes/applications_and_solutions_2012-3.pdf

[186] - Small microstructure analysis equipment (scanning electron microscope (SEM)) Vega LMS. UseScience. (n.d.). Retrieved January 29, 2022, from

https://scientificservices.eu/id/item/5820/small-microstructure-analysis-equipment-scanning-electron-microscope-sem-vega-lms.html

[187] - Parasuraman, K., Mishra, M., & Balakrishnan, G. (2016, August 17). Schematic of pulsed laser deposition system. | Microstructure and Optical Properties of Nano Multilayers of CeO2/ZrO2 and Gd2O3/CeO2 Prepared by Pulsed Laser Deposition. ResearchGate. Retrieved from https://researchgate.net/figure/Schematic-of-pulsed-laser-deposition-system_fig1_306227437

[188] - Hamad, A. H. (2016, November 6). (PDF)Effects of Different Laser Pulse Regimes (Nanosecond, Picosecond and Femtosecond) on the Ablation of Materials for Production of Nanoparticles in Liquid Solution. ResearchGate. Retrieved January 29, 2022, from https://www.researchgate.net/publication/307887440_Effects_of_Different_Laser_Pulse_Regimes_Nanosecond_Picosecond_and_Femtosecond_on_the_Ablation_of_Materials_for_Production_of_Nanoparticles_in_Liquid_Solution

[189] - Verma, S. K., Maheshwari, S., Singh, R. K., & Chaudhari, P. K. (2016, September 28). Laser in dentistry: An innovative tool in modern dental practice. ResearchGate. Retrieved from https://www.researchgate.net/publication/247153953_Laser_in_dentistry_An_innovative_tool_in_modern_dental_practice

[190] - Krivosik, P. (n.d.). Magnetization Dynamics Group - Pld System. Retrieved from http://www2.physics.colostate.edu/groups/PattonGroup/systems/pld_desc.html

[191] - Pulsed laser deposition - PUDITEC. puditec.com. (n.d.). Retrieved from https://www.puditec.com/pld

[192] - Afsahi, M., &; Oraizi, H. (2018, January 13). (PDF) transmission line modeling and numerical simulasion ... ResearchGate. Retrieved, from https://www.researchgate.net/publication/228360641_Transmission_Line_Modeling_

and_Numerical_Simulasion_for_the_Analysis_and_Optimum_Design_of_Metamaterial_Multilayer_Structures

[193] - Al Shara, S., Mahasneh, A. A., & Al-Qararah, A. M. (2011, January 6). Solution of Time-Independent Schrodinger Equation for a Two-Dimensional Quantum Harmonic Oscillator Using He's Homotopy Perturbation Method. ResearchGate. Retrieved from https://www.researchgate.net/publication/228531722_Solution_of_Time-Independent_Schrodinger_Equation_for_a_Two-Dimensional_Quantum_Harmonic_Oscillator_Using_He's_Homotopy_Perturbation_Method

[194] - The Moscow Institute of Physics and Technology (MIPT). (2020, August 14). New phase of nanoconfined water discovered. Smart Water Magazine. Retrieved from https://smartwatermagazine.com/news/moscow-institute-physics-and-technology-mipt/new-phase-nanoconfined-water-discovered.

[195] - http://charma.uprm.edu/~mendez/Lectures/OpenStax_v3/v3_ed0_openstax_03.pdf. vdocuments.mx. (n.d.). Retrieved from https://vdocuments.mx/http://charma.uprm.edu/~mendez/Lectures/OpenStax_v3/v3_ed0_openstax_03.pdf

[196] - https://physics.unm.edu/Courses/Gruzdev/Phys554Sp20/documents/lecture1.pdf. (n.d.). Retrieved from https://physics.unm.edu/Courses/Gruzdev/Phys554Sp20/documents/lecture1.pdf

[197] - Dislocation - University of Babylon. (n.d.). Retrieved from http://www.uobabylon.edu.iq/eprints/publication_12_10332_983.pdf

[198] - File:point defects in Crystal Structures.svg. Wikimedia Commons. (n.d.). Retrieved from https://commons.wikimedia.org/wiki/File:Point_defects_in_crystal_structures.svg

[199] - American Univesity of Beirut. Facilities. (n.d.). Retrieved from https://www.aub.edu.lb/fas/crsl/Pages/facilities.aspx

[200] - Park, M. J., Park, K., Kim, D. H., & Jang, D. Y. (2008, July 9). Design and analysis of a thermionic SEM column using 3D finite element analysis. ResearchGate. Retrieved from https://www.researchgate.net/publication/243652746_Design_and_analysis_of_a_thermionic_SEM_column_using_3D_finite_element_analysis

[201] - Wikimedia Foundation. (n.d.). Thomas Eugene Everhart. Wikipedia. Retrieved, from https://en.wikipedia.org/wiki/Thomas_Eugene_Everhart

[202] - University of Washington Center for Quantitative Science, U. by the T. E. C. P. (2020, November 23). 7.3 heat transfer processes: Calculus-integration. 7.3 Heat Transfer Processes | Calculus-Integration. Retrieved from https://bookdown.org/huckley/Physical_Processes_In_Ecosystems/7-3-heattransfer-heat.html

[203] - Santhanam, V. (2021, February 28). Raman spectrosocpy - Sri Chandrasekharendra Saraswathi ... Theory of Raman Spectroscopy Department of Chemistry SCSVMV. Retrieved from https://kanchiuniv.ac.in/coursematerials/Raman%20Spectra.pdf

[204] - Raman scattering in den fluoreszenz-emissions-spektren by Edinburgh Instrumentsdirectindustry. 2 Bain Square, Livingston EH54 7DQ, UK - Edinburgh Instruments. (n.d.). Retrieved from https://trends.directindustry.de/edinburgh-instruments/project-25178-187745.html

[205] - Scigelova, M., Hornshaw, M., Giannakopulos, A., & Makarov, A. (2011, May 9). Fourier transform mass spectrometry. Molecular & cellular proteomics : MCP. Retrieved from https://www.ncbi.nlm.nih.gov/pmc/articles/PMC3134075/

[206] - Www.facebook.com/umairhussaini. (2020, June 1). What is aliasing in DSP and how to prevent it? Technobyte. Retrieved from https://technobyte.org/whats-aliasing-dsp-how-to-prevent-it/

[207] - Wayne, K. (2005, March 26). 5. D ivide and C Onquer - Princeton University. Princeton University. Retrieved from https://www.cs.princeton.edu/courses/archive/spring18/cos423/lectures/05DivideAndConquerI-2x2.pdf

[208] - YouTube. (2020, July 1). Baseline correction in origin for FTIR | XRD | XPS | UV-vis spectra #baseline. YouTube. Retrieved from https://www.youtube.com/watch?v=vk9zs7jGjvM

[209] - Contents. courses.physics.ucsd.edu. (n.d.). Retrieved from https://courses.physics.ucsd.edu/2019/Fall/physics239/LECTURES/C02.pdf

[210] - Camps, Camps♦Camps -17.6k22 gold badges1616 silver badges108108 bronze badges, & Xivi76Xivi762. (1968, May 1). Labeling of high symmetry points in Brillouin Zone. Matter Modeling Stack Exchange. Retrieved from https://mattermodeling.stackexchange.com/questions/1086/labeling-of-high-symmetry-points-in-brillouin-zone

[211] - Reticoli - webusers.fis.uniroma3.it. (n.d.). Retrieved from http://webusers.fis.uniroma3.it/~gallop/Reticoli_light.pdf